



HAL
open science

Characterization, modeling and aging behavior of GaN power transistors

Fadi Nader Fouad Zaki

► **To cite this version:**

Fadi Nader Fouad Zaki. Characterization, modeling and aging behavior of GaN power transistors. Electric power. Université Paris Saclay (COMUE), 2018. English. NNT: 2018SACLN001. tel-01794546

HAL Id: tel-01794546

<https://theses.hal.science/tel-01794546>

Submitted on 17 May 2018

HAL is a multi-disciplinary open access archive for the deposit and dissemination of scientific research documents, whether they are published or not. The documents may come from teaching and research institutions in France or abroad, or from public or private research centers.

L'archive ouverte pluridisciplinaire **HAL**, est destinée au dépôt et à la diffusion de documents scientifiques de niveau recherche, publiés ou non, émanant des établissements d'enseignement et de recherche français ou étrangers, des laboratoires publics ou privés.

Characterization, modeling and aging behavior of GaN power transistors.

NNT : 2018SACLN001

Thèse de doctorat de l'Université Paris-Saclay
préparée à l'Institut français des sciences et technologies des
transports, de l'aménagement et des réseaux/
laboratoire SATIE.

École doctorale n°575: electrical, optical, bio: physics and
engineering (EOBE)
Spécialité de doctorat: Physique

Thèse présentée et soutenue à l'École Normale Supérieure Paris-Saclay, le 29/01/2018, par

Fadi Nader Fouad Zaki

Composition du Jury :

Frédéric Morancho Professeur des universités, Université de Toulouse III Paul Sabatier	Rapporteur
Olivier Latry Maître de Conférences - HDR, Université de Rouen	Rapporteur
Stéphane Lefebvre Professeur des universités, CNAM	Examineur
Dominique Planson Professeur des universités, INSA Lyon	Président
René Escoffier Docteur- Ingénieur, CEA-LETI	Examineur
Ali Ibrahim Docteur- Ingénieur, IFSTTAR	Examineur
Zoubir Khatir Directeur de recherche, IFSTTAR	Directeur de thèse

“Happiness lies in the joy of achievement, in the thrill of creative effort”.

**Franklin D. Roosevelt,
32nd president of US (1882 - 1945).**

**For the people who let me be seduced by science, my parents Nader Fouad
and Mervat Nagy, to my family,...**

Abstract

Characterization, modeling and aging behavior of GaN power transistors.

Seeking green cities, reducing the greenhouse effect and finding a substitute to oil uses are all strong reasons that attract research and industry to find other alternatives. One of these solutions is a broader use of electrical energy. Over the years, this energy sector has been widespread by using power electronics in many automotive, aeronautical and military applications. A power electronics system is mainly composed of power components such as diodes and transistors. Depending on the applications, these components may have specific characteristics to withstand severe operating conditions such as high temperature, high power, and high-frequency operations. In order to reach these characteristics, the power devices must be made of specific semiconductor materials. Initially, the most common semiconductor material (Silicon) is used, but it shows some performance limitations for power electronics applications. Over the last two decades, with research and development, there has been new materials that have demonstrated better characteristics than Silicon. Silicon Carbide (SiC) and Gallium Nitride (GaN) have shown many advantages for use in power electronics. They present the materials estimated to be widely used for power electronics shortly; they have attracted significant interest benefiting from their excellent semiconductor properties.

The presence of advantages for a device is not sufficient before its emergence in real applications. The reliability issue is essential and represents an inevitable phase before validating its use. Although GaN components have shown many advantages, users are wondering: "*Are we ready to use these components in real applications?*" Much current research is underway to answer this question. In this thesis, we will participate in the answer. The main objective of this thesis is to study some elements of the GaN High Electron Mobility Transistors (HEMT) reliability for power applications. The power transistors reliability study is carried out by a lot of theoretical and experimental works. It can be performed at the semiconductor, packaging or system level. In this thesis, we present theoretical and experimental works carried out only at the semiconductor level.

GaN transistors suffer from a reversible physical phenomenon called *trapping*; this phenomenon represents a source of instability of the device physical and electrical characteristics. It has presented an essential element for the reliability works of GaN HEMTs. The full understanding of the effect of this phenomenon and its evolution with ageing is not yet fully accomplished. In this thesis, we present theoretical and experimental works to understand better the reliability linked to this phenomenon and the possible evolution with ageing in power cycling conditions. This work was carried out within the framework of the French MEGaN project, funded by the public investment bank Bpifrance. These studies were carried out on two different components; the first one is manufactured and supplied by a project partner CEA–LETI, the second one is a commercial power device fabricated by GaN Systems Inc.

Regarding the nature of these two used devices, they are lateral transistors, with an internal structure based on a heterostructure of two different semiconductor materials AlGaIn and GaN. Due to the difference in polarization at the heterointerface and the difference in gaps between AlGaIn and GaN, a 2–D confined electron gas (2DEG) is formed at the hetero–interface. The 2DEG density is dependent on

many parameters, among them, the concentration of Aluminum in the AlGaN layer passing through intentional and unintentional doping (traps) and the thickness of the different layers. All these parameters are controllable except the presence of these unintentionally introduced traps that uncontrollably may modify the 2DEG density. Furthermore, the existence of these traps can also modify the electric field distribution in the structure, and consequently the 2DEG mobility. The modification of these physical parameters will affect thereafter the device electrical characteristics such as the threshold voltage and the on-state resistance.

Contributions:

In order to further understand theoretically and experimentally the effect of these traps, this work contributes by three main topics, both theoretical as well as experimental.

- Relative weight between surface traps and Oxygen barrier traps of Al₂O₃/AlGaN/GaN Normally–ON MOS–HEMTs (chapter 2).

We present an original theoretical study of the relative weight between surface and Oxygen barrier traps located under the gate on the 2DEG density. This theoretical study was carried out by developing a semi-analytical 1D charge model based on the nonlinear Poisson and Schrödinger equations. Regarding barrier traps, we have developed a new analytical expression of the electric field distribution throughout the AlGaN barrier. This expression estimates the electric field distribution by taking into account the traps energy level located in the barrier and the ionized traps profile by the Fermi–Dirac distribution. The model was applied to the case of Oxygen and implemented by an iterative method to solve the electric field expression and to calculate the potential distribution. In order to get input data for the model, especially traps information, such as activation energies and cross-sections, a secondary ion mass spectrometry (SIMS) and deep level transient spectroscopy (DLTS) measurements were performed by the project partner CEA–LETI on a Normally–ON MOS–HEMT. A mean Oxygen traps density up to $2 \times 10^{18} \text{cm}^{-3}$ was revealed in the AlGaN barrier associated with an activation energy of 0.44 eV and a cross-section of $1.4 \times 10^{-14} \text{cm}^2$. Regarding interface traps, we have taken a mathematical form developed in the literature that describes the well-known U-shape of the interface traps for a similar structure to the studied one. The model allows to estimate:

1. The potential and electric field distribution.
2. The ionized Oxygen profile according to the applied gate voltage.
3. The total ionized traps charge in the AlGaN barrier and the total interface traps charge.

The weight of the different charges source on the total charges under the gate has been estimated by using these estimated theoretical quantities. Finally, the theoretical results showed that there is no absolute domination of Oxygen traps from the barrier or the interface and their impact on the 2DEG density depends strongly on the polarization conditions. A non-linear relation between the 2DEG density and the applied gate voltage – contrarily to the existing results of analytical models – was found.

- Characterization of long-term traps of commercial power devices (GaN Systems Inc.) (chapter 3)
Characterization of long-term (long time constants) traps of commercial GaN–Systems power devices is presented. These characterizations are based on the transient current measurements method divided between drain and gate lag measurements for different temperatures and polarization conditions. The measurements were made over several time scales to detect long and short

traps. The Prony multi-exponential method to extract trapping time constants has been used. The activation energies and cross sections based on the Arrhenius law have been extracted. We present the detailed measurements methodology followed and the test bench used. These measurements have shown that trapping and de-trapping may occur during the same transient process. We found that the measured transient currents are in some cases susceptible to quantitative and qualitative changes responding to different OFF state stress conditions between stress time and stress level.

- Power cycling of Normally–ON power devices (chapter 4)

Aging power cycling tests were performed on $\text{Al}_2\text{O}_3/\text{AlGaIn}/\text{GaN}$ MOS–HEMTs manufactured by CEA–LETI to understand its effect on the traps state evolution. Very few works have been done in the literature to our knowledge concerning power cycling tests on HEMTs. We used the methodology presented in chapter 3 to perform transient measurements before and after this ageing test. This test was performed on components reported on a direct copper bonding (DCB) with the help of the 3D Power Hybrid Integration platform (3DPHI). The instrumentation of the test bench has been adapted for these components.

Junction temperature measurements were performed using the Temperature Sensitive Electrical Parameters (TSEP) method. The components underwent a ΔT_j of $100\text{ }^\circ\text{C}$ for two thousand cycles. Final characterizations have shown that there is indeed a shift in threshold voltage and on-state resistance that correlates with a shift in the transient current measurements.

So, it has been demonstrated for the first time that a power cycling test affects the evolution of the traps of $\text{Al}_2\text{O}_3/\text{AlGaIn}/\text{GaN}$ structure. We noticed a quantitative and qualitative change in the transient current measurements.

In summary, the state of the art presented in chapter 1 was the basis of this reliability study, the theoretical results in chapter 2 showed the relevance of the two traps sources (barrier and interface) under the gate on the 2DEG density, the experimental measurements presented in chapter 3 proved the existence of traps in commercial components GaN Systems, this chapter also formed the basis for the experimental study of aging in chapter 4. This work could participate in the image of the reliability study of these power devices.

Résumé étendu en Français

Caractérisation, Modélisation et Comportement au vieillissement des transistors GaN de puissance.

Contexte : Les besoins de villes durables, la réduction de l'effet de serre et la recherche d'un suppléant aux énergies fossiles sont autant de raisons qui poussent la recherche et l'industrie à trouver d'autres alternatives. Une de ces solutions est une utilisation plus large de l'énergie électrique. Au fil des années, ce vecteur d'énergie a été largement répandu en utilisant l'électronique de puissance dans des applications dans de nombreux domaines tels que l'automobile, l'aéronautique, ferroviaire et militaire. Les systèmes électroniques de puissance sont composés en partie de composants actifs de puissance tels que des diodes et des transistors. Les applications nécessitant des conditions de fonctionnement sévères en termes de températures ambiantes, de variations de températures de fortes amplitudes ou de fortes tensions requièrent des composants avec des caractéristiques spécifiques. Pour certaines des applications pour lesquelles les contraintes sont élevées, les composants doivent être à base de matériaux grands gaps comme le carbure de silicium (SiC) ou le nitrure de galium (GaN), le silicium quant à lui présentant certaines limitations.

Les atouts et avantages liés à un composant ne sont malgré tout pas suffisants pour sa diffusion dans les applications. Les problèmes de fiabilité sont importants et représentent une phase inévitable avant de valider son utilisation. Bien que les composants GaN aient montré de nombreux avantages, la question de leur fiabilité reste posée pour leur utilisation dans les applications. De nombreuses recherches sont en cours pour répondre à cette question. Les travaux menés dans cette thèse participent à cette réponse. L'objectif principal de cette thèse est d'étudier certains éléments de la fiabilité des transistors GaN à haute mobilité électronique (HEMT) pour les applications de puissance. L'étude de la fiabilité des composants à semi-conducteurs nécessite des approches théoriques et expérimentales. Les composants doivent être conformes aux environnements sévères (correspondant à des applications réelles), et doivent également fonctionner de manière cohérente pendant de longues périodes. Parmi ces domaines, côté théorique, on peut citer la physique des semi-conducteurs, la modélisation mathématique et les simulations numériques multi physiques. En revanche, côté expérimental, cela commence par des caractérisations électriques, thermiques et physiques ainsi que des tests expérimentaux de vieillissement. Enfin, il est à noter l'importance de l'analyse des défaillances dans ce processus. Ces champs fournissent les éléments nécessaires pour étudier les modes de dégradation des composants de puissance et réaliser une étude de fiabilité.

Dans l'état actuel de la technologie, les transistors GaN souffrent encore d'un phénomène physique réversible appelé "piégeage", ce phénomène représente une source d'instabilité des caractéristiques physiques et électriques du composant. Il est un des éléments de fiabilité qu'il reste à résoudre pour les transistors HEMTs à base de GaN dans le domaine de la puissance. La pleine compréhension des effets de ces mécanismes et de leurs évolutions avec le vieillissement n'est pas encore complètement accomplie. Dans cette thèse, nous présentons des travaux théoriques et expérimentaux pour mieux comprendre la fiabilité liée à ce phénomène et l'interaction possible avec le vieillissement dans des conditions de cyclage de

puissance.

Ces composants sont des transistors latéraux avec une structure interne basée sur une hétérostructure de deux matériaux semi-conducteurs AlGaIn et GaN. En raison de la différence de polarisation à l'hétérointerface et de la différence de bande interdite entre AlGaIn et GaN, un gaz d'électrons confiné 2-D (2DEG) est formé à l'hétérointerface. La densité d'électrons dans le canal (ou du 2DEG) dépend de nombreux paramètres, parmi lesquels la concentration d'aluminium dans la couche AlGaIn passant par le dopage intentionnel et non intentionnel et l'épaisseur des différentes couches. Tous ces paramètres sont contrôlables sauf la présence des pièges introduits involontairement qui peuvent modifier de manière incontrôlable la densité du 2DEG. De plus, l'existence de ces pièges peut également modifier la distribution du champ électrique dans la structure, et par conséquent la mobilité et la densité 2DEG. La modification de ces paramètres physiques affectera par la suite les caractéristiques électriques des composants telles que la tension de seuil et la résistance à l'état passant.

Contributions:

Afin de mieux comprendre théoriquement et expérimentalement l'effet de ces pièges, ce travail contribue avec trois points principaux, à la fois théoriques et expérimentaux.

- Poids relatif entre les pièges de surface et les pièges d'oxygène dans la barrière AlGaIn des MOS-HEMT normalement-on en $\text{Al}_2\text{O}_3/\text{AlGaIn}/\text{GaN}$ (Chapitre 2).

Il a été montré précédemment que les états d'interface à la surface d'AlGaIn avec une densité d'état allant jusqu'à $1 \times 10^{13} \text{ cm}^{-2}$ peuvent avoir un impact significatif sur les caractéristiques électriques du composant. Ces états peuvent être localisés: entre la grille et le drain dans des composants non passivés et forme ensuite la grille virtuelle, ou située sous la grille dans des composants passivés.

La raison de cette haute densité d'états d'interface s'explique principalement par la formation de lacunes d'azote à la surface d'AlGaIn lors du recuit à haute température. Il faut noter que des efforts technologiques ont été faits pour neutraliser leurs effets comme passiver la surface par SiO_2 , Si_3N_4 ou SiON ou bien effectuer un traitement N_2O .

La réduction des états de l'interface modifie l'équilibre des effets des pièges éventuellement présents dans les couches de volume du composant. Certaines recherches ont récemment rapporté les effets des états d'interface lorsque le composant est correctement passivé et ont montré que leur effet devient négligeable par rapport aux pièges de la barrière.

Comme source de ces défauts en vrac, il a été rapporté la diffusion possible d'une haute densité d'oxygène pendant la fabrication et la formation de liaisons Ga-O dans la couche d'AlGaIn qui induit par la suite des pièges d'oxygène dans la barrière. L'un des problèmes restants est de comprendre les effets des poids relatifs entre les pièges d'interface et de volume sur le comportement du composant. En particulier, les effets relatifs de ces sources des pièges sur la dépendance de la densité 2DEG et de la tension de grille doivent être mis en évidence.

Dans la première partie de cette thèse, nous étudions théoriquement cette question. Plus précisément, nous présenterons une étude théorique du poids entre les pièges de l'oxygène dans la barrière et les pièges de surface AlGaIn sur la concentration de 2DEG dans différentes conditions de polarisation de grille. Pour ce faire, un modèle de charge 1D semi-analytique a été développé en utilisant les équations couplées de Poisson et de Schrödinger non linéaires.

Ce modèle est basé sur une nouvelle expression analytique de la distribution du champ électrique sous la grille incluant le profil d'oxygène ionisé dans la barrière AlGaIn. Cette expression estime la distribution du champ électrique en tenant compte du niveau d'énergie des pièges situés dans la barrière et du profil des pièges ionisés par la distribution de Fermi-Dirac. Le modèle a été appliqué

au cas de l'oxygène et mis en oeuvre par une méthode itérative pour résoudre l'expression du champ électrique et calculer la distribution du potentiel. Afin d'obtenir des données d'entrée pour le modèle, des mesures de *Secondary Ion Mass Spectrometry* (SIMS) et de *Deep Level Transient Spectroscopy* (DLTS) ont été effectuées par le CEA-LETI sur un MOS-HEMT normalement-ON. Une densité moyenne de pièges à oxygène allant jusqu'à $2 \times 10^{18} \text{cm}^{-3}$ a été révélée dans la barrière AlGaN associée à une énergie d'activation de 0.44 eV et un cross section de $1.4 \times 10^{-14} \text{cm}^2$.

En ce qui concerne les pièges d'interface, nous avons pris une forme mathématique développée dans la littérature qui décrit la forme en U bien connue des pièges d'interface pour une structure similaire à celle étudiée.

Le modèle permet d'estimer: i) la distribution du potentiel et du champ électrique, ii) le profil d'oxygène ionisé en fonction de la tension de grille appliquée, iii) la charge ionisée totale dans la barrière AlGaN et la charge totale à l'interface. En utilisant ces quantités théoriques estimées, le poids des différentes sources de charges sur les charges totales sous la grille a été estimé. Enfin, les résultats théoriques ont montré qu'il n'y a pas de domination absolue des pièges d'oxygène de la barrière ou de la surface et que leur impact sur la concentration de 2DEG dépend fortement des conditions de polarisation. Nous avons également observé un comportement non-linéaire de la densité 2DEG avec la tension de la grille contrairement aux résultats existants des modèles analytiques (qui estime une relation linéaire).

- Caractérisation des pièges à long terme des composants commerciale (GaN Systems Inc.) (Chapitre 3)

Les phénomènes de piégeage posent un problème réel qui entrave le bon fonctionnement des composants HEMT. Leurs effets sont réversibles et agissent sur le comportement électrothermique des composants.

Ils peuvent avoir plusieurs effets sur les caractéristiques électriques statiques et transitoires des composants. Etant donné que ces pièges sont généralement introduits involontairement avec des densités élevées, ils peuvent entraîner des disparités importantes dans le comportement des composants avec la même référence du fabricant.

Les pièges situés sous la grille peuvent provoquer un décalage important de la tension de seuil. Les pièges situés entre le drain et la grille peuvent avoir un effet direct sur la densité 2DEG, sur les caractéristiques I-V et sur la résistance à l'état passant. En mode transitoire, nous pouvons observer une variation significative du courant transitoire en réponse à un changement de l'état de polarisation de la grille ou du drain. Afin d'utiliser correctement ces composants, nous devons comprendre explicitement le comportement de ces pièges et quantifier leurs effets dans différentes conditions de polarisation et de température. Sur ce point, nous présentons une étude expérimentale détaillée des pièges pour les composants de commutation commerciaux de GaN Systems Inc. L'étude vise à comprendre le comportement des pièges dans ces composants et à présenter une méthodologie de caractérisation qui sera utilisée par la suite pour le troisième point de la thèse pour évaluer l'effet du vieillissement sur l'évolution des pièges. Pour ces mesures, nous présenterons le banc de test et l'équipement utilisé pour les réaliser. Nous présenterons également une méthodologie qui vise à étudier la capacité à détecter et caractériser ces paramètres de piégeage, sur une grande échelle de constantes de temps, en fonction du temps de l'application en blocage de la tension de grille. Les mesures de température de jonction ont été réalisées à l'aide d'un capteur thermique à fibre optique pour vérifier que l'auto-échauffement reste négligeable lors des mesures.

Pour extraire les paramètres physiques des pièges, c'est-à-dire les énergies d'activation et les sections efficaces, la décomposition du signal basée sur l'algorithme de Prony a été utilisée pour extraire les constantes de temps et a été complétée par le modèle Shockley-Read-Hall. Nous présenterons également le flux de traitement du signal effectué avant d'extraire les constantes de temps, y compris le filtrage, le lissage et la décimation. Certaines mesures de transitoires seront également présentées avec la dépendance de la température pour expliquer le comportement de piégeage. Ces mesures ont montré que le piégeage et le dé-piégeage de charges peuvent se produire au cours de la même mesure transitoire. Nous avons constaté que les courants transitoires mesurés sont très sensibles aux changements quantitatifs et qualitatifs répondant à différentes conditions de stress à l'état OFF. Des pièges qui sont corrélés avec l'absence d'azote ou la présence du carbone, oxygène ou hydrogène dans la position de substitution ont été relevés à partir de ces mesures.

- Cyclage de puissance des MOS–HEMT en $\text{Al}_2\text{O}_3/\text{AlGaIn}/\text{GaN}$ (Chapitre 4).

Le vieillissement peut entraîner une dégradation irréversible des caractéristiques électriques du composant. Les composants de puissance sont généralement intégrés dans des modules de puissance. Ainsi, les modes de dégradation peuvent se produire soit au niveau semi-conducteur, soit au niveau de l'assemblage. Pour les modules de puissance basés sur des transistors de silicium, une dégradation au niveau de l'assemblage peut probablement survenir, et il est rare que le niveau des composants soit détérioré. Cela est dû à la maturité de la technologie des composants à base de silicium. Cependant, en ce qui concerne les dégradations qui peuvent survenir au niveau de l'assemblage, on peut avoir une délamination de l'une des couches de matériaux de l'assemblage, la dégradation au niveau de la brasure est également répandue et la détérioration au niveau des fils de liaison. Ces dégradations sont principalement dues à l'effet cumulé induit par l'auto-échauffement à chaque cycle.

Ces effets accumulés se reflètent dans l'évolution de l'état mécanique des matériaux. Certains matériaux peuvent entrer dans la zone plastique sous l'impact de contraintes mécaniques (comme le cuivre). Pour les matériaux fragiles tels que les céramiques (Si_3N_4), ils peuvent casser directement après avoir dépassé la limite de l'élasticité. Concernant la dégradation induite au niveau du composant, le semi-conducteur peut être dégradé soit par une contrainte mécanique directe générée par l'assemblage sur le Composant, soit par une contrainte mécanique indirecte provoquée par l'auto-échauffement induit par la puissance injectée dans le Composant. Dans les deux cas, une modification au niveau microstructural peut modifier les caractéristiques électriques du Composant, par exemple, une densité de défauts supplémentaires peut être générée à l'intérieur du cristal. Cependant, ces tests accélérés sont bien connus pour étudier la fiabilité des composants de puissance et estimer la durée de vie du Composant. Des essais de vieillissement basés sur des cycles de puissance ont été réalisés sur des MOS–HEMT $\text{Al}_2\text{O}_3/\text{AlGaIn}/\text{GaN}$ GaN fabriqués par le CEA–LETI pour comprendre son effet sur l'évolution des pièges dans ce troisième point.

Très peu de travaux ont été effectués dans la littérature à notre connaissance concernant les tests de cycles de puissance sur les HEMT et surtout pour étudier les effets des pièges. Nous avons utilisé la méthodologie présentée au point 2 pour effectuer des mesures transitoires avant et après ce test de vieillissement. Ce test a été réalisé sur des composants rapportés sur DCB à l'aide de la plateforme 3D Power Hybrid Integration (3DPHI).

Une instrumentation du banc d'essai a été adaptée pour ces composants. Les mesures de température de jonction ont été effectuées en utilisant la méthode des paramètres électriques sensibles à la température (TSEP). Les composants ont subi un ΔT_j de 100 °C pendant deux mille cycles. Les caractérisations finales ont montré qu'il y a effectivement un décalage de la tension de seuil et

de la résistance à l'état passant qui est corrélé avec un changement dans les mesures de courant transitoire et lié au vieillissement.

Ainsi, il a été démontré pour la première fois qu'un test de cyclage de puissance a un effet sur l'évolution des pièges de la structure $\text{Al}_2\text{O}_3/\text{AlGaIn}/\text{GaIn}$. Nous avons remarqué un changement plutôt quantitatif et non qualitatif dans les mesures de courant transitoire. Ce résultat a montré que la densité des pièges existants a probablement augmenté, mais cela doit être confirmé par d'autres caractérisations. Nous n'avons pas observé de changement de qualité, ce qui montre qu'il n'y a probablement pas eu d'évolutions au niveau de l'introduction de nouveaux niveaux d'énergie dans la structure. Il est à noter que nous avons aussi effectué plusieurs campagnes de vieillissement sur des composants commerciaux GaN-systèmes, mais une source d'instabilités significatives, des comportements non compréhensibles et aussi la non-maturité du composant après vieillissement ont rendu ces campagnes infructueuses. Par exemple, nous avons mené des campagnes où les composants se sont détériorés lors des premières caractérisations après vieillissement, ceci représentait un point de blocage pour l'analyse et l'étude du vieillissement. En outre, le processus de packaging industriel complexe, les secrets de fabrication des structures internes ont multiplié les difficultés vis-à-vis du problème traité.

En résumé, l'état de l'art présenté en chapitre 1 est la base de cette étude de fiabilité, les résultats théoriques du chapitre 2 ont montré la pertinence des deux sources de pièges sous la grille sur la densité 2DEG, les mesures expérimentales présentées en chapitre 3 font preuve à l'existence de pièges dans les composants commerciaux GaN Systems, ce chapitre a également constitué la base de l'étude expérimentale du vieillissement en chapitre 4. Ce travail pourrait participer à l'image de l'étude de fiabilité de ces dispositifs de puissance.

Acronyms

AC	Alternating current
Al	Aluminium
ALD	Atomic Layer Deposition
AlGaAs	Aluminium Gallium Arsenide
AlGaN	Aluminium Gallium Nitride
AlN	Aluminium Nitride
Al ₂ O ₃	Alumina
Au	aurum
C-DLTS	Conductance Deep Level Transient Spectroscopy
CEA	Commissariat à l'énergie atomique
Cu	Copper
DC	Direct Current
DCB	Direct Copper Bonding
DGD	Drain to Gate Delay
DLTS	Deep Level Transient Spectroscopy
DT	Direct Tunneling
DUT	Device Under Test
EPC	Efficient Power Conversion
Fe	Ferrum
Ga	Gallium
GaAs	Gallium Arsenide
GaN	Gallium Nitride
GHG	Greenhouse Gas
HCSMU	High Current Source-Measure Unit
HEMT	High Electron Mobility Transistor
HFET	Heterojunction Field Effect Transistor
HfO ₂	Hafnium dioxide
H ₂ SO ₄	Sulfuric acid
HTRB	High-Temperature Reverse Bias
HTSC	High Temperature Source Current
HVDC	High Voltage Direct Current
HVPE	Hydride Vapor Phase Epitaxy
HVSMU	High Voltage Source-Measure Unit
I-DLTS	Current deep-level transient spectroscopy
IGBT	Insulated Gate Bipolar Transistor
MCSMU	Mid Current Source-Measure Unit
Mg	Magnesium

MIS	Metal Insulator Semiconductor
MOCVD	Metalorganic Vapour Phase Epitaxy
MODFET	Modulation-Doped Field Effect Transistor
MOS	Metal-Oxide Semiconductor
MOSFET	Metal-Oxide Semiconductor Field Effect Transistor
MOVPE	Metalorganic Vapour Phase Epitaxy
NBTI	Negative Bias Temperature Instability
NH ₃	Ammonia
Ni	Nickel
N-OFF	Normally – OFF
N-ON	Normally – ON
N ₂	Nitrogen
N ₂ O	Nitrous oxide
OMVPE	Organometallic Vapor Phase Epitaxy
OST	OFF-Stress Time
PAMBE	Plasma-Assisted Molecular-Beam Epitaxy
PAT	Phonon-Assisted Tunneling
PBTI	Positive Bias Temperature Instability
PECVD	Plasma-Enhanced Chemical Vapor Deposition
RF	Radio Frequency
SBD	Schottky Barrier Diodes
Sc ₂ O ₃	Scandium Oxide
Si	Silicon
SiC	Silicon Carbide
SIMS	Secondary Ion Mass Spectrometry
SiN	Silicon mononitride
Si ₃ N ₄	Silicon Nitride
SiO ₂	Silicon Dioxide
SiON	Silicon Oxynitride
SMU	Source-Measure Unit
SRH	Shockley-Read-Hall
T-ALD	Thermal-Atomic Layer Deposition
TCAD	Technology Computer-Aided Design
TDDDB	Time Dependent Dielectric Breakdown
TEM	Transmission Electron Microscopy
Ti	Titanium
TiAl	Titanium Aluminide
TiN	Titanium Nitride
T _j	Junction Temperature
TP	Trapping Process
TSC	Thermally Stimulated Current
TSEP	Temperature Sensitive Electrical Parameter
V _{Ga}	Gallium Vacancy
V _N	Nitrogen Vacancy
2DEG	2–D Electron Gas
3DPHI	3D Power Hybrid Integration

Acknowledgment

This thesis was carried out within the SATIE laboratory in the TEMA team headed by the research director Zoubir Khatir. The thesis was also carried out in the framework of the MeGan project which aims to develop electronic power modules based on Gallium Nitride to be used in electric vehicles. This project is financed by the *Banque publique d'investissement Bpifrance* and has been led by Renault SAS pilot.

I was very lucky to be very well surrounded during this thesis. I want to thank in these words all the people who have made these years full of learning, joy and pleasant moments. I start first to thank my PhD director Zoubir Khatir for all the efforts that he made during the thesis. I learned a lot with him on all levels starting with scientific level until professional and personal levels. I will never forget the incredible time he gave during the thesis, all scientific discussions almost daily and all advice in my choices of research points. I am very glad of the trust he has given me for performing the experiments. I particularly thank him for his good management of the works in the TEMA team, the collaboration with the team members and the ease of access to the tools to carry out the experimental works have made the work very simple and effective.

All my thanks go to my supervisor Ali Ibrahim for the effort he put to set-up the manipulations, especially the power cycling. He taught me a lot of things starting with the methodologies of mounting manipulations until analysis and results treatment. I will never forget the moments of joy we had during coffee breaks and baby-foot games!.

I would like to thank warmly Frederic Mornacho and Olivier Latry for accepting to be reporters of my thesis, I also thank the jury president Dominique Plansone, Stéphane Lefebvre and René Escoffier to have accepted to be reviewers of my thesis.

This thesis should not have seen the light without the incredible help from René Escoffier, for all the components that we had from CEA–LETI, for the very interesting meetings we had either on Grenoble or on Paris. Thank you René for all the samples you prepared in order to do the measurements during this thesis.

As part of the MeGan project, the module reliability work could not have been completed without the help of Benoit Thollin from CEA–LETI, Yves Bienvenu from MINES Paristech, Regis Muret and Donatien Martineau from Safran electrical & power team.

My deepest thanks go to Andres Echeverri, Alexis Divay and Olivier Latry for the great welcome I received at the *Groupe de Physique des Matériaux* (GPM) in Rouen, for the very interesting exchanges we had together concerning the transient current measurements. I would never forget the nights we spent together measuring transient currents in the lab. Great thanks to Olivier Latry for the confidence he has given us to carry out these measurements. Thank you also for the very interesting works that was done by electro-photoluminescence. Thanks also to Eugénie for the weeks she has spent helping us in these measurements.

I also want to thank Thierry Kociniowski and François Jomard from GEMaC for the time they have put on the SIMS measurements. My gratitude is also going to Alex Xiaoshan for helping with C-V measurements at ENS-Cachan. It was also a pleasure to work with Matthieu Landel and Stéphane Lefebvre

concerning traps measurements for handling short circuits. I would like to thank Rachida Chakir for her help in the numerical simulations carried out during the thesis. I also thank Malika Elharizi for the work done together for the power cycling.

I had the chance to supervise three Master-2 students, i would like to thank Jianzhi, Magnim and Basile for their participation in this work.

During the thesis, i had pleasant moments with the researchers and the engineers of the TEMA team, among them, i thank Alexandre, Richard, Jean-Pierre, Laurent, Sonha-Tran, Franck and Damien; without forgetting to thank - my friends in the struggle - the other PhD students, Merouane, Nausicaa, Malika, Rabeb.

Thank you very much Patricia Guerrero, Fulvio Michelis and Georges Albert for the incredible time you spent to help and support me all along the thesis. I would like to thank my friends who supported me a lot during this thesis especially, Jean, Heba and Mohamed Essam.

A big big thank you to the people who made a lot of effort for the preparation of the defense, I start by Nausicaa Dorcin who worked as a special photographer, thank you very much. I also thank a lot Raouf Khalil and Michael Magued for the effort they made in the organization. I also want to thank the members of Intento who could come to encourage me, among them, i thank Rami, Marine, Janahan, Eldar, Hao and Marc.

I want to thank especially one of my best friends Merouane Ouhab for the times of joy we spent together, i will never forget the laughs we had together during the thesis on all the jokes.

Many thanks go to the people that I could cross during the thesis in IFSTTAR-Satory and especially Isnié Rusani, Mohamed, Xiran, Ines and Gérard leblus.

During my thesis we had many moments of joy in the TEMA laboratory, like ping-pong competitions in the breaks, message to Pascale Dupeyrat: you must admit that i won you an infinite number of times.

Last but not least, I want to thank my parents Nader and Mervat for their advice, their humors during difficult moments and especially their supports in every moment, for Gehane and Georges, thank you for being here for me, I love you, thank you Gigi for the effort you did in organizing this defense.

Contents

Abstract	IV
Résumé étendu en Français	VII
Acronyms	XII
Acknowledgment	XIV
1 Reliability study of GaN HEMTs: State of the art	1
1.1 Introduction	3
1.2 Power electronics applications and needs	3
1.3 GaN high electron mobility transistors for switching applications.	5
1.3.1 Power transistors materials and limits of their traditional solutions	5
1.3.1.1 Benefits of GaN components use in power electronics	6
1.3.1.2 Advantages for use in RF applications	7
1.3.2 High electron mobility transistor technologies	9
1.3.3 Polarization-induced surface charges and the source of electrons.	12
1.3.4 Structures.	14
1.3.4.1 Normally–ON Structures	15
1.3.4.2 Normally–OFF Structures	15
1.4 Axis 1 – Physics understanding of traps.	18
1.4.1 A brief explanation of the traps physical parameters	21
1.4.1.1 Poole Frenkel effect potential barrier lowering	23
1.4.1.2 Phonon assisted tunneling PAT	23
1.4.1.3 Direct tunneling DT	24
1.4.2 Traps’ effects in HEMTs	25
1.4.2.1 Effects on static I–V characteristics	25
1.4.2.2 Effects on transient drain–source current	26
1.4.2.3 Traps effect during switching process	27
1.5 Axis 2 – Traps Characterizations	29
1.5.1 Transient drain current measurements	29
1.5.2 Review of methods used for traps Characterization.	32
1.6 Axis 3 - GaN HEMTs models	34
1.6.1 Equivalent circuit model:	34
1.6.2 Physics-based model:	36
1.7 Axis 4 - Reversible and irreversible degradation of GaN HEMTs	41
1.7.1 Positive bias temperature instability (PBTI) - Reversible	42
1.7.2 Negative bias temperature instability (NBTI) - Reversible	43
1.7.3 Time-dependent dielectric breakdown - Irreversible	44
1.8 Conclusion	45

2	Theoretical investigation of effects of Oxygen traps on the 2DEG density of MOS-HEMTs	46
2.1	Introduction	48
2.2	Potential structures	49
2.2.1	<i>Normally-ON (N-ON) Structure</i>	49
2.2.1.1	Structure form	49
2.2.1.2	Structure characteristics	50
2.2.2	<i>Normally-OFF (N-OFF) Structures</i>	50
2.2.2.1	Normally-OFF component manufactured by the CEA	50
2.2.2.2	Commercial component GaN Systems	51
2.2.3	<i>Chosen structure and physical problem</i>	52
2.3	Basic analytical model	53
2.3.1	<i>Conventional Energy Band Diagram</i>	53
2.3.2	<i>2DEG model formulation</i>	54
2.4	Modification of the basic analytical model	58
2.4.1	<i>Incorporation of the oxide layer.</i>	58
2.4.1.1	Formulations	58
2.4.1.2	Implementation Method	60
2.4.1.3	Modeling results and discussion:	61
2.4.2	<i>Incorporation of the interface (Al₂O₃/AlGaN) states:</i>	63
2.4.2.1	Theoretical formulation:	63
2.4.2.2	Modeling results and discussion:	65
2.5	Oxygen traps in the AlGaN barrier and the weight between interface and barrier traps	67
2.5.1	<i>DLTS and SIMS Results</i>	68
2.5.2	<i>Semi-analytical model.</i>	69
2.5.2.1	Physical problem definition	69
2.5.2.2	Generic semi-analytical formulation	70
2.5.2.3	Implementation	73
2.5.3	<i>Theoretical results with a single traps level.</i>	73
2.5.3.1	Potential distribution	75
2.5.3.2	Ionized traps profile distribution	75
2.5.3.3	Electric field distribution	76
2.5.3.4	Relative weight between Q_{it} and Q_{HEMT}	77
2.5.3.5	Nonlinear dependence of 2DEG density with gate voltage	79
2.6	Conclusion	81
3	Traps characterization of commercial components GaN Systems Inc.	82
3.1	Introduction	84
3.2	Highlighting traps	85
3.3	Transient Current measurements & extraction of traps parameters	86
3.3.1	<i>Methodology</i>	87
3.3.1.1	Identification of the measurement parameters	87
3.3.1.2	Test bench preparation and measurements	89
3.3.1.3	Post processing, signal processing and parameters extraction:	89
3.3.2	<i>Test bench and equipment:</i>	89
3.3.2.1	Global system:	89
3.3.2.2	Fast switcher:	90
3.3.2.3	Self-heating control:	92

3.3.3	<i>Experimental results</i>	93
3.3.3.1	Signal processing:	93
3.3.3.2	Signal decomposition:	94
3.3.3.3	Physical parameters extraction	96
3.3.4	<i>Drain lag of the GaN Systems commercial devices</i>	97
3.3.4.1	High sampling rate (200 μ s)	97
3.3.4.2	Low sampling rate (10 ms)	100
3.3.4.3	Traps physical parameters extraction from Arrhenius law - Drain lag: .	102
3.3.4.4	A sensitivity study for transient current measurements OFF Stress level:	103
3.3.5	<i>Gate lag of the GaN-Systems commercial devices:</i>	104
3.4	Conclusion:	107
4	Power cycling reliability testing of Al₂O₃/AlGaN/GaN on Si devices	108
4.1	Introduction	110
4.2	Device presentation and its characteristics	111
4.2.1	<i>Electrical and thermal characteristics</i>	111
4.2.2	<i>DUT external structure mounted on DCB</i>	111
4.2.3	<i>Diversity of devices electrical characteristics</i>	112
4.3	General methodology of power cycling	114
4.4	Equipment	116
4.5	Characterizations before ageing	117
4.5.1	<i>Characterization methodology</i>	117
4.5.1.1	General characterizations before ageing	118
4.5.2	<i>Traps measurements before ageing.</i>	122
4.5.2.1	Drain lag measurements before ageing and difficulty for parameters extraction	122
4.5.3	<i>Gate lag measurements before ageing</i>	123
4.6	Power cycling test results	127
4.6.1	<i>Test-bench:</i>	127
4.6.2	<i>Thermosensitive parameter</i>	128
4.6.3	<i>Experimental results</i>	129
4.6.3.1	Power cycles	129
4.6.3.2	Ageing monitoring	130
4.7	Characterizations and analysis after ageing.	132
4.8	Conclusion	141
	General conclusion	142
	Publications	144
	References	145
A	General implementation method of the semi-analytical model using the object-oriented programming	161
B	Alternative analytical model	163
B.1	Physical problem:	164
B.2	Mathematical description:	165
B.2.1	<i>Electric field distribution:</i>	165
B.2.1.1	Zone1:	165
B.2.1.2	Zone2:	166
B.2.1.3	Zone3:	166
B.2.2	<i>Potential distribution:</i>	166
B.2.2.1	Zone1:	166

- B.2.2.2 Zone2: 167
- B.2.2.3 Zone3: 167
- C Basic features of the B1505A Power Device Analyzer/Curve Tracer 169**
- D Role of the diode used in the N1267A HVSMU/HCSMU fast switcher 171**
- E Optical microscope images of decapsulated GaN Systems component 173**

List of Figures

1.1	Simple illustration of the power electronics system in a electric vehicle.	4
1.2	Power devices operating regions a) Voltage vs. Frequency b) Current vs. Frequency [Ras 10].	5
1.3	A variety of applications in the field of power electronics [Men 17b].	5
1.4	Treasure roadmap for power electronics applications.	7
1.5	Advantages of the GaN components compared to other components used in power electronics and RF applications [Gal 17].	7
1.6	Physical and electrical parameters of the different materials that were mostly used for power electronics (Si, SiC, GaAs, GaN, and diamond) [Men 17b].	8
1.7	Physical and electrical parameters of the different materials that were mostly used for power electronics (Si, SiC, GaAs, GaN, and diamond)-complement [Men 17b].	8
1.8	Two different bandgap materials consisting the heterostructure, E_{FS} is the Fermi level over the entire heterostructure - <i>before contact</i>	10
1.9	The two different bandgap materials consisting the heterostructure - <i>after contact</i>	10
1.10	A heterostructure formed by the combination of the two materials with different gaps: the blue area corresponds to the charges concentration in the channel (2DEG density); E_{FS}, E_{Fm} are the Fermi levels in the semiconductor and metal respectively; E_C is the conduction band. The potential shape of the large gap layer indicates its n-doping. . . .	11
1.11	Comparison of experimental measurements between carrier mobility in bulk and doped channel modulation GaAs at low field [Lad 86].	11
1.12	Ga(Al)-face & N-face growth of GaN/AlGaIn/GaN heterostructure [Amb 00].	13
1.13	Spontaneous and piezoelectric polarizations directions for the Ga(Al)-face & N-face growth of GaN/AlGaIn/GaN heterostructure [Amb 00].	14
1.14	An example of a normally ON component made with field plate [Sai 03].	15
1.15	Example of recessed-Gate Structure.	16
1.16	P-Gate structure with AlGaIn P-doped [Uem 07].	17
1.17	Possible traps location in the structure.	20
1.18	Electron energy diagram in equilibrium at zero electric field.	21
1.19	Possible emission and capture ways that can occur at a traps level [Sch 06].	22
1.20	The activation energy as a function of the applied voltage [Mit 04].	23
1.21	An electron/hole emission mechanism from traps through a potential barrier according to Poole-Frenkel emission, phonon-assisted tunneling and direct tunneling [Joz 10]. . . .	24
1.22	$I_{DS}-V_{DS}$ and $gm-V_{GS}$ for several pairs of reverse bias points at the drain and the gate ($V_{GSQ}; V_{DSQ}$) [Bis 13].	25
1.23	$I_{DS}-V_{DS}$ results with observed kink effect [Men 09].	26
1.24	Trapping effect on the transient response of drain polarization change [Tir 07].	26
1.25	Trapping effect on the transient response of gate polarization change [Tir 07].	27

1.26	Proposed measurement system to study the effect of polarization conditions and the emergence of traps on the dynamic resistance during switching process [Ros 17].	28
1.27	On resistance as a function of drain quiescent point and DGD value for a single temperature [Ros 17].	28
1.28	On resistance variation as a function of drain quiescent point in soft and hard switching for different temperatures [Ros 17].	29
1.29	Example of transient current fitted by $n = 100$ exponentials [Joh 11].	30
1.30	Example of time constants spectrum [Joh 11].	31
1.31	Extraction of the activation energy using the Arrhenius law [Joh 11].	31
1.32	Equivalent circuit model [Nak 08].	34
1.33	Comparison between theoretical and experimental results [Nak 08].	35
1.34	Nonlinear equivalent circuit model.	35
1.35	Type of the results of a circuit-based model used to validate characteristics of GaN component used in microwaves applications [Cab 04].	36
1.36	Measurements and experimental values of the mobility function of temperature for three different charge concentrations [Woo 08].	37
1.37	Physical origin of the degradations modes.	42
1.38	Threshold voltage shift due to the stress level and the temperature due to the positive bias [Acu 17].	42
1.39	Threshold voltage recovery that the component has undergone due to the stress level and the temperature due to the positive bias [Acu 17].	43
1.40	The threshold voltage shift depending on the temperature for stress (left) and recovery (right) [Men 16b].	43
1.41	TDDDB on three different samples with three different gate oxide of MISHEMTs [Wu 15].	44
2.1	N-ON MOS–HEMT Structure fabricated by the CEA–LETI.	49
2.2	Fully recessed gate N-OFF structure fabricated by the CEA–LETI.	51
2.3	Simplified scheme for the commercial component GaN Systems.	51
2.4	Conventional energy band diagram.	53
2.5	Corresponding structure with schottky contact.	54
2.6	Comparison between the original and the approximated equations.	57
2.7	Energy band diagram with the oxide layer.	59
2.8	Flowchart for the calculation method of the analytical model with the integration of the oxide layer.	60
2.9	n_s - Surface electric field (ξ_s) relationship with oxide consideration.	61
2.10	n_s - Oxide voltage drop V_{OX} relationship with oxide consideration.	62
2.11	Comparison between the behaviors of the $n_s - V_{GS}$ relationship for Schottky contact and Metal-oxide HEMT structures.	62
2.12	Simulation results of the U form of the $D_{it0}(E)$ distribution (Red: with surface treatment, blue: without surface treatment).	64
2.13	Interface trapped charges function of the surface potential for different densities of D_{it0}	65
2.14	The different distribution charges for HEMT, interface traps and total charges. These simulations were performed with a D_{it0} density of $5 \times 10^{11} cm^{-2} e.V^{-1}$ for two different densities of donors densities (Left, $N_D = 1 \times 10^{18} cm^{-3}$ and right $N_D = 2 \times 10^{18} cm^{-3}$)	66
2.15	The different distribution charges for HEMT, interface traps and total charges. These simulations were performed with a D_{it0} density of $1 \times 10^{12} cm^{-2} e.V^{-1}$ for two different densities of donors densities (Left, $N_D = 1 \times 10^{18} cm^{-3}$ and right $N_D = 2 \times 10^{18} cm^{-3}$)	66

2.16	Illustration of the zone where the interface trapped charges may have an impact on the total charges of the system.	67
2.17	SIMS measurements.	68
2.18	Schematic energy band diagram including two donor trap energy levels (E_{TD_1} and E_{TD_2}) and a single acceptor trap level E_{TA_1}	69
2.19	Schematic illustration of the traps energy levels.	71
2.20	Iterative method to find the corresponding V_{GS} . ϵ' is equal to 0.1%.	74
2.21	Potential distribution throughout the AlGaIn layer for a <i>protect</i> V_{GS} range from -4V to 3V.	75
2.22	Ionized traps profile throughout the AlGaIn layer for a V_{GS} range from -4V to 3V.	76
2.23	Electric field distribution throughout the AlGaIn layer for a V_{GS} range from -4V to 3V.	76
2.24	Interface trapped charges, HEMT charges, and total charges function of the gate voltage for HEMT with surface treatment.	78
2.25	Interface trapped charges, HEMT charges, and total charges function of the gate voltage for HEMT without surface treatment.	78
2.26	2DEG concentration function of the gate voltage for two values of barrier trap density ($2 \times 10^{18} cm^{-3}$ and $1 \times 10^{18} cm^{-3}$).	80
2.27	2DEG concentration function of the gate voltage for a low density of barrier traps.	80
3.1	Double pulse parameters.	85
3.2	I–V measurements with different quiescent points (V_{GSQ}) -6V (blue) to 0V (magenta) with step of +2V at two temperatures 10°C & 80°C.	86
3.3	Process steps of the methodology.	87
3.4	Applied stress parameters.	88
3.5	Example of real type measured transient current and on-resistance.	88
3.6	Different part of the overall system.	90
3.7	Fixed DUT in the temperature homogenization box.	90
3.8	SMUs system in the OFF and ON state [Key 15].	91
3.9	Internal structure of the switcher and connection with the DUT [Key 15].	92
3.10	Decapsulated device for measuring a local temperature by optical fiber.	92
3.11	Trap parameters extraction methodology.	93
3.12	Red line shows the experimental measurements, blue line presents the filtered and decimated signal.	94
3.13	Vector z and its representation of frequencies and exponential coefficients in Prony's method.	95
3.14	Comparison between the fitted signal estimated by Prony and the original signal, these drain lag measurements was carried out at a high temperature (100 °C) with a model order of 40.	96
3.15	Transient measurements (200 μs sampling rate) for a temperature range from 0 °C to 30 °C.	98
3.16	Transient measurements (200 μs sampling rate) for a temperature range from 40 °C to 70 °C.	98
3.17	Transient measurements (200 μs sampling rate) for a temperature range from 80 °C to 100 °C.	99
3.18	Prony fitting with measured signals (200 μs for sampling rate) for two temperatures (40 °C and 100 °C) – linear scale.	100
3.19	Arrhenius plot for activation energy for Drain Lag measurements for high sampling rate.	100
3.20	Transient measurements (10ms sampling rate) for a temperature range from 80 °C to 100 °C.	101
3.21	Prony fitting with measured signals (10 ms of sampling rate) for 100°C – linear scale.	102

3.22	Arrhenius plot for activation energy for Drain Lag measurements for high and low sampling rate.	102
3.23	(Drain Lag) Transient current with OFF-Stress Time = 1s (Left 0 °C), (right 60 °C).	103
3.24	(Gate Lag) Transient current with OFF-Stress Time = 1s.	104
3.25	(Gate Lag) Transient current with OFF–Stress Time = 50s.	105
3.26	(Gate Lag) Transient current with OFF–Stress Time = 100s.	105
3.27	Arrhenius plot for activation energy for Gate Lag measurements for different OFF-Stress time.	106
4.1	The external component structure composed of three pairs of drain/source (Left), the component mounted on a DCB (right).	111
4.2	Dispersion of electrical characteristics for 4 different components, C stands for component.	112
4.3	Electrical characteristics of the 4 components.	113
4.4	Conventional test bench and concept of power cycling [Ibr 16].	114
4.5	Method of fixing the component on a metal plate.	116
4.6	Test bench schematic.	116
4.7	Methodology used for characterization before/after ageing.	118
4.8	$I_{DS} - V_{DS}$ for the two devices.	119
4.9	$I_{DS} - V_{GS}$ for the two devices.	120
4.10	Deduced trans-conductance for the 2 devices.	120
4.11	$I_{DS} - V_{DS}$ Characteristics of the 2 devices with temperature for $V_{GS} = -3V$ with a linear step of the temperature of 20°C.	121
4.12	$I_{DS} - V_{GS}$ characteristics of the 2 devices with temperature for $V_{DS} = 100mV$ with a linear step of 20°C.	121
4.13	Threshold voltage for the two devices with temperature.	122
4.14	Drain lag transient measurements (with temperature).	123
4.15	Transient gate lag measurements for some chosen temperatures (40°C, 50°C, 70°C and 90°C) for both devices (First device-left) and (Second device-right)	124
4.16	Arrhenius before ageing (First device).	125
4.17	Arrhenius before ageing (First device) – different scale.	125
4.18	Arrhenius before ageing (Second device).	126
4.19	Arrhenius before ageing (Second device)– different scale.	126
4.20	Test bench.	127
4.21	Devices reported on DCB mounted on the metal plate.	128
4.22	Measurements flow to establish and use the thermosensitive parameter (T_j is assumed to be T_S).	128
4.23	Relationship between the junction temperature and the voltage measurement ($I_{sense}=500mA$).	129
4.24	Power cycling test for both devices-two cycles in a row; the color red presents the measured drain-source voltage while the color blue presents the power current.	130
4.25	Sense current and deduced junction temperature during cooling.	131
4.26	Deduced junction temperature during cooling and measured drain-source voltage for the cut for the first device for the first 500 cycles.	131
4.27	$I_{DS} - V_{DS}$ characteristics before and after ageing for the two devices.	132
4.28	$I_{DS} - V_{GS}$ characteristics before and after ageing for the two devices.	133
4.29	Trans-conductance characteristics before and after ageing for the two devices.	133
4.30	Threshold voltage characteristics (with temperature) comparison before and after ageing.	134
4.31	Transient measurements of the drain lag before and after ageing for both devices for (70 °C).	135

- 4.32 Transient measurements of the drain lag before and after ageing for both devices for (80 °C). 135
- 4.33 Transient measurements of the drain lag before and after ageing for both devices for (90 °C). 136
- 4.34 Transient current of the gate lag after ageing- First device. 136
- 4.35 Comparison of transient current of gate lag before and after ageing. 137
- 4.36 Arrhenius before and after ageing (First device). 137
- 4.37 Arrhenius before and after ageing (First device)-Different scales. 138
- 4.38 Arrhenius before and after ageing (Second device)-Different scales. 139
- 4.39 Arrhenius before and after ageing (Second device). 140

- A.1 Implementation method of the semi-analytical using the OOP. 162

- B.1 Possible potential distribution. 164
- B.2 Possible electric field distribution, a) General case , b) Case when high positive voltage is applied , c) Case when a high negative voltage is applied. 165

- E.1 Different top view of the decapsulated component. 174
- E.2 Different top view of the decapsulated component. 174
- E.3 Different oblique view of the decapsulated component. 175
- E.4 Different oblique view of the decapsulated component. 175

Chapter 1

Reliability study of GaN HEMTs: State of the art

1.1 Introduction

Semiconductor devices reliability study needs both theoretical and experimental approaches. The involved fields become wider when one speaks of the power electronics devices reliability. The components must comply with harsh environments (corresponding to real applications), and also must show the consistent operation for long periods of time. Among these involved fields, theoretical side, one can cite semiconductor physics, mathematical modeling, and Multiphysics numerical simulations. On the other hand, experimental side, it starts with electrical, thermal and physical characterizations as well as experimental ageing tests. It is also notable the use of equipment for failure analyzes. These fields provide the necessary elements in order to study the power devices degradation modes and to perform a reliability study. In this chapter, the works underlying the gallium nitride (GaN) power devices reliability will be presented. These contributions can be divided into four axes:

- Semiconductor physics.
- Mathematical modeling.
- Electrical characterization.
- Accelerated ageing tests.

These axes represent the essential pillars on which the thesis is based upon.

Concerning the first axis, the semiconductor physics will give us the possibility to understand the device behavior, to analyze the experimental results by answering the question **what do we exactly observe?** For the second axis, it is the step to predict the behavior based on the semiconductor physics equations; this second axis will answer the question **what will be observed?**. Thirdly, the electrical characterizations that give us the actual behavior of the component according to the different test conditions which mainly contains temperature and polarization conditions. This point answers the question of **what we are currently observing?**. Finally, the ageing tests or the component will be put under accelerated tests to study its degradation modes and reuse axis 1, 2 and 3 to answer the question **how the component ages?**.

Specifically, we will apply all these axes to trapping/de-trapping mechanisms. This phenomenon causes instability during normal operation, and its effect may also evolve with degradation. So, we will start with presenting physics comprehension, passing through its mathematical modeling, its characterizations methods (especially electrically) and finally the study of the effect of ageing on the evolution of this phenomenon. However, there had been a lot of literature work that has been done, which shows at what level this phenomenon catches the interest of researchers for at least the last two decade.

Here, we will begin by explaining the GaN HEMT structure, their specificities, their advantages, and disadvantages. Next, we will present a literature survey of the four axes applied to the trapping phenomena. We will also try to present a more in-depth study of the general degradation modes of GaN devices by focusing on trapping phenomena. We will show the parts of the puzzle that may be missing in the existing works, and which can be added to reinforce the existing reliability study of these components. Finally, of course, all these axes will have the color of power electronics since these components have also been studied for radio-frequency applications.

1.2 Power electronics applications and needs

The field of power electronics is a vast field. It immersed in many applications like electric vehicles, electric planes, and satellites. These applications affect several sides beginning from the daily life uses passing through industrial until military and spatial applications. There are many benefits of the use of

power electronics systems which may vary according to the application. Furthermore, in the direction of making our life greener, the power electronics take over the reduction of greenhouse gas emissions (GHG) and subsequently the limitation of fossil energy consumption. There are also several forms of the participation of power electronics in a system, for example for automotive applications; we can find entirely electric systems or hybrid systems where the fuel and the electrical system are used simultaneously.

For automotive applications, as shown in *Figure 1.1*, the power electronics system can be mainly divided into three main parts that are the power electronics system, the power converters and the power electronics components (especially transistors).

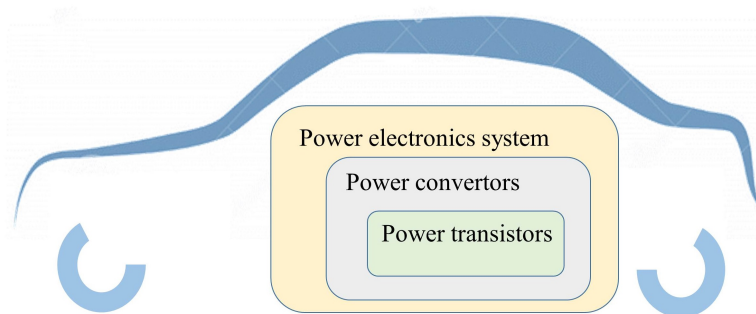


Figure 1.1: Simple illustration of the power electronics system in a electric vehicle.

1. Power electronics components (such power transistors and diodes):

These components should be adapted and ready to work in harsh conditions, especially under varied temperature (cold and high temperature) and polarization conditions (high voltage and high current). These transistors can be manufactured under different architectures, according to the needs of the applications, various technology well-responded. Power MOSFETs are used to respond to fast switching applications [Yos 97]. The Insulated Gate Bipolar Transistor (IGBT) was explicitly developed to decrease conduction losses and to operate at high voltages [Ber 98 and Bla 95]. The semiconductor super-junction devices have appeared to overcome the trade-off between the breakdown voltage and the on-resistance of conventional unipolar devices. There is always a compromise for the users choice of the power devices between high-frequency and high-power applications. The devices that give the possibility of working with high power can, for example, serve in HVDC converters and renewable energy inverters. On the other hand, components able to work in high frequencies can serve in switching mode power supply and resonant converters. *Figure 1.2* shows how the devices were positioned according to power and frequency operation regions [Ras 10].

2. Power electronics systems:

By using power components and especially power transistors, we can manufacture electronic architectures and especially power converters. These converters will have several types of architectures depending on their use; they can be AC to DC (rectifier), DC to AC (inverter), DC to DC (DC-to-DC converter) or AC to AC (AC-to-AC converter). These converters are used to create electronic functions mainly based on power conversions. We will not go further in the explanation of these converters as the goal of the thesis is to focus on the component and not the converters. However, for more information on converter architectures and their applications, one can consult [Ras 10].

1.3. GAN HIGH ELECTRON MOBILITY TRANSISTORS FOR SWITCHING APPLICATIONS

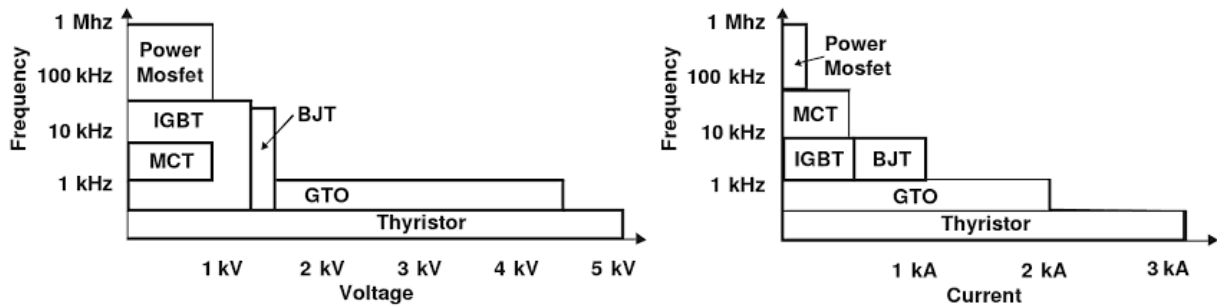


Figure 1.2: Power devices operating regions a) Voltage vs. Frequency b) Current vs. Frequency [Ras 10].

3. Power electronics converters:

Points 1 and 2 presented the subsections of the power electronics system, as examples of these systems, one can cite actuator driver, interfaces for energy storage and interfaces for the electrical energies generation [Bla 04, Rib 10]. These power systems can be related to many applications varying at its power consumption (1W to 1 GW). As shown in Figure 1.3, the power semiconductor devices evolved with time according to the personal, home and infrastructure applications.

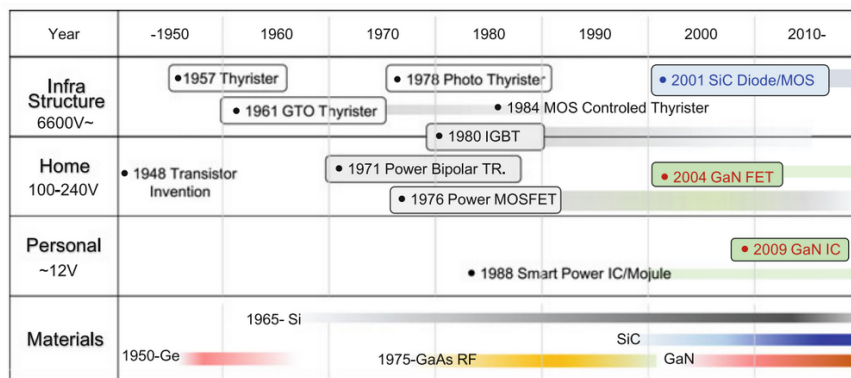


Figure 1.3: A variety of applications in the field of power electronics [Men 17b].

We note that the choice of materials is related to the range of the operating voltage. In the next section, we will focus on the first point of the power system: the power transistors, we will present the traditional solutions of these components materials, we will also present, in some details, the needs and limits of these solutions. We will instead focus on the used materials; we will try to answer this question **why do we need other materials such as GaN for power electronics applications?**.

1.3 GaN high electron mobility transistors for switching applications

1.3.1 Power transistors materials and limits of their traditional solutions

The power transistors different architectures were made up of semiconductor-based materials. Silicon has been very well taken over for many years, and it still does. The community uses silicon for MOS-FETs, thyristors, and IGBT. Silicon was used in several architectures that touched many applications with different operating voltages. Nevertheless, with technological development and applications with

1.3. GAN HIGH ELECTRON MOBILITY TRANSISTORS FOR SWITCHING APPLICATIONS

more constraints such operations at high temperature with higher power density, users need more integrated power systems. The materials that build these components have attracted considerable interest in research because silicon has reached its limits.

The main limitations of silicon can be concluded in the following few points:

1. The operating temperature is limited; anyway, the maximum operating temperature depends on the operating voltage level.
2. The relative low carrier mobility in silicon, in addition to its large parasitic capacitance which limits its uses for very high-frequency applications.
3. The breakdown voltage is relatively low due to its narrow bandgap.

However, we can consider that the silicon is somehow leaky when the operating constraints begin to be harsh, and it is not very integrated at the volume level. In addition, it is not compatible to be used in very high-frequency applications. Initially, Gallium Arsenide (GaAs) responded well for RF applications while Silicon Carbide (SiC) responded for high power applications. The choice of GaAs material and the GaAs-based HEMT concept will be explained in section III.2. Now, we will briefly describe the interest behind the SiC. Silicon carbide has presented a lot of interest by giving much more improvements in physical and electrical properties compared to silicon [Bal 93, Ela 02 and Rab 12]. The band gap of SiC either 6H-SiC or 4H-SiC is around 3eV which is wider compared to Si (1.1 eV). The critical electric field is around 2.2 MV/cm compared to Si 0.25 MV/cm and finally its thermal conductivity which is in the order of 5 W/cmK compared to Si which is around 1.5 W/cmK. All these properties have given the SiC more advantageous regarding operation in a high-temperature environment, with a high voltage blocking, and small switching losses. All these advantages provide the SiC with the preference of being used in the power applications. At present, there is a lot of research on the reliability of SiC power transistors in order to finally validate its use in these power applications [Gaj 16, Sin 06 and Tre 10]. An interesting comparison between silicon and silicon carbide is presented by [Gla 11]. Another comparison between the performances of Si and SiC MOSFETs has been given by [Ong 07]. Although the SiC has advantages over Si-based devices, the manufacture of SiC transistors is expensive. Therefore, the scientific community of power electronics has been looking for a component with similar performance but less costly. GaN components, produced on silicon wafers with a relatively low price, have responded well to this need. However, it is estimated that the GaN-based components will share the emergence of the wide bandgap devices in the applications of power electronics. SiC associated with GaN present an intermediate step before finding the treasure that is expected to be the diamond. *Figure 1.4* shows an expected roadmap to find the treasure that supposed to be the diamond.

However, the advantages of the GaN components can be summarized as follows:

1.3.1.1 Benefits of GaN components use in power electronics

1. High operating temperature implies a reduced heat requirement in power electronics systems.
2. High breakdown voltage.
3. Lower voltage drop for single-pole devices.
4. Increased output power.
5. Higher frequency operation.

1.3. GAN HIGH ELECTRON MOBILITY TRANSISTORS FOR SWITCHING APPLICATIONS

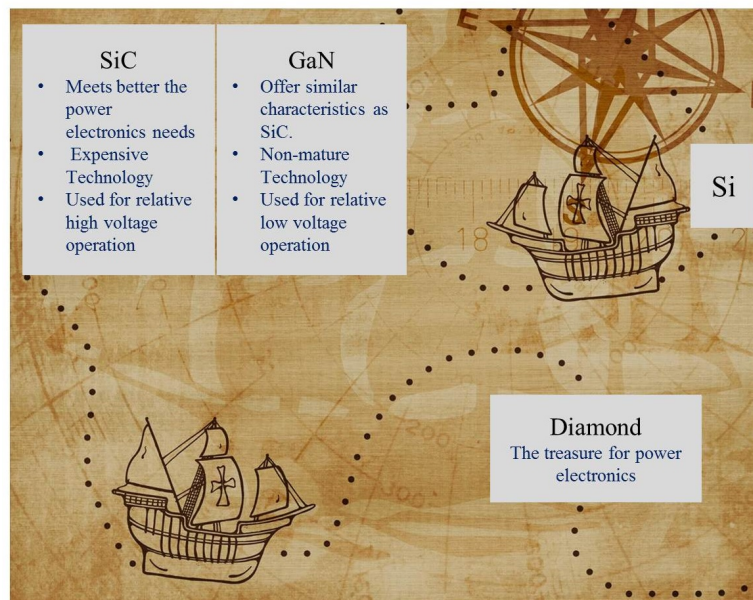


Figure 1.4: Treasure roadmap for power electronics applications.

1.3.1.2 Advantages for use in RF applications

1. High maximum oscillation frequency implies an improved transient characteristic and switching speed.
2. Low noise.

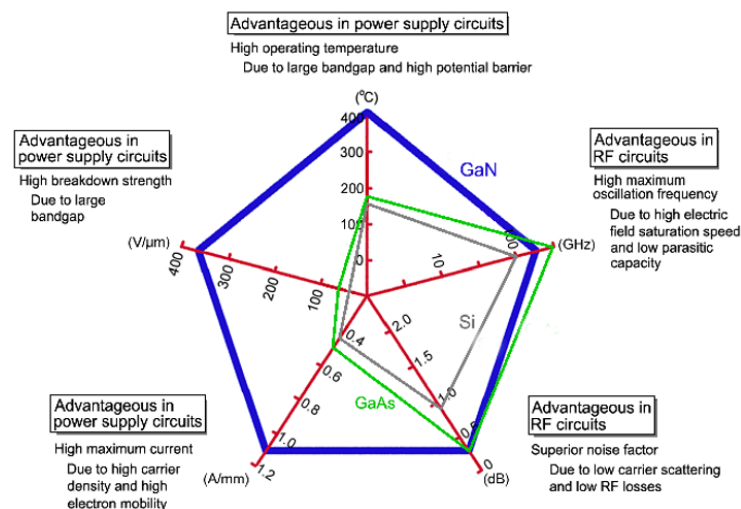


Figure 1.5: Advantages of the GaN components compared to other components used in power electronics and RF applications [Gal 17].

Figure 1.5 summarizes a comparison between Si, GaAs, and GaN from the viewpoint of use in power electronics and RF applications. The figure of merit shows the advantages of the GaN components over the other two components through parameters that affect power electronics. For RF applications, GaAs

1.3. GAN HIGH ELECTRON MOBILITY TRANSISTORS FOR SWITCHING APPLICATIONS

can have a particular advantage which is mainly due to high electrical field saturation velocity, low parasitic capacitance and also the high electron mobility.

Now we will briefly present a more in-depth comparison between the various materials used in power electronics and RF applications; we will try to answer the following question **why exactly GaN components have these advantages?** The physical parameters, as shown in the following table [Men 17b], will give some elements of answer to this question. GaN materials are better than the Si and GaAs ones at the level of thermal conductivity, and better than Si, GaAs, and SiC on bandgap energy. It is also better than SiC on its carrier mobility but less than Silicon and the GaAs.

Parameters	Symbol	Unit	Si	GaAs	AlN	InN	GaN	SiC	Diamond
Crystal structure	–	–	Diamond	Zincblend	Wurtzite	Wurtzite	Hexagonal, cubic	Hexagonal, cubic	Diamond
Density	–	g/cm ³	2.328	5.32	3.26	6.81	6.1	3.21	3.515
Mole	–	g/mol	28.086	144.64	40.9882	128.83	83.73	40.097	12.011
Atomic density	–	atom/cm ³	5.00E+22	4.42E+22	4.79E+22	3.18E+22	4.37E+22	4.80E+22	1.76E+23
Lattice constant	–	Å	5.43095	5.6533	3.1114/a, 4.9792/c	3.544/a, 5.718/c	Hex 3.189/a, 5.185/c, cubic 4.52	(6H)3.086/a, 15.117/c, (4H) 3.073/a, 10.053/c, (3C) 4.3596/a, 3.073/c	3.567
Melting point	–	°C	1415	1238	2200	1100	2573, @60 kbar	2830	4373, @125 kbar
Specific heat	–	J(g °C)	0.7	0.35	0.748	0.296	0.431	0.2	0.52
Linear thermal expansion coefficient	–	°C ⁻¹	2.60E-06	6.90E-06	5.27E-6/a 4.15E-6/c	3.8E-6/a 2.9E-6/c	5.6E-6/a 3.2E-6/c	~5E-6	8.00E-07
Thermal conductivity	–	W/(cm °C)	1.5	0.46	2.85		2.1	2.3–4.9	6–20
Transition type	–	–	Indirect	Direct	Direct	Direct	Direct	Indirect	Indirect
Bandgap energy	Eg	eV	1.12	1.42	6.2	0.65	3.39(H)	3.02/6H 3.26/4H 2.403/3C	5.46–5.6
Separation energy	Γ-L, Γ-X	eV	Indirect	Γ-L0.29, Γ-X0.48s	Γ-ML 0.7 Γ-K 1.0	Γ-A > 0.7 Γ-Γ > 1.1 Γ-K > 2.7	Γ-Γ*1.9 Γ-M 2.1	Indirect	Indirect

Figure 1.6: Physical and electrical parameters of the different materials that were mostly used for power electronics (Si, SiC, GaAs, GaN, and diamond) [Men 17b].

Dielectric constant	εr	–	11.7	12.9, 10.89@RF	8.5	15.3	12	10.0(6H) 9.7(4H)	5.7
Electron affinity	χ	eV	4.05	4.07	1.9	5.8	3.4	4	(NEA)
Intrinsic carrier density	ni	cm ⁻³	1.45E+10	1.79E+06	9.40E-34	9.20E+02	1.67E-10	1.16E-8(6H) 6.54E-7(4H)	1.00E-26
Effective density of states	Nc	cm ⁻³	2.80E+19	4.70E+17	4.10E+18	1.30E+18	2.24E+18	4.55E+19(6H) 1.35E+19(4H) 1.53E+19(3C)	1.00E+20
Effective density of states	Nv	cm ⁻³	1.04E+19	7.00E+18	2.84E+20	5.30E+19	1.16E+19	1.79E+19	1.00E+19
Effective mass	m* _e	m* _e l/m ₀ m* _e t/m ₀	0.9163/l, 0.1905/t	0.067	0.4	0.1–0.05	0.2	1.5/l, 0.25/t	1.4/l, 0.36/t
Effective mass	m* _h	m* _h l/m ₀ m* _h h/m ₀	0.16/l, 0.49/h	0.082/l, 0.45/h	0.6	1.65	0.6/h	0.8	0.7/l, 2.1/h
Electron mobility	μ _e	cm ² /(V s)	1500	8500	300	3200	1000	460–980	2200
Hole mobility	μ _h	cm ² /(V s)	450	400	14	220	~5	20	1800
Lattice matching	–	–	~SiGe	AlAs, InGaP	~GaN	–	~SiC, sapphire	~GaN, IN	–

Figure 1.7: Physical and electrical parameters of the different materials that were mostly used for power electronics (Si, SiC, GaAs, GaN, and diamond)-complement [Men 17b].

Therefore, the material may have better performances compared to traditional semiconductor materials, and it is not expensive to be manufactured.

1.3.2 High electron mobility transistor technologies

The story begins with III-V composites used to build primarily two different bandgap materials, which were subsequently associated to form a heterostructure as illustrated in *Figure 1.8*. The formed heterostructure is the basis of the high electron mobility transistors (HEMTs). This technology is also named modulation-doped field effect transistor (MODFETs). Many semiconductor materials have well responded to this technology. Among them the Aluminum Gallium Arsenide/Gallium Arsenide (AlGaAs/GaAs) heterostructure [Mim 80 and San 87]. AlGaAs presents a relatively large bandgap semiconductor, and GaAs plays the role of the relatively small (or narrow) bandgap material. Relative merely designates the relative comparison between the different materials since the GaAs crystal bandgap is not very large compared to other materials.

The steps of formation of the conventional HEMT can be summarized as following and schematically shown in *Figure 1.8*, *Figure 1.9* and *Figure 1.10*.

1. At thermal equilibrium, after a contact between these different bandgap materials, an anisotype or isotype heterojunction, dependent on doping types in these materials, is formed.
2. A discontinuity in the conduction and valence band resulted at the hetero-interface due to the difference between the bandgaps and the alignment of the Fermi level as shown in *Figure 1.9*.
3. The discontinuity formed in the conduction band induces an electron quantum confinement. It produces a 2-D electrons sheet at the hetero-interface in possession of the narrower bandgap material. This discontinuity value is in general independent of doping in these materials.
4. The electrons density in the confinement lie within quantized discrete energy levels which are governed by the Poisson-Schrodinger coupled equations.
5. A Schottky contact is formed by adding a metal layer to the other side of the larger bandgap material. This metal gate layer will control the 2DEG density in the channel.
6. By adding other metal contacts to create drain and the source contacts, one will have a conventional HEMT transistor.

A comparison before and after the formation of the heterostructure can be briefly schematized as follows. For more information about the details of the heterostructure formation, one can consult [Sze 07].

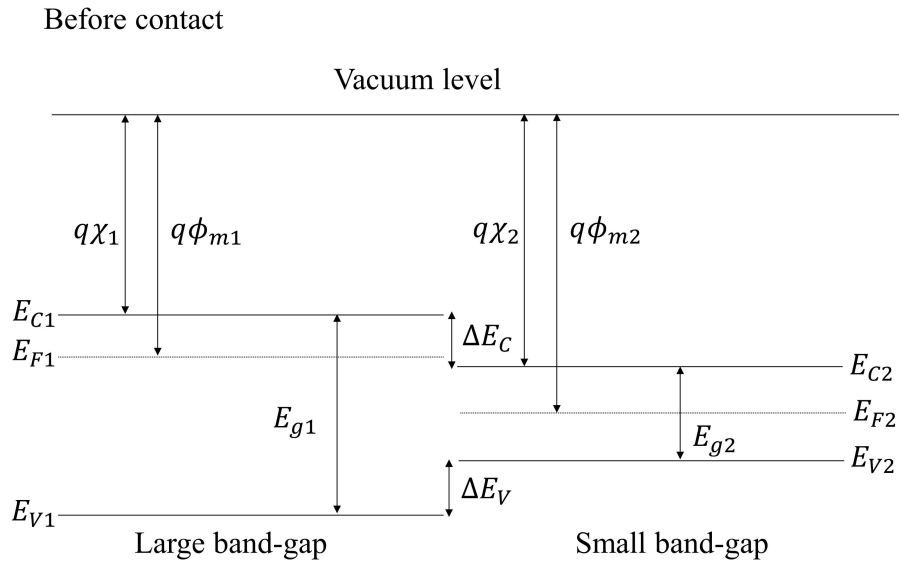


Figure 1.8: Two different bandgap materials consisting the heterostructure, E_{FS} is the Fermi level over the entire heterostructure - before contact.

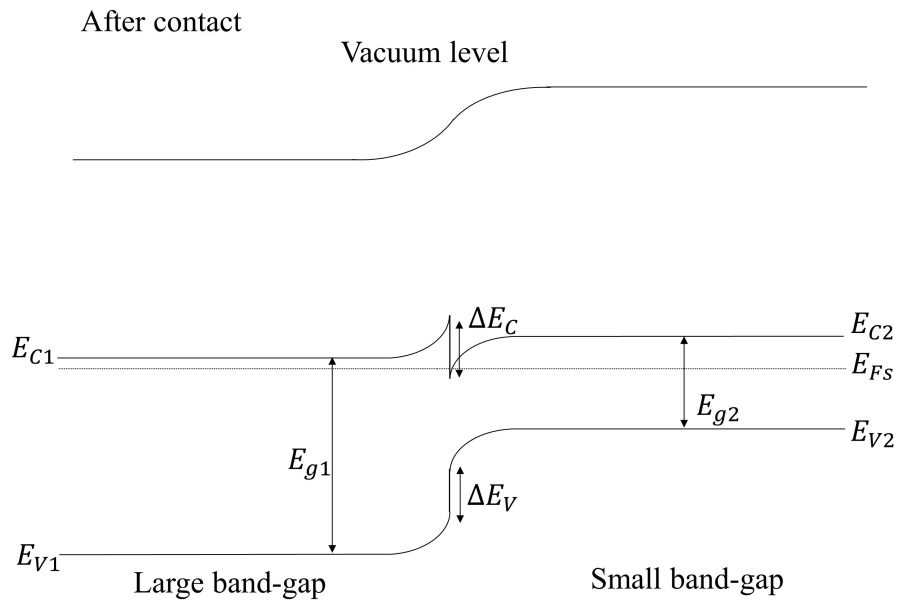


Figure 1.9: The two different bandgap materials consisting the heterostructure - after contact

So by applying a gate voltage, we can control the charges concentration in the channel. Moreover, by applying drain-source voltage, we will end up with a FET planar high electron mobility transistor.

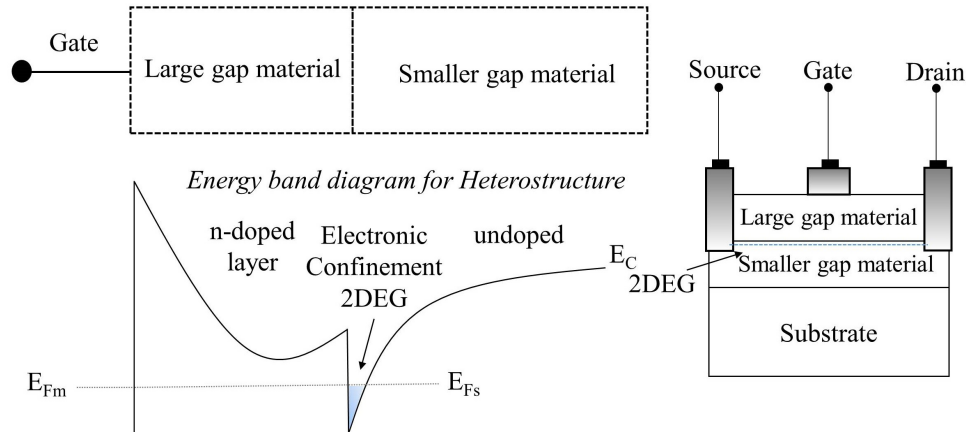


Figure 1.10: A heterostructure formed by the combination of the two materials with different gaps: the blue area corresponds to the charges concentration in the channel (2DEG density); E_{FS}, E_{Fm} are the Fermi levels in the semiconductor and metal respectively; E_C is the conduction band. The potential shape of the large gap layer indicates its n -doping.

T. R. Lenka et al. [Len 11] present some characteristics of this 2-DEG confinement. This confined 2-DEG offers mainly a significant advantage to these structures; it is the improvement of the electron mobility during conduction. Some authors measured an important electron mobility value for a modulation doped transistor AlGaAs/GaAs up to $8 \times 10^6 \text{ cm}^2/\text{V}\cdot\text{s}$ and up to $1.05 \times 10^7 \text{ cm}^2/\text{V}\cdot\text{s}$ at shallow temperature (0.04K) and low carrier concentrations up to $n = 2.8 \times 10^{11} \text{ cm}^{-2}$ [Sak 91 and Sak 96]. The electron/hole mobility in the same material containing its ionized dopants is much less than this value [Ren 96]. *Figure 1.11* shows an experimental measurements comparison between carrier mobility in bulk and doped channel modulation GaAs, for two doping values of GaAs. We can clearly notice that with 2-D doped channel modulation, we have much higher electron mobility at low temperature ($< 50\text{K}$) than the bulk GaAs.

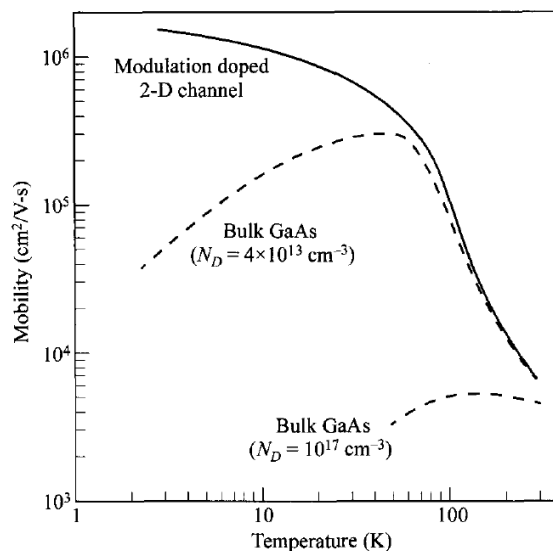


Figure 1.11: Comparison of experimental measurements between carrier mobility in bulk and doped channel modulation GaAs at low field [Lad 86].

1.3. GAN HIGH ELECTRON MOBILITY TRANSISTORS FOR SWITCHING APPLICATIONS

The reason behind this high mobility is strictly linked to the low-ionized impurities scattering [Wol 70]. For more details on the impurity scattering theory, one could consult these references [Cha 81 and Con 50]. It must be noted that this confinement also gives a lot of optical properties; for example, GaAs- based heterostructure is used for laser applications [Che 88]. Therefore, this heterostructure, having many interesting physical properties, has been immersed in several applications. The following table gives some examples of AlGaAs/GaAs heterostructure applications. However, there is a variety of applications behind the use of this heterostructure which may affect many fields either optical or electrical. Moreover, GaAs has a direct band gap so it can emit light with an excellent efficiency.

Applications	References
Laser diodes using spontaneous emission quantum propriety	[Bot 89, Ris 77, Win 85, Win 84, Yab 89 and Zin 89]
Light emitting diode	[Has 96, Koc 90, Sch 93 and Tom 10]
Solar cells	[Kos 13, Nel 78, Sug 88 and Yam 85]
Field effect transistor	[Che 95, Hu 97, Kat 84, Mim80 and Sol 84]
Monolithic microwave integrated circuits	[Bas 89]
Microwave frequency integrated circuits	[Wei 88 and Lar 91]
Optical windows	[Das 93]

Table 1.1: Some applications of AlGaAs/GaAs heterostructure.

For heterostructures based on GaN, the electron mobility is not high compared to heterostructures based on AlGaAs. The reason behind is instead the existence of different scattering mechanism that degrades the electron mobility. These mechanisms are more relevant for AlGaN/GaN heterostructures. Among these mechanisms, Jena et al. [Jen 08] specify the acoustic and optical phonon, alloy disorder and finally the dipole scattering (explained in the next section). The weight of these mechanisms changes with the temperature. The mobility is estimated to be around $600 \text{ cm}^2/\text{V.s}$ for 200K and a 2DEG density of $2.2 \times 10^{12} \text{ cm}^{-2}$ and decrease further for higher temperatures. Jena et al., [Jen 08] present a detailed study on the effect of these different physical mechanisms on the behavior of the electron mobility with temperature.

1.3.3 Polarization-induced surface charges and the source of electrons

It was an essential scientific substantiation at the end of the 1990s when O. Ambacher and his research group were able to investigate the dominant source behind the formed sheet electron density at the hetero-interface of AlGaN/GaN heterostructure [Amb 99 and Amb 00]. It was the spontaneous and piezoelectric polarization-induced surface charge. Here we will briefly explain this polarization mechanism which is going to be a vital element towards the understanding of the functioning of these components. We are not going to delve into its properties and the physics behind, but we will present a macroscopic overview that will serve us to understand and take it into account in our study. For more details, one can refer to [Woo 08 and Yu 99].

We will mainly focus on the nature, consequences and the *side effects* of this polarization.

1. Nature and consequences of polarization induced bound charges in AlGaN/GaN heterostructures:

The crystals GaN and AlN are pyroelectric materials [Byk 96 and Shu 98]. One property of these materials is the spontaneous polarization. A spontaneous polarization means that an internal polarization exists without any external applied electric field. This property is related to their

crystalline form which is wurtzite. F. Bernardini et al. [Ber 97] give the calculated spontaneous polarization of III-V nitrides crystals. The estimated theoretical values of this polarization are relatively high, the calculated values by ab initio calculations were found to be for AlN $|P_{AlN}^{SP}| = 0.081 \text{ C/m}^2$ and for GaN $|P_{GaN}^{SP}| = 0.029 \text{ C/m}^2$.

For its direction, this spontaneous polarization is always in the $[000\bar{1}]$ direction. This direction does not change whatever the direction of the external electric field. For GaN, it depends only on the growth polarity ($-Ga$ face or $-N$ face). It should be noted that although this spontaneous polarization is relatively large, the change of this polarization with temperature is relatively small which gives the advantage of using these materials in high-temperature environments [Woo 08]. The pyroelectric materials are also piezoelectric, therefore for III-V strained nitrides, a piezoelectric polarization is added to the spontaneous polarization [Woo 08]. Finally, the total polarization is the sum of these two polarizations. For a single material, as AlGaN, $P_{AlGaN} = P_{AlGaN}^{PZ} + P_{AlGaN}^{SP}$.

Up to now, we are talking about the unitary material without the heterostructure formation. Since the polarization-induced charges are formed at the two interfaces of a single material with opposite signs and their effect may vanishes. So it seems that this polarization will not affect the 2-DEG concentration. Contrariwise, during the heterostructure formation, the situation changes; the difference in polarization at the hetero-interface will count on the 2-DEG concentration.

The resulting charge from this polarization difference at the interface ($\sigma_{AlGaN/GaN}$) can be written as follows,

$$\sigma_{AlGaN/GaN} = P_{GaN} - P_{AlGaN} = (P_{GaN}^{SP} + P_{GaN}^{PZ}) - (P_{AlGaN}^{SP} + P_{AlGaN}^{PZ}) \quad (1.1)$$

Actually, the growth polarity can change the polarization direction on 2DEG. O. Ambacher et al. [Amb 99 and Amb 00] have grown a GaN/AlGaN/GaN structure with a difference growth polarity between (Ga(Al)-face and N-face). As shown in *Figure 1.12* and *Figure 1.13*, for Ga(Al)-face, the polarization direction is downwards; the formation of the 2-DEG is realized between the AlGaN and the bottom of the GaN layer. On the other side, for N-face, the direction of this polarization is upwards or the formation of the 2-DEG is realized between the AlGaN and the top of the GaN layer. P_{PE} denotes piezoelectric polarization.

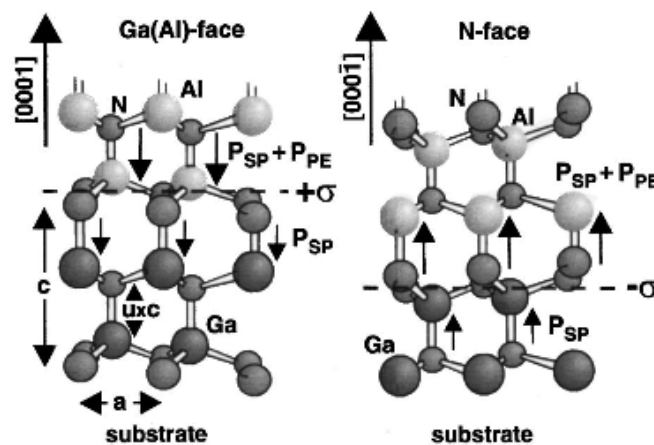


Figure 1.12: Ga(Al)-face & N-face growth of GaN/AlGaN/GaN heterostructure [Amb 00].

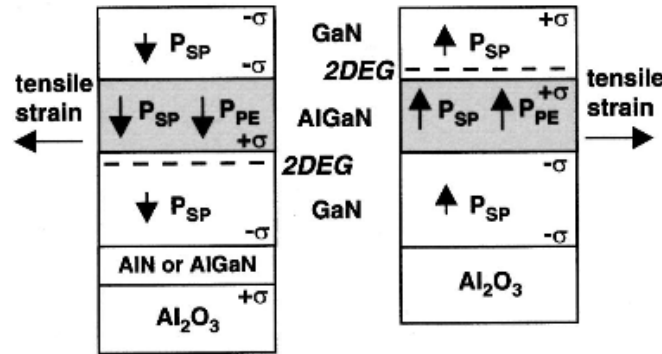


Figure 1.13: Spontaneous and piezoelectric polarizations directions for the Ga(Al)-face & N-face growth of GaN/AlGaN/GaN heterostructure [Amb 00].

Now, we are interested in having an overall effect of this polarization on the 2DEG concentration. C. E. C. Wood et al. [Woo 08] give a simple explicit formulation of the dependence of this polarization at the interface as a function of the aluminum density in the AlGaN layer.

$$P_{AlGaN/GaN}^{PZ}(x) = (-0.0525x + 0.0282x(1-x))C/m^2 \quad (1.2)$$

$$P_{AlGaN}^{SP}(x) = (-0.090x - 0.034x(1-x) + 0.021x(1-x))C/m^2 \quad (1.3)$$

x is the aluminum concentration in the AlGaN alloys.

It must be noted that this polarization was created in the initial state only during the formation of the heterostructure.

2. The side effects of this polarization:

Like everything, we cannot win without sacrificing something. Although the advantages of this polarization, the dipole scattering resulting from this polarization present a non-negligible mechanism that affects the electron mobility. Its dipole moments in the AlGaN barrier layer are not equal in each cell unit since the AlGaN alloy is a disordered system (where Al and Ga are arranged randomly). Therefore, we find ourselves with dipoles that have magnitudes that fluctuate in the AlGaN barrier, which significantly affect the electron mobility [Jen 00 and Zha 04]. This polarization affects the electrical properties of the heterostructure and could cause some instabilities or shift in its electrical characteristics during operations.

1.3.4 Structures

After the presented interest behind the GaN HEMT devices, we present some of their developed structures in the literature. A good understanding of these structures geometrically and physically will present the basis that will be used to implement the physical models in this thesis. Different structures and geometries have been developed to improve the devices breakdown voltage, electric fields distribution and the dynamic On-resistance [Sai 03]. In this section, we will present the variety of the threshold voltage for different structures. The presented structures are divided into two types: Normally-OFF structures (positive threshold voltage) and Normally-ON structures (negative threshold voltage). For safety reasons, power electronics applications require components with positive threshold voltages [Che 09b and Hua 14]. In the next subsections, we will present some examples of these structures. The real structures used in this thesis will be shown and detailed in chapter 2.

1.3.4.1 Normally–ON Structures

Normally–ON comes principally from the nature of the HEMT components. During the hetero-structure formation, there is a created sheet carrier density that is ready to be in conduction. By applying a drain voltage and if the 2DEG density is high enough, a conduction current may take place even if there is no control of the gate voltage. Therefore, the device will be in its ON-State. To block this component, it will be necessary to apply a negative gate voltage which will subsequently open the electron channel, and renders the component to its OFF-State. Some examples of Normally–ON structures are presented by [Lee 02 and Sai 03].

As shown in *Figure 1.14*, an example of a Normally–ON structure grown on SiC substrate, the device consists of an AlGaN/GaN heterostructure with 30% aluminium concentration. The component has a Schottky contact (Metal/Semiconductor contact). Field plates are used in order to redistribute the electric fields, which will improve the device’s breakdown voltage. The AlN layer is used to adapt the mesh between GaN and SiC.

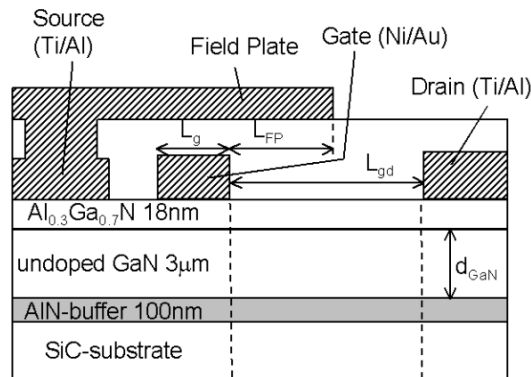


Figure 1.14: An example of a normally ON component made with field plate [Sai 03].

1.3.4.2 Normally–OFF Structures

In order to meet the needs of power electronics, especially in switching applications, several technological solutions have been developed [Bou 09, Chu 08, Hil 10, Miz 07 and Tan 13]. Here we focus only on two methods: the recessed-gate structure and the p-gate structure.

1. Recessed-Gate Structure :

This method is considered one of the well-known for fabricating Normally–OFF GaN HEMTs. The general idea is to perform an etching depth in the AlGaN layer only under the gate in order to control the threshold voltage. As will be shown in the modeling section, the threshold voltage increases with the decrease in the AlGaN layer thickness. W. Saito et al. [Sai 06] observed the possibility of controlling the threshold voltage without much altering the On-state resistance of the device. This structure also improved the device trans-conductance [And 03 and Oka 04]. As shown in *Figure 1.15a*, there is an etching almost only under the gate. A TEM image presented in *Figure 1.15b* that shows an etching up to 9.5nm of the AlGaN barrier thickness. However, although the method moves the threshold voltage to higher values, it is not always functional. This depends on the value of the threshold voltage before the recess and the density of the impurities in the GaN and AlGaN layers under the gate.

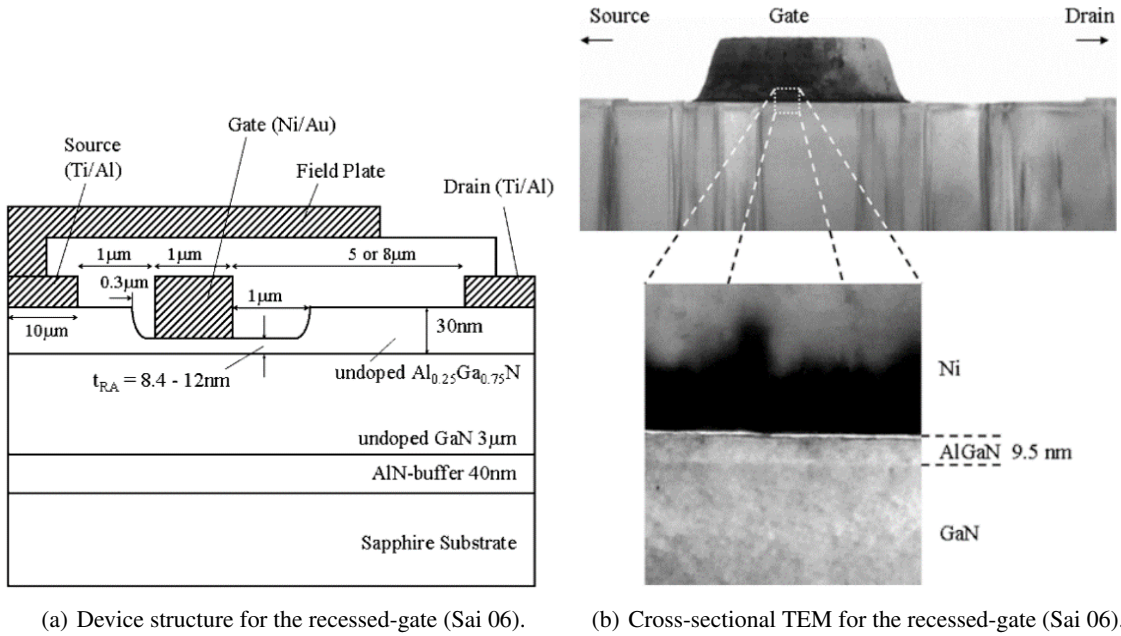


Figure 1.15: Example of recessed-gate structure.

In the following table, we present a small review of the work performed in literature around the recessed-gate structure effect on the threshold voltage.

Threshold voltage	Notes	References
$V_{TH} = -0.14V$	Although the author used the recessed gate method, he did not completely succeed to get a positive threshold voltage. The threshold voltage (before recess) was -4 V.	[Sai 06]
$V_{TH} = +0.06V$	Recessed gate with an electrode-less wet etching technique.	[Lee 12]
$V_{TH} = +0.8 \pm 0.06V$	MIS structure with tri-gate (Recessed tri-gate).	[Lu 12]
$V_{TH} = +1.5V$	MISFET with piezo neutralization technique structure.	[Ota 09]
$V_{TH} = +3V$	The author improved the method by using a dielectric instead of a Schottky contact, enhanced with a triple cap layer.	[Kan 10]
$V_{TH} = +5.2V$	MIS structure with recessed gate.	[Oka 08]

Table 1.2: A small review of recessed gate technology.

2. P-Gate structure:

For the P-Gate structure, a P-doped AlGa_N (Figure 1.16) or GaN layer is grown under the gate. This layer lowers the Fermi level and makes the channel Normally-OFF. This method also depends on the impurities introduced into the layers under the gate and the thickness of the different layers. This method has also been used for some current commercial components as the GaN Systems, EPC and Panasonic devices.

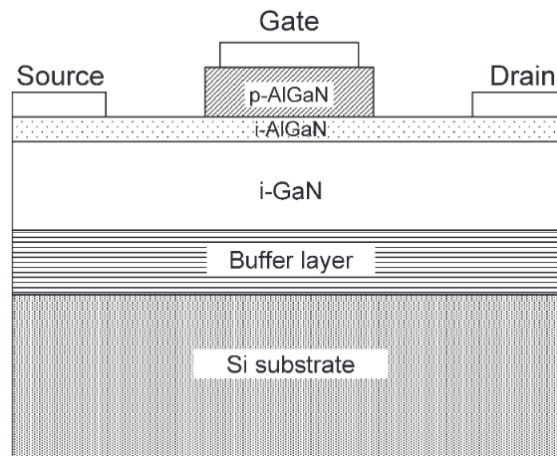


Figure 1.16: P-Gate structure with AlGaN P-doped [Uem 07].

We chose to present only two forms of Normally–OFF structures, i.e, the recessed gate and the p-gate as those structures will be the ones of interest that will be used in this thesis.

After presenting some fundamental principles of the GaN HEMT, now we will move on to the principal axes that will affect the thesis.

1.4 Axis 1 – Physics understanding of traps

Although the component has many advantages, there are limiting phenomena which will hinder the proper operation of these devices. One of these critical phenomena is the trapping/de-trapping mechanism which impedes the appropriate electro-thermal behavior of the device. This phenomenon presents a fundamental source of the GaN electrical characteristics instability and performance degradation. Research work around this phenomenon has increased and become really varied over the last two decades mainly for devices used in RF applications. Some authors seek to reveal the physical reason origin behind its effects observed on the electrical characteristics. For example, S. Binari et al. [Bin 01] have demonstrated the effect of the surface traps on the continuous wave power density at high frequency 3.8 GHz. Other authors seek only to study its effects, like J. M. Tirado et al. [Tir 07], who studied the dispersion of the drain current when the gate and the drain were pulsed. We can also find authors who present detailed reviews of the work around the phenomenon, like S. Binari et al. [Bin 02], who presented a study of the trapping effect on the transient behavior by comparing GaN with SiC devices for RF applications. Researchers have also tried to find some technological solutions in order to reduce or to eliminate their effects: H. Kim et al. [Kim 03a] have demonstrated the effect of SiN passivation on the elimination of some traps effects and Z. H. Liu et al. [Liu 11] proved a reduction in the trapping effects with a suppression of the gate leakage current using SiN/Al₂O₃ passivation. In this section, we will present a review of the traps nature, mechanism, location and effects on the electrical and physical characteristics of the device. The discussion will be limited to traps in GaN HEMTs. A quick review of the work carried out so far on their characterizations and modeling will be presented in the next section.

Starting with the traps definition, they present some sub-categories of defects arising from several sources and described in [Schr06]. They can be classified as unintentional defects and result from unintentionally introduced impurities, dislocations or even from self/foreign interstitial or vacancies. Therefore, traps are related to defects that have not been controlled, especially during the manufacturing process. However, traps are unwanted and undesirable. They cause an adverse effect on the device's electrical characteristics, starting from a permanent shift of the characteristics (threshold voltage, on-state resistance) until a reversible shift during the device operation. Roughly speaking, they present a significant source of instability.

Regarding the technological reasons for their formation in bulk GaN, there has been extensive research on the traps in bulk GaN grown by various methods. F. D. Auret et al. [Aur 99] have studied their introduction in epitaxial grown n-GaN during 2 MeV proton bombardment. The authors also defined the rates of the bombardment for the creation of two energy levels. They have also studied the traps formation within epitaxial n-GaN irradiated with 5.4 MeV He ions irradiation [Aur 98]. However, no traps level related to dislocations was detected by this method or by a particle implanted GaN method. A. Y. Polyakov et al. [Pol 02] have observed the existence of hole traps which may probably correspond to dislocation density in n-GaN films grown by hydride vapor phase epitaxy (HVPE). A little review of the work concerning the detection of holes traps in GaN bulk which are grown by different mechanisms have been presented by [Aur 04], the presented growth was instead (Organometallic vapor phase epitaxy (OMVPE) and HVPE) for undoped and doped GaN. On the other hand, H. Cho [Cho 01] have also studied the growth rate effect of undoped GaN film grown by metalorganic chemical vapor deposition; they found that decreasing the growth rate will increase the edge dislocations. Traps in n-GaN grown by reactive molecular beam epitaxy have also been studied according to growth conditions, a dominant trap was detected. The authors attributed it to N-vacancy defect [Fan 98]. Traps levels introduced during Ammonia-based molecular beam epitaxy was also studied, where a relationship between the NH₃/Ga flux rate and the concentration of the nitrogen and gallium vacancies (V_N, V_{Ga}) related defect was found. It has been proven that the higher rate of NH₃/Ga flux, the lower concentration of traps using this process [Are 08].

However, traps sources and locations have not only been studied for GaN bulk; traps resulted from threading dislocations are also observed for AlGaIn/GaN/SiC Schottky barrier diodes (SBDs) [Fan 05]. The same authors also studied the GaN-doped carbon on traps density detected for SBDs. They found that the density of the traps decreased in the low-[C] (low doped carbon concentration) SBD. They have also attributed this density to dislocations due to the difference between the microstructures [Fan 10]. Other traps sources also have been detected, besides the GaN bulk traps, due to the non-adaptation of mesh between the AlGaIn and GaN layers at the hetero-interface of the SBD, there are surface traps that appear after growth at the hetero-interface. It can name interface traps or heterointerface traps. Z.-Q. Fang et al. [Fan 10] have detected two hole traps in this region.

These observations change when one talks about HEMTs, the structure is more complex, and traps can result from other technological reasons. It should be noted that the identification of a trap's location does not become straightforward. A. Sasikumar et al. [Sas 14] explains the controversy behind the identification of a trap between buffer and barrier layer of the HEMTs. However, other authors have studied specific regions of the device. R. Vetury et al. [Vet 01] studied the surface traps (surface of the AlGaIn layer) effects on the static and transient characteristics of the HEMT. They showed how these surface traps are dominant especially when the surface is not passivated. A study was also performed to describe the passivation effect on the devices RF characteristics [Gre 00]. The effect of the SiN passivation of the AlGaIn surface on the reduction of the traps state in the HEMT components was investigated by [Ver 02]. On the other hand, other researchers detected traps in the GaN bulk [Men 14], the AlGaIn barrier [Gas 12] and other regions.

Overall, traps' location in HEMTs can be found in the following regions:

- AlGaIn Surface traps: they are under the gate in Schottky gate structure or the access region between the gate and the drain.
- Interface traps: they are under the gate in MIS structure or at the interface between the oxide and the AlGaIn layer. They can also be found under the gate in fully recessed gate MIS structure at the interface between the oxide and the GaN layer.
- Bulk GaN traps: they are probably created during the growth of GaN.
- AlGaIn barrier traps: they can be found in the doped or undoped barrier.
- Hetero-interface traps: these levels are located at the interface of the heterostructure, it is also called heterojunction traps.
- Oxide traps: they are located in the oxide in a MIS-HEMT structure.

We present in *Figure 1.17*, a scheme illustrating the common different traps locations studied in the literature.

1.4. AXIS 1 – PHYSICS UNDERSTANDING OF TRAPS

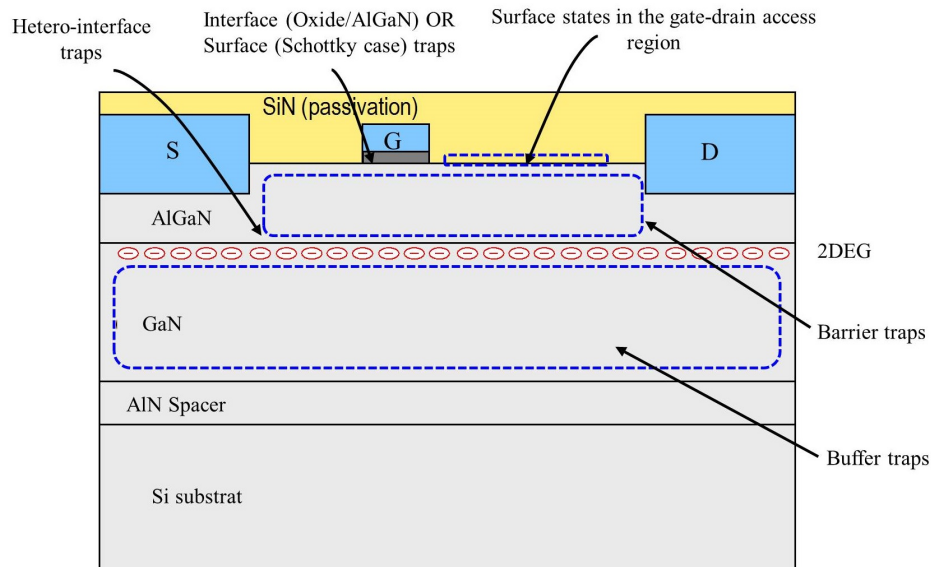


Figure 1.17: Possible traps location in the structure.

In Table 1.3, we present a review of the location of the traps in the HEMTs devices discussed in the literature.

Location	Identification	Process notes	References
Surface and buffer layers	–	<ul style="list-style-type: none"> • Grown by MOCVD • AlN nucleation layer • Passivated (SiN) & un-passivated devices 	[Bin 01]
Interface (Dielectric/AlGaN)	Donor traps	<ul style="list-style-type: none"> • AlGaN/GaN MIS-HEMT with Si₃N₄/Al₂O₃ bilayer dielectrics 	[Wu 15a]
Interface (Dielectric/GaN)	N–Vacancies (at the surface), Probably generated during the gate recess	<ul style="list-style-type: none"> • AlGaN/GaN MOS–HEMT • ALD-Al₂O₃ dielectric • Fully-recessed gate structure 	[Shi 16]
Surface	Two hole traps and one electron traps	<ul style="list-style-type: none"> • AlGaN/GaN heterostructure grown by MOCVD on a sapphire substrate 	[Oki 03]
Surface and buffer layers	Traps were identified as hole traps	<ul style="list-style-type: none"> • GaN/AlGaN/GaN grown by MOCVD on SiC substrate 	[Faq 07]
AlGaN barrier and surface	Two hole traps (surface) and one electron traps (AlGaN barrier)	<ul style="list-style-type: none"> • AlGaN/GaN heterostructure grown by MOCVD on a sapphire substrate • Si₃N₄ surface passivated 	[Gas 12]
Buffer	Related to Fe concentration in the GaN buffer	<ul style="list-style-type: none"> • AlGaN/GaN HEMT grown by MOCVD on SiC • Fe doped GaN 	[Car 13]
Oxide and interface (Oxide/AlGaN)	–	ALD–HfO ₂ /AlGaN/GaN MOS–HEMT	[Sun 13]
Buffer layer	Intrinsic defects whose concentration depends on the buffer doping (Not related to iron)	<ul style="list-style-type: none"> • Grown on SiC substrate • Fe-doped buffer 	[Men 14]
Buffer	Donor traps (point defects) and acceptor traps (Ga–Vacancies)	<ul style="list-style-type: none"> • AlGaN/GaN HEMT grown by MOCVD on Si 	[Yan 14]
Hetero-junction (Hetero-interface) and surface	N–Vacancies (at the surface) and dislocations (at the hetero-interface)	<ul style="list-style-type: none"> • AlGaN/GaN heterostructure grown by plasma-assisted molecular beam epitaxy • Dislocations reduced to a high temperature rapid N₂ thermal annealing 	[Par 10]

Interface (Oxide/AlGaN)	–	<ul style="list-style-type: none"> • ALD-Al₂O₃/AlGaN/GaN MOS–HEMT • Grown by MOCVD on SiC substrate 	[Ma 13]
Barrier and buffer	–	<ul style="list-style-type: none"> • AlGaN/GaN grown by PAMBE • Passivated surface 	[Sas 12]

Table 1.3: Review of traps sources and locations in AlGaN/GaN HEMTs

Now we will present a physical explanation of the traps and describe their mechanisms. As the intentionally introduced impurities, traps are introduced energy levels into the material bandgap. They may also be donors or acceptors, having usually higher activation energies and deeper energy levels than donors and acceptors of the intentional doping. Several factors manage their participation and their influence on the potential distribution throughout the material and its temperature. Their impact on the electrical characteristics of the component also depends firmly on the traps physical parameters comprising their density, their activation energy, and their cross sections.

1.4.1 A brief explanation of the traps physical parameters

The discussion will be instead oriented around the electrons emission from traps. Nevertheless, the discussed physical parameters are the same when one speaks about the electrons' capture. It is the mechanism that changes between emission and capture. We begin with the thermal activation energy. It can be defined as the required energy to thermally excite an electron from a trap to the conduction band. This may be written in the following form [Sch 06]:

$$\Delta E = E_C - E_T \tag{1.4}$$

When there is no applied electric field through the traps barrier, this activation energy is named zero-field ionization energy. ΔE is the activation energy, sometimes it is denoted E_A , E_C is the conduction energy level, E_T is the traps level and T is the temperature.

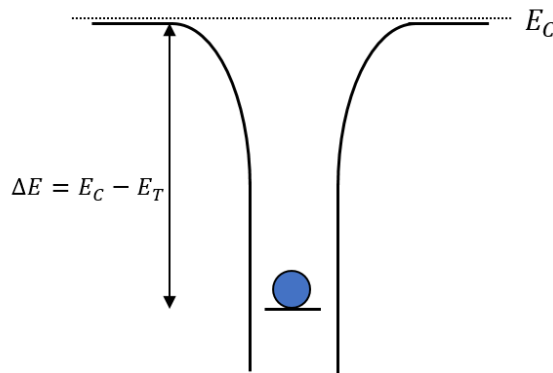


Figure 1.18: Electron energy diagram in equilibrium at zero electric field.

There are several ways for electron/hole to be emitted from their potential barrier. Schroder [Sch 06] has defined four ways that an electron/hole can be emitted/captured (*Figure 1.19*). He considered that traps are deep levels. An electron can be captured by the conduction band (a), this electron can be re-emitted (b) or recombined (c). After recombination, the recombined electron can perform the same steps but in the opposite direction. It can be generated through the trap by the process (d). In the mathematical model proposed in his book, an emission of an electron from the valence band to the trap's level

corresponds to a capture of a hole into the valence band. *Figure 1.19* shows these four mechanisms. n is the free electrons density in the conduction band, p is the density of holes in the maxima energy level of the valence band. E_C is the minima energy level of the conduction band, E_V is the maxima energy level of the valence band, E_T is the traps energy level introduced into the band gap, e_n and e_p are the emission rate for electrons and holes respectively while c_n and c_p are and capture rate for electrons and holes respectively.

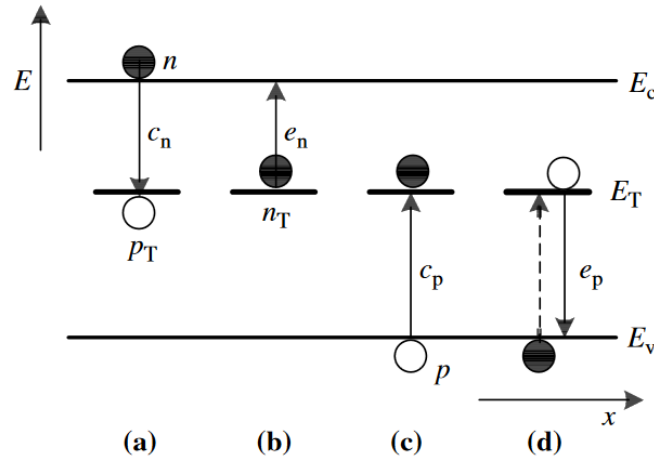


Figure 1.19: Possible emission and capture ways that can occur at a traps level [Sch 06].

The emission and capture parameters are defined as follows:

Parameters	Physical description	Mathematical description
Emission rate for electrons: e_n (1/s)(Same for holes)	Electrons emitted per second from electron occupied G–R (or traps) centers.	$e_n = \frac{1}{\tau_e}$ τ_e presents the emission time constant.
Capture coefficient c_n ($\frac{cm^3}{s}$)	When multiplying by the free electrons density in the conduction band, $c_n n$ presents the electrons density captured by second from the conduction band.	$c_n = \sigma_n v_{th}$ σ_n presents the capture cross section and v_{th} is the thermal velocity.
Emission time constant (τ_e)	The change of state does not happen instantaneously, but it has a particular dynamic which itself can evolve according to the conditions surrounding it. The emission time constant defined the time taken for the change of the traps state.	$\tau_e = \frac{\exp(\frac{E_C - E_T}{kT})}{\sigma_n v_{th} N_C}$ k is the Boltzmann constant, T is the temperature and N_C present the density of states in the conduction band.

Table 1.4: Emission and capture process parameters.

The cross–section can be defined as an area around the traps that quantifies the probability of capturing an electron. If an electron passes through this section, there is a high possibility of being captured. Therefore, the larger the cross-section, the higher the likelihood of capturing electrons. Thus it is always denoted by *Capture Cross-Section*.

The mechanism shown in *Figure 1.19* is called (Shockley–Read–Hall or trap–assisted) generation/recombination. The electrons can have a direct generation/recombination with the conduction/valence band. However, Schroder did not consider in his model the radiative or Auger processes. Furthermore, the electron/holes in these traps can be subjected to several mechanisms of emission and capture. The electron/hole must get an energy equal to the activation energy to be generated or recombined. Based on this mechanism, Schroder calculated in his book [Sch 06] the emission and capture time constants of the electrons/holes.

However, this emission activation energy or the energy required for the emission of an electron from the trap level to the conduction band, can change according to the applied electric field and according to other emission mechanisms described by [Mit 03]. There are mainly three emission mechanisms defined in the literature [Mit 04].

1.4.1.1 Poole Frenkel effect potential barrier lowering

It describes the electric field impact on the electrons emission. The energy needed to excite an electron to the conduction band will be shared between the thermal fluctuations and the electric field. O. Mitrofanov et al. [Mit 04] studied this mechanism on the emission of electrons from the traps found in the AlGa_N barrier of AlGa_N/Ga_N HEMTs. The authors defined the decreased barrier amount $\Delta\phi_{PF}$ due to electric field.

$$\Delta\phi_{PF} = \left(\frac{q^3}{\pi}\right)^{1/2} \times \sqrt{F} \quad (1.5)$$

q is the elementary charge, ϵ is the dielectric and F is the electric field. A relation between the activation energy and the applied voltage is given by the following graph. In this graph, E_T designates the zero-field ionization energy. The activation energy is written as following:

$$E_A = E_T - \Delta\phi_{PF} \quad (1.6)$$

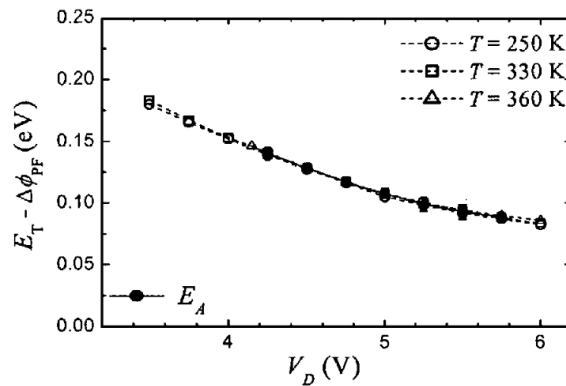


Figure 1.20: The activation energy as a function of the applied voltage [Mit 04].

1.4.1.2 Phonon assisted tunneling PAT

This phenomenon is one of the mechanisms of the quantum mechanical tunneling. This mechanism is favored by the increase in crystal temperature. As shown in *Figure 1.21*, the electron can escape from the barrier by absorbing the energy of a phonon. The probability of emission by phonon depends mainly on the shape of the potential distribution. Quantum model for phonon-assisted tunnel ionization of deep

levels in a semiconductor has been presented in the literature [Mak 82]. However, we will not go into detail in quantum models.

1.4.1.3 Direct tunneling DT

As shown in *Figure 1.21*, the electrons can tunnel directly between the traps and the conduction band. This mechanism depends strongly on the applied electric field, on the distance between the trap levels and the minima of the conduction band. These mechanisms have been well explained in the literature, as well as the models describing their behavior in the GaN components.

- Dominant mechanism

The dominance of these mechanisms changes with the temperature and the applied electric field. Direct tunneling is temperature independent and is dominant at low temperatures. For temperatures higher than 250K, Poole-Frenkel emission becomes the most dominant mechanism. At very high temperatures, the phonon-assisted tunneling becomes very important [Mit 03]. As shown in *Figure 1.21*, the different mechanisms of emission through the potential barrier. r_{max} is the distance to the maximum of the barrier during the Poole-Frenkel emission, $V_i = E_g - E_t$ is the zero-field ionization energy, δV_i is the lowering barrier potential, E_{th} is the energy needed to emit an electron by phonon.

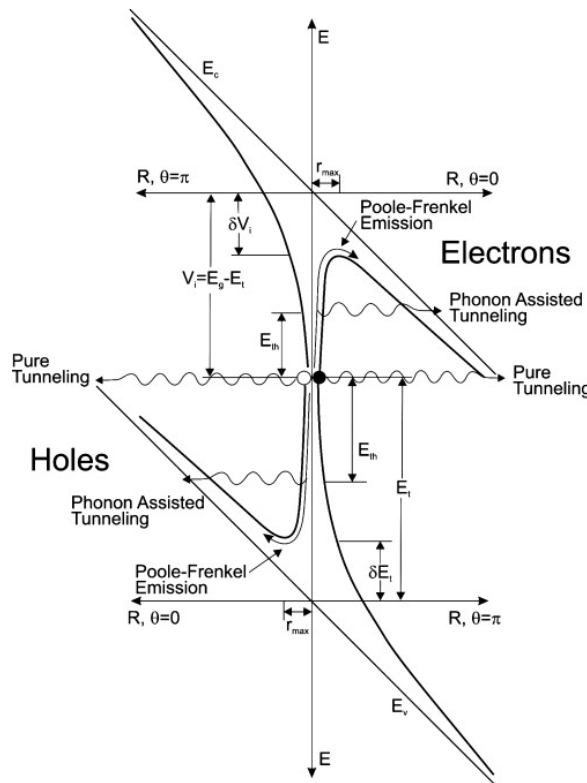


Figure 1.21: An electron/hole emission mechanism from traps through a potential barrier according to Poole-Frenkel emission, phonon-assisted tunneling and direct tunneling [Joz 10].

However, taking into account of all these phenomena, either in modeling or characterization is not always necessary. Most characterization and modeling methods do not take these phenomena into account and consider that the SRH mechanism alone is sufficient. Until now, we are discussing a single trap in a potential barrier; now we will present the effect of the traps on the electrical characteristics of the component.

1.4.2 Traps' effects in HEMTs

Until now, the discussion is around the traps in their potential barrier; We will address the effect of the traps in semiconductor structures especially in HEMT transistors. Traps are randomly distributed in structures with uncontrolled densities, which varies according to the technology process. These traps' effects depend on their density, location, activation energies but above all, on the state of their charges in the initial state and on the response to any change of the applied electrical stress or the surrounding temperature. Foremost, the traps' charge state may evolve according to any change in temperature or applied stress. The change of state does not happen instantaneously, but it takes a certain dynamic which itself can evolve according to the conditions surrounding it. Therefore, traps may affect either static or transient device characteristics. Their effect can change according to polarization and temperature conditions. We can find their effects on $I_{DS} - V_{DS}$, $I_{DS} - V_{GS}$, V_{TH} , drain transient current $I_{DS}(t)$, dynamic-ON resistance, etc. For example, the effect of traps on the threshold voltage has been studied theoretically and experimentally by [Hua 11 and Lag 12]. The traps (which will be non-intentional additional charges) will affect the electric field distribution and the potential distribution in the device.

Now, we will present some traps effects on the electrical characteristics of the HEMTs.

1.4.2.1 Effects on static I-V characteristics

- Reverse polarization point on the pulsed I-V electrical characteristics

Phenomenon: By changing the polarization point in the OFF state in pulsed measurements, there is a change in the measured electrical characteristics.

Explanation: During pulse measurements, as shown in *Figure 1.22*, there is a sweep in the polarization levels between the ON and OFF states. For components without trap mechanisms, changing the OFF state polarization level does not affect the ON state measurements. On the other hand, for components with trap densities, an ionized partial traps density and sometimes the total density itself changes (depending on their activation energies) with the change in this polarization level. Therefore, the observation of this phenomenon with a change in the OFF- state polarization, either the gate or the drain voltages, indicates the presence of the traps. This phenomenon is sometimes used to characterize and quantify the effect of the traps [Bis 13].

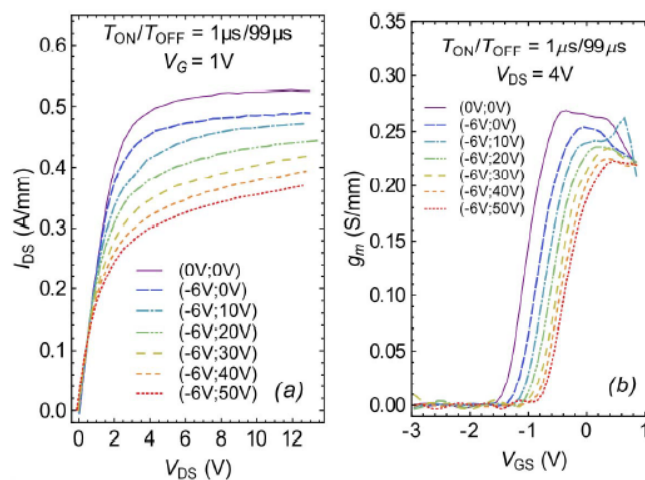


Figure 1.22: $I_{DS}-V_{DS}$ and g_m-V_{GS} for several pairs of reverse bias points at the drain and the gate (V_{GS_0} ; V_{DS_0}) [Bis 13].

- Kink effect: This phenomenon is also observed in the I-V characteristics.

Phenomenon: A brutal jump in the drain current occurs under high drain-source voltage as shown in *Figure 1.23*.

Explanation: This is based on the variation of pinch OFF voltage that occurs with the change of the drain-source polarization [Men 09]. For structures without traps, the threshold voltage is estimated to be constant. For the HEMTs components, which have a trap density in the structure, with the change of state of drain-source polarization, a change in the state of charges can occur. Therefore, the pinch OFF voltage probably shifts to negative values (due to traps that begin to be activated at these voltage levels) and so a brutal jump in the drain current occurs under this high voltage.

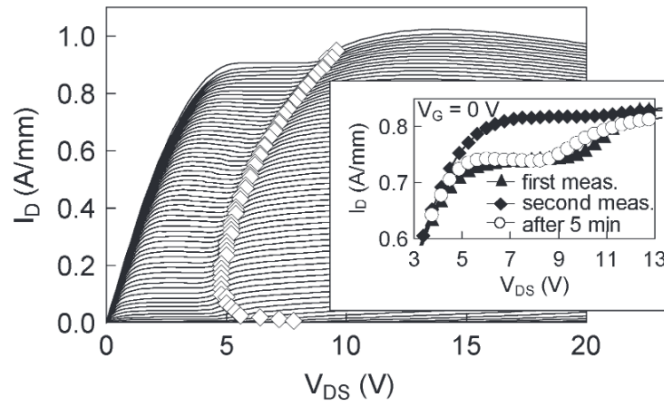


Figure 1.23: I_{DS} - V_{DS} results with observed kink effect [Men 09].

1.4.2.2 Effects on transient drain-source current

These traps' dynamics induce two transient phenomena called Drain lag and Gate Lag. The definition of these terms can be explained briefly as:

- Drain lag:

This phenomenon is observed in the transient measurements of either current or dynamic resistance after a drain voltage stress difference.

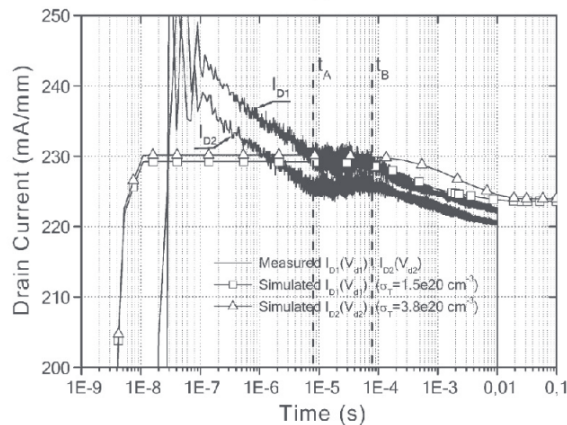


Figure 1.24: Trapping effect on the transient response of drain polarization change [Tir 07].

Phenomenon: It can be observed in *Figure 1.24* [Tir07] with the delay to reach the stability of the power current due to changes in the polarization of the drain. In other words, it is the delayed response of the channel current to modulation of the applied drain electrical stress. Explanation: Electrical stress is applied to the drain-source terminals of the device in the OFF state for a certain time. Then, the component is switched to ON state, and the transient current is measured. Since traps have relatively long time constants, there will be a variation in current or the On-state resistance.

The traps responsible for this phenomenon are located in the gate-drain access region. They may be in the bulk of the AlGaN or GaN layer or the drain-gate interface state.

- Gate lag:

This phenomenon is observed in the transient measurements of either current or dynamic resistance after a gate voltage stress difference.

Phenomenon: As shown in *Figure 1.25*, it is the delay of the stability of the power current due to the changes in the gate polarization. In other words, it is the delayed response of the channel current to modulation of the applied gate electrical stress. Explanation: Electric stress is applied to the gate-source terminals of the device in the OFF state for a certain time. Then, the component is switched to the ON state, and the transient current is measured. Since traps have relatively long time constants, there will be a variation in current or for the On-state resistance. The traps responsible for this phenomenon are located under the gate-drain access region. They may be in the bulk of the AlGaN or GaN layer or the drain-gate interface state.

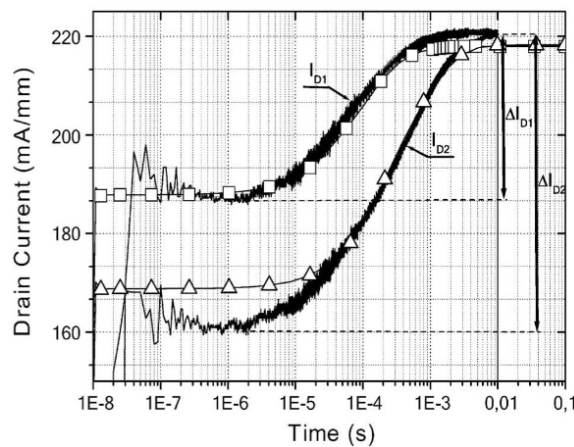


Figure 1.25: Trapping effect on the transient response of gate polarization change [Tir 07].

1.4.2.3 Traps effect during switching process

Since components will be used in power electronics, it is essential to discuss the effects of the trap on switching process. I.Rosetto et al. [Ros 17] investigated the impact of soft and hard switching conditions on dynamic ON resistance. The applied stress and measurement method based on the double pulse is presented in *Figure 1.26*. V_{DSQ} , V_{GSQ} present the values of the drain and gate quiescent point, $t_{onDrain}$ & t_{onGate} present the ON-state time of the drain and gate stress application respectively while t_{OFF} presents the OFF–state time of the gate stress. DGD presents the time range between $V_D = \frac{V_{DS}}{2}$ and $V_{GS} = V_{TH}$. The measurements were made during the pink column.

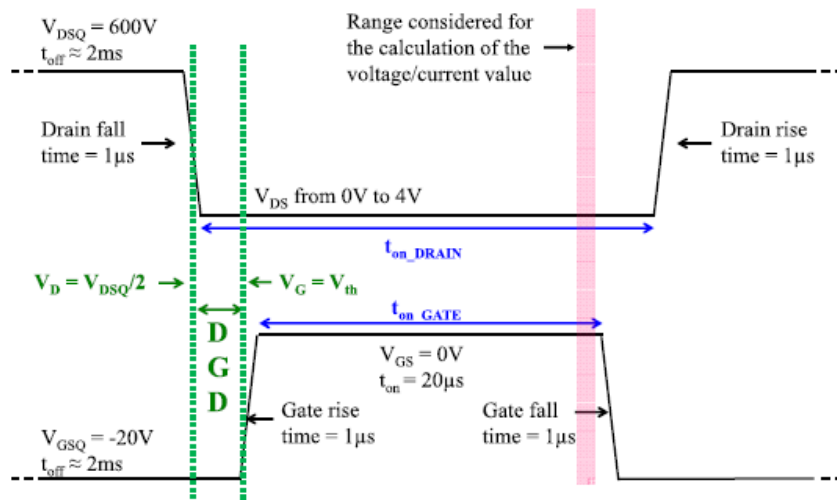


Figure 1.26: Proposed measurement system to study the effect of polarization conditions and the emergence of traps on the dynamic resistance during switching process [Ros 17].

The authors studied several parameters like V_{DSQ} , DGD and temperature. As shown in Figure 1.27, they studied the effect of change of DGD duration for a given temperature. They found that there is almost no difference up to 300V in the ON-state resistance. They also studied the variation of the dynamic R_{ON} function of the DGD for different V_{DSQ} values for a single temperature.

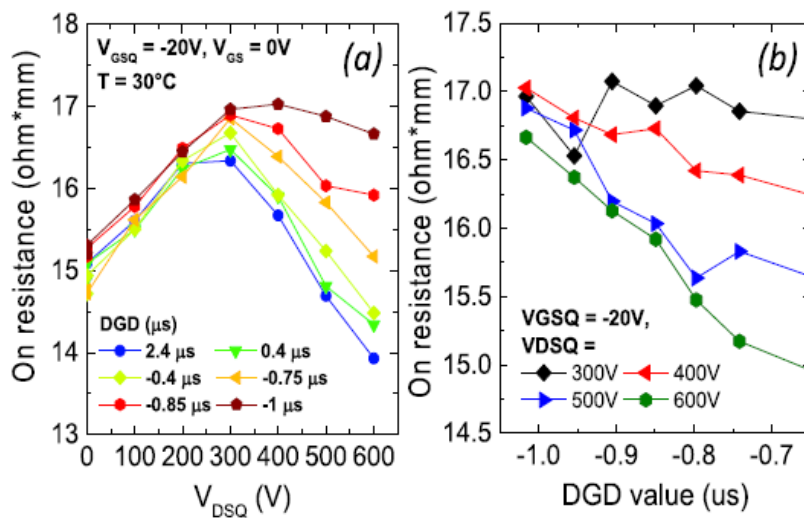


Figure 1.27: On resistance as a function of drain quiescent point and DGD value for a single temperature [Ros 17].

As shown in Figure 1.28, their measurements indicate that temperature has a negligible influence on dynamic R_{ON} at high V_{DSQ} ($V_{DSQ} > 300$ V) for soft switching and the dynamic R_{ON} decreases with temperature, following a monotonous behavior. They found a difference instead in hard switching where they assigned this effect to hot electrons that play a significant role in trapping during stress.

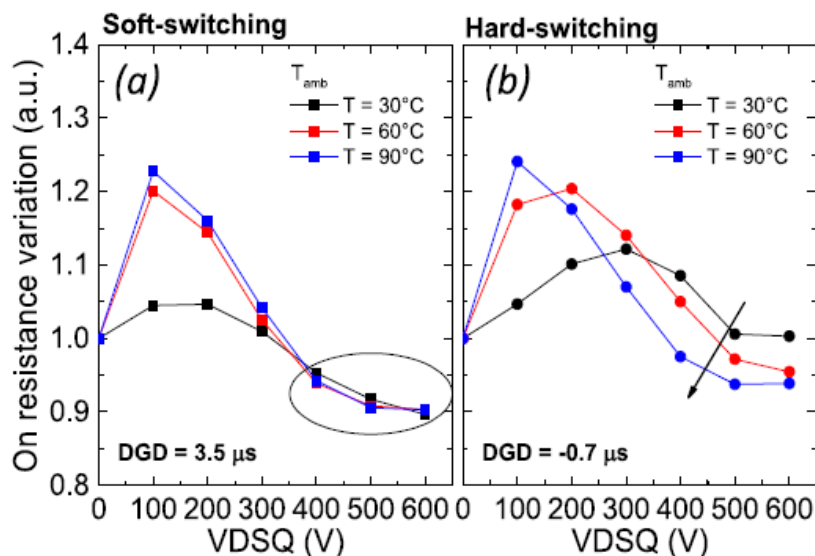


Figure 1.28: On resistance variation as a function of drain quiescent point in soft and hard switching for different temperatures [Ros 17].

Now we go to axis two: the traps Characterization.

1.5 Axis 2 – Traps Characterizations

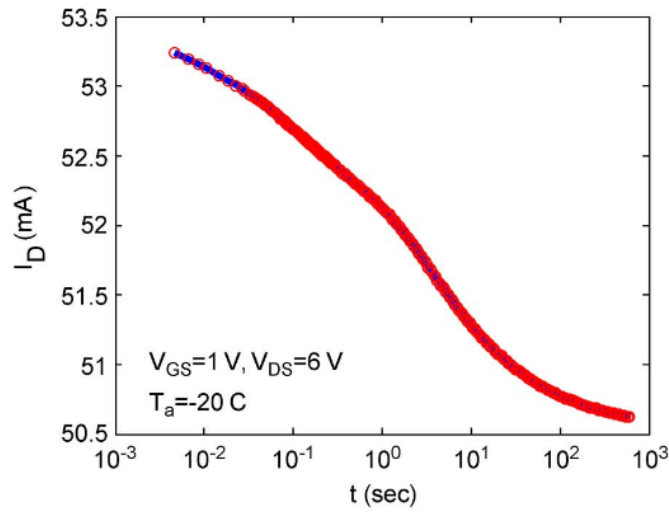
Traps characterization is the step to reveal experimentally the physical parameters discussed in the previous section. The revealed information depends on the characterization method. We find methods that reveal only activation energies and cross-section. There are others that can give some information about the traps density and location. Here, we will present the best-known methods briefly to characterize traps in the GaN HEMTs and the advantages and limitations of each method. We will also present a small review of the results extracted from each characterization method from the literature. Nonetheless, these characterizations are mainly divided into three types: Electrical, optical characterization, and sometimes electro-optical methods [Men 11]. Generally speaking, electrical methods are easier to retrieve activation energies and cross-sections. They normally do not give an exact idea about the location of the traps or their distribution profile. M. Meneghini et al. [Men 11] presented a survey of the electrical methods used to characterize the physical parameters of the traps. They are mainly divided into five methods. On the other hand, the optical methods are more used to detect the traps location and density. Most of these optical methods require sophisticated equipment. Among the best-known methods, one can cite cathodoluminescence, electroluminescence, and secondary ion mass spectrometry. Here, we will concentrate only on an electrical method that will be used in the thesis: the transient drain current measurements.

1.5.1 Transient drain current measurements

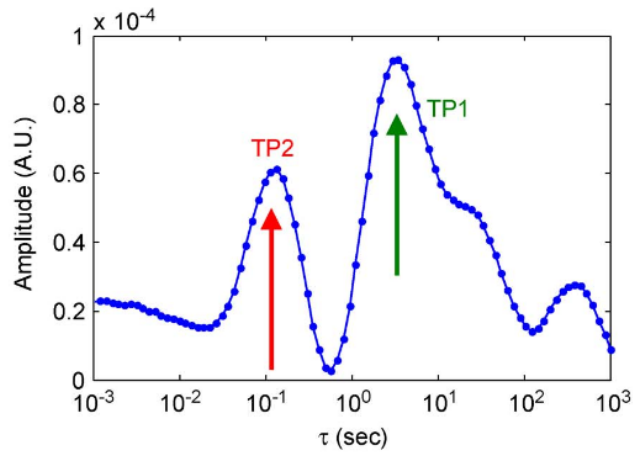
This method is well-known and based on the extraction of the traps time constants (or equivalent emission rate) from the transient drain current measurements. This is done by a multi-exponential analysis of the drain current transient. The transient behavior is the response to a change in the (OFF and ON) state polarization. The results of this fit will be used to reveal and plot the time constant spectrum that will be used to extract the most dominant time constants. The detailed method and the extraction methodology of the parameters will be detailed and presented in chapter 3.

$$I_{fitted} = \sum_{i=1}^n a_i \times \exp\left(\frac{-t}{\tau_i}\right) + I_{\infty} \quad (1.7)$$

Where I_{fitted} is the fitted current, a_i are the exponentials amplitudes, τ_i the correspondent time constants and I_{∞} is the steady-state current. As Shown in *Figure 1.29*, there is an example of a transient current adjusted by $n = 100$ exponentials. The time constants spectrum is also presented where a dominance of two trapping process was found (TP means trapping process).



(a) Transient drain current and fitted multi-exponential signal.



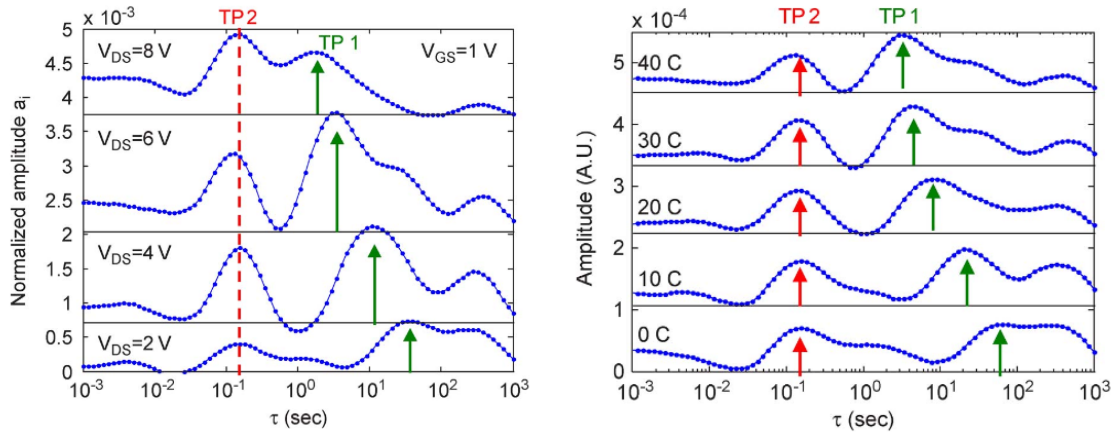
(b) Time constants spectrum with two traps process.

Figure 1.29: Example of transient current fitted by $n = 100$ exponentials [Joh 11].

These trapping process which occurred at some time constants may shift with the temperature. Their behavior can also be changed with the change in the polarization conditions. As shown in the following figures, by changing the ON–State drain bias (*Figure 1.30a*), the time constants spectrum describing the traps may change. An overlapping of the different trapping process can also happen. In this example,

1.5. AXIS 2 – TRAPS CHARACTERIZATIONS

they were able always to identify the two trapping process. On the other hand, with the temperature change (*Figure 1.30b*), an important shift in the time constants may happen, trapping process will be faster at high temperature. Also, this shift is not always significant; it depends on several parameters whose activation energy.



(a) Time constants spectrum with the ON-state polarization (b) Time constants spectrum with the temperature change.

Figure 1.30: Example of time constants spectrum [Joh 11].

Finally using these revealed time constants, we can plot an Arrhenius law in order to extract the activation energy and the cross-section. The method for plotting Arrhenius law will be detailed during its use in chapter 3.

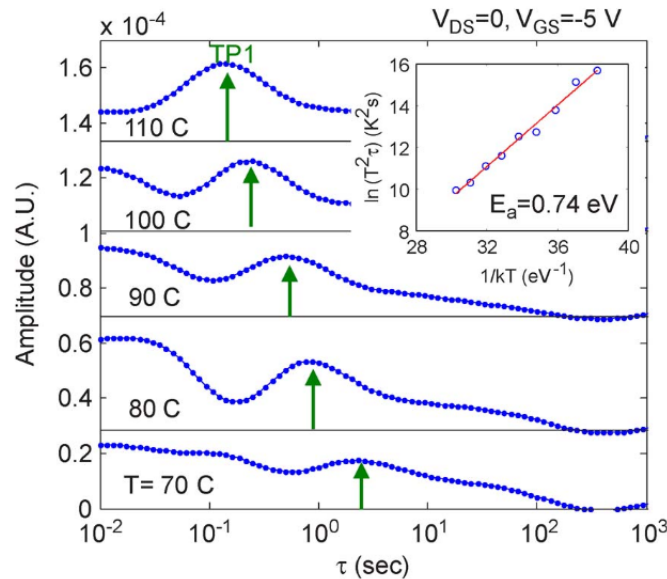


Figure 1.31: Extraction of the activation energy using the Arrhenius law [Joh 11].

- Advantages: It is a simple method for detecting activation energy and cross section of traps. They do not require very advanced equipment.

1.5. AXIS 2 – TRAPS CHARACTERIZATIONS

- Limitations: It is sometimes complicated to identify the location of the traps by this method, an overlap between the signatures of the traps, for example between the barrier and surface traps under the gate, may happen. The traps density cannot be revealed by this method. It is essential to pay attention to the overlap between self-heating and traps as the separation of these two factors is a difficult task. Since they may have similar time constants, verification is mandatory.

1.5.2 Review of methods used for traps Characterization

However, the trap characterization methods are very variant between optical and electrical; we now present a review we carried out of the different characterization methods used and the revealed information found in the HEMT components. These methods can vary according to their detection ability, there are methods like DLTS that can be limited for a relative short time scale. These methods can not detect traps with long time constants. They are rather in the order between 10 ns until 100 of seconds. Above or below this order, there are other methods that are used for the detection of these traps. For the details of the characterization methods and the application field, one can consult the references presented in the next table.

Characterization method	Revealed information	HEMT under test	Conclusions	References
Transient current	$E_C - E_T = 0.37eV$ $\sigma_n = 1.2 \times 10^{-16} cm^2$	Air-exposed and H ₂ plasma treated HFETs	1. N-Vacancy near surface traps is responsible for the current collapse. 2. Al ₂ O ₃ passivation + N ₂ plasma treatment can eliminate their effects.	[Has 03]
Backgating current deep level transient spectroscopy	Minority traps $E_C - E_T = 0.37eV$ Majority traps $E_C - E_T = 0.2eV$ $E_C - E_T = 0.21eV$	Schottky-gate HEMT. No passivation layer.	Traps located in the GaN layer.	[Mar 03]
Current deep level transient spectroscopy (I-DLTS)	$E_C - E_T = 1.43eV$	AlGaN/GaN HFET with and without SiN passivation.	SiN passivation of the surface can eliminate a significant source of traps.	[Ver 02]
Constant drain current deep level transient spectroscopy	$E_C - E_T = 0.57eV$	AlGaN/GaN HEMT compared to InAlN/GaN.	1. Traps are not linked to the AlGaN barrier but rather to the GaN buffer. 2. This traps signature was found on both devices.	[Sas 13]
Thermally stimulated current (TSC) spectroscopy combined with high-voltage back-gating	$E_C - E_T = 0.54eV$ $E_C - E_T = 0.65eV$ $E_C - E_T = 0.75eV$	AlGaN/GaN HEMT with low-resistivity Si substrate.	1. These traps are probably attributed to Carbon doping, Ga-Vacancies and point defects. 2. Traps are localized in the GaN buffer.	[Yang 14]
Conductance Deep Level Transient Spectroscopy CDLTS	$E_C - E_T = 0.07eV$ $\sigma_n = 2.65 \times 10^{-15} cm^2$ $E_C - E_T = 0.20eV$ $\sigma_n = 3.03 \times 10^{-17} cm^2$ $E_C - E_T = 0.50eV$ $\sigma_n = 2.57 \times 10^{-15} cm^2$ $E_C - E_T = 0.83eV$ $\sigma_n = 3.14 \times 10^{-14} cm^2$	AlGaN/GaN HEMT.	Traps are located between the substrate and the 2DEG channel.	[Gas 06]

1.5. AXIS 2 – TRAPS CHARACTERIZATIONS

Capacitance deep level optical spectroscopy	Traps located in the AlGaN $E_C - E_T = 3.85eV$ Traps located in the GaN $E_C - E_T = 2.64eV$ $E_C - E_T = 3.30eV$	AlGaN/GaN HEMT	Identified traps located in the AlGaN and GaN layer separately.	[Arm 06]
Capacitance DLTS associated with micro-cathodoluminescence	$E_C - E_T = 1eV$ $E_C - E_T = 0.9eV$	Comparison between Deep traps in unpassivated and Sc ₂ O ₃ passivated AlGaN /GaN HEMTs	Sc ₂ O ₃ passivation was found to reduce the concentration of prominent surface trap significantly.	[Pol 03]
I-DLTS	$E_C - E_T = 0.76eV$ $\sigma_n = 2 \times 10^{-15} cm^2$ $E_C - E_T = 0.50eV$ $\sigma_n = 5 \times 10^{-16} cm^2$ $E_C - E_T = 0.18eV$ $\sigma_n = 4.5 \times 10^{-19} cm^2$	Short gate HEMTs GaN/AlGaN/GaN grown on SiC	Traps characterization associated with numerical simulations provide more reliable trap identification.	[Faq 07]
Drain Current DLTS	AlGaN/GaN HEMTs $E_C - E_T = 0.68eV$ $\sigma_n = 2.5 \times 10^{-12} cm^2$ $E_C - E_T = 0.58eV$ $\sigma_n = 1.1 \times 10^{-15} cm^2$ $E_C - E_T = 0.34eV$ $\sigma_n = 2.2 \times 10^{-20} cm^2$ $E_C - E_T = 1.1eV$ $\sigma_n = 5.8 \times 10^{-16} cm^2$ AlGaN/GaN MIS-HEMTs $E_C - E_T = 0.49eV$ $\sigma_n = 8.5 \times 10^{-17} cm^2$ $E_C - E_T = 0.62eV$ $\sigma_n = 8.8 \times 10^{-18} cm^2$	Comparison between Al-GaN/GaN HEMT and Al-GaN/GaN MIS-HEMT	Hole traps were not observed in the HEMTs while observed in the MIS-HEMTs.	[Oki 04]
Pulsed and Transient current	$E_C - E_T = 0.63eV$ $\sigma_n = 2.3 \times 10^{-14} cm^2$ $E_C - E_T = 0.82eV$ $\sigma_n = 8.5 \times 10^{-13} cm^2$	Four samples with different Fe buffer doping.	1. Traps located in the buffer are responsible for the current collapse phenomenon. 2. Increasing Fe buffer doping will increase the traps in the buffer.	[Men 14]
Gate lag measurements (pulsed I-V) and I-DLTS	$E_C - E_T = 1.4eV$ $E_C - E_T = 1.3eV$ $E_C - E_T = 1.08eV$	Undoped AlGaN/GaN power HFET with SiN passivation	DLTS spectra of the stressed device revealed the evidence of trap creation due to hot electron stress.	[Kim 03b]
Reverse deep level transient spectroscopy	$E_C - E_T = 0.25eV$ $\sigma_n = 1.2 \times 10^{-15} cm^2$ $E_C - E_T = 0.55eV$ $\sigma_n = 2.2 \times 10^{-15} cm^2$ $E_C - E_T = 0.85eV$ $\sigma_n = 1 \times 10^{-16} cm^2$	GaN/AlGaN/doped-Fe GaN HEMTs	Traps in this sample are located in the buffer.	[Pol 07]
Simultaneous temperature-dependent measurements of resistance transients (RTs) and spatially resolved surface potential transients	$E_C - E_T = 0.57eV$	AlGaN/GaN HEMT on SiC	This traps signature associated with HEMTs degradation is located in the GaN buffer and not in the AlGaN barrier or at the AlGaN surface.	[Car 13]

Combined pulsed and transient current/voltage characteristics	$E_C - E_T = 0.099eV$ $E_C - E_T = 0.63eV$	Split wafer experiments 3 HEMT Samples: 1- Ni/ Au gate, (passivated). 2- Ni/ Au gate, (not passivated) 3- ITO gate (passivated)	1. Surface traps have a low thermal activation energy of 99 meV. 2. The activation energy of 0.63 eV is located under the gate contact of the HEMTs: these traps are located in the Al-GaN or GaN layers.	[Men 13]
Conductance Deep Level Transient Spectroscopy	$E_C - E_T = 0.074eV$ $\sigma_n = 2.1 \times 10^{-15} cm^2$ $E_C - E_T = 0.061eV$ $\sigma_n = 2.56 \times 10^{-15} cm^2$	AlGaN/GaN HEMTs	There is a direct correlation between the parasitic effects in the output characteristics and the presence of deep traps of Al-GaN / GaN on Si.	[Gas 08]

Table 1.5: Review of methods used for traps characterization.

1.6 Axis 3 - GaN HEMTs models

The modeling of GaN components is an inevitable step in the path of behavioral comprehension either qualitatively or quantitatively. Much research has been presented in the literature to model the different types of HEMT components. In fact, there are two types of models that have been used to model them.

1.6.1 Equivalent circuit model:

This type is based on the electrical behavior modeling based on experimental measurements, which are subsequently used to establish a generic model. It consists mainly of electrical elements such as capacitors, resistances, and inductances. These electrical elements can also be written in analytical forms as a function of electrical or thermal stresses.

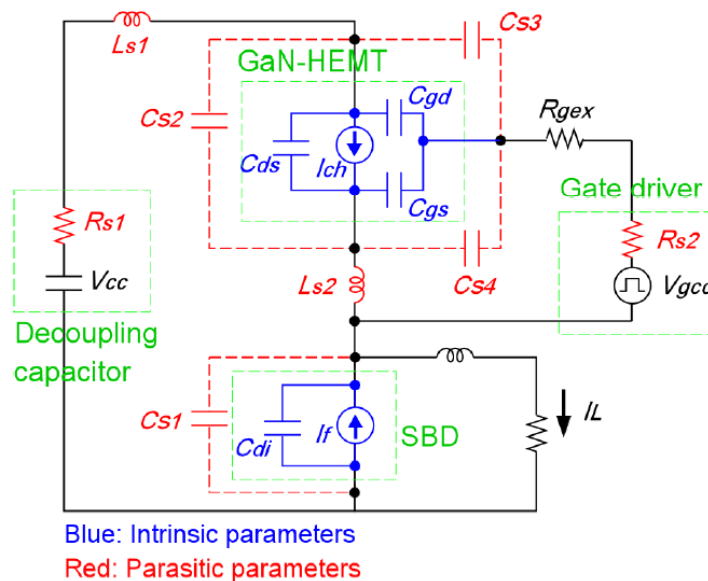


Figure 1.32: Equivalent circuit model [Nak 08].

A. Nakajima et al. have modeled the GaN component taking into account the device properties, such

as current collapse and short-channel effects [Nak 08]. The purpose of the model was to estimate the behavior of GaN devices in switching applications. The model presented in *Figure 1.32* is composed totally of the electrical circuit.

One of the results showing the comparison between the theoretical and experimental results of the signal during switching is presented in *Figure 1.33*.

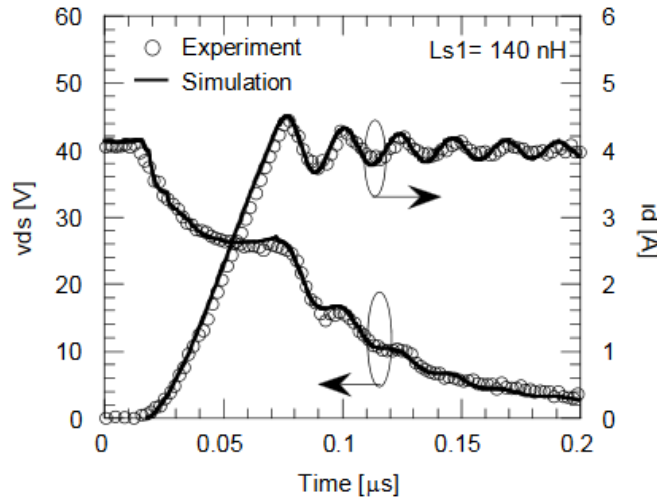


Figure 1.33: Comparison between theoretical and experimental results [Nak 08].

Figure 1.34 presents another model for GaN HEMT; the authors have modeled the GaN component for microwaves operations issues [Cab 04].

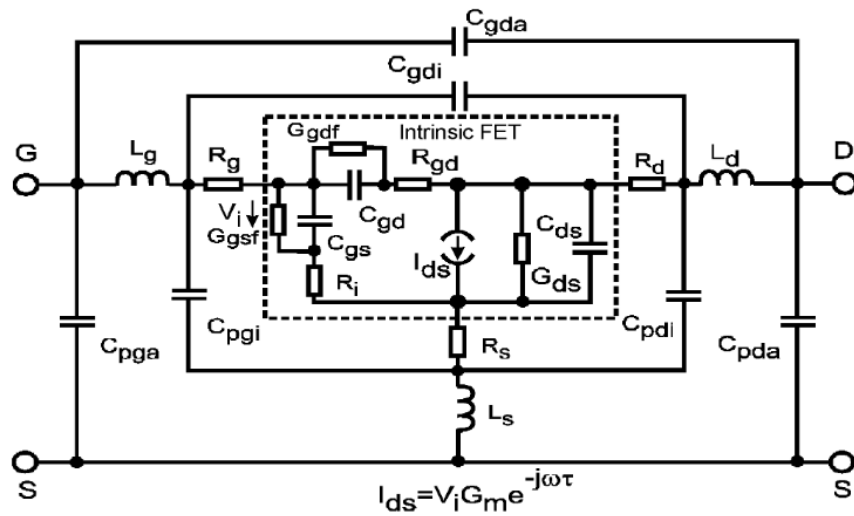


Figure 1.34: Nonlinear equivalent circuit model.

The authors presented some validation of the device’s electrical characteristics as gain, S parameters and output power as a function of input power. However, this model aims to get the quantitative results by adjusting its elements to be coherent with the experimental results. Although this model (as presented in *Figure 1.35*) fits quantitatively with experimental results, it lacks prediction, i.e., it would always be necessary to carry out experimental Characterizations to establish the model. Furthermore, it

lacks behavior understanding, so this type of model can offer the behavior but cannot explain it. These limitations can make it useful only in simulations of electrical circuits, but it does not play perfectly the role for technology development or to understand degradation modes.

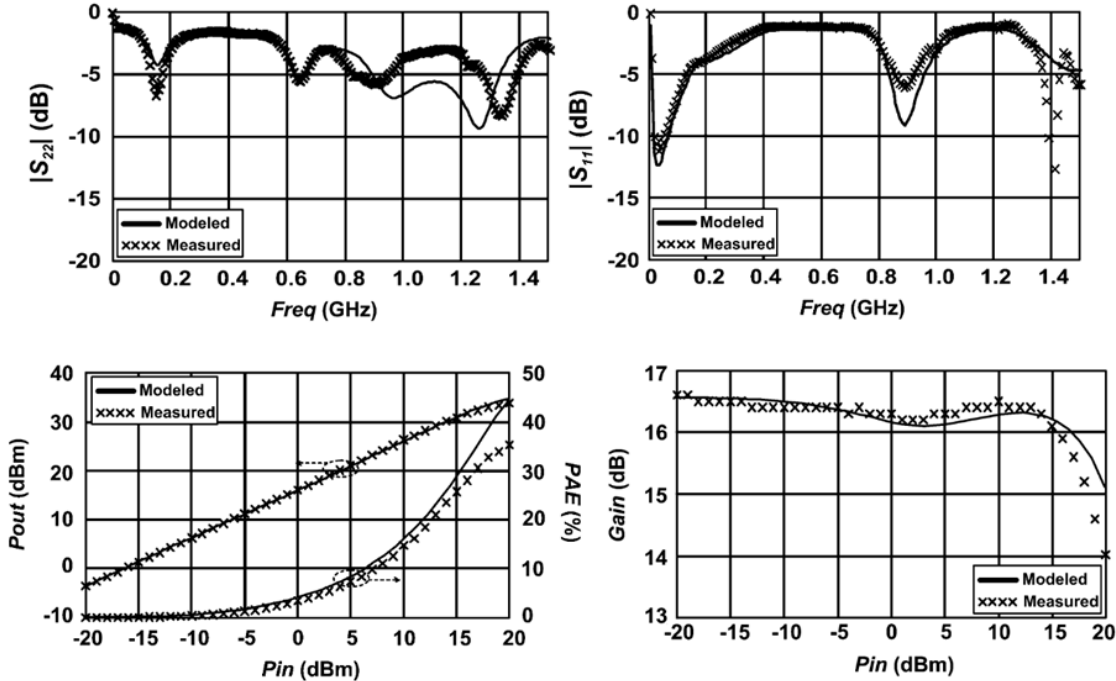


Figure 1.35: Type of the results of a circuit-based model used to validate characteristics of GaN component used in microwaves applications [Cab 04].

1.6.2 Physics-based model:

This type is based on physics equations and geometric dimensions of the device. These models are mainly based on the semiconductor physics where quantum physics theory can be involved. These models can be carried out using analytical [Li 08] or numerical solutions [Cha 05] for semiconductor physics equations. The concerned equations are Poisson-Schrödinger coupled equations and the three transport equations (3 moments of the Boltzmann equation).

In this section, we discuss only the physics-based analytical models. In the literature, several analytical models were presented. Here, we will present a brief explanation of the underlying equations used in most of these models. Then, we present a short review of the work carried out and the results obtained from these analytical models [Che 09a, Che 10, Kha 12, Kha 11, and Li 08]. However, the following forms will be more detailed in chapter 2 since they will be re-used as basic formulations to integrate and study traps. The following steps are well explicated in [Del 82 and Kol 82].

Basic formulations of the 2DEG density:

These formulations are developed for a 2DEG density only under the gate and without any drain polarization. Upon application of a drain voltage, the 2DEG density distribution becomes linear as a function of the applied potential until reaching the saturation threshold.

Method	Final formulation
1. Integrating Poisson equation to find a relation between the electric field at the hetero-interface (ξ_i) and the potential drop at the AlGaIn barrier terminals.	$V_S = \frac{qN_D}{2\epsilon_1} d^2 - \xi_i d$ V_S the potential drop at the AlGaIn barrier terminals is, N_D is the density of the ionized donors in the AlGaIn, d is the thickness of the AlGaIn and ϵ_1 is the electrical permittivity of the AlGaIn.
2. Applying Gauss's theorem to the interface to find a relation between the electric field at the interface and the concentration of charges (n_S).	$\xi_i = \frac{q \int n(y) dy}{\epsilon_2}$; $\int n(y) dy = n_S$; $V_S = \frac{qN_D}{2\epsilon_1} d^2 - \frac{qn_S d}{\epsilon_2}$.
3. Energy band diagram is used to find a relationship between the potential drop at the AlGaIn barrier terminals and the Fermi level (E_F).	$qV_S + \Delta E_c = q\phi_B - qV_{GS} + E_F$. ΔE_c is the discontinuity formed at the hetero interface, ϕ_B is the Schottky barrier formed on the AlGaIn side and V_{GS} is the applied gate voltage.
At this stage, an equation with two unknowns (n_S & E_F) is found but, we need another equation between them to solve the system.	
4. Using an approximation of the Schrodinger equation in a triangular well, we find the second relation between n_S & E_F	$n_S = DkT \ln \left[1 + \exp \left(\frac{E_{FS} - \gamma_0 (n_S)^{1/3}}{kT} \right) \right] + DkT \ln \left[1 + \exp \left(\frac{E_{FS} - \gamma_1 (n_S)^{1/3}}{kT} \right) \right]$
At this stage, two equations with two unknowns (n_S & E_F) were found, so we can solve this system.	

Table 1.6: 2DEG mathematical form under the gate :To find a form of the 2DEG concentration in the channel as a function of the gate voltage and the threshold voltage.

2DEG Mobility:

The 2DEG mobility is dependent on several physical phenomena which may control its behavior. They are some known-phenomena like optical and acoustic phonon, dipole scattering and dislocations. As shown in *Figure 1.36*, [Woo 08] three experimental measurements were performed for three different samples with different concentrations of 2DEG. We first note that the charges concentration affect the value of the mobility. We also notice that mobility drops significantly with temperature, and this drop is mainly due to the optical phonon effect, which increases with temperature. Thus, in normal operation, mobility falls compared to the value at low temperatures.

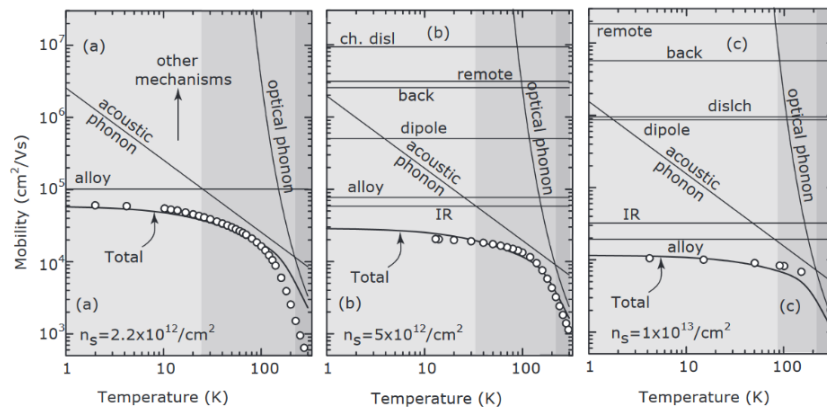


Figure 1.36: Measurements and experimental values of the mobility function of temperature for three different charge concentrations [Woo 08].

1.6. AXIS 3 - GAN HEMTS MODELS

For reasons of difficulty in the modeling of mobility, many authors used phenomenological models that describe the mobility behavior of the device under test responding to a change in temperature and applied gate voltage. As following, we present two mobility formulations used in the analytical models presented in the literature Eq.1.8 [Mia 07] and Eq.1.9 [Che 09a].

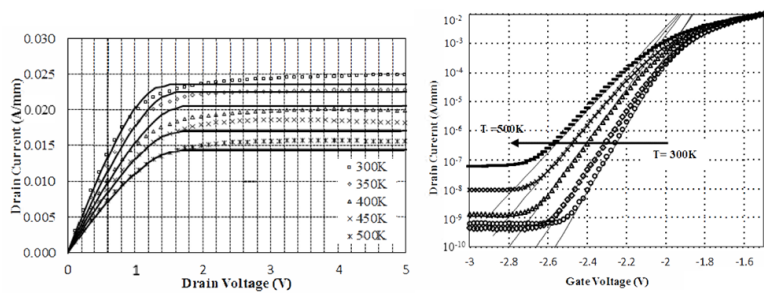
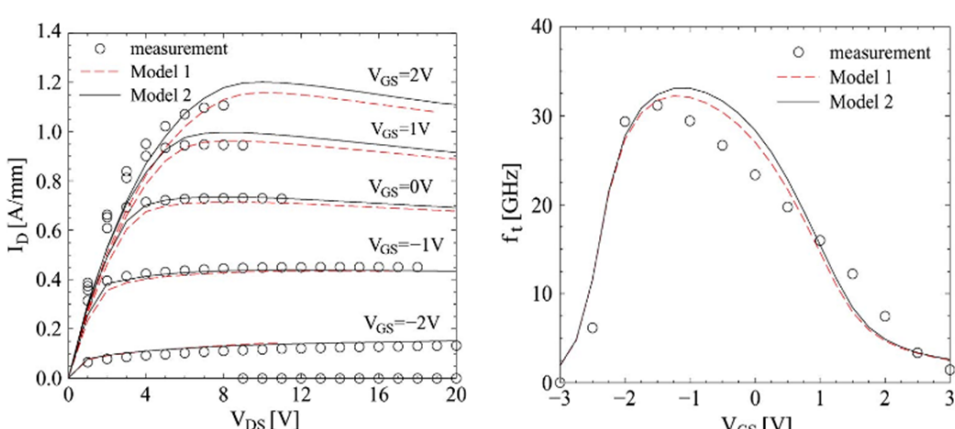
$$\mu_0 = \frac{p_1(V_{gs} - V_{th} + p_4)^{3/2}}{p_2 + (V_{gs} - V_{th} + p_3)^2} \quad (1.8)$$

p_1, p_2 and p_3 are adjustable parameters.

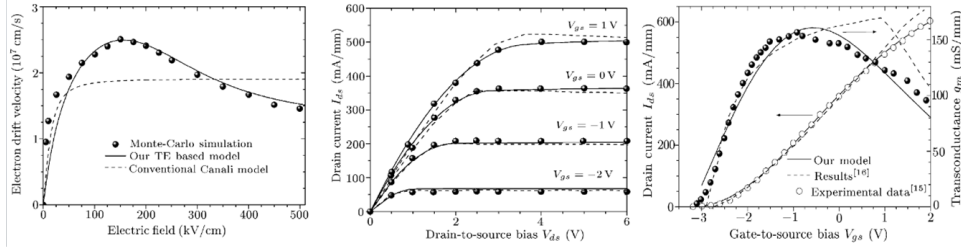
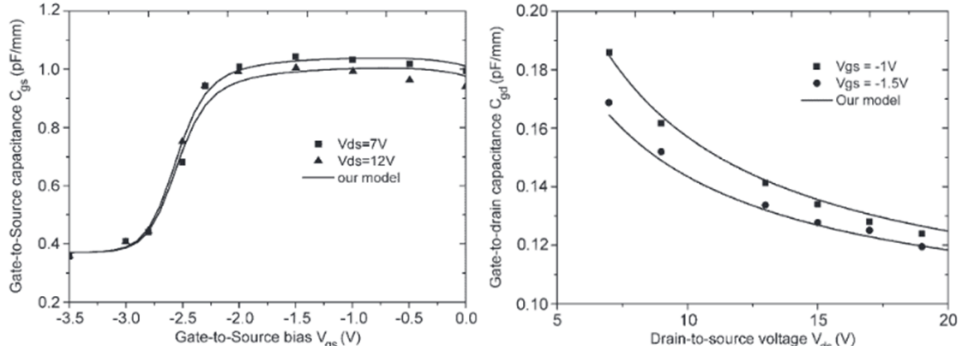
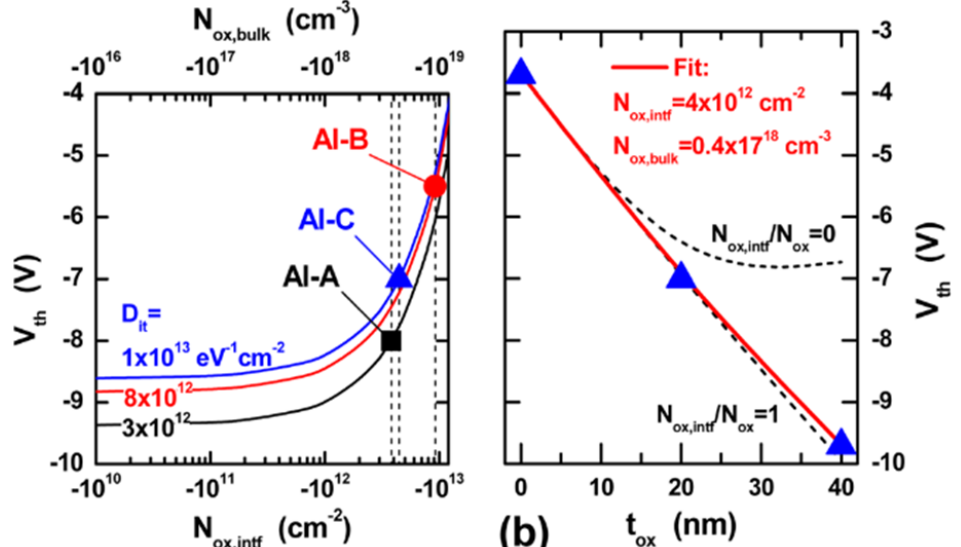
$$\mu_{LF} = \frac{\mu_0}{1 + p_1 V_{gt} + p_2 V_{gt}^2} \quad (1.9)$$

p_1, p_2 are also adjustable parameters, μ_{LF} is the low field mobility.

These two parameters (electron mobility and 2DEG density) present the essential elements to calculate the conduction current. In the next table, we will present a small review of the analytical models' results given in the literature.

Structure	Model	References
Schottky-Gate Al-GaN/GaN HEMT	<p>These results of the analytical model were verified with TCAD Sentaurus. The model studies the temperature effect on the Schottky barrier height, Fermi-level, 2DEG density, Gate threshold and sub-threshold voltages and the Drain current-voltage characteristics.</p> 	[Wan 13]
Physics-Based Modeling for HEMTs	<p>The authors presented a hydrodynamic model for the electron mobility; they study the decrease in the transconductance g_m at higher gate bias and they present phenomenological low and high field mobility model.</p> 	[Vit 12]

1.6. AXIS 3 - GAN HEMTS MODELS

<p>Schottky-Gate Compact model</p>	<p>The presented analytical models were developed for the dc, and small signal characteristics of AlGaN/GaN-based HEMT. The authors also developed a phenomenological low-field mobility model.</p>  <p>The figure contains three subplots. The left plot shows Electron drift velocity (10^7 cm/s) vs Electric field (kV/cm) from 0 to 500. It compares Monte-Carlo simulation (black circles), the authors' TE-based model (solid line), and a Conventional Canali model (dashed line). The middle plot shows Drain current I_{ds} (mA/mm) vs Drain-to-source bias V_{ds} (V) from 0 to 6. It shows curves for $V_{gs} = 1V, 0V, -1V, -2V$. The right plot shows Drain current I_{ds} (mA/mm) and Transconductance g_m (mS/mm) vs Gate-to-source bias V_{gs} (V) from -3 to 2. It compares the authors' model (solid line), Results [16] (dashed line), and Experimental data [15] (open circles).</p>	<p>[Wan 13]</p>
<p>Schottky-Gate Compact model</p>	<p>The presented analytical model includes the 2DEG density, drain current, and capacitance characteristics. The model is based on a unified charge control expression to be applied to both sub-threshold regions and strong inversion regions taking into account the parasitic channel effect in the AlGaN layer.</p>  <p>The figure contains two subplots. The left plot shows Gate-to-Source capacitance C_{gs} (pF/mm) vs Gate-to-Source bias V_{gs} (V) from -3.5 to 0.0. It shows data for $V_{ds}=7V$ (black squares) and $V_{ds}=12V$ (black triangles), along with the authors' model (solid line). The right plot shows Gate-to-drain capacitance C_{gd} (pF/mm) vs Drain-to-source voltage V_{ds} (V) from 5 to 20. It shows data for $V_{gs} = -1V$ (black squares) and $V_{gs} = -1.5V$ (black circles), along with the authors' model (solid line).</p>	<p>[Che 09a]</p>
<p>Threshold voltage analytical model</p>	<p>The authors presented an analytical model for the threshold voltage that includes the surface, oxide traps. The model is fitted with the experimental measurements.</p>  <p>The figure contains two subplots. The left plot shows V_{th} (V) vs $N_{ox,intf}$ (cm^{-2}) and $N_{ox,bulk}$ (cm^{-3}). It shows curves for different interface trap densities D_{it}: $1 \times 10^{13} eV^{-1} cm^{-2}$ (red), 8×10^{12} (blue), and 3×10^{12} (black). Points are labeled AI-A, AI-B, and AI-C. The right plot shows V_{th} (V) vs t_{ox} (nm). It shows a fit with $N_{ox,intf} = 4 \times 10^{12} cm^{-2}$ and $N_{ox,bulk} = 0.4 \times 10^{18} cm^{-3}$. Dashed lines represent $N_{ox,intf}/N_{ox} = 0$ and $N_{ox,intf}/N_{ox} = 1$.</p>	<p>[Tap 12]</p>

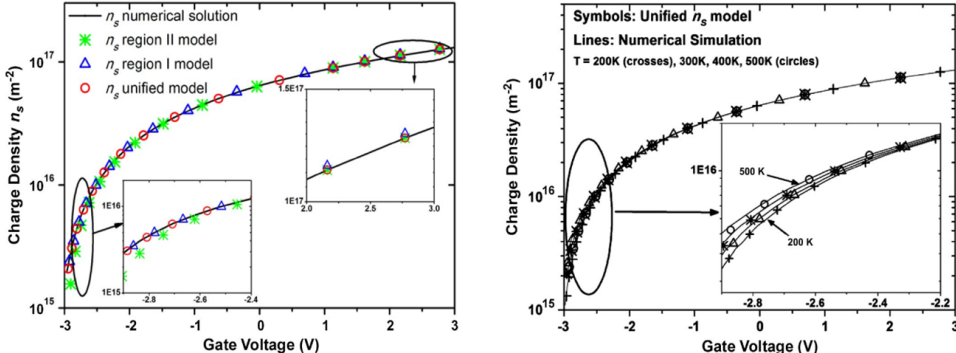
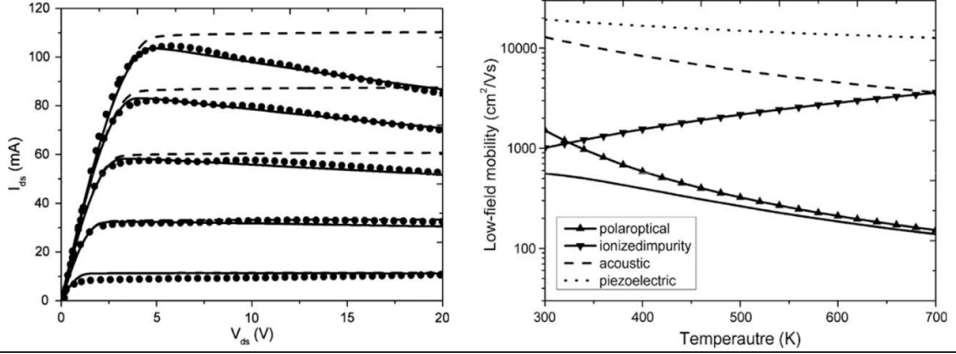
<p>Physics-based analytical model</p>	<p>These authors presented a comparison between the analytical and numerical model for the 2DEG density considering only two sub-bands in the electronic confinement.</p> 	<p>[Kha 11]</p>
<p>Analytical model for MODFETs</p>	<p>The authors presented an analytical model of the device's electrical characteristics. The same model was also presented in another paper but taking into account the effect of self-heating.</p> 	<p>[Li 08] and [Che 10]</p>

Table 1.7: A small review of some existing analytical models.

Now, we pass to the last axis on reliability tests.

1.7 Axis 4 - Reversible and irreversible degradation of GaN HEMTs

The device must pass through some reliability tests before being fully validated to be used in real applications. Among these tests, some tests induce reversible or irreversible degradations which can happen gradually or catastrophically. There are many methodological tests to evaluate reversible and irreversible degradations; we will briefly mention a few of them. M. Ruzzarin et al. [Ruz 16] performed a comparison between two types of reversible tests that are High-Temperature Reverse Bias (HTRB) and High-Temperature Constant Current Source (HTSC). The HTRB test consists of applying a reverse gate voltage to block the component at a high temperature and by applying a high electric field on the drain terminal, we can evaluate the stability of several electrical parameters of the device. The author showed the effect of this test on the stability of the threshold voltage and dynamic on-resistance. The applied test conditions are for gate voltage $V_{GS} = -10V$, $V_{DS} = 150V$ and $T = 150^{\circ}C$. The authors observed an instability in the threshold voltage; they also observed a rather constant behavior for the on-state resistance. In the other hand, HTSC test is similar to the HTRB test, but instead of applying a negative voltage to the OFF state (reverse bias), a constant current is injected. The authors defined four current values (100nA, 1uA, 2uA, and 10uA) and observed a contrary behavior to that of the HTRB, instability in the on-state resistance; they also observed a rather constant behavior for the threshold voltage.

For tests that induce irreversible degradations, there are in mainly three types of test protocols which are step-stress, step-stress-recovery and stress-recovery cyclic stress loading [Che 12]. J.D. Alamo et al. [Ala 09] presented a step-stress test and compared the electrical characteristics before and after the stress. The authors observed a degradation in the electrical characteristics and the evolution of the traps in the structure.

The device's degradation modes are highly dependent on the type of stress tests. In this section, we will begin by mimicking some types of (reversible and irreversible) degradations modes. The degradation modes of GaN HEMTs are very variable between reversible and irreversible modes. For reversible degradation, we can have mainly electrical characterizations shift while biasing the component in the OFF or ON state. Any instability occurs in the device's electrical characteristics during the ON-state and which can vary with the temperature fall under two main electrical tests: positive bias temperature instability (PBTI) and negative bias temperature instability (NBTI). These instabilities can be in the form of a shift of the threshold voltage or a shift in the dynamic on-resistance. For irreversible degradation, we have permanent degradation at the device's electrical characteristics level. This permanent degradation may be due to the increase in defects in the structure, to the degradation of the Ohmic contacts or the delamination of the passivation. We may have time-dependent gate breakdown or a dielectric breakdown (TDDB). We can also have degradation under the vertical electric field effect, which can cause a breakdown of bulk materials.

G. Meneghesso et al. [Men 08] presented an overview of the physical origin of the degradations modes. As shown in *Figure 1.37*, it is possible to have surface or volume traps. These traps are activated due to the change in the polarization state. Trapping may also occur due to hot electron or mechanical stress. We may even have surface traps due to passivation delamination.

We can have degradation by the tunnel effect. It occurs at the gate level, or an electrons density can penetrate the barrier under the impact of the electric field. We may also have direct degradations in the Ohmic contacts at the drain and source or in the Schottky contact at the gate-semiconductor contact.

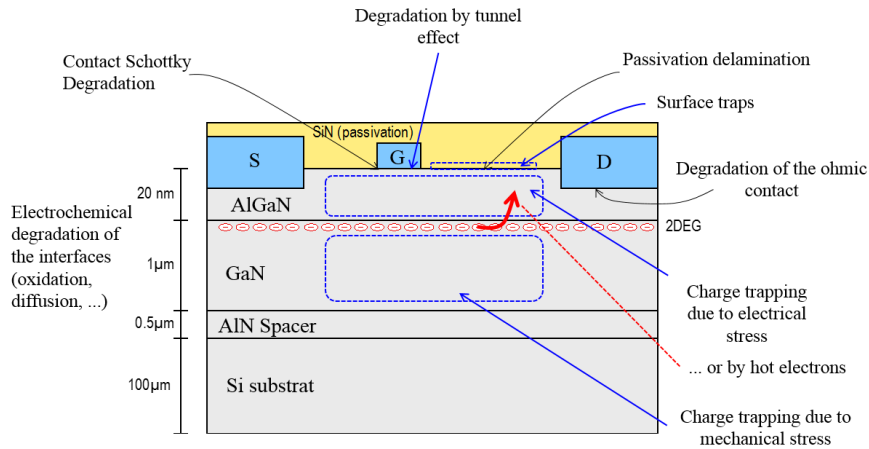


Figure 1.37: Physical origin of the degradations modes.

Now we present some results of three degradation modes: the positive bias temperature instability, the negative bias temperature instability (for reversible degradation mode) and the time-dependent dielectric breakdown (for irreversible degradation mode).

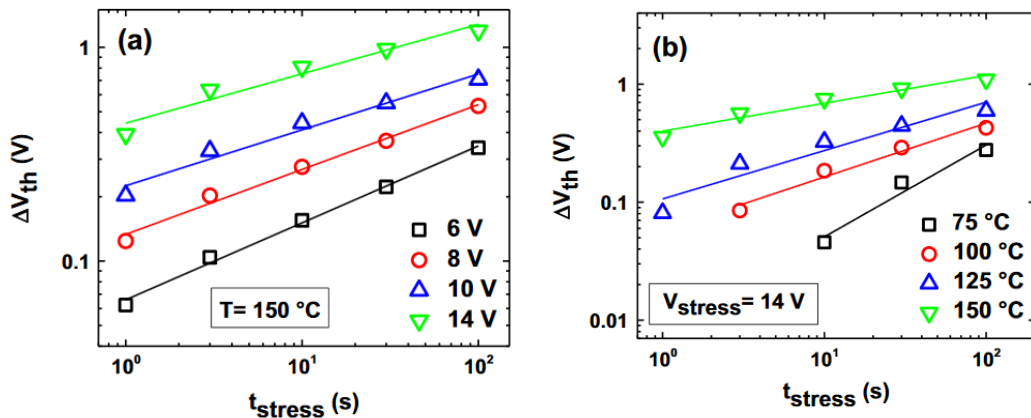
1.7.1 Positive bias temperature instability (PBTI) - Reversible

- Phenomenon studied for GaN HEMTs:

Applying a positive stress at the gate terminal induces a threshold voltage shift. The origin of this shift is preferably related to the trapping and de-trapping under the gate.

- Results:

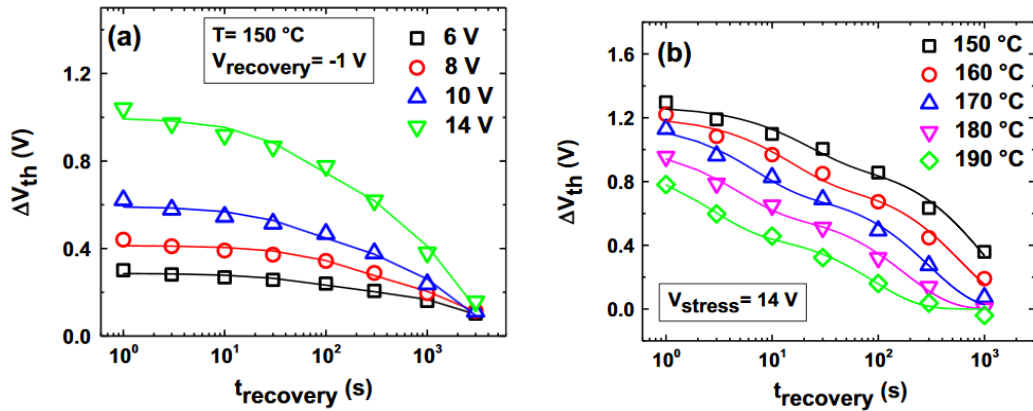
E. Acurio et al. [Acu 17] have studied this phenomenon on a fully recessed-gate AlGaIn/GaN MOS–HEMT. The authors have found that there is a shift of the threshold voltage always in the same way. This threshold voltage shift direction does not change regardless of stress level or stress time or device temperature. The authors also proposed to apply a negative voltage to the gate to cover this effect.



(a) Threshold voltage shift due to the stress level.

(b) Threshold voltage shift due to the temperature.

Figure 1.38: Threshold voltage shift due to the stress level and the temperature due to the positive bias [Acu 17].



(a) Threshold voltage recovery that the component has undergone due to the stress level. (b) Threshold voltage recovery that the component has undergone due to the temperature.

Figure 1.39: Threshold voltage recovery that the component has undergone due to the stress level and the temperature due to the positive bias [Acu 17].

The authors also estimated the activation energies responsible for this phenomenon. The authors identified two traps signature, the first one considered as slow traps associated with an activation energy of 0.93 eV. A second activation energy was also identified between the range of 0.45 eV and 0.82 eV, corresponding to fast trap.

1.7.2 Negative bias temperature instability (NBTI) - Reversible

Phenomenon studied for GaN HEMTs: a negative stress applied at the gate terminal induces a threshold voltage shift. The origin of this shift is rather related to the trapping and de-trapping under the gate.

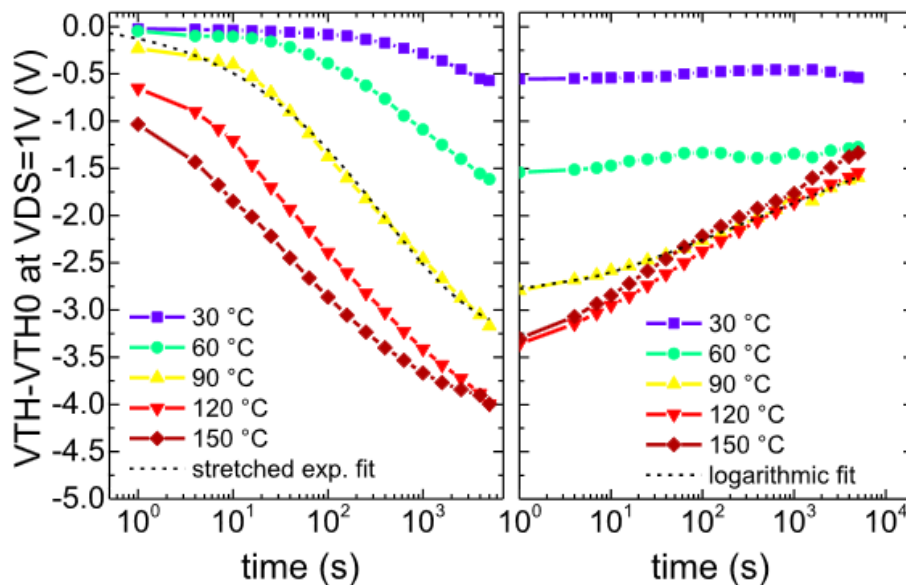


Figure 1.40: The threshold voltage shift depending on the temperature for stress (left) and recovery (right) [Men 16b].

Results: M. Meneghini et al. [Men 16b] studied this phenomenon on a D-mode MIS-HEMT grown

on Si substrate. The authors found that high temperature (up to 150°C) combined with applied negative bias (-10V) can induce a significant negative threshold voltage shift. They also observed a correlation with a decrease in the on-resistance.

1.7.3 Time-dependent dielectric breakdown - Irreversible

Phenomenon studied for GaN HEMTs: This phenomenon is applied to the MIS-HEMT components by the application of a positive voltage on the gate to estimate a lifetime, or the component resists before a gate current avalanche occurs.

Results: T.-L. Wu et al. [Wu 15] studied this phenomenon in three different samples with three different gate oxide of MISHEMTs as shown in *Figure 1.41*. The authors estimated a lifetime of 20 years by fitting the data with a power law to gate voltage (4.9V) and with an exponential law to gate voltage (7.2V) at 150°C. The lifetime was extrapolated to 0.01% of failures. This comparison between the lifetimes for the three different dielectric gives an idea of their reliability. These results give the advantage to the use of alumina for MISHEMT structures.

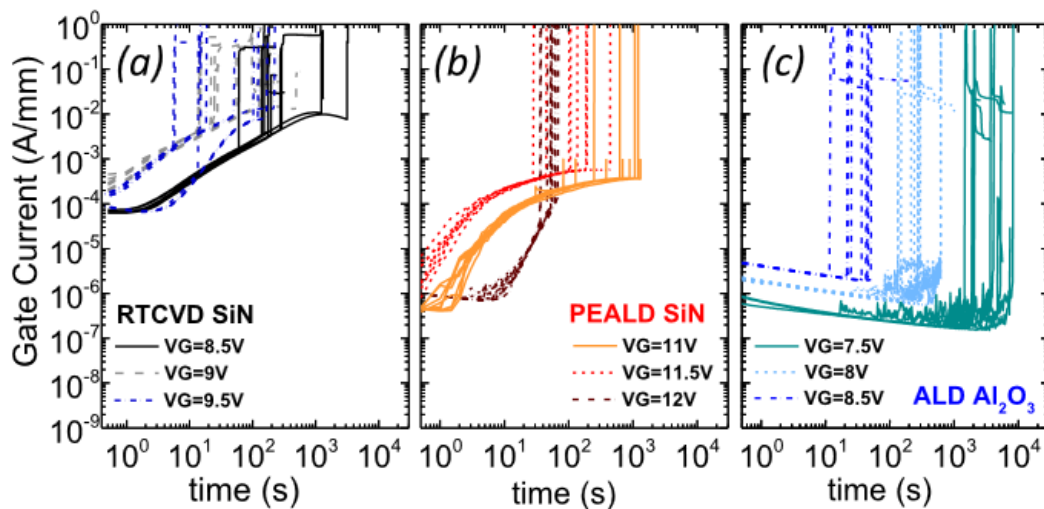


Figure 1.41: TDDB on three different samples with three different gate oxide of MISHEMTs [Wu 15].

1.8 Conclusion

The research work on GaN components is exponentially expanding recently. These components have shown an interest in the scientific community. We have not scanned all the works presented in literature, but we presented a brief list of bibliographic studies on four axes that will affect the thesis.

We have focused on the work carried out around traps since it is the phenomenon that affects the most these components. We have presented the relevance of GaN-based power devices in the field of power electronics. A comparison between Silicon, Silicon Carbide, and Gallium nitride was presented to show the interest in these new devices. The structures recessed-gate and p-gate GaN were presented, which will be used later in this manuscript. A detailed explanation of the formation of the hetero-structure and the density 2DEG was also presented, it will be used as the base for modeling in chapter 2. The source of the electrons in the electronic confinement has also detailed to better understand how these components work.

Physical properties of traps, which represents the first axis, have been presented. A detailed explanation of the traps sources was discussed. An important review based on results of literature was presented in this axis which corresponds to place the traps according to their localization in the structure by identifying them. A physical explanation of traps and its physical parameters such as activation energy and cross-section was presented.

Numerous characterization studies have been carried out in order to characterize and analyze traps in these devices (second axis). The characterizations of these traps were carried out and proved by several techniques. We have seen a wide variety of revealed information. This variety is correlated with the variety of the manufacturing steps between studied devices. We have also presented the different locations in the device where traps can be found.

We have detailed a single method of trap characterization which is the transient drain current measurements; this method will be used in the thesis. A review of trap characterization methods was also presented in order to be a database used in this thesis for the analysis of the trap signatures. We presented the third axis which revolves around the modeling of the HEMTs; we presented a small review of the existing models focusing on the analytical models. Finally, we presented some tests of reliability which induces a reversible or irreversible degradation that corresponding to the 4th axis.

Chapter 2

Theoretical investigation of effects of Oxygen traps on the 2DEG density of MOS–HEMTs

2.1 Introduction

Physics-based modeling is an inevitable path towards a deep understanding of semiconductor devices. The user of power devices needs to understand and predict its behavior, especially if their characteristics are unstable as it is still the case with the non-mature GaN-HEMTs, even if they are available in the market [Cha 15, Hir 14 and Li 16]. As said in chapter 1, these characteristics instabilities are related to traps incorporation in the form of surface states [Gas 12 and Vet 01] or bulk impurities [Lia 16 and Loo 05] and activated by electrical or mechanical stresses [Tap 10]. Trapping and detrapping mechanisms generate reversible degradation modes like a shift of threshold voltage, dynamic on-state resistance, PBTI, and NBTI. Concerning bulk impurities, they can be found either in the GaN buffer or in the AlGaN barrier. As a result, a reversible, temporary shift of the electrical characteristics occurs before reaching an equilibrium state [Bin 01, Bin 02 and Tir 07]. These instabilities cause a significant issue for the reliability study for these devices [Ala 09, Men 08 and Men 16a]. Physical models may also help to the understanding of irreversible degradation modes. As the physics instability phenomena themselves can evolve with degradation [Joh 06, Joh07 and Par 09], these models should estimate the effect of the developed parameters.

Most existing electrothermal analytical models do not contain a traps analytical/semi-analytical description [Che 10, Kha 11, Lee 04 and Li 08]. Even for authors who have studied the traps impact, they have considered and modeled mainly the surface-states effects on the threshold voltage [Tap 12], and there is a general lack of consideration of barrier/buffer traps effect on the 2DEG density. This little review comes from the fact that these surface states have a very high density especially for non-passivated devices or even where surface treatments have not been well processed. With technological progress, these surface states become less critical, and bulk states can manifest [Lia 16]. Few authors have considered bulk traps, but the complete ionization approximation or the trapped electron fraction probability are always assumed [Woo 08]. However, it is not always the case in reality since there is a high dependence of the traps state on the polarization conditions and the temperature of the system [Tra 99].

To the best of the author's knowledge, there is not a precise study of the weight of each of these traps (interface and barrier). In this chapter, we discuss the problem related to reversible degradation mode. We will present a physical explanation of the charges weight between these two traps sources under the gate and the possible effect on the 2DEG density. We present a semi-analytical model that considers the ionized traps profile in the AlGaN barrier associated with interface states model for MOS-HEMTs structures. The effect of the ionized traps profile in the AlGaN barrier which changes with the polarization conditions of the 2DEG density will be studied. We will review a concrete case for the incorporation of traps such as Oxygen in the barrier. We will also present a study of the charges weight between the interface and the Oxygen barrier traps on the 2DEG concentration. The model's features and capabilities will also be discussed. This model may provide a background for theoretical behavior understanding.

We begin the chapter with a presentation of the potential structures that were available during the thesis to establish the model. Then, we present and justify the choice of the structure by explaining the physical problem. Then, we describe the 2DEG basic analytical model presented in the literature. These basic equations will be developed to study the proposed physical problem (weight between interface and barrier Oxygen traps). We prescribe the modifications made on this model to be adapted to our structure. Finally, we explain the obtained simulation results.

2.2 Potential structures

To perform a physics-based study, it requires physical and geometric parameters. In this section, we will present the potential structures and the chosen one for our modeling. Structure complexity is strongly related to the model complexity. It could strongly affect the choice of the model type between numerical and analytical. In general, with geometric complexity, analytical models are not suitable, which explains the interest to go through numerical models in most cases. Nevertheless, we must note that overall, numerical models are more complicated to be implemented and some mathematical problems can occur such as convergence and computation time. Therefore, it is necessary to seek precisely the need behind the modeling at the structural and physics level before delving into different models. In this section, we will present the various structures. The next section will refer to the chosen one, and we will discuss the physical problem to be investigated on the selected structure. Three structures will be presented, which will get our attention either at the modeling level or the experimental level. These structures were chosen based on the availability of geometrical & physical information needed in the physics-based models. Two of these structures are fabricated by CEA-LETI. The first one belongs to the MOS-HEMT Normally ON (N-ON) family, the second one to the recessed-gate MOS-HEMT Normally OFF (N-OFF) family while the third structure is the GaN Systems commercial component which falls under the p-gate MOS-HEMT N-OFF family.

2.2.1 Normally-ON (N-ON) Structure

The N-ON structure presented here was manufactured and developed by the CEA-LETI.

2.2.1.1 Structure form

It is very similar to the conventional structures widely studied and characterized in the literature [Has 04a, Hor 13, Lu 13 and Ma 13]. We present the structure under the gate of the device in *Figure 2.1*, which is mainly composed of $\text{Al}_2\text{O}_3/\text{AlGaIn}/\text{GaN}$ MOS-HEMTs. A short technological process can be summarized as follows: the structure is formed of a 20 nm of aluminium oxide (Al_2O_3) deposited by Thermal-Atomic Layer Deposition (T-ALD) on 25 nm $\text{Al}_{0.25}\text{Ga}_{0.75}$ unintentionally doped barrier. The growth of the AlGaIn layer was carried out beyond a $1\mu\text{m}$ of GaN grown by Metalorganic Chemical Vapor Deposition (MOCVD). This heterostructure was grown on a Silicon substrate in the [0001] orientation. The gate metal is made up of 60 nm Titanium Nitride (TiN) deposited by Plasma-Enhanced Chemical Vapor Deposition (PECVD). The device was passivated by PECVD using Silicon nitride (Si_3N_4).

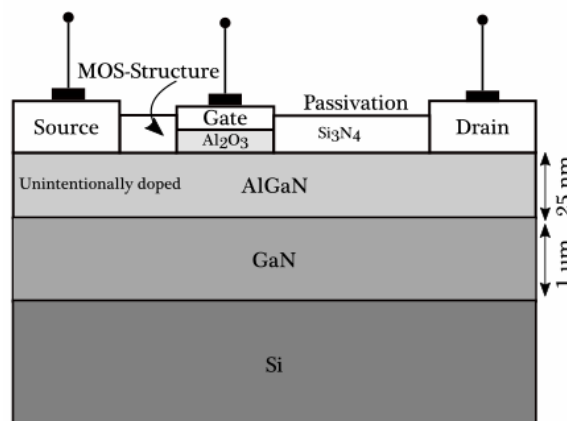


Figure 2.1: N-ON MOS-HEMT Structure fabricated by the CEA-LETI.

2.2.1.2 Structure characteristics

We will focus only on three essential points that may be necessary for our physics model, based on these points; we take approximations for modeling into account. We will specifically discuss the impact of the use of an oxide layer under the gate, surface passivation by Si_3N_4 and undoping the barrier on the model formulations and approximations.

1. The use of a thin oxide layer under the gate:

GaN devices with Schottky contacts have shown a significant gate leakage current due principally to a large density of surface states, which eventually could affect the drain breakdown voltage [Sai 05]. To reduce the gate leakage current, the use of Al_2O_3 gate oxide passivation has well–responded to form an improved MOS–HEMT [Has 04a, Ye 05 and Yua 07]. Besides, a remarkable reduction of the current collapse and improvements in the general component characteristic such as mobility, transconductance has been observed by D. Gregusova [Gre 07]. So, we must take into consideration the use of an oxide layer in the energy band diagram and the possible oxide charges that may exist.

2. Surface passivation by Si_3N_4 in the drain–gate region:

Regarding surface traps, a vital source of these states is localized at the surface within the gate and the drain access region in non–passivated devices, which subsequently form the so–called virtual gate [Vet 01]. Several solutions were discussed in the literature to neutralize their effects like passivating the surface by SiO_2 , Si_3N_4 or SiON [Aru 04]. In this structure, the manufacturer used one of these solutions by passivating the surface using Si_3N_4 . Thus, we could neglect surface traps in the passivated region, and the virtual gate phenomenon could be ignored.

3. Undoped barrier:

Even though n –doping the barrier will improve the 2DEG concentration and shift the threshold voltage to negative values, the manufacturer did not dope the AlGaN layer since these components will be used in power electronics applications. It implies that there would only exist trap energy levels in the barrier. However, the manufacturer supplied SIMS measurements (*Figure 2.17*), which conclusively have proved the existence of a high traps density in the AlGaN barrier. This traps' density drops very remarkably in the GaN layer. We will present the details of the SIMS measurements in the barrier traps modeling section.

2.2.2 Normally–OFF (N–OFF) Structures

Now we will switch to N–OFF structures. For the different structural details, one can consult the Normally–OFF structures subsection of chapter 1. We will begin by discussing the N–OFF structure manufactured by the CEA–LETI then we will present the commercial structure GaN systems.

2.2.2.1 Normally–OFF component manufactured by the CEA

The structure is schematically shown in (*Figure 2.2*). It presents the N–OFF structure proposed by the CEA–LETI. This structure belongs to the fully recessed gate family, where the idea is based on the full etch of the AlGaN barrier under the gate. As explained in chapter 1, without any applied gate bias, the 2DEG channel is in a high impedance under the gate (OFF state). It is necessary to apply a positive bias to the gate to create an inversion layer (MIS–type channel) and ensuring the 2DEG density continuity between the source and drain.

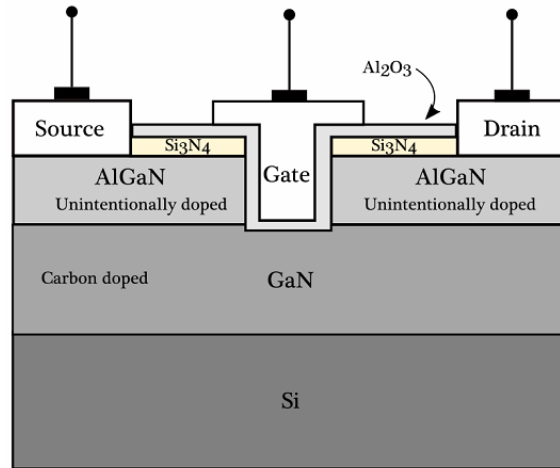


Figure 2.2: Fully recessed gate N-OFF structure fabricated by the CEA–LETI.

Same as N–ON structure, the oxide is used to minimize the gate leakage current, while the surface passivation is used to reduce the surface states effects. The GaN layer is doped with carbon to improve the $R_{DS_{ON}}$. There are different zones of the barrier which are in contact with the oxide layer resulting in a non–homogenous 2–DEG density and 2–D polarization along the channel. These points will subsequently complicate the realization of an analytical model, and a numerical model maybe needed. Furthermore, a study of the trapping in this structure will be much more complicated as we can end up mainly with complex trapping behavior [Has 03, Lin05 and Tur 13]. Furthermore, we did not have information on trap density or profile in the structure.

2.2.2.2 Commercial component GaN Systems

The GaN Systems Inc. devices (schematically presented in *Figure 2.3*) are one of the most well-known manufacturers of GaN power devices.

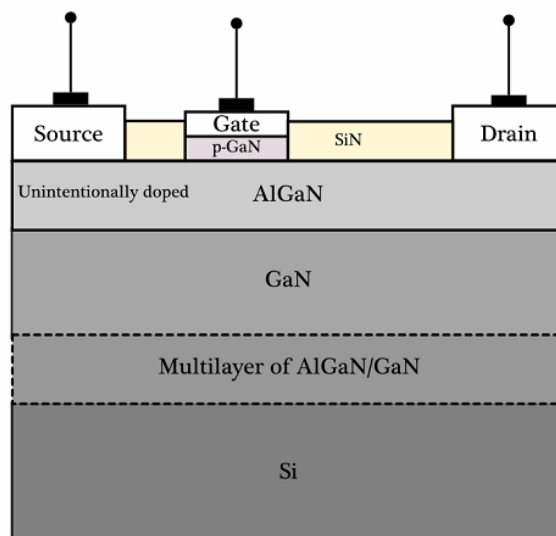


Figure 2.3: Simplified scheme for the commercial component GaN Systems.

Concerning its structure, it is based on a p-GaN Schottky contact under the gate; it consists precisely of a Metal/p-GaN/AlGaIn/GaN above several layers of AlGaIn/GaN. Although the p-GaN makes the component N-OFF, due to the electron conduction mechanisms through the Schottky barrier, the gate leakage current is expected to be higher than the MOS structures [Sze 07]. The internal structure of this commercial component and its packaging system are somewhat quite complicated. It is very compact aiming to have an extremely low inductance, an optimal thermal resistance, and no wire-bonds. The structure under the gate is formed of p-GaN/heterostructure. The p-GaN layer is grown only under the gate to make the device Normally-OFF. This heterostructure is raised on several AlGaIn/GaN layers to decrease the mechanical stress of the Silicon substrate. This mechanical stress comes from the mismatch between the mesh of the Silicon and the GaN. These intermediate layers also play a role of mechanical isolation between the substrate and the heterostructure to avoid affecting the 2DEG density. On the drain and source sides, TiAl and TiN metals are forming an ohmic contact directly with the AlGaIn and which will lead to the conduction of the electrons in the channel. Finally, the component is passivated with SiN.

2.2.3 Chosen structure and physical problem

Modeling all structures was not possible because of the lack of needed geometrical and physical data. As we want to model the trap's effect in the structure, we are in need to localized impurity measurements as model inputs. We must specify that within the framework of this thesis no SIMS measurements were performed on the traps in 2D nor 1D for GaN Systems. Furthermore, we estimated the need to perform numerical modeling for the CEA's fully-recessed normally-OFF structure. Also, no SIMS measurements were also performed on these normally-OFF devices.

So we chose the structure whose we have trap measurements. We also decided to model a case that was discussed in the literature and found in these devices: the impact of Oxygen traps introduced into the AlGaIn layer of conventional HEMT. We want to estimate the impact of the charges weight between surface and barrier traps when we have a high density of surface traps. So N-ON CEA structure was chosen for this purpose since the structure seems simple to be modeled analytically or semi-analytically to understand the effect of Oxygen on the 2DEG density where traps measurements were performed. In conclusion, we need to model a MOS-HEMT structure while introducing some trap energy levels into the AlGaIn and compare their impact with the interface ($\text{Al}_2\text{O}_3/\text{AlGaIn}$) traps.

Now we will go on a brief presentation of the basic analytical model existing in literature to adapt it to our MOS structure. We will then introduce the interface traps effect with a model presented in the literature. We present our modeling of barrier traps (Oxygen) to study the weight between these two traps sources.

2.3 Basic analytical model

In this section, for the chosen structure (N–ON), we begin by briefly presenting the basic analytical equations which are already developed in the literature. We adopted the model developed by [Che 10 and Li 08] as this model is supposed to predict the electro–thermal behavior of the Schottky gate HEMT including the analytical form of 2DEG density. Therefore, it is precisely the basis for developing a model to study the effect of traps on 2DEG density for our chosen structure. These model equations will be then adapted to our structure by considering the oxide and introducing the existing model of interface traps. We will then be able to change its formulations to study the barrier trap’s effect. In this section, we present all the specificities of the model without any account of the particularities of our structure intended to be modeled. In the next section, we will present the modifications made on this model.

2.3.1 Conventional Energy Band Diagram

We start with the traditional energy band diagram presented in *Figure 2.4*, which illustrates the 1–D vertical section under the gate of the Schottky contact. At thermal equilibrium, as with the conventional heterostructures discussed in chapter 1, a discontinuity in the conduction band induced quantum–well is formed due to the gap difference between AlGaN and GaN materials. In the GaN side, there is only the free electron density resulting from the formation of the heterostructure. The potential distribution shape throughout the AlGaN layer causes the formation of the depletion zone, which contains the ionized donor density. Furthermore, we can see that a conduction band minimum is located in the AlGaN layer. This shape reflects the fact of having two electric fields in opposite directions in the AlGaN barrier. The heterostructure and the 2DEG formation are explained in details in chapter 1.

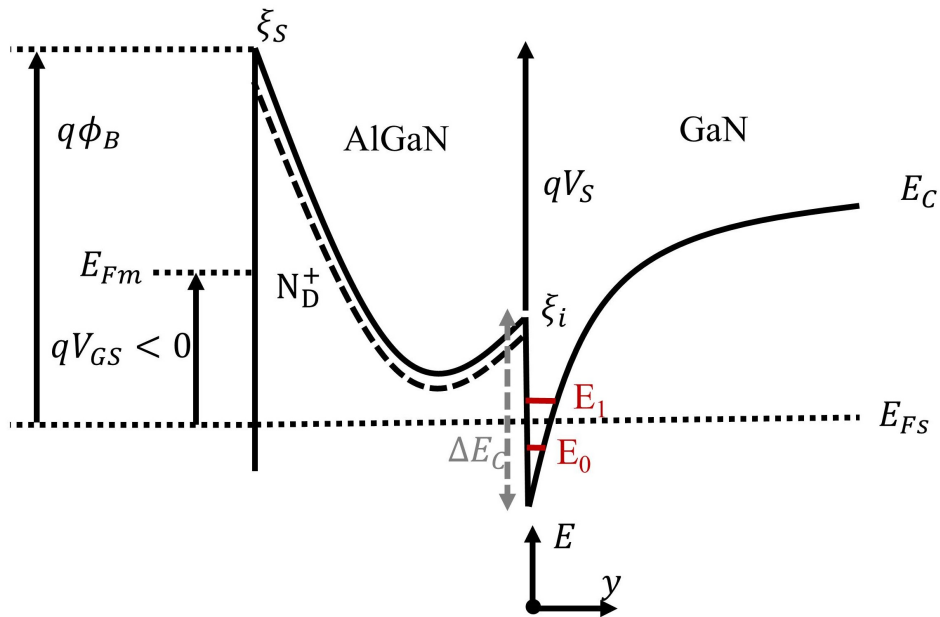


Figure 2.4: Conventional energy band diagram.

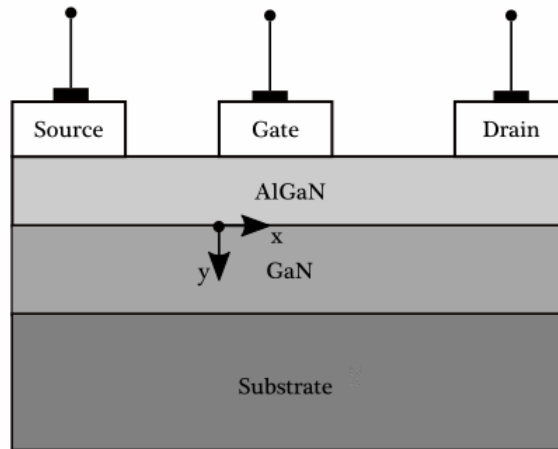


Figure 2.5: Corresponding structure with schottky contact.

Table 2.1 presents the band diagram parameters.

Parameter	Description
E_{Fm} (e.V)	Fermi level in the Metal
E_{Fs} or E_F (e.V)	Fermi level in the heterostructure
$V_{GS}(V)$	Applied Gate voltage
$V_S(V)$	AlGaN potential drop
$E_0(e.V)$	First energy subband
$E_1(e.V)$	Second energy subband
$\xi_i(V.m^{-1})$	Electric field at hetero-interface (AlGaN/GaN)
$\xi_s(V.m^{-1})$	Surface (Metal/AlGaN) electric field
$q(C)$	Elementary charge
$N_D^+(cm^{-3})$	Ionized donor density

Table 2.1: Energy band diagram Parameters

2.3.2 2DEG model formulation

To model a HEMT drain current, we mainly need physical models of carrier mobility, 2DEG concentration and geometric parameters of the device. Adjustable parameters and physical approximations are always required to perform this model analytically. We have summarized the approximations concerning the 2EDG density as follows:

1. Homogeneous distribution and ionization donor density along the AlGaN layer, i.e., for all polarization and temperature conditions, the donors are considered to be ionized and uniformly distributed.
2. Polarization–induced bound charge is created when forming the heterostructure, the change in this polarization when mechanical stress occurs is not taken into account.
3. The quantum well is considered triangular; two subbands energy are sufficient to calculate an approximate total charge concentration.
4. There is no consideration of barrier, bulk and interface traps.

2.3. BASIC ANALYTICAL MODEL

Some of these approximations will not be affected by our modifications (points 1, 2 and 3). On the other hand, point four will be modified as we aim to introduce traps level in the AlGaN barrier. We must note that for the way to take into account impurities in the AlGaN layer, it will be different from that taken in the first point. The consideration of the homogeneous ionized impurities distribution throughout the AlGaN layer will be modified.

The main steps to calculate the 2DEG density distribution along the channel $n_s(x)$ – the charges concentration distribution in confinement along the x–direction under the gate – can be summarized as follows:

1. Integrate Poisson equation throughout the AlGaN layer to find a relation between the electric field at the heterointerface ξ_i and the voltage drop along the AlGaN layer V_S .

The mathematical steps of the first point were grouped as follows with the boundary conditions. The potential at the heterointerface is taken as an arbitrary point of reference or $V(0) = 0$.

$$\Delta V = \frac{\rho}{\epsilon_0 \epsilon_1}, \quad \frac{d^2 V(y)}{dy^2} = \frac{-qN_D}{\epsilon_0 \epsilon_1} \quad \text{for } 1D \text{ in the } y\text{-direction} \quad (2.1)$$

$$\frac{dV(y)}{dy} = \frac{-qN_D}{\epsilon_0 \epsilon_1} y + C_1, \quad \frac{dV(y)}{dy} = -\xi_i \quad \text{at } y = 0, \quad \text{where} \quad \frac{dV(y)}{dy} = \frac{-qN_D}{\epsilon_0 \epsilon_1} y - \xi_i \quad (2.2)$$

$$V(y) = \frac{-qN_D}{2\epsilon_0 \epsilon_1} y^2 - \xi_i y + C_2, \quad V(y) = 0 \quad \text{at } y = 0, \quad \text{where} \quad V(y) = \frac{-qN_D}{2\epsilon_0 \epsilon_1} y^2 - \xi_i y \quad (2.3)$$

$$V_S = V(0) - V(-d) = \frac{qN_D}{2\epsilon_0 \epsilon_1} d^2 - \xi_i d \quad (2.4)$$

$$V_P = \frac{qN_D}{2\epsilon_0 \epsilon_1} d^2 \quad (2.5)$$

$$V_S = V_P - \xi_i d \quad (2.6)$$

ϵ_1 is the AlGaN relative permittivity, ϵ_0 is the vacuum permittivity, d is the AlGaN width, $V(y)$ presents the potential distribution along the AlGaN layer, V_S is the surface potential and V_P is the pinch-off voltage.

2. Applying Gauss theorem at the hetero-interface to find a relation between the electric field at the heterointerface ξ_i and the 2DEG density n_s . This 2DEG density is evenly distributed under the gate (when no drain voltage is applied).

$$\xi_i = \frac{q}{\epsilon_0 \epsilon_2} \int_0^{y_0} n(y) dy \quad (2.7)$$

$$\int_0^{y_0} n(y) dy = n_s, \quad \text{and} \quad \xi_i = \frac{q}{\epsilon_0 \epsilon_2} n_s \quad (2.8)$$

ϵ_2 is the GaN permittivity and y_0 is the confinement limit in the GaN layer.

3. Find a 2DEG density – Fermi level relationship, for this purpose, the energy band diagram is used to find a relationship between the voltage drop V_S , the gate voltage V_{GS} and the Fermi level E_{FS} .

$$qV_S + \Delta E_C = q\phi_B - qV_{GS} + E_{FS} \quad (2.9)$$

2.3. BASIC ANALYTICAL MODEL

ΔE_C is the discontinuity at the hetero-interface and ϕ_B is the Schottky barrier. Now by using the developed relationships of the surface potential (Eq.2.6, Eq.2.8 and Eq.2.9), the 2DEG density can be written in the following form:

$$V_S = V_P - \frac{qn_s}{\epsilon_0\epsilon_2}d = \phi_B - V_{GS} + \frac{E_{FS} - \Delta E_C}{q} \quad (2.10)$$

$$n_s = \frac{\epsilon_0\epsilon_2}{qd}(V_{GS} - V_{TH}) \quad (2.11)$$

$$V_{TH} = \phi_B - V_P - \left(\frac{\Delta E_C - E_{FS}}{q} \right) \quad (2.12)$$

$$(2.13)$$

V_{TH} is the threshold voltage. At this point, we have an equation (2.11) with two unknowns n_s and E_{FS} for which we need a second relation. This second relation will come by solving Schrödinger equation in the formed quantum well.

4. Solve Schrödinger equation with a triangular well approximation and use the Fermi-Dirac distribution to find a relation between n_s and E_{FS} .

First of all, we must note that the analytical solution of the Schrödinger equation is relatively complex for the real quantum well. Not taking into account the approximation of a triangular quantum well will complicate the analytical model. Furthermore, authors always consider only two subbands levels in the quantum well which as the charges concentration in the higher energy levels is negligible compared to that of the first two levels [Del 82]. For a triangular quantum well, the energy levels are written as follows [Del 82]:

$$E_n \approx \left(\frac{h^2}{8\pi^2 m_e^*} \right)^{1/3} \left(\frac{3\pi}{2} q \xi_i \right)^{2/3} \left(n - \frac{1}{4} \right)^{2/3} \quad (2.14)$$

$n = 0, 1, etc...$ are the $(n+1)$ energy levels in the quantum well, m_e^* is the effective mass of electrons in the GaN layer and h is the Planck constant. Assuming that the effective mass of the electrons is constant, two relationships (2.15 and 2.16) between the two energy levels (E_0 and E_1) in the quantum well and the electric field can be established.

$$E_0 = \gamma_0 (\xi_i)^{2/3} \quad (2.15)$$

$$E_1 = \gamma_1 (\xi_i)^{2/3} \quad (2.16)$$

$$\gamma_n = \left(\frac{h^2}{8\pi^2 m_e^*} \right)^{1/3} \left(\frac{3\pi}{2} q \right)^{2/3} \left(n - \frac{1}{4} \right)^{2/3} \quad (2.17)$$

Using the solution of the Schrödinger equation, the Fermi-Dirac distribution and the density of states allow us to find the second relation between the Fermi level and the charge concentration n_s (Eq.2.18). One can consult [Liu 99] for more information of mathematical integration.

$$n_s = DkT \ln \left[1 + \exp \left(\frac{E_{FS} - \gamma'_0 (n_s)^{1/3}}{kT} \right) \right] + DkT \ln \left[1 + \exp \left(\frac{E_{FS} - \gamma'_1 (n_s)^{1/3}}{kT} \right) \right] \quad (2.18)$$

D corresponds to the two-dimensional state density, k is the Boltzmann constant, T is the temperature, γ'_0, γ'_1 are some grouping of constants related to the first and second energy subbands level

respectively. We implemented this relation in *Figure 2.6* using an iterative method. To facilitate the analytical modeling, this equation has been approximated by a quadratic equation presented by [Kol 82] as following.

$$E_{Fs} = k_1(T) + k_2(T)\sqrt{n_s} + k_3(T)n_s \quad (2.19)$$

In order to determine the three unknown coefficients $k_1(T)$, $k_2(T)$ and $k_3(T)$, one need to solve Eq.2.18 numerically and use three arbitrary pairs (E_{Fsi}, n_{si}) in Eq.2.19. This approximated equation was compared with the original one with the calculated parameters, for an effective mass of $0.22m_e$. The three calculated coefficients found are $k_1 = -0.2525 \text{ eV}$, $k_2 = 1.9845 \times 10^{-9} \text{ eV.m}$, $k_3 = -1.9052 \times 10^{-15} \text{ eV.m}^2$.

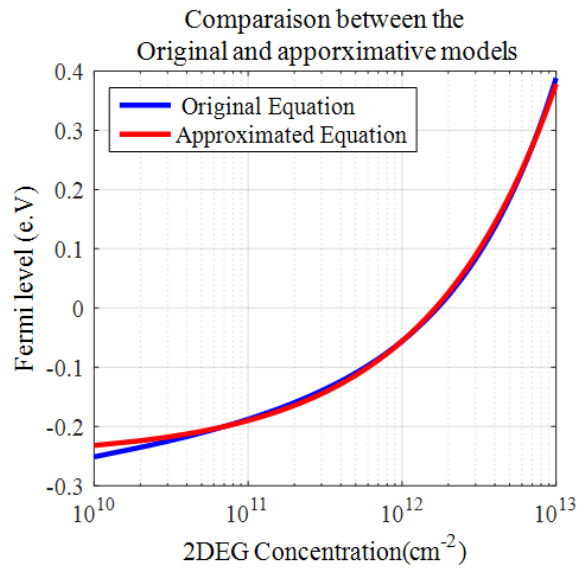


Figure 2.6: Comparison between the original and the approximated equations.

At this point, we have two relations (2.11 and 2.19) with two unknowns (n_s, E_{Fs}) to find the 2DEG density as a function of the Fermi level for different gate polarization.

Now we will present the polarization effect induced bound charges on this density.

5. Spontaneous and piezoelectric polarization induced bound charges.

As explained in chapter 1, it was proved for III-V materials based on nitrides that a high density of polarization-induced charges at the heterointerface of the heterostructure. This polarization induces heterointerface charges is merely introduced in the analytical model through the threshold voltage as follows [Che 10].

$$V_{TH} = \phi_B - V_P - \left(\frac{\Delta E_C - E_{Fs}}{q} \right) - \frac{q\sigma_{\text{AlGaIn}}}{\epsilon_0\epsilon_2} d_{\text{AlGaIn}} \quad (2.20)$$

6. Introducing the dependence of the charges concentration $n_s(x)$ on the drain voltage along the channel V_X by integrating along the channel. We will not detail this point since we are rather interested in the charges density and its dependence only on the gate bias.

However, for the linear mode, the $n_s(x)$ distribution is linearly dependent on V_X . For the saturation mode, the channel is divided into two regions (linear and saturation). The saturation limit in these HEMTs devices is indicated by the drift velocity saturation and not by the cancellation of the charge concentration. It should be noted that all these steps are only applicable for region under the gate, outside of this zone there are parasitic resistances that replace the other part of the channel. Now we will proceed to the modification of the presented basic equations to be adaptable to our structure and to take into account the different types of traps on the 2DEG density.

2.4 Modification of the basic analytical model

2.4.1 Incorporation of the oxide layer

The HEMTs structures have been well modeled and studied for Schottky contacts regardless of Metal–(GaN/AlGaN/GaN) [Tap 12] or Metal– AlGaN/GaN [Che 10, Kha 11, Li 08]. Y. Zhang et al. [Zha 13] give a comprehensive model of only the threshold voltage of MOS–HEMT and its control by gate oxide thickness in fluorinated GaN. There is a lack of analytical models that study the inclusion of an oxide layer on the 2DEG density.

The incorporation of the oxide requires an estimation of the electric field at the Oxide/semiconductor interface that will be presented in this section. This electric field is exposed to several parameters, among them, donor density, bulk and interface traps and finally the 2DEG density. So we are interested in understanding how the insertion of an oxide layer will affect the 2DEG density. In this section, we present only this effect without taking into account the charges that may exist in the oxide. The inclusion of oxide charges will be incorporated in the semi-analytical model presented in section 2.5.

2.4.1.1 Formulations

As shown in *Figure 2.7*, the next theoretical integration is performed with a case where the oxide Al_2O_3 does not contain any charges. So the electric field is assumed constant and the potential is linear across the layer. The mathematical formulations of the insertion of an oxide layer into physics-based models has been well explained for traditional MOS structures [Sze 07] where a potential drop V_{OX} is added to the potential drop of the heterostructure. Equation 2.20 will be modified as following, ϕ_B can be replaced by $\phi_m - V_{OX} - \chi$. The potential V_{OX} can take positive or negative value depending on the electric field direction that passes through it. Equation 2.9 will be modified as follows.

$$\phi_m - qV_{GS} = qV_{OX} + \chi + qV_S + \Delta E_C - E_{Fs} \quad (2.21)$$

ϕ_m is the metal work function and χ is the electron affinity.

In order to estimate the potential drop across the oxide V_{OX} , we need to evaluate the electric field at the interface $(\text{Al}_2\text{O}_3/\text{AlGaN})\xi_s$. This electric field depends on the ionized dopant density in the AlGaN layer, the electric field at the hetero–interface ξ_i and the electric field resulting from the ionized interface states. Concerning interface states, we treat them in section 2.4.2.

The oxide voltage drop depends on the charges in the heterostructure; this relationship can be written in the form of Eq.2.22 Q_{HEMT} designates the total charge under the gate below the oxide. This charge density Q_{HEMT} is composed of two sources. The first source is the negative 2DEG charge density and the second source is the total positive charge of ionized donors in the AlGaN layer Q_D^+ . This total charge will be modified in the next sections when we include the traps density in the AlGaN layer and the interface traps. So, we will end up with a voltage drop across the oxide that depends on the 2DEG density.

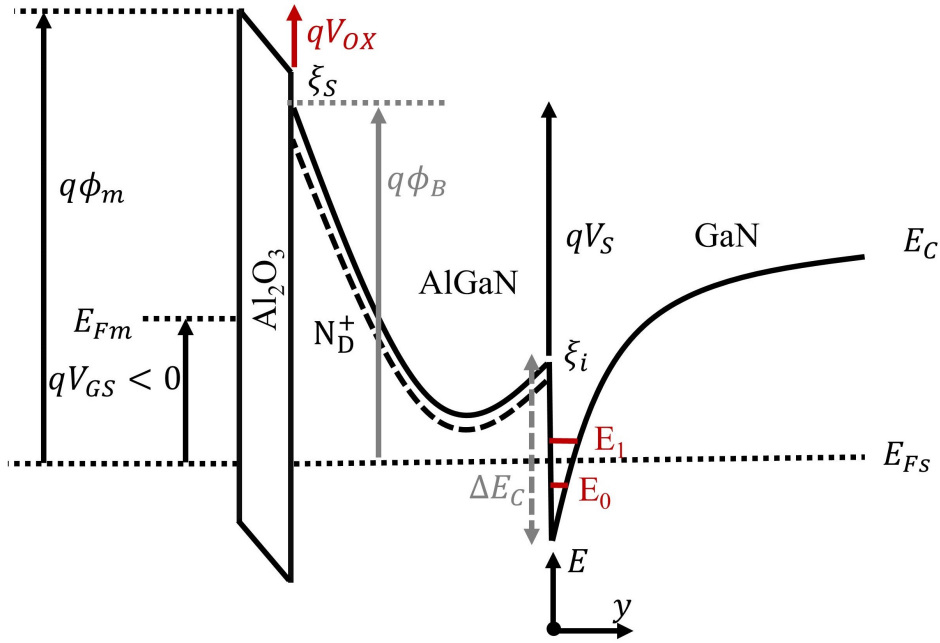


Figure 2.7: Energy band diagram with the oxide layer.

Finally, the system of equations for calculating the 2DEG density taking into account the oxide layer is presented as follows. We get three expressions (2.22, 2.25 and 2.19) with three unknowns n_s , E_{Fs} and V_{OX} . The difference of the permittivity between 25% Al doped GaN and GaN is not large, so we use $\epsilon_0\epsilon_2$ to designate the material permittivity of the heterostructure.

$$V_{OX} = E_{OX}d_{OX} = \frac{Q_{HEMT}d_{OX}}{\epsilon_0\epsilon_{OX}} \quad (2.22)$$

$$Q_{HEMT} = Q_D^s - qn_s = -\epsilon_0\epsilon_s\xi_s \quad (2.23)$$

$$\xi_s = -\frac{Q_D^s}{\epsilon_0\epsilon_s} + \frac{qn_s}{\epsilon_0\epsilon_s} \quad (2.24)$$

$$n_s = \frac{\epsilon_0\epsilon_s}{qd}(V_{GS} - V_{TH} + V_{OX}) \quad (2.25)$$

$$V_{TH} = \phi_m - \chi - V_P - \left(\frac{\Delta E_C - E_{Fs}}{q}\right) - \frac{q\sigma_{AlGaIn}}{\epsilon_0\epsilon_s}d_{AlGaIn} \quad (2.26)$$

d_{OX} is the thickness of the oxide layer ϵ_{OX} is the oxide relative permittivity, E_{OX} is the electric field across the oxide, and Q_{HEMT} is the total charge in the HEMT. The parameters used in the modeling are presented in Table 2.2.

Parameter	Corresponding value
Schottky barrie $\phi_B(V)$	1.165 [Amb 99]
Ionized donor density $N_D(cm^{-3})$	1×10^{18} Typical value for n-doping
Discontinuity $\Delta E_C(e.V)$	0.3430 [Amb 99]
Oxide thickness $d_{OX}(cm)$	30×10^{-7}
E_{OX}	9.8
ξ_s	10.325 [Amb 99]
$\phi_m(V)$	4.7 [Amb 99]

$\chi(V)$	2.5 [Amb 99]
$\sigma_{AlGaN/GaN}(cm^{-2})$	1×10^{13} [Amb 99]

Table 2.2: Energy band diagram parameters.

2.4.1.2 Implementation Method

The implementation is done by an iterative method based on the dichotomy to compute three unknown parameters (n_s, E_{Fs} and V_{OX}) of the three equations 2.22, 2.25 and 2.19.

This method is presented in the following flowchart:

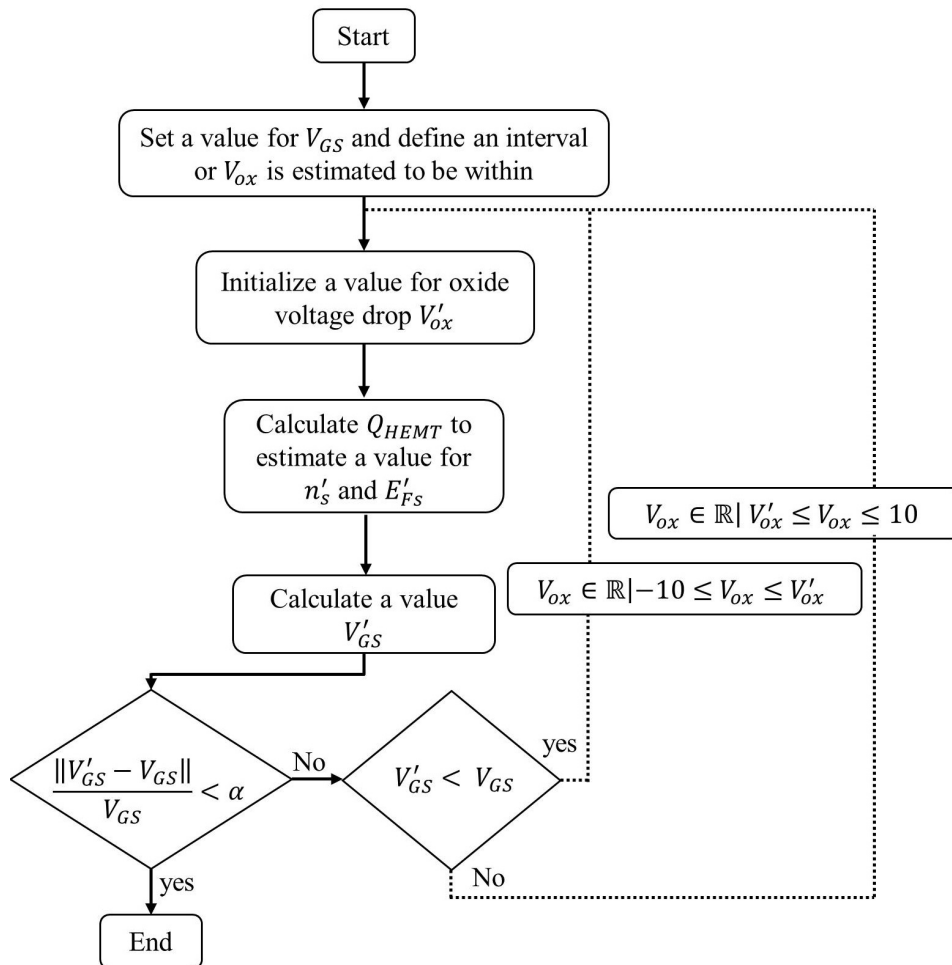


Figure 2.8: Flowchart for the calculation method of the analytical model with the integration of the oxide layer.

The steps of this iterative method are the following:

1. We begin by fixing a value for the applied gate voltage.

2.4. MODIFICATION OF THE BASIC ANALYTICAL MODEL

2. We define an interval where V_{OX} is estimated to be within, $V_{OX} \in \mathbb{R}|_{-10 \leq V_{OX} \leq 10}$. This interval is strictly increasing, or the solution is estimated to be unique. The limits of this interval are sufficient since the applied gate voltage will not exceed anyway these values.
3. We assume an initial value of oxide potential drop V'_{OX} , by using 2.22, we can find the quantity Q_{HEMT} to estimate a value of n'_s by using 2.23.
4. We calculate the value of the E'_{F_s} using equation 2.19.
5. Now, we use the calculated E'_{F_s} , n'_s and the estimated V'_{OX} in order to calculate the value of V'_{GS} by the relation 2.25.
6.
 - If $\frac{|V'_{GS} - V_{GS}|}{V_{GS}} < \alpha$, it means that the corresponding values E'_{F_s} , n'_s and V'_{OX} are the searched values. The convergence conditions equal to $\alpha = 0.1\%$.
 - If $\frac{|V'_{GS} - V_{GS}|}{V_{GS}} > \alpha$ and $V'_{GS} < V_{GS}$, the estimated V'_{OX} will be the new limit of the interval, $V_{OX} \in \mathbb{R}|_{-10 \leq V_{OX} \leq V'_{OX}}$.
 - If $\frac{|V'_{GS} - V_{GS}|}{V_{GS}} > \alpha$ and $V'_{GS} > V_{GS}$, the estimated V'_{OX} will be the new other limit of the interval, $V_{OX} \in \mathbb{R}|_{V'_{OX} \leq V_{OX} \leq 10}$.

2.4.1.3 Modeling results and discussion:

We present two relationships between n_s and ξ_s (the electric field at the interface ($\text{Al}_2\text{O}_3/\text{AlGaIn}$)) and a relation between the oxide potential drop V_{OX} and n_s . These relationships may give us an idea about the effect of the incorporation of the oxide in the structure. For three different doping values of the AlGaIn layer, we observe the following:

1. n_s – Surface electric field (ξ_s) relation:

Increase in the 2DEG density will generate an increase in the surface electric field as the sum of the total charges under the oxide will increase. By increasing the doping concentration, the surface electric field decreases (more 2DEG density will be needed to compensate this donor's positive charges).

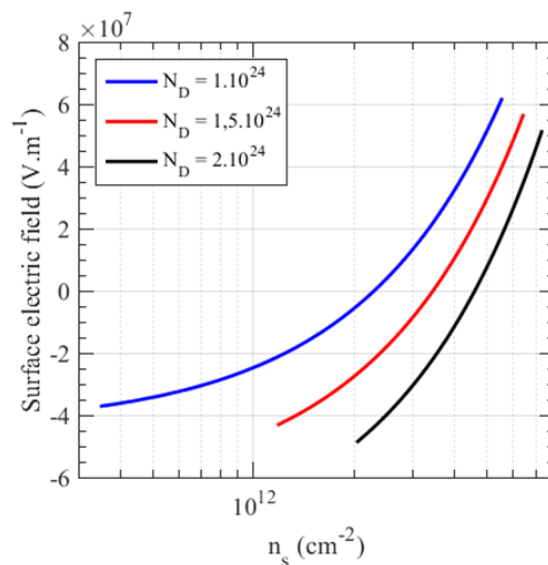


Figure 2.9: n_s - Surface electric field (ξ_s) relationship with oxide consideration.

2. n_s – Oxide voltage drop (V_{OX}) relation:

By increasing the doping, the electric field increases and thus the oxide voltage drop increases.

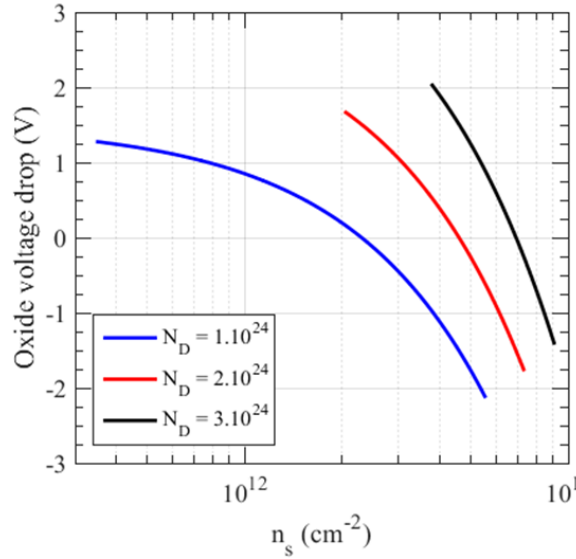


Figure 2.10: n_s – Oxide voltage drop V_{OX} relationship with oxide consideration.

3. n_s – Oxide voltage drop V_{GS} relation:

Now we perform a comparison between the behavior of the $n_s - V_{GS}$ relationship for the metal–semiconductor Schottky contact and the metal-oxide semiconductor contact (Figure 2.11).

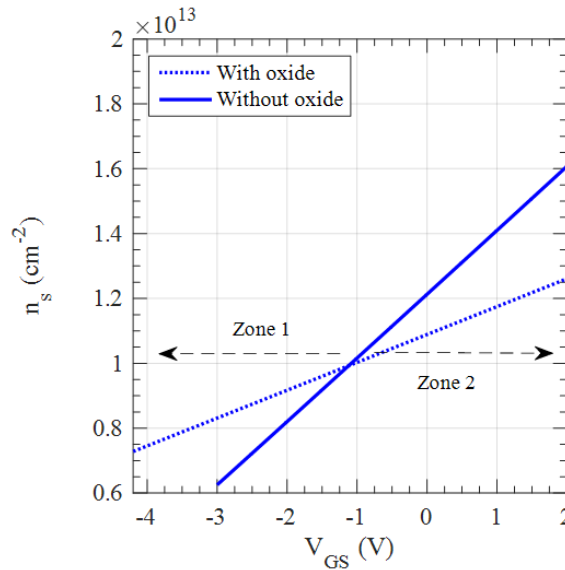


Figure 2.11: Comparison between the behaviors of the $n_s - V_{GS}$ relationship for Schottky contact and Metal-oxide HEMT structures.

This comparison was made by considering a donor density of $5 \times 10^{18} \text{cm}^{-3}$ to study the effect of inserting an oxide layer on the 2DEG density behavior responding to applied gate voltage. Firstly,

we observed a linear behavior of the $n_s - V_{GS}$ relation regardless of a Schottky contact or a MOS structure. On the other hand, an oxide layer does not necessarily enhance the 2DEG density. We observed two zones defined by the lines intersection, for low values of V_{GS} , the density of 2DEG is enhanced by the presence of oxide, on the other hand for higher values of V_{GS} , this oxide is penalizing for the 2DEG density. This observation is based on the fact that the potential across the oxide changes sign with the change of sign of the electric field which is affected by the applied gate voltage. The point of the intersection reflects that the potential drop across the oxide is almost zero.

2.4.2 Incorporation of the interface ($\text{Al}_2\text{O}_3/\text{AlGaN}$) states:

2.4.2.1 Theoretical formulation:

The incorporation of interface states has been well explained in the literature [Mic 08], we will briefly explain their participation in our study case. For $\text{Al}_2\text{O}_3/\text{AlGaN}/\text{GaN}$ HEMTs, the experimental measurements carried out by the C–V dispersion or photo–assisted C–V methods proved the existence of the predictable U form of the $D_{it}(E)$ through the bandgap. The U –shape is a relation between the energy levels and the density of the interface traps which has been experimentally validated. We find high interface traps densities at the extremities of the gap which undergo a minimum at the mid-gap. Without surface treatment, the density of interface traps charge can reach high values as $2 \times 10^{13} \text{cm}^{-2} \text{eV}^{-1}$ to $3 \times 10^{13} \text{cm}^{-2} \text{eV}^{-1}$ near the conduction band, the minimum states densities around the mid-gap were estimated to be low as $1 \times 10^{12} \text{cm}^{-2} \text{eV}^{-1}$ [Hor 13]. These values are important to use the mathematical form that includes these interface states. Simply, the incorporation of the interface traps is resumed as an additional charge associated with the total charges under the oxide and will thereafter altered the electric field through the oxide. We must note that the treatment of the AlGaN surface is carried out using N_2O just before the oxide deposition. These experimental measurements of the surface traps presented in the article are performed before and after this treatment. These measurements were introduced in the model to make the comparison of the surface traps effect before and after surface treatment. The mathematical forms of interface traps incorporation and the whole system equations can be written as following:

$$V_{OX} = E_{OX} d_{OX} = \frac{(Q_{HEMT} + Q_{it}) d_{OX}}{\epsilon_0 \epsilon_{OX}} \quad (2.27)$$

$$Q_{it} = q \int_{E_V}^{E_C} D_{it}^D(E) [1 - f(E)] dE - q \int_{E_V}^{E_C} D_{it}^A(E) f(E) dE \quad (2.28)$$

$$\text{Approximated form } Q_{it} = \begin{cases} -q \int_{E_{CNL}}^{E_F} D_{it}^A(E) dE & \text{for } E_F \text{ above } E_{CNL} \\ +q \int_{E_F}^{E_{CNL}} D_{it}^D(E) dE & \text{for } E_F \text{ below } E_{CNL} \end{cases} \quad (2.29)$$

$$D_{it}^{A,D}(E) = D_{it0} \exp \left[\left(\frac{|E - E_{CNL}|}{E_{0A,0D}} \right)^{n_{A,D}} \right] \quad (2.30)$$

$$Q_{HEMT} = Q_D^s - qn_s = -\epsilon_0 \epsilon_s \xi_s \quad (2.31)$$

$$\xi_s = -\frac{Q_D^s}{\epsilon_0 \epsilon_s} + \frac{qn_s}{\epsilon_0 \epsilon_s} \quad (2.32)$$

$$n_s = \frac{\epsilon_0 \epsilon_s}{qd} (V_{GS} - V_{TH} + V_{OX}) \quad (2.33)$$

$$V_{TH} = \phi_m - \chi - V_P - \left(\frac{\Delta E_C - E_{Fs}}{q} \right) - \frac{q \sigma_{\text{AlGaN}}^{\text{GaN}}}{\epsilon_0 \epsilon_s} d_{\text{AlGaN}} \quad (2.34)$$

2.4. MODIFICATION OF THE BASIC ANALYTICAL MODEL

Q_{it} presents the interface trap charges C/cm^2 , $D_{it}^{D,A}$ is the interface trap density (states/ $cm^2 \cdot eV$), for donor and acceptor respectively. $f(E)$ is the Fermi-Dirac distribution. D_{it0} presents the minimum value of the U form, E_{CNL} is the charge neutral level (when Fermi level coincides with this level, we have zero interface charges) and finally $n_{A,D}$ and $E_{0A,AD}$ are adjustable parameters for quantitatively validate to the experimental measurements. The approximated form is used when neglecting the temperature effect, which comes from of the Fermi Dirac distribution.

In order to approximate to a real case, we used the measurements carried out by [Hor 13] on the same studied structure $Al_2O_3/AlGaIn/GaN$. We have modeled these states effects using two different values of density D_{it0} before and after the surface treatment performed by the author. The adjustable parameters shown in *Table 2.3* can be modified for other structures; they are very dependent on adjustment with experimental results. The results of our simulation to match the experimental results are approximate, as shown in *Figure 2.12*; we presented the U forms of the $D_{it}(E)$ distribution without and with surface treatment. For our simulation, for the rest of the chapter, we will consider the worst case where there is no surface treatment and we have a relative high density of $D_{it}(E)$ distribution, which can reach $2 \times 10^{13} cm^{-2} eV^{-1}$ at the extremities of the gap. The values of the simulation parameters have been taken from [Mic 08].

Parameter	Corresponding value
Charge neutrality level $E_{CNL}(e.V)$	$E_C - 1.1$
Adjustment parameter $E_{0A}(e.V)$	0.6
Adjustment parameter $E_{0D}(e.V)$	1.52
Adjustment parameter n_A	1.9
Adjustment parameter n_D	1.9
Minimum densities of states $D_{it0}(cm^{-2}e.V^{-1})$	without surface treatment = 1×10^{12} with surface treatment = 5×10^{11}

Table 2.3: Surface states simulation parameters

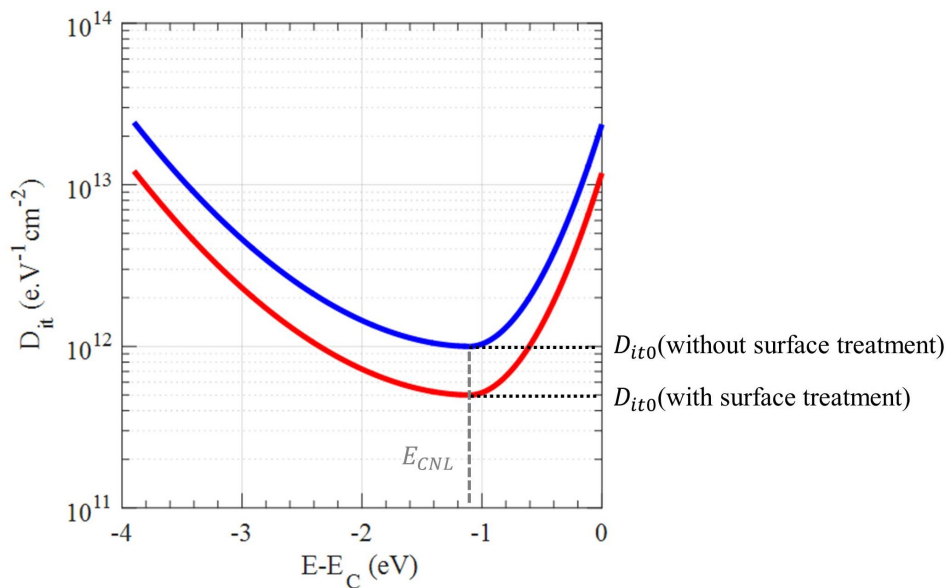


Figure 2.12: Simulation results of the U form of the $D_{it0}(E)$ distribution (Red: with surface treatment, blue: without surface treatment).

In order to correctly calculate the value of the ionized interface charges, we need to estimate the Fermi potential value but this time concerning the top of the E_C . By adding the value of the hetero–interface discontinuity and the potential drop across the AlGaIn layer, we can easily find the value $E_F - E_C$. For the implementation, we have developed the iterative method so that it takes into account the modification of the total charges, which will include interface traps.

2.4.2.2 Modeling results and discussion:

First, we are interested in understanding the relationship between the surface potential and the interface-trapped charges. As previously explained, the interface traps are either acceptors or donors, which are dependent on the relative difference in the neutral level. All states above this neutral level are acceptors, and all the levels below it are donors while considering a continuum of states along the bandgap. Now let us explain how these states work depending on the surface potential. By applying a gate bias voltage, the Fermi level, the surface potential and the 2DEG change. This change is governed by the equations presented in the theoretical integration part (2.27 to 2.34). As shown in *Figure 2.13*, we begin by studying this behavior function of the gate voltage and the minimum density of these traps' U distribution $D_{it0} = 2 \times 10^{11} \text{ cm}^{-2} \text{ eV}^{-1} - 1 \times 10^{12} \text{ cm}^{-2} \text{ eV}^{-1}$. We notice clearly that this absolute value of the density decreases until reaching minimum of charges (at the point where E_F coincides with E_{CNL}), then the density increases again.

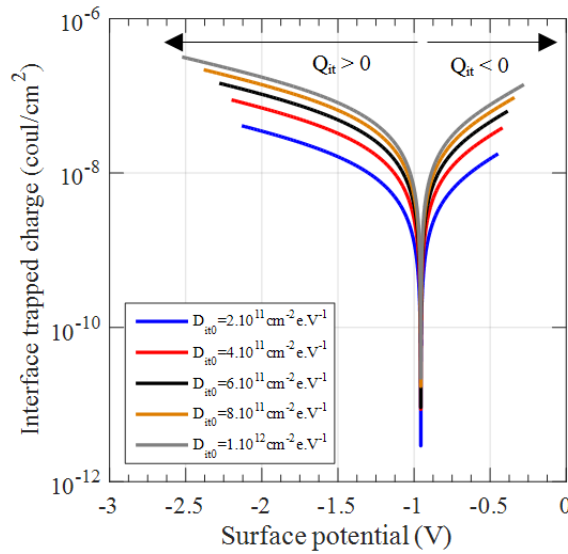


Figure 2.13: Interface trapped charges function of the surface potential for different densities of D_{it0} .

- The weight of the interface traps by comparing with the donor's density.

Now we are going to move to a critical point, which consists of quantifying the influence of these interface traps. One method of proving it is to split of the total charges into interface charges and HEMT charges (which corresponds to the sum of the positive donors and the negative 2DEG concentration). This way will give us an idea about the real effects of these interface states. As shown in *Figure 2.14*, for the D_{it0} density, we use the value of the structure with a surface treatment, the corresponding interface states density is $5 \times 10^{11} \text{ cm}^{-2} \text{ eV}^{-1}$. Then we changed the values of the donors in the AlGaIn layer between two values ($1 \times 10^{18} \text{ cm}^{-3}$ & $2 \times 10^{18} \text{ cm}^{-3}$).

2.4. MODIFICATION OF THE BASIC ANALYTICAL MODEL

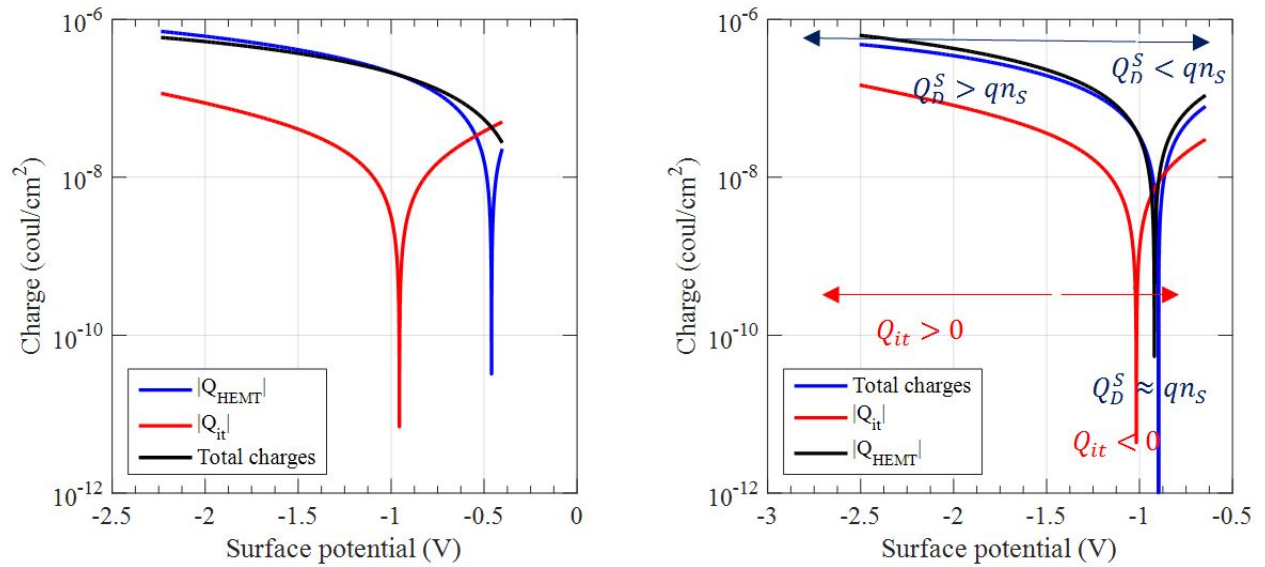


Figure 2.14: The different distribution charges for HEMT, interface traps and total charges. These simulations were performed with a D_{it0} density of $5 \times 10^{11} \text{cm}^{-2} \text{e.V}^{-1}$ for two different densities of donors densities (Left, $N_D = 1 \times 10^{18} \text{cm}^{-3}$ and right $N_D = 2 \times 10^{18} \text{cm}^{-3}$)

Considering the Q_{HEMT} distribution in both cases, we observe that this total density (donors + 2DEG) reaches a minimum value which itself changes according to the donors. This minimum reflects the exact point of compensation between the donors' density and the 2DEG.

For both cases, especially with a donor density of $1 \times 10^{18} \text{cm}^{-3}$, the total charges is governed solely by the HEMT distribution, as if the interface traps density has a low effect on these total charges.

Now let us move to the worst-case scenario where there has been no surface treatment and a high density $1 \times 10^{12} \text{cm}^{-2} \text{eV}^{-1}$ as shown in Figure 2.15.

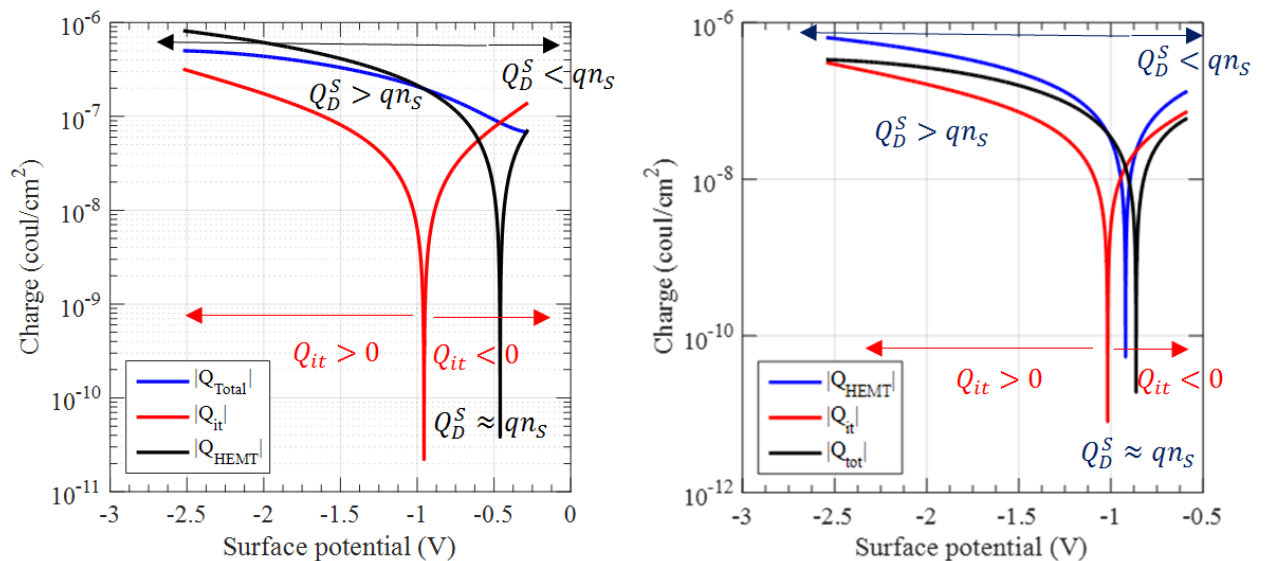


Figure 2.15: The different distribution charges for HEMT, interface traps and total charges. These simulations were performed with a D_{it0} density of $1 \times 10^{12} \text{cm}^{-2} \text{e.V}^{-1}$ for two different densities of donors densities (Left, $N_D = 1 \times 10^{18} \text{cm}^{-3}$ and right $N_D = 2 \times 10^{18} \text{cm}^{-3}$)

2.5. OXYGEN TRAPS IN THE ALGAN BARRIER AND THE WEIGHT BETWEEN INTERFACE AND BARRIER TRAPS

These results were carried out with a high density of D_{it0} , using the adjusted equation of the U form distribution, a very high interface traps values at the bandgap extremities may be founded. We also observe that for negative surface potential, the ionized interface trap density is higher since the difference between the neutral level and the Fermi level is significant. Therefore, we can say that in this area, the interface traps have an effect on the total charges under the oxide.

These interface traps may have also a significant effect in the area where the total HEMT charges reaches its minima as shown in *Figure 2.16*.

In general, even with these high values of interface charges, for doping density $N_D = 1 \times 10^{18} \text{cm}^{-3}$ and $N_D = 2 \times 10^{18} \text{cm}^{-3}$, the effect is more important but not so significant.

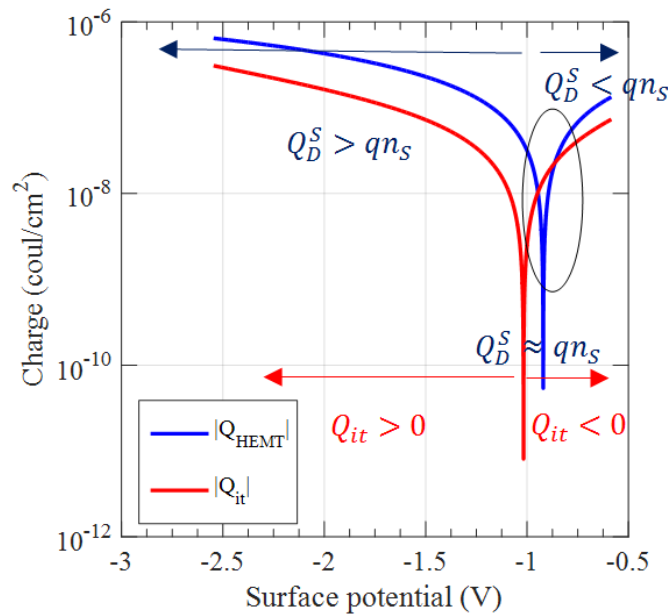


Figure 2.16: Illustration of the zone where the interface trapped charges may have an impact on the total charges of the system.

We have presented the incorporation of oxide and interface traps for the $\text{Al}_2\text{O}_3/\text{AlGaIn}/\text{GaIn}$ structure. We have seen that interface traps can have a low impact on the total charges when a surface treatment is performed, but it can also have a more critical impact when incorporating a higher density at the neutral level. However, there was no introduction of the bulk traps either in the barrier or buffer. These introduced traps into these bulk layers can have a significant effect on the electrical characteristics. In the next section, we will start by introducing traps levels in the AlGaIn barrier to see their impact on the 2DEG density. We will study a real case, or these traps presented the unintentionally introduced Oxygen.

2.5 Oxygen traps in the AlGaIn barrier and the weight between interface and barrier traps

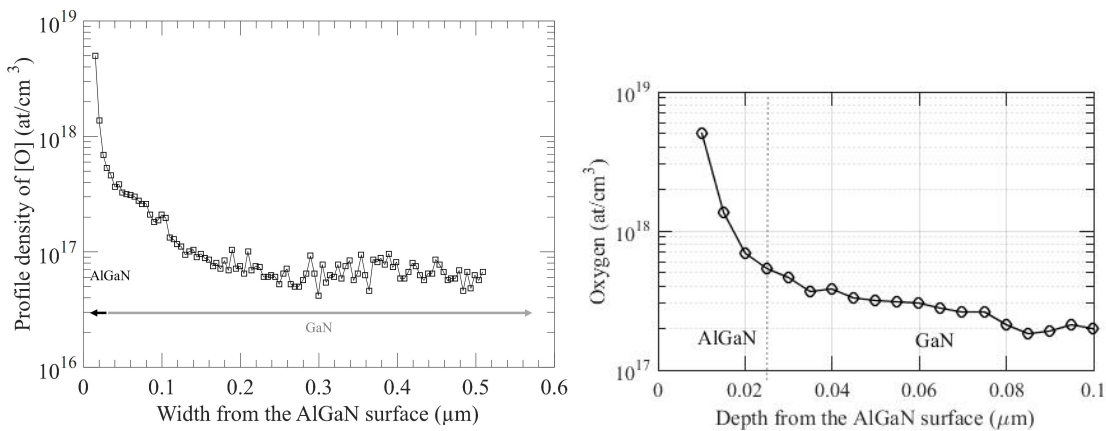
It has been previously shown that interface states at the AlGaIn surface with states density up to $1 \times 10^{13} \text{cm}^{-2}$ may have a significant impact on the electrical characteristics of the device [Jog 03 and Lu 13]. This has been observed wherever these states are located: between the gate and the drain in nonpassivated devices and subsequently form the so-called virtual gate [Vet 01], or located under the gate in passivated devices [Fag 10]. The reason behind this high density of interface states was explained mainly by the formation of nitrogen vacancies at the AlGaIn surface at high-temperature annealing [Cao 09 and Has

2.5. OXYGEN TRAPS IN THE ALGAN BARRIER AND THE WEIGHT BETWEEN INTERFACE AND BARRIER TRAPS

04b]. It should be noted that technological efforts were made to neutralize their effects like passivating the surface by SiO_2 , Si_3N_4 or SiON [Aru 04] or performing N_2O radical treatment [Hor 13]. The reduction of the interface states modifies the balance of traps effects eventually present in the bulk layers of the device. Some authors have recently reported the effects of interface states when the component is correctly passivated and have shown that their effect becomes negligible compared to barrier traps [Lia 16]. As a source of these bulk defects, it has been reported the possible diffusion of a high density of Oxygen during manufacturing and the easy formation of Ga–O bonds in the AlGaN layer [Don 06, Yan 13] which subsequently induces a high Oxygen traps in the barrier. One of the remaining problems is to understand the effects of the relative weights between the interface and bulk traps on the behavior of the device. In particular, the relative effects of these trap sources on the dependence of the 2DEG density and the gate voltage has to be highlighted. In this section, we investigate this question theoretically. More precisely, we will present a theoretical study of the weight between Oxygen barrier traps and AlGaN surface traps on the 2DEG concentration under different gate bias conditions. For this purpose, a semi-analytical 1D charge model has been developed using the non-linear Poisson and Schrödinger coupled equations. This model is based on a new analytical expression of the electric field distribution under the gate including the ionized Oxygen profile into the AlGaN barrier.

2.5.1 DLTS and SIMS Results

DLTS and SIMS measurements were supplemented by CEA–LETI to make this comparison. The DLTS measurements have revealed a dominant peak for an activation energy of 0.44eV and a cross–section of $1.4 \times 10^{-14}\text{cm}^{-2}$ which may confirm the presence of O_N . Concerning the behavior of the Oxygen incorporation into GaN alloys, several authors have shown that Oxygen is preferentially introduced into AlGaN, rather in GaN, with high density and acts as a donor [Jan 04, Wal 98]. SIMS measurements were performed using a Cameca–IMS 7F machine with Cesium Ion Gun System. Some elements such as Oxygen, Silicon, chlorine and carbon have been measured. Here we present only the results of Oxygen, given in *Figure 2.17*, since the density of the other elements is rather low ($< 5 \times 10^{17}\text{cm}^{-3}$) compared with Oxygen, especially in the AlGaN barrier and begin to reach the limit of detection of the equipment.



(a) Oxygen profile in the structure 25nm AlGaN layer and the first $0.52 \mu\text{m}$ of the GaN layer. (b) Oxygen profile in the structure 25nm AlGaN layer and the first 75nm of the GaN layer (zoom for the zone of interest).

Figure 2.17: SIMS measurements.

However, We can observe a rapid decay in the Oxygen density when passing from the AlGaN to the GaN. The density drops from ($5 \times 10^{18}\text{cm}^{-3}$) to the first measured value in the GaN layer ($5 \times 10^{17}\text{cm}^{-3}$)

2.5. OXYGEN TRAPS IN THE ALGAN BARRIER AND THE WEIGHT BETWEEN INTERFACE AND BARRIER TRAPS

and continues to decrease until reaching negligible values ($2 \times 10^{17} \text{ cm}^{-3}$) at $0.1 \mu\text{m}$ from the AlGaN surface. This value continues to decrease until reaching the detection limit of the equipment (*Figure 2.17(a)*).

These detected densities are very high, and an understanding of their effect comparing to interface states is necessary. Therefore, physical modeling must take rigorously into consideration bulk traps and especially barrier traps. The developed semi-analytical model takes principally into account the ionized traps profile whose effects vary sharply with the different gate conditions.

2.5.2 Semi-analytical model

2.5.2.1 Physical problem definition

To achieve the objectives, it is necessary that the model represents correctly both the effects of the surface traps and the bulk traps, especially in the AlGaN barrier. Concerning the interface states, we use the formulations developed in the last section. On the other hand, concerning bulk traps, the physical problem relies mainly on taking into account realistic ionized trap profiles in AlGaN barrier. For our study case, we focus only on the AlGaN barrier traps since they are at least one order of magnitude larger than the GaN buffer traps where their values are considered negligible. To clarify the problem, as an illustration, it is given in *Figure 2.18* a schematic energy band diagram including two donor trap energy levels (E_{TD_1} and E_{TD_2}) and a single acceptor trap level E_{TA_1} .

In this figure ξ_i is the electric field at the hetero-interface, ξ_s is the electric field at the $\text{Al}_2\text{O}_3/\text{AlGaN}$ interface, E_{F_m} and E_{F_s} are the Fermi level of the metal and semiconductor (AlGaN/GaN) respectively, V_{GS} is the applied gate voltage, and q is the elementary charge.

Since the applied gate voltage can alter the curvature of the energy band diagram, the ionization profile in the AlGaN layer can change meaningfully with different gate bias. We can find cases where all traps are ionized or cases where all traps are neutral, or typical cases where more complex ionized traps profile exists.

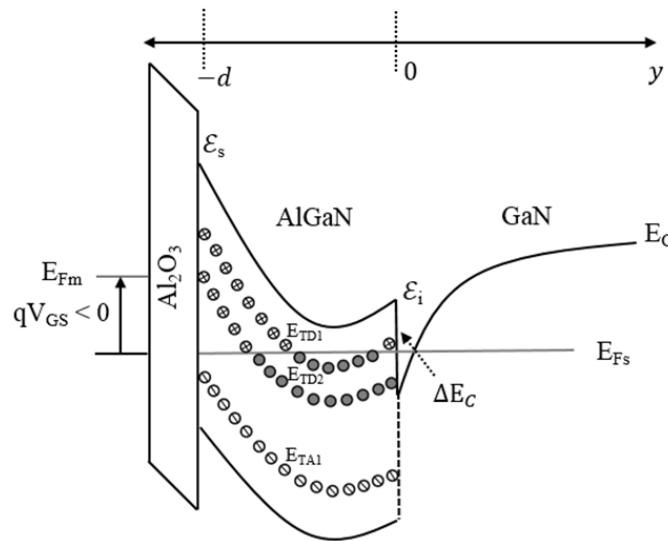


Figure 2.18: Schematic energy band diagram including two donor trap energy levels (E_{TD_1} and E_{TD_2}) and a single acceptor trap level E_{TA_1} .

Homogeneous ionized impurities profile approximation is used in the literature [Che 10 and Li 08]. The originality of the proposed model is precise to be able to represent more realistic profiles of ionized

traps for one or several donors and acceptor levels in the AlGaN barrier.

2.5.2.2 Generic semi–analytical formulation

To carry out this model, we start with some assumptions taken into account.

- Considering the trapping and de–trapping mechanisms, we neglected the Poole–Frenkel emission and the phonon–assisted tunneling which may affect the traps electron energy. Subsequently, the traps activation energy is assumed to be constant throughout the AlGaN layer.
- Although the traps density varies, we have considered a homogeneous distribution density (mean value) in AlGaN layer. Therefore, we focused only on the traps ionized profile and not the density distribution itself which may change from one device to another. This second approximation may cause some inaccuracies in the results, since the total ionized density may change slightly.

The generic semi–analytical model presented here is based on the conventional non-linear Poisson equation taking into account ionized traps density profile for donors ($N_{TD}^+(y)$) and acceptors ($N_{TA}^-(y)$) using the Fermi–Dirac statistics. The use of the Fermi–Dirac distribution is necessary since the difference between the activation energy and Fermi level is neither positive nor negative monotonically, the traps level can cross two times the Fermi level.

As shown in Eq.2.35, Poisson formulation incorporates several donors and acceptors trap energy levels. The spontaneous P_{sp} and piezoelectric P_{pz} polarization induced charges have been taken into account as a sheet charge with $P = P_{sp} + P_{pz}$ [Li 08].

$$\frac{d^2V(y)}{dy^2} = \frac{-q}{\epsilon_0\epsilon_s} \left(\sum_{i=1}^N N_{TD_i}^+(y) - \sum_{j=1}^M N_{TA_j}^-(y) \right) + \nabla P \quad (2.35)$$

N, M are the numbers of energy levels of donors and acceptors traps.

As detailed in the previous section, to estimate the energy levels in the quantum well, the Schrödinger equation is solved at the hetero–interface using the triangular–well approximation [Ras 02].

The ionized trap profile can be expressed as follows:

$$N_{TD_i}^+(y) = \frac{N_{TD_i}}{1 + g_{TD} \exp\left(\frac{E_F - E_{TD_i}(y)}{kT}\right)} \quad (2.36)$$

$$N_{TA_j}^-(y) = \frac{N_{TA_j}}{1 + g_{TA} \exp\left(\frac{E_{TA_j}(y) - E_F}{kT}\right)} \quad (2.37)$$

N_{TD_i}, N_{TA_j} are the homogeneous density of donors and acceptors traps respectively, $g_{TD} = 2, g_{TA} = 4$ are the degeneracy factor for donors and acceptors, $E_{TD_i}(y)$ and $E_{TA_j}(y)$ are the energy levels distribution of the donor and acceptor traps, respectively. The trap energy levels, illustrated in *Figure 2.19*, can be written as function of the potential distribution as following:

$$E_{TD_i} = E_C(y) - E_{A_{Di}} \quad (2.38)$$

$$E_{TA_j} = E_C(y) + E_{A_{Aj}} - E_G \quad (2.39)$$

$$E_C(y) = -qV(y) + \Delta E_C \quad (2.40)$$

2.5. OXYGEN TRAPS IN THE ALGAN BARRIER AND THE WEIGHT BETWEEN INTERFACE AND BARRIER TRAPS

E_{AD_i} , $E_{A_{A_j}}$ are the activation energies for donor and acceptor traps respectively.

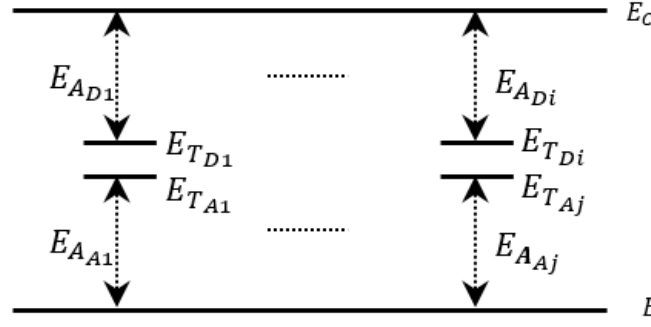


Figure 2.19: Schematic illustration of the traps energy levels.

The following set of relations (2.41-2.43) presents some normalized variables used in the model:

$$V_N(y) = \frac{qV(y)}{kT} \quad (2.41)$$

$$V_{F\alpha,1} = \frac{E_{Fs} - \Delta E_C + E_{A,\alpha}}{kT} \quad (2.42)$$

$$V_{F\alpha,2} = -\frac{E_{Fs} + E_g - \Delta E_C - E_{A,\alpha}}{kT} \quad (2.43)$$

α is the traps level number whatever donor or acceptor, $V_N(y)$ is the normalized potential, $V_{F\alpha,1}$, and $V_{F\alpha,2}$ are the normalized Fermi potential for donor and acceptor traps respectively and $E_{A,\alpha}$ is the activation energy for donor or acceptor. The first derivative of Eq.2.35 is analytically solved with the boundary conditions as following:

- The electric field at the hetero-interface ξ_i is also directly related to the 2DEG density using Gauss's theorem where $\xi_i = \frac{qn_s}{\epsilon_0\epsilon_s}$ assuming no traps in the GaN layer.
- An arbitrary potential is set $V(0) = 0$ at the hetero-interface.

We present now the steps to find the original analytical expression of the electric field distribution throughout the AlGa_N layer with traps incorporation; the following formulation does not include polarization induced bound charges (∇P) since it is explicitly introduced into the n_s value.

If we define the net barrier charge:

$$N(y) = \sum_{i=1}^N N_{TD_i}^+(y) - \sum_{j=1}^M N_{TA_j}^+(y) \quad (2.44)$$

Using the normalized variables of (Eq.2.41 to Eq.2.43), the Poisson equation can be rewritten in the next form:

$$\frac{d^2 V_N(y)}{dy^2} = -\frac{q^2}{kT\epsilon_0\epsilon_s} N(y) \quad (2.45)$$

By multiplying both sides of Eq.2.45 by $\left(2 \frac{dV_N(y)}{dy} dy\right)$ and the next mathematical form trick

$$\frac{d^2V_N(y)}{dy^2} \left(2 \frac{dV_N(y)}{dy} dy \right) = d \left(\frac{dV_N(y)}{dy} \right)^2 \quad (2.46)$$

Eq.2.45 can be integrated into the next form:

$$\int_{\frac{dV_N(0)}{dy}}^{\frac{dV_N(y)}{dy}} d \left(\frac{dV_N(y)}{dy} \right)^2 = \int_{V_N(0)}^{V_N(y)} - \frac{2q^2}{kT\epsilon_0\epsilon_s} N(y) dV_N(y) \quad (2.47)$$

Using the next integration tips, for example, to integrate the donor traps charges, considering that the electric potential at the heterointerface is zero, so $V_N(0) = 0$,

$$\int_{V_N(0)}^{V_N(y)} \left(\sum_{i=1}^N N_{TD_i}^+(y) \right) dV_N(y) = \sum_{i=1}^N N_{TD_i} \left(V_N(y) - \ln \left(\frac{1 + 2 \exp(V_{F\alpha,1} + V_N(y))}{1 + 2 \exp(V_{F\alpha,1})} \right) \right) \quad (2.48)$$

Finally, the general expression of the electric field distribution in the AlGa_N layer can be expressed as following,

$$E(y) = \pm \sqrt{\left| \xi_i^2 - \frac{2kT}{\epsilon_0\epsilon_s} \left(\sum_{i=1}^N N_{TD_i} X_{i,1} - \sum_{j=1}^M N_{TA_j} X_{j,2} \right) \right|} \quad (2.49)$$

with,

$$X_{\zeta,n} = V_N(y) + (-1)^n \ln \left(\frac{1 + g \exp(V_{F\zeta,n} - (-1)^n V_N(y))}{1 + g \exp(V_{F\zeta,n})} \right) \quad (2.50)$$

In Eq.2.50, for donors, we have $n = 1$, $\zeta = i$ and $g = g_{TD}$ whereas for acceptors $n = 2$, $\zeta = j$ and $g = g_{TA}$.

Eq.2.49 expresses analytically the fact of the existence of two electric fields, which oppose each other into the AlGa_N barrier due to the double interface property of this layer. It must be noted that we consider here no other charges than the 2-DEG in the GaN layer as traps in this layer are assumed negligible. If one wants to take into account traps in the GaN layer, ξ_i in Eq.2.49 should be modified.

Eq.2.49 is complicated to solve analytically, and a numerical resolution is used to compute the AlGa_N surface potential (at the Al₂O₃/AlGa_N interface). To complete this model, which must be adapted to a MIS structure, as presented in the last section, we also used the following relationships to calculate the oxide voltage drop and the interface trapped charges:

$$V_{OX} = E_{OX} d_{OX} = \frac{(Q_{HEMT} + Q_{it}) d_{OX}}{\epsilon_0 \epsilon_{OX}} \quad (2.51)$$

$$Q_{HEMT} = Q_T^s - qn_s = -\epsilon_0 \epsilon_s \xi_s \quad (2.52)$$

Here, Q_T^s presents the net surface charge density due to ionized traps $N_{TD_i}^+$ and $N_{TD_j}^-$ in the barrier:

$$Q_T^s = \int_{-d_{AlGaN}}^0 q \left(\sum_{i=1}^N N_{TD_i}^+ - \sum_{j=1}^M N_{TA_j}^- \right) dy \quad (2.53)$$

Q_{HEMT} is the total heterostructure surface charge density defined as the sum of ionized traps and 2DEG charges. Finally, Q_{it} is the interface trap charges (C/cm^2) that can be expressed by:

$$Q_{it} = \begin{cases} -q \int_{E_{CNL}}^{E_F} D_{it}^A(E) dE & \text{for } E_F \text{ above } E_{CNL} \\ +q \int_{E_F}^{E_{CNL}} D_{it}^D(E) dE & \text{for } E_F \text{ below } E_{CNL} \end{cases} \quad (2.54)$$

E_{CNL} is the charge neutrality energy level below which the states are considered as donor levels and above which as acceptor levels. As the last section, for donor and acceptor interface trap densities, $D_{it}^{D,A}$ (states/cm².eV) we used the model presented by [Mic 08].

$$D_{it}^{D,A}(E) = D_{it0} \exp\left(\frac{|E - E_{CNL}|}{E_{0A,0D}}\right) \quad (2.55)$$

D_{it0} , $n_{A,D}$ and $E_{0A,0D}$ are adjustable parameters fitted with experimental measurements presented by [Hor 13]. Finally, we took the typical fixed oxide charge density for Al₂O₃.

2.5.2.3 Implementation

Eq.2.49 has been discretized using the finite difference approximation and solved iteratively to calculate the gate voltage and the corresponding 2DEG concentration.

$$E(y_0) = -\left(\frac{V(y_0 + h) - V(y_0)}{h} + R_1(y_0)\right) \quad (2.56)$$

y_0 is the point where the derivative is evaluated, $R_1(y_0)$ is the rest of the Taylor series which is considered as negligible.

The iterative method is presented in *Figure 2.20*. We assume an arbitrary 2DEG density initial value and an arbitrary zero potential at the hetero-interface. So we get with an initial value problem, which has been resolved using Euler Method. Then, we calculate the surface potential and subsequently the gate voltage. This flow is iterated until finding the desired gate voltage.

Finally, the results obtained can be summarized as follows: the total density & ionization traps profiles, the potential /electric field distribution in the barrier, the total charges and the behavior of 2DEG concentration responding to gate voltage. The main advantage of this implementation is manifested by its implementation simplicity mostly without convergence problems compared to a complete numerical solution carried out on the nonlinear Poisson equation. The implementation was done using an object-oriented programming using Matlab program and the general flow is presented in Appendix A. Above all, we also present in Appendix B an essay of an analytical formulation in order to model volume traps.

2.5.3 Theoretical results with a single traps level

As mentioned before, to get closer to the real case, we restricted this study to the case of Oxygen in the barrier. Therefore the model will contain only one donor trap level. This case study could be used for other purposes in the case of several trap energy levels or even for donors.

2.5. OXYGEN TRAPS IN THE ALGAN BARRIER AND THE WEIGHT BETWEEN INTERFACE AND BARRIER TRAPS

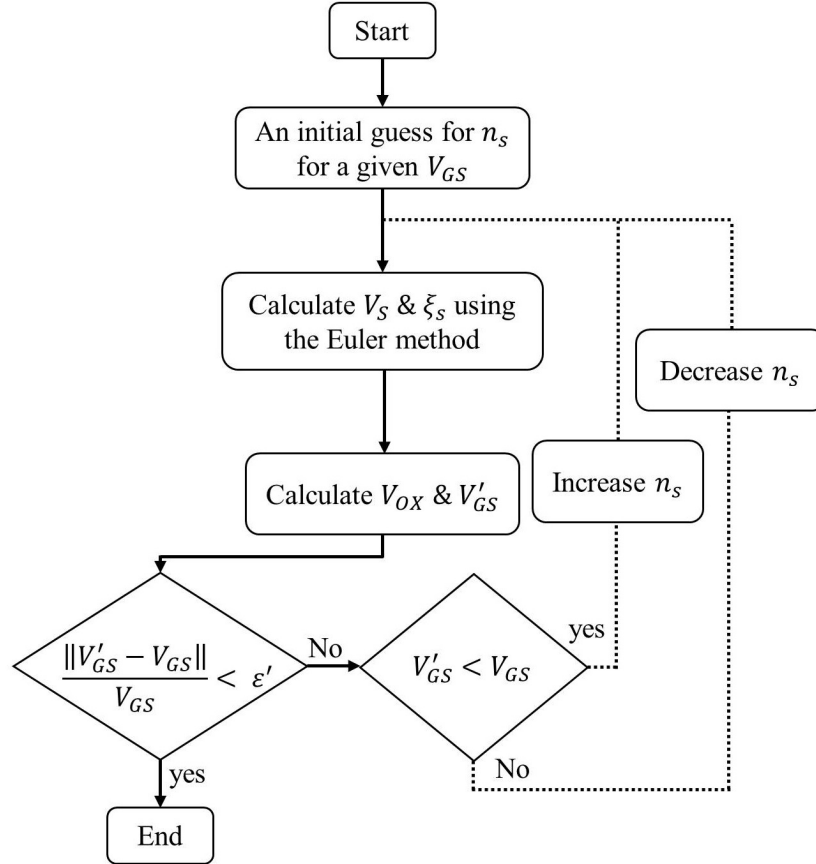


Figure 2.20: Iterative method to find the corresponding V_{GS} . ϵ' is equal to 0.1%.

Table 11 gives the model parameters values. Concerning interface traps, we have used the experimental results performed by Hori et al. [Hor 13] to make a comparison between the weight of bulk and interface traps in the case of existence and absence of a surface treatment. It should be noted that surface treatment was carried out using a radical N_2O treatment. Its experimental results give the values of the interface traps before and after this treatment.

Parameter	Description	Value
$N_{TD}(m^{-3})$	Homogeneous Oxygen-donor density (Mean value from SIMS)	2×10^{24}
$E_{TD}(e.V)$	Oxygen-donor level (DLTS)	0.44
$d_{OX}(nm)$	Al_2O_3 thickness	30
$d_{AlGaN}(nm)$	AlGaN thickness	25
$d_{GaN}(\mu m)$	GaN thickness	1
$x_{Al}(nm)$	Aluminum concentration in AlGaN	25%
$L(\mu m)$	Gate length	2
$W(mm)$	Gate width	100
$T(K)$	Temperature	300
ϵ_i	Al_2O_3 relative permittivity	9
ϵ_s	AlGaN relative permittivity	10.3
$E_{CNL}(e.V)$	Charge neutral level [Hor 13]	-1.1

2.5. OXYGEN TRAPS IN THE ALGAN BARRIER AND THE WEIGHT BETWEEN INTERFACE AND BARRIER TRAPS

$D_{it0}(cm^{-2}e.V^{-1})$	Density of interface states - Worst case (Without surface treatment)	1×10^{12}
$D_{it0}(cm^{-2}e.V^{-1})$	Density of interface states - Best case (With surface treatment)	5×10^{11}
$N_C(cm^{-3})$	Effective density of states	3.012×10^{18}
$N_{OX,bulk}(cm^{-3})$	Fixed oxide states of Al_2O_3	$-3.8 \times 10^{18} cm^{-3}$
n_A, n_D	Adjustable parameters to fit experimental results [Hor 13]	1.9, 1.9
$E_{0A}, E_{0D} e.V$	Adjustable parameters [Mic 08]	0.6, 1.52

Table 2.4: Model parameters

2.5.3.1 Potential distribution

Using the model, *Figure 2.21* gives the low level of the conduction band (E_C) obtained from the potential distribution throughout the AlGa_N barrier for different gate voltage from -4V to +3V.

However, we note that as the gate voltage increases, the band bending decreases that leads to traps neutralization and thus a reduction of the charge trap density as well as of the 2DEG concentration. It can be noticed that for a gate voltage of 3V, the potential is almost linear which reflects the non-existence of charges in the barrier.

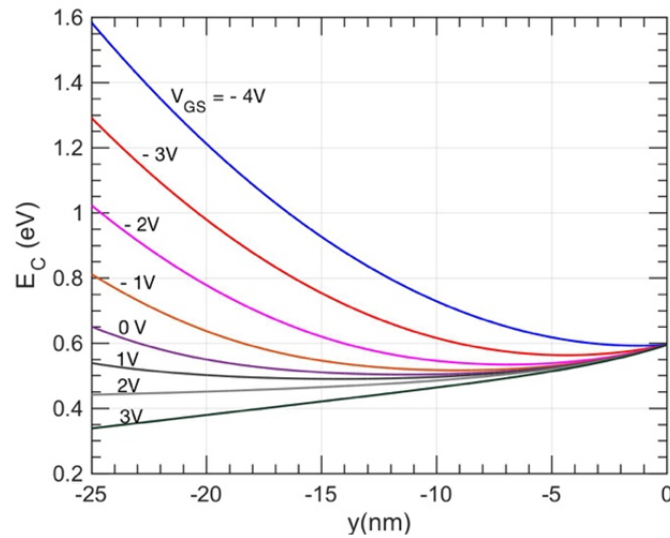


Figure 2.21: Potential distribution throughout the AlGa_N layer for a V_{GS} range from -4V to 3V.

2.5.3.2 Ionized traps profile distribution

As results, the effect of the gate bias on the ionization/neutralization behavior of the traps is given in the following. In *Figure 2.22*, it can be seen the effect of the gate voltage on the ionization distributions of Oxygen within the AlGa_N layer.

2.5. OXYGEN TRAPS IN THE ALGaN BARRIER AND THE WEIGHT BETWEEN INTERFACE AND BARRIER TRAPS

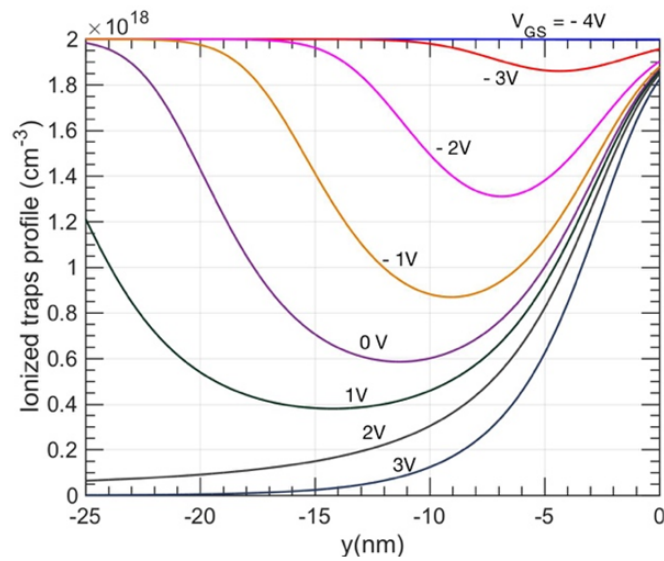


Figure 2.22: Ionized traps profile throughout the AlGaN layer for a V_{GS} range from $-4V$ to $3V$.

As expected, we can observe that for the most negative values of V_{GS} , almost all trap centers are ionized and we find the totality of the Oxygen density (N_{TD1} or N_{TD} as we study only one level). As the gate voltage increases, a small fraction of the distributed Oxygen becomes neutral as the trap energy level approaches or falls below the Fermi level. It should be noted that the minima of the energy conduction band corresponding to the minima of ionized density. When the Fermi level is above the Oxygen level, two regions (ionized and neutral) are formed. The transition between these regions is governed by the Fermi distribution function at 300K for our calculations.

2.5.3.3 Electric field distribution

The corresponding electric field distributions, taking into account the ionization profile, is shown in *Figure 2.23* where we can observe the following points:

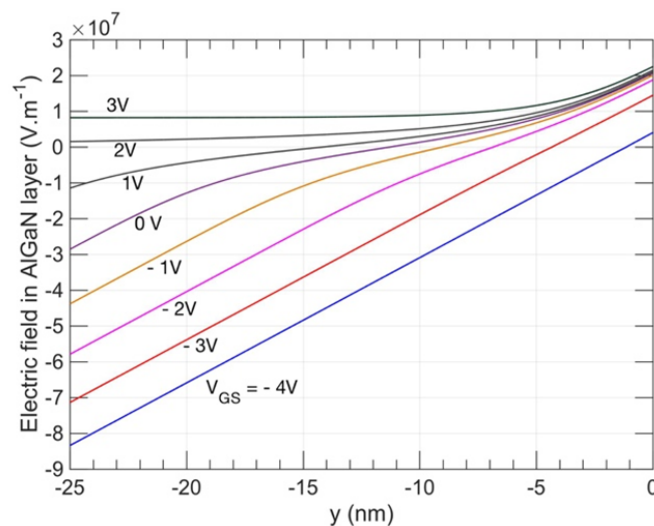


Figure 2.23: Electric field distribution throughout the AlGaN layer for a V_{GS} range from $-4V$ to $3V$.

2.5. OXYGEN TRAPS IN THE ALGAN BARRIER AND THE WEIGHT BETWEEN INTERFACE AND BARRIER TRAPS

- The electric field slope is almost the same for all curves closer to the hetero-interface. Accordingly, with what has been observed for the ionization profile, there are always ionized traps close to this region.
- For low 2DEG density ($2.35 \times 10^{11} \text{ cm}^{-2}$, corresponding to $V_{GS} = -4V$), the electric fields are almost linear, coherent with a total ionization of the traps density throughout the barrier.
- Finally, for high 2DEG density ($1.28 \times 10^{12} \text{ cm}^{-2}$, corresponding to $V_{GS} = 3V$), we find a constant electric field for a part of the barrier near the Oxide/AlGaN surface, which implies the nonexistence of these charges in this region. So traps in this region are not ionized.

2.5.3.4 Relative weight between Q_{it} and Q_{HEMT}

As explained earlier, the studied device has been realized by neutralizing as much as possible the interface states density. The model is used here to estimate the relative weights between interface states and Oxygen traps. The theoretical results will indicate which traps source will be dominant for different gate polarization conditions. Furthermore, the effect of surface states is given by considering both the worst case (without any surface treatment) and the best case (with surface treatment). The N_2O surface treatment has been performed by Hori et al. [Hor 13] on a very similar structure ($Al_2O_3/AlGaN/GaN$) than ours. Their measurements are used here to perform some comparisons.

As results, *Figure 2.24* and *Figure 2.25* give the dependence of the charges and the gate voltage respectively without and with surface treatment. The absolute values of both interface charges (Q_{it}), the heterostructure charges ($Q_{HEMT} = Q_T^s - qn_s$) and the total charges ($Q_{it} + Q_{HEMT}$) are shown respectively in blue, red and black curves.

The peaks denote the change of sign of these charges. In these figures, it can be observed that:

- Concerning interface traps, the change in sign of the charges occurring at $-2.51V$ (where the Fermi level coincides with the neutral level) reflects the change of state of the ionized interface traps density from donors to acceptors. At this point, the charges which dominate the heterostructure charges (Q_{HEMT}) is instead the ionized positive Oxygen charges ($Q_T^s \gg qn_s$), so the total charges at this level is estimated to be equal to the ionized trap surface charge in AlGaN (Q_T^s)
- Then, with the increase in gate voltage, the interface charge increases in negative values. In the same time, the 2DEG density increases and ionized traps decreases in such a way that the total charge decreases until it vanishes when charge equilibrium is reached between positive charges (Q_T^s) and negative charges ($Q_{it} - qn_s$).
- Then, by further increasing the gate voltage, the 2DEG density (n_s) rises whereas the Oxygen ionized traps (N_{TD}^+) is reduced. This situation leads to the minima of the heterostructure charges (Q_{HEMT}). At this point, the total charge is only constituted by the high negative interface trap charge.
- Beyond this point, it takes place a very high negative total charge due to both a high negative interface charge (Q_{it}) and a high 2DEG density ($-qn_s$).

2.5. OXYGEN TRAPS IN THE ALGAN BARRIER AND THE WEIGHT BETWEEN INTERFACE AND BARRIER TRAPS

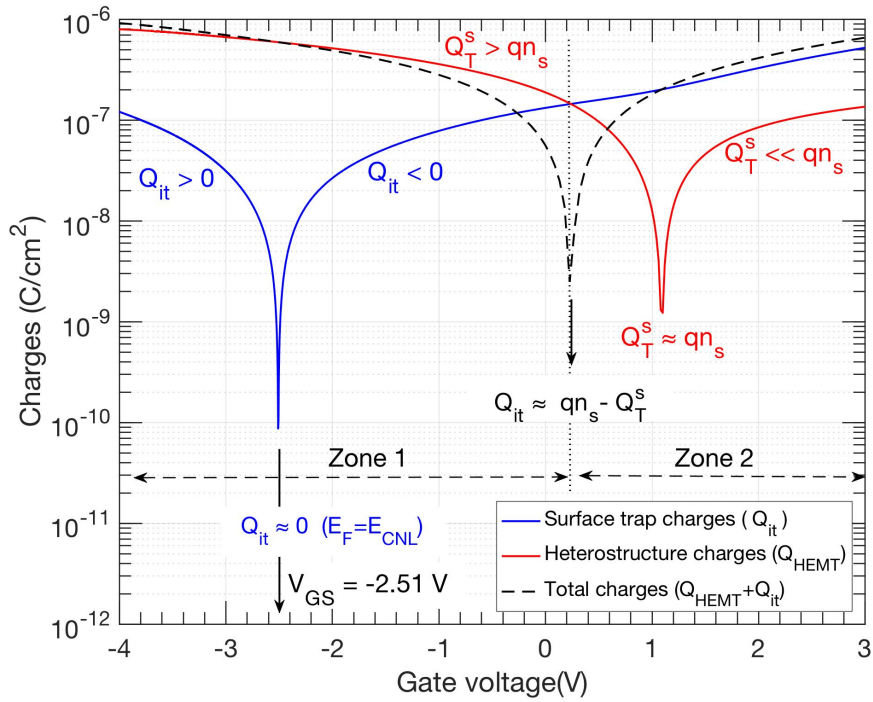


Figure 2.24: Interface trapped charges, HEMT charges, and total charges function of the gate voltage for HEMT with surface treatment.

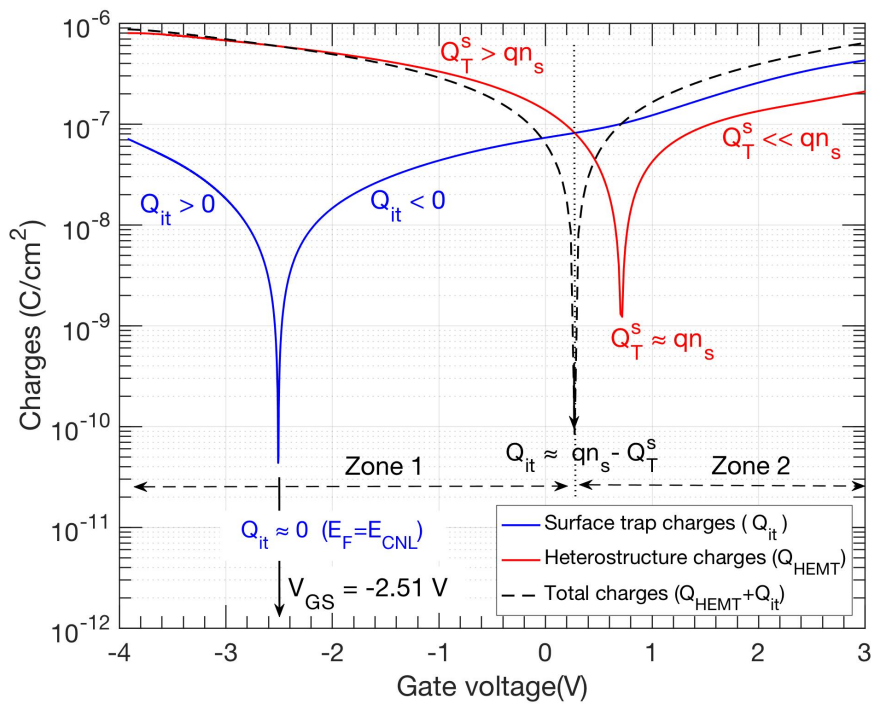


Figure 2.25: Interface trapped charges, HEMT charges, and total charges function of the gate voltage for HEMT without surface treatment.

2.5. OXYGEN TRAPS IN THE ALGAN BARRIER AND THE WEIGHT BETWEEN INTERFACE AND BARRIER TRAPS

We note that there is no domination of traps effect either of the barrier or the interface in an absolute way. There is rather gate voltage zone where barrier traps are dominant (zone 1) and other where the interface traps are dominant (zone 2). However, for a surface treatment case (*Figure 2.25*), we note that even with an interface trap density of $1 \times 10^{12} \text{states}/\text{cm}^{-2}$ near the bandgap extremities, the effect of interface traps is much reduced.

2.5.3.5 Nonlinear dependence of 2DEG density with gate voltage

Finally, we present the relationship between the 2DEG concentration and the applied gate voltage. A non-linear behavior of the 2DEG is observed for this relationship.

In *Figure 2.26*, this dependence is plotted for two values of Oxygen densities ($N_{TD} = 1.10^{18} \text{cm}^{-3}$ and $N_{TD} = 2.10^{18} \text{cm}^{-3}$) to show the influence of this density. For each N_{TD} value, results are given without interface traps (blue curve), with low interface traps (surface treatment, red curve) and with high interface traps (no surface treatment, black curve).

From this figure, we can observe the following, based on the charges-gate voltage relationship (sub-section 2.5.3.4):

- The higher the Oxygen traps density, the more negative the threshold voltage, which can be defined for densities of the order of some $1 \times 10^{11} \text{cm}^{-2}$
- The three curves, with different interface trap levels, coincide with the point where the interface charges are negligible ($E_F = E_{CNL}$). For $N_{TD} = 2 \times 10^{18} \text{cm}^{-3}$, this occurs for $V_{GS} = -2.51V$, whereas for $N_{TD} = 1 \times 10^{18} \text{cm}^{-3}$ it is for $-1.25V$.

It can also be observed three main regions depending on the gate voltage:

- For low gate voltage values, the relationship is almost linear governed mainly by the positive charges of ionized bulk traps (Oxygen).
- Then, for intermediate voltages, a plateau on the 2DEG density is reached due to the negative charge compensation from interface traps. This has also been observed by [Dan 99].
- Beyond this plateau, and for positive gate voltages, we found the second step with a rise of the 2DEG density. The positive charges in the gate induce this second step. This latter charge is more or less compensated by interface charge when it exists. So, the lower the interface charge, the lower the compensation and therefore the higher the 2DEG density increase. The ideal case of no interface charge (blue curves) gives rise to the highest increase in the 2DEG.

In *Figure 2.27*, it can also be observed the ideal case of a shallow level of barrier traps. We found that for a density of 2×10^{17} (10x times of ameliorated barrier) there is almost no effect of the barrier traps on the 2DEG concentration, threshold voltage has shifted in positive values, and the interface traps purely dominate the behavior.

2.5. OXYGEN TRAPS IN THE ALGAN BARRIER AND THE WEIGHT BETWEEN INTERFACE AND BARRIER TRAPS

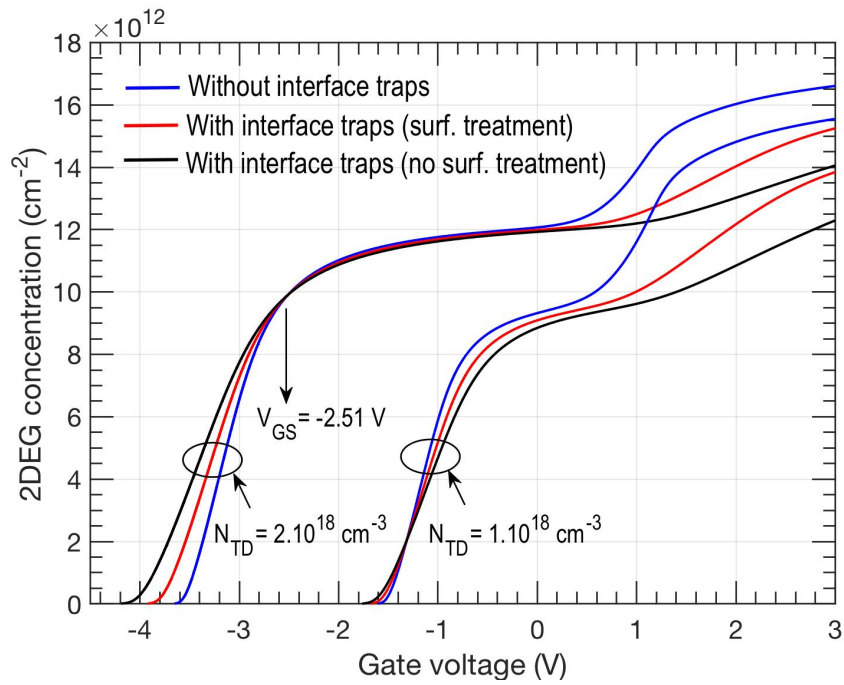


Figure 2.26: 2DEG concentration function of the gate voltage for two values of barrier trap density ($2 \times 10^{18} \text{ cm}^{-3}$ and $1 \times 10^{18} \text{ cm}^{-3}$).

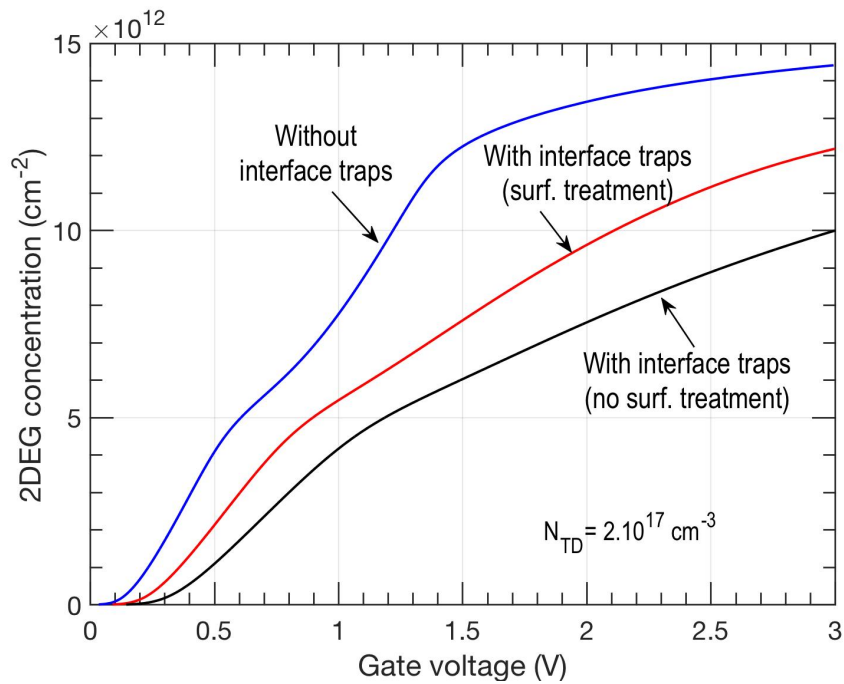


Figure 2.27: 2DEG concentration function of the gate voltage for a low density of barrier traps.

2.6 Conclusion

The problem of traps remains the most compelling for these new components. A theoretical study has been presented in this chapter to participate in the understanding of the behavior of these traps. A new semi-analytical model has been presented in order to estimate the behavior of the barrier Oxygen traps and its effect on the potential and electric field distributions throughout the AlGa_N layer. The model was used specifically to investigate the weight between surface and heterostructure charges (including barrier traps) on the 2DEG density for different gate bias points. We applied it on a fabricated structure Al₂O₃/AlGa_N/Ga_N on Si substrate.

Concerning the input parameters for the model, The Oxygen traps parameters were used from experimental measurements while the interface traps were taken from the literature for a similar device with and without an N₂O radical surface treatment. All the steps of integration and modifications in the model have been explicit in this chapter.

The results showed that there is no absolute dominance of interface traps or barrier traps, but depending on the polarization conditions the weight of these traps change. It has also been observed a variation of the threshold voltage, this variation is strongly due to the traps in the barrier layer while the interface traps have a very important effect for high values of gate voltage. It has been shown that in the case of a surface treatment ($D_{i0} = 5 \times 10^{11} \text{cm}^{-2} \text{e.V}^{-1}$), the barrier traps manifest clearly on the total charges behavior. We have also shown that the non-linear relation between the gate voltage and the 2DEG density depends on the different trap densities and the gate polarization condition either for the interface or the barrier.

This model can be more developed to estimate the effect of the 2D traps on the On-state resistance in order to study thereafter the effect of the polarization of the drain on the distribution of ionized charges in the structure. It can also be used to calculate the drain source current in the linear regime of the I-V characteristics by this simple relation $I_{DS} = qW\mu_n s$ after taking into account the horizontal potential distribution along the channel due to the drain polarization. It may also be useful to calculate the gate capacitance respond to the applied gate voltage.

The results of this chapter were published in [Zak 18a].

Chapter 3

Traps characterization of commercial components GaN Systems Inc.

3.1 Introduction

Trapping phenomena present a real problem hindering the proper functioning of HEMT devices. Their effects are reversible and act on the electrothermal behavior of the devices. They can have several effects on the static and transient electrical characteristics of the device. Since these traps are usually introduced unintentionally with high densities, they can lead to significant disparities in the behavior of the components with the same manufacturer's reference. The traps located under the gate can cause a significant shift in threshold voltage. The traps located between the drain and the gate can have a direct effect on the 2DEG density, on the I-V characteristics and the ON-state resistance. In the transient mode, we can observe significant transient current variation in response to a change in polarization state of the gate or the drain. As explained in chapter 1, we can subsequently find either gate or drain lag.

In order to properly use these components, we must explicitly understand the behavior of these traps and quantify their effects under different polarization and temperature conditions. In this chapter, we present a detailed experimental study of traps for GaN Systems Inc. commercial switching devices. The study aims to understand the behavior of traps in these devices and to present a characterization methodology that will be used in chapter 4 to evaluate the effect of ageing on the traps evolution.

However, for this purpose, we present experimental measurements based on two well-known electrical methods: the reverse polarization quiescent point method and the transient current measurements method. The first one was used to identify the traps relevance without extracting their physical parameters.

The second method refers to that presented in the transient drain current measurements of chapter 1 (based on the multi-exponential analysis). For these measurements, we will present the test bench and the equipment used to perform them. We will also present a methodology that aims to study the ability to detect and characterize these trapping parameters, on a large scale of time constants, as a function of the OFF-Stress Time (OST) of the applied gate voltage. The junction temperature measurements were carried out using a fiber optic thermal sensor to verify that the self-heating remains negligible during measurements. To extract the traps physical parameters, i.e., activation energies and cross sections, the signal decomposition based on the Prony algorithm was used to extract time constants and was supplemented by the Shockley-Read-Hall model to extract the parameters of the traps. We will also present the signal processing flow performed before extracting the time constants including filtering, smoothing, and decimation. Some drain and gate lag transients measurements will also be presented with temperature dependence to explain the trapping behavior.

3.2 Highlighting traps

It is possible by technological improvements to significantly reduce the traps densities and their effects. Therefore, we must always check whether there are traps in the structure and whether their effects are relevant. This step is sometimes necessary to have a quick idea if there is a need to go to perform transient current measurements. The transient current measurements are quite slow and take many steps of analysis and signal processing. However, this step can be performed using several characterization techniques. One of the best known - which will be used in this chapter - is the reverse polarization method. However, this method may also be used to extract some electrical parameters shifts due to traps.

The method involves changing the gate or drain polarization point in the OFF state while observing the effect on the pulsed I–V electrical measurements. The parameters of these pulses can be summarized as follows; during the OFF state, the gate and the drain are biased at V_{GSQ} & V_{DSQ} respectively, these polarization are also called gate and drain quiescent bias point respectively. Then, a positive gate pulse is applied above the threshold voltage, it is followed by a drain voltage pulse after a time delay T_D . Measurements are performed during the ON state during a time (measurement time) T_m . We always consider only the mean value of the last ($T_m=20 \mu s$) of the measured transient current. V_{GS} & V_{DS} are also the polarization levels in the ON–state. The sampling rate of the used analyzer is $2 \mu s$, therefore $20 \mu s$ allow us to take the average of 10 measurement points.

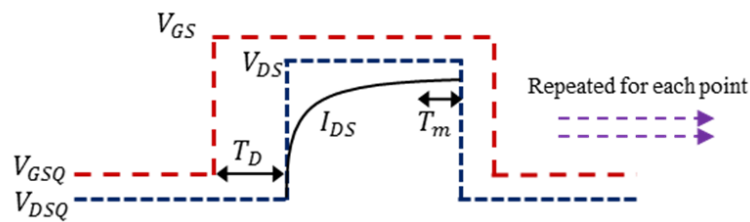


Figure 3.1: Double pulse parameters.

The values of the used parameters in the next performed measurements are presented in the following table.

Parameters	Corresponding values
T_D	$50 \mu s$
T_D	$20 \mu s$
V_{DSQ}	0 V (In these measurements we want to study only the effect of the gate lag)
V_{GSQ} (several I-V characteristics)	(-6 to 0) V with a step of 2V
Drain pulse width	$100 \mu s$
Gate pulse width	1 ms
V_{GS}	3V
Temperature	From $10^\circ C$ to $80^\circ C$

Table 3.1: Parameter values used during pulsed measurements

As shown in *Figure 3.2*, the measurements performed on GaN Systems devices for the traps detection is presented. Even if the difference between the polarization for the drain (between the ON and OFF)

states is not high, we can also affect due to traps located in the gate–drain region. The presented measurements are performed for only two temperature values (10°C and 80°C). However, it is undoubtedly noticed that there is an effect of changing the polarization point of the gate bias on the electrical characteristics of the two temperatures 10 °C and 80 °C. We can see that the ON–state resistance increases with temperature. An increase in the saturation level of the current without modification of the slope at the origin by increasing V_{GSQ} was also observed.

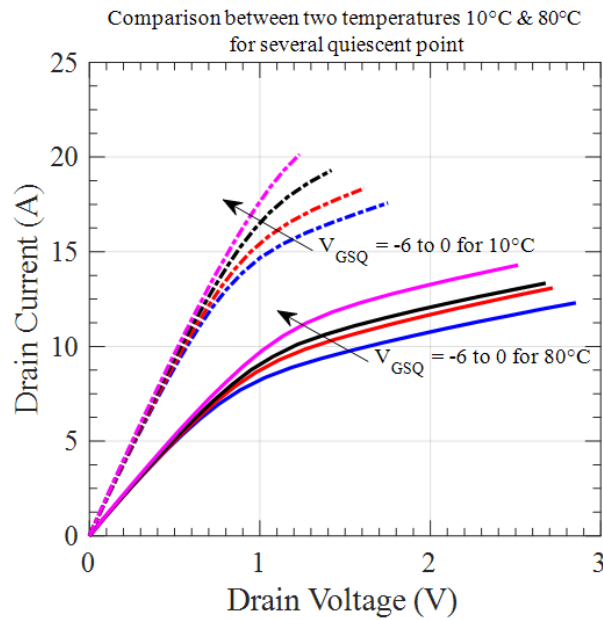


Figure 3.2: I – V measurements with different quiescent points (V_{GSQ}) -6V (blue) to 0V (magenta) with step of +2V at two temperatures 10°C & 80°C.

After highlighting trap effects, we will now try to understand more deeply the traps behavior and their effects under different polarization and temperatures conditions.

3.3 Transient Current measurements & extraction of traps parameters

Here, we will present the well-known measurement method. We will explain how we proceed for the traps parameters extraction, describe the test bench used and we will analyze the experimental results. We present new results that have not yet been presented, in our knowledge, in the literature for commercial power GaN devices of GaN Systems. The transient current measurements have manifested itself as a simple electrical method that can offer quantitative information on the activation energies and cross sections of traps. Although this method is often used in literature, it has some limitations. We start with the difficulty of time constants extraction especially when an overlap between several time constants occurs. The method is sometimes imprecise since the time constants are always estimated according to the SRH model leading to errors in activation energies extraction. There are also some parameters that cannot be extracted with this method like the traps density. Furthermore, it must be added the difficulty of locating the traps in the structure. It is tough to know whether the characterized traps are localized in the AlGa_N or GaN layer using an electrical characterization method. However, some authors – as said in chapter 1 – have located traps according to their activation energies. They rely on the

nature of the possible signature and the possibility of being introduced in a different layer. Most of the methods used to locate traps and quantify their density are in general optical methods like (SIMS or electro photoluminescence).

3.3.1 Methodology

As shown in *Figure 3.3*, the traps Characterization methodology can be divided into three essential parts.

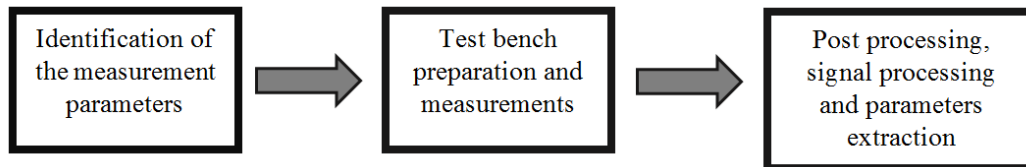


Figure 3.3: Process steps of the methodology.

3.3.1.1 Identification of the measurement parameters

- The time scale of a single measurement:

It is essential to define the range of time constants to be detected, we cannot detect the traps time constants on all time scales. In general, traps have deep levels in the bandgap, and therefore they are still believed to have relatively high time constants between ($\sim 1\text{ms}$ to $\sim 100\text{s}$).

- Temperature range:

To estimate the traps activating energies and the cross sections, it is necessary to extract them by the Arrhenius law presented in chapter 1. The time constants as a function of the temperature are necessary; the wider the temperature range with many temperature points, the more precise are the physical parameters of the traps.

- Timeout:

The rest time needed for each measurement must be rigorously defined so that the component returns to the initial state.

- Applied stress parameters (polarization levels, OFF– Stress Time,...):

The polarization levels in the OFF and the ON states and the applied stress time must be defined. The most severe polarization (within the limits of the DUT characteristics) must be used, so as not to degrade the DUT during measurements. We have grouped the parameters of the applied stress as follows.

Parameters	Descriptions
$V_{GS_{OFF}}$	Applied Gate voltage in the OFF-state.
$V_{GS_{ON}}$	Applied Gate voltage in the ON-state.
$V_{DS_{OFF}}$	Applied Drain voltage in the OFF-state.
$V_{DS_{ON}}$	Applied Drain voltage in the ON-state.
$I_{DS_{on}}$ limit	Drain current limit; this limit ensures the neglect of the self-heating during the measurements.
Sampling interval	Multiplying the sampling interval by the measurement points number gives the total duration of the measurement.
OFF Stress time	The stress application time in the OFF state.

Table 3.2: Applied stress parameters

3.3. TRANSIENT CURRENT MEASUREMENTS & EXTRACTION OF TRAPS PARAMETERS

These parameters are illustrated in *Figure 3.4*. However, the change in these parameters will modify the trap response. An increase in the duration of the OFF state leads to the detection of traps having longer emission or capture time constants; the stress level can also change the traps signature since more traps will be more or less activated. In this chapter, for each measurement, we will present the applied stress parameters.

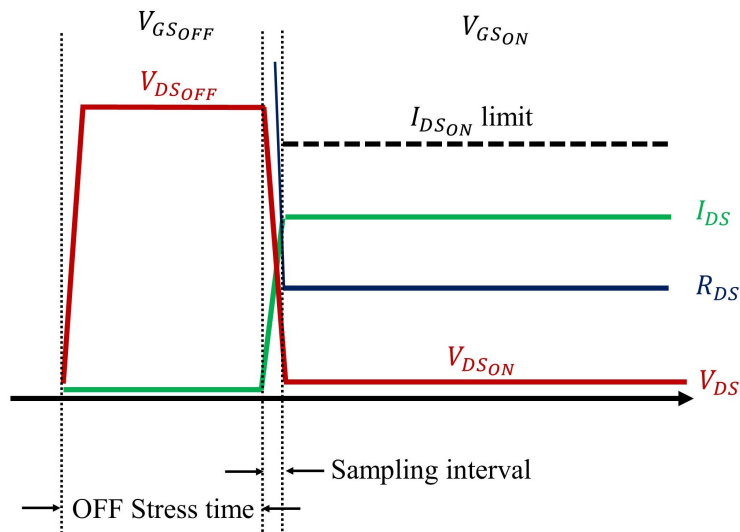


Figure 3.4: Applied stress parameters.

As a concrete example of the real type of data that can be interpreted. The following figure (*Figure 3.5*) shows the transient measurement of current and on-resistance after the application of 200V on the drain-source terminals for 1 second. Extraction of trap parameters could be carried out either by resistance measurement or by current measurement.

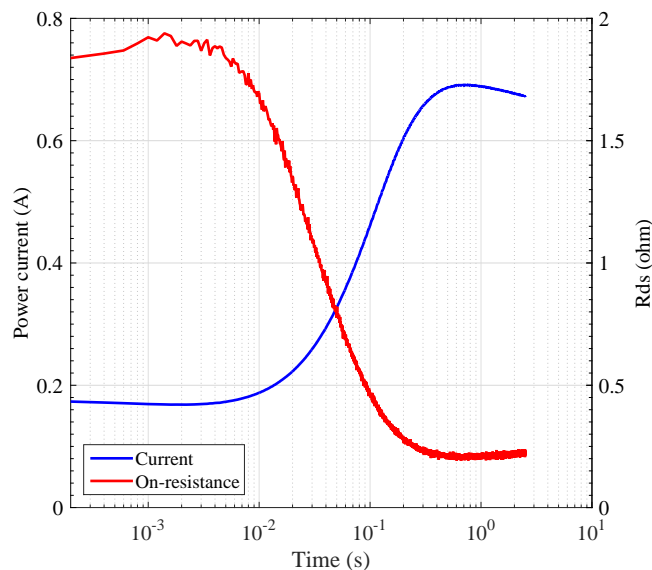


Figure 3.5: Example of real type measured transient current and on-resistance.

3.3.1.2 Test bench preparation and measurements

- Temperature stabilization and homogenization: Since the transient measurements are carried out with temperature steps, one has to verify the homogenization of the temperature for the component and the surrounding environment at each step. Temperature fluctuations during measurements can induce erroneous results. Similarly, between the step changes, one must define a time according to the manipulation to achieve the thermal stabilization at the device level.
- Self-heating: These measurements are very likely to be disturbed by self-heating induced by the transient current. One must verify that it is negligible by a direct or indirect measurement of the junction temperature.
- Avoiding any fluctuations: Avoid all sources of fluctuations such as long lengths of power and measure cables, decrease the noise on the power sources and use the accurate measuring device with high sampling rate.

3.3.1.3 Post processing, signal processing and parameters extraction:

- Undersampling some measurements data:
Sampling during measurements is always carried out with a linear step. Therefore there are measured data useless on the qualitative and quantitative results. It is, therefore, necessary to define the zones to carry out an undersampling.
- Smoothing and filtering: The signal to be processed must be filtered and smoothed since the algorithm used is very sensitive to noises.
- Parameters extraction: Fit the original transient signal by multi-exponential signals, extract the corresponding time constants and finally draw Arrhenius law and extract the physical parameters.

Now we present the applied methodology on our measurements; we start with the description of the test bench developed and used.

3.3.2 Test bench and equipment:

3.3.2.1 Global system:

As shown in *Figure 3.6*, the system consists of a Power Device Analyzer "Agilent B1505A Power Device Analyzer / Curve Tracer" which contains five different source-measure units (SMUs). They are high voltage, high current and 3 Mid-current SMUs. These SMUs are associated with an ultra-high current expander "N1265A, Ultra-high current expander". The operating principles of this equipment are presented in Appendix C. A fast switcher is used which played the role of fast switching between the ON and OFF state. A thermo-regulator (air streamer) "TP04310" that allows sweeping the temperature from -90°C to $+225^{\circ}\text{C}$ was used, it is based on blowing hot/cold air. A thermo-couple is connected to the device substrate and plays the role of feedback for temperature regulation. The device under test is placed in a well-insulated box to maintain a constant temperature inside. The box is designed to homogenize the temperature.

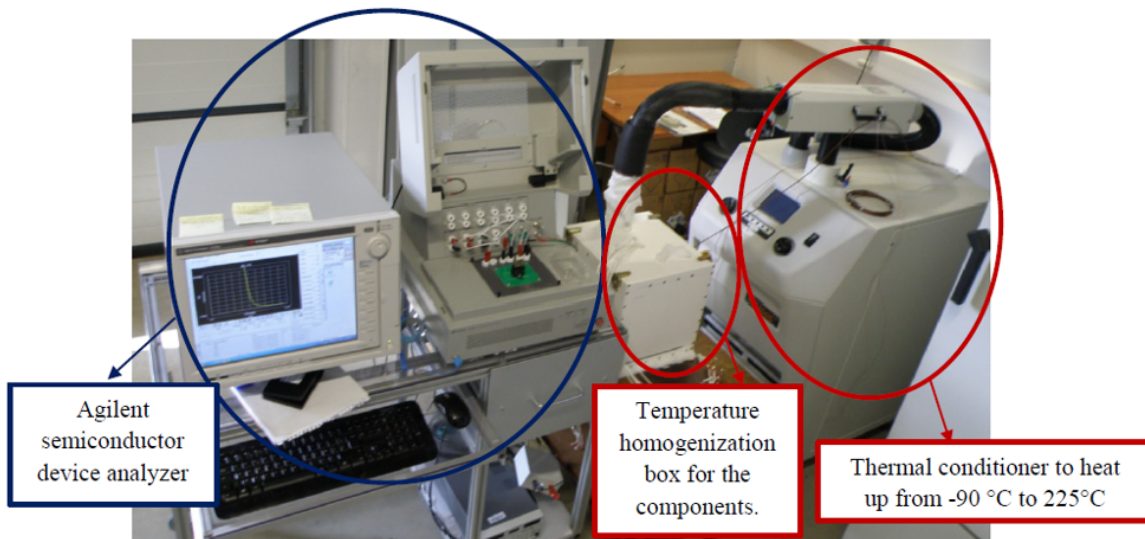


Figure 3.6: Different part of the overall system.

The GaN-HEMT power device under test is mounted on an aluminum substrate to ensure proper thermal conductivity. This substrate is mounted on a metallic plate using thermal grease to perform measurements in a controlled temperature environment. This metal plate is fixed on another plate elaborated to homogenize the blown air by the thermos-regulator. Finally, cables that hold high temperatures were used to connect with the component under test.

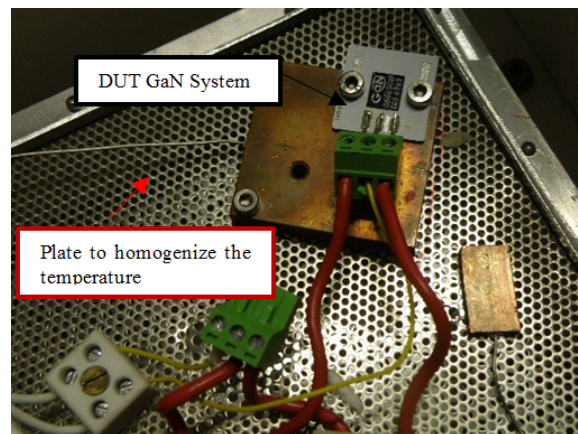


Figure 3.7: Fixed DUT in the temperature homogenization box.

3.3.2.2 Fast switcher:

One of the essential equipment used in these measurements is the N1267A HVSMU/HCSMU fast switcher. The idea is to switch very promptly between 2 SMUs; the first SMU is the high voltage SMU (HVSMU) which offers the high voltage in the OFF state on the device terminals. This SMU offers a very limited current which does not exceed 8mA, therefore in the ON state, this SMU will not be sufficient to supply the drain current. The second SMU is the high current SMU (HCSMU), which plays the role of supplying the current in the ON state. This system allows to apply very high voltages in the OFF state which can reach up to 3 kV, thus detecting the traps within the limits of the device characteristics.

3.3. TRANSIENT CURRENT MEASUREMENTS & EXTRACTION OF TRAPS PARAMETERS

As shown in the figure below, the system in the OFF and ON states. VHV is the applied voltage by this HVSMU, VHC is the applied voltage by this HCSTMU, $I_{d(off)}$ is the OFF current supplied by the HVSMU. The role of the diode used in *Figure 3.8* is explained in Appendix D (a part from the manual of the N1267A fast switcher).

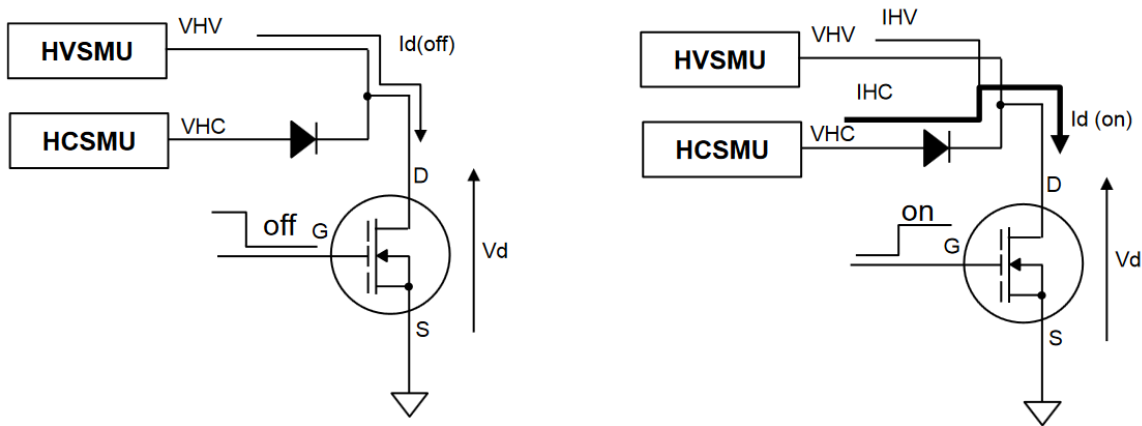


Figure 3.8: SMUs system in the OFF and ON state [Key 15].

The internal structure of this fast switcher and the connection with the DUT are shown schematically as follows. This switcher consists mainly of a transistor which performs the switch operation between the two SMUs. This switcher is well controlled by another SMU that comes from the power analyzer. A MCSMU performs the control of this transistor, or the voltage drop across the SMU is presented by $V_{SwitchControl}$. In addition to the SMUs used for the drain–source and which are connected to the switcher, there is another MCSMU which is used to polarize the DUT gate.

The system parameters can be summarized as follows:

Parameters	Descriptions
V_{HVSMU}	Voltage at the high voltage SMU terminal.
I_{HVSMU}	Current generated by the high voltage SMU terminal (It is limited to 8mA).
$V_{SwitchControl}$	Voltage at the mid-current SMU terminal (which controls the fast switcher transistor).
$I_{SwitchControl}$	Current generated by mid current SMU terminal.
V_{Gate}	Voltage at the mid-current SMU terminal.
I_{Gate}	Gate current of the DUT.
V_{HCSTMU}	Voltage at the mid-current SMU terminal (which controls the DUT).
I_{HCSTMU}	Current generated by the high current SMU terminal (It is limited to 8mA).
I or I_{DS}	DUT drain source current

Table 3.3: Internal structure of the fast switcher and the connection with the DUT parameters.

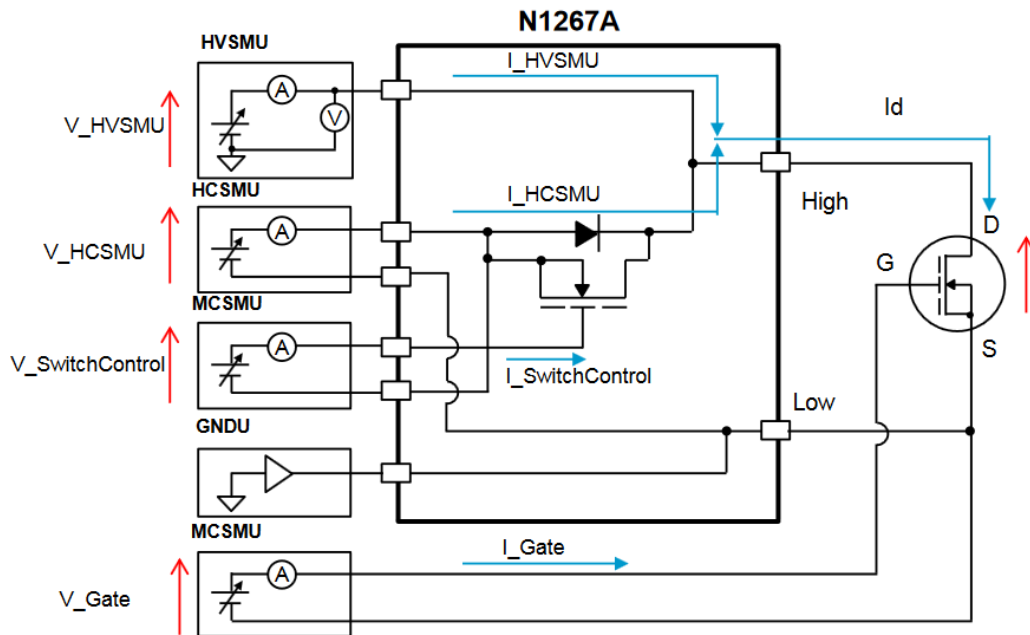


Figure 3.9: Internal structure of the switcher and connection with the DUT [Key 15].

3.3.2.3 Self-heating control:

Transient current measurements are recognized to be easily disturbed by the self-heating effect. The measured dynamic ON–state resistance may increase under this temperature effect. However, junction temperature measurements are always necessary to check its effect, especially if the transient current or the dynamic resistance is submitted to longtime measurements. This self-heating can lead to erroneous measurements as the temperature effect can synchronize with the effect of the traps. For our measurements, the main idea was to analyze a transient current lower than 1A to reduce the self-heating. However, to verify this hypothesis, as shown in Figure 3.10, the power device has been decapsulated to make the chip apparent and to measure its temperature by contact with a fiber optic thermal sensor.

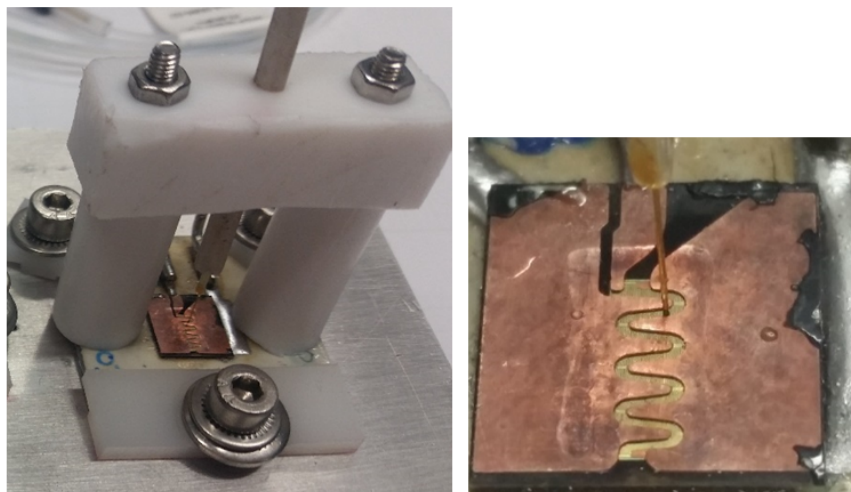


Figure 3.10: Decapsulated device for measuring a local temperature by optical fiber.

The diameter of the fiber is $70\ \mu\text{m}$ and allows a local temperature measurement with a time response about 1ms. Temperature measurements have shown that the self-heating effect for our measurements (Current $< 1\text{A}$) is almost negligible.

Optical microscope images of the decapsulated GaN Systems component are presented in Appendix E.

3.3.3 Experimental results

We now turn to the experimental measurements and their analyses. These experimental measurements go through several stages before extracting the traps physical parameters. First, the type of these measurements is transient current which depends on the sampling frequency and the points number of measurements to identify the total time of measurement. These measurements are carried out with temperature control and therefore by increasing the number of temperature points; we will have more precision for the parameters extraction. The noise is an essential factor which affects the measurements. Therefore, signal processing is almost necessary before using these experimental data. Finally, the extracted information is time constants that will be used to plot Arrhenius and finally to extract the traps parameters. We present an example of this parameter extraction which will be used here. The flow of the extraction is presented in the next diagram.

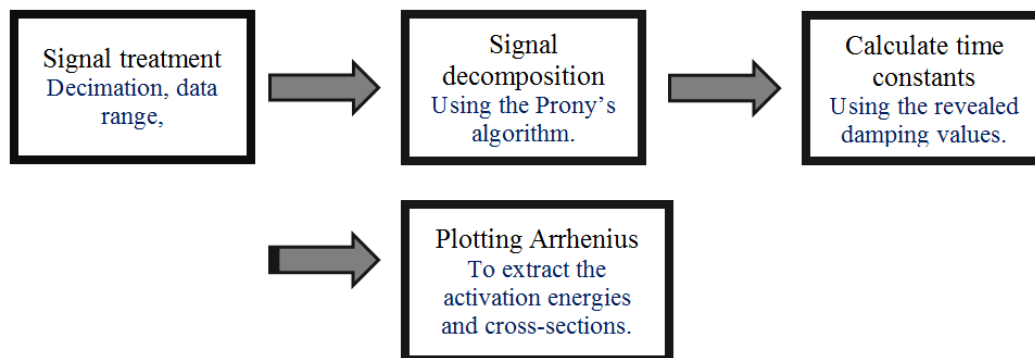


Figure 3.11: Trap parameters extraction methodology.

3.3.3.1 Signal processing:

This stage presents the step immediately after the transient current measurements; it consists of preparing the measured signals "without losing the information" before proceeding to the signal decomposition. This step consists of 3 small sub-steps: an example of this treatment is shown in *Figure 3.12*.

- Smoothing and filtering.
- Decimation: reducing the sampling rate of the measured transient signal.
- Data range: In some cases where the signal is composed of several observed exponential.

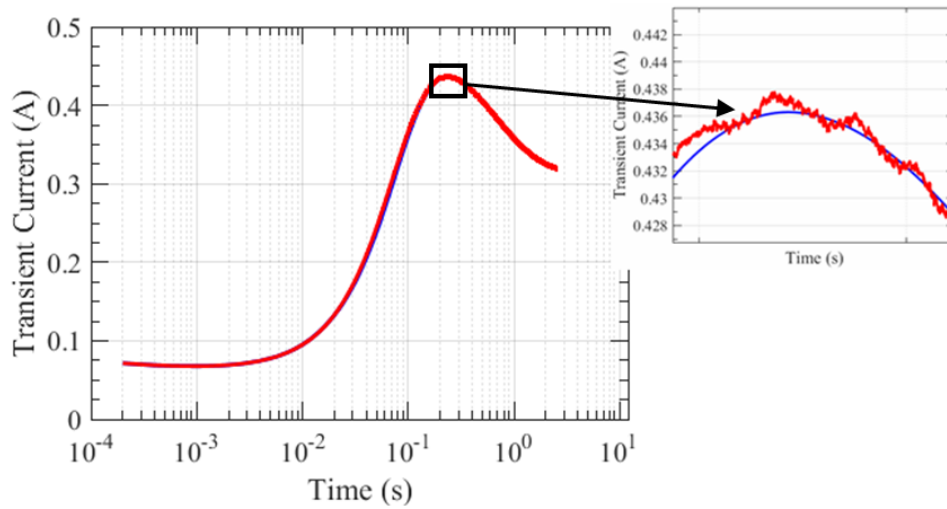


Figure 3.12: Red line shows the experimental measurements, blue line presents the filtered and decimated signal.

3.3.3.2 Signal decomposition:

The decomposition of the measured signal is performed using a mathematical algorithm. Among these algorithms, there is Prony method and Levenberg-Marquardt algorithm. We will present only the Prony algorithm which will be used in the decomposition of the signals during this thesis. The method is based on the decomposition of the signal into a series of damped complex exponential. This method is used to calculate the damping factors that are related to the time constants sought for traps. This method gathers to the Fourier signal decomposition but with estimating the damping factors. The signal may be decomposed as follows.

$$\hat{f}(t) = \sum_{i=1}^M \frac{1}{2} A_i e^{\pm j\phi_i} e^{\lambda_i t} \quad (3.1)$$

Parameter	Description
$\hat{f}(t)$	Fitted signal
M	Model order
A_i	Time-independent amplitudes
λ_i $\lambda_i = \sigma_i \pm j\omega_i$	Eigenvalues of the system, they are sometimes denoted z_i . σ_i is the damping coefficients, ω_i is the frequency components (for the case where there is a damped oscillation), j is the imaginary part.
ϕ_i	Phase components (for the case where there is a damped oscillation).
t	Time

Table 3.4: Prony method parameters.

This method is realized using algorithms implemented on Matlab©which is available free online. The two useful revealed information is the system eigenvalue and the corresponding amplitudes. For the case of traps time constants extraction, there are no sinusoids, the system is considered to be stable, and therefore we always take the real part of the eigenvalues. This part corresponds to real damping coefficients. In *Figure 3.13*, we show the poles and zeros of the eigenvalues and the different cases of

sinusoids. In traps extraction case, the extracted values are always on the abscissa axis. We can typically find positive or negative damping factors. These factors reflect different traps behavior (trapping or de-trapping).

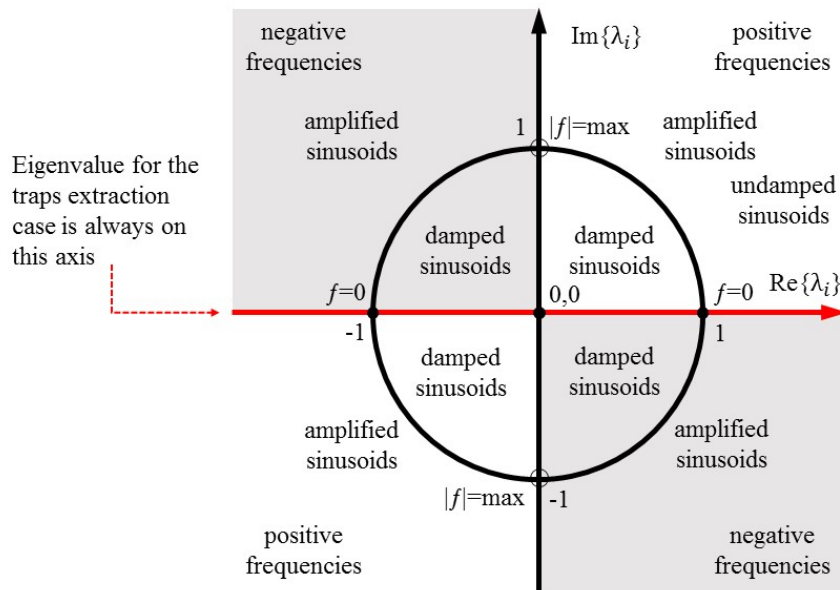


Figure 3.13: Vector z and its representation of frequencies and exponential coefficients in Prony's method.

As presented in chapter 1, the multi-exponential fit is used to decompose the measured transient current. The traps time constants are inversely related to the absolute value of the real part of the system eigenvalue.

$$\tau_i = \frac{1}{|\sigma_i|} \quad (3.2)$$

In *Figure 3.14*, an example of a measured, filtered, smoothed and fitted signal with the Prony method using the model with an order $M = 40$.

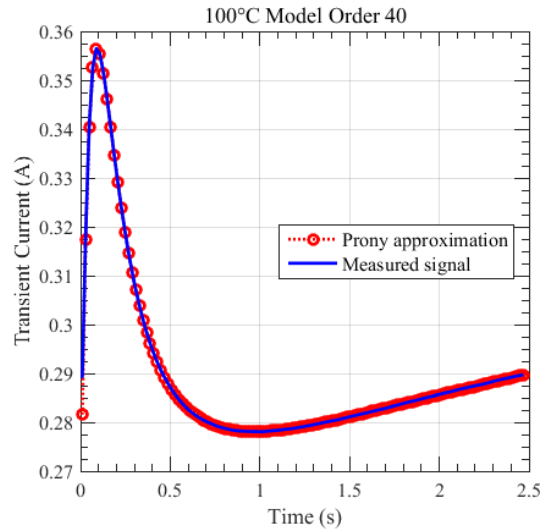


Figure 3.14: Comparison between the fitted signal estimated by Prony and the original signal, these drain lag measurements was carried out at a high temperature (100 °C) with a model order of 40.

These measurements are repeated at different temperatures to follow the evolution of these time constants. The time constants must strictly decrease with the temperature increase according to the SRH model. One of the limitations of this method is the identification of the time constants corresponding to the traps for each temperature. This difficulty arises from the overlap which may occur when several traps get involved. The time constants may overlap and the identification of the signature may be complicated.

3.3.3.3 Physical parameters extraction

After identifying the traps time constants, we now proceed to extract the physical parameters such as activation energies and cross-section. As explained in chapter 1, this step is performed by using an Arrhenius plot which is based on the activation energies and cross-section extraction from the SRH model. Eq.3.3 presents the final form of the emission rate used for parameters extraction, for more details, one can consult [Sch 06].

$$e_{ni} = \sigma_{ni} v_{th} N_C \exp\left(-\frac{E_C - E_{Ti}}{kT}\right) \quad (3.3)$$

e_{ni} is the emission rate for traps, σ_{ni} the corresponding cross-section, N_C the effective density of states in the conduction band, k the Boltzmann constant, T the Temperature v_{th} is the electron thermal velocity. The effective density of states can be written in the following form:

$$N_C = 2 \left(\frac{2\pi m_n kT}{h^2} \right)^{3/2} \quad (3.4)$$

m_n presents the electron density-of-states effective mass and h is the Planck constant. The thermal velocity takes the following form:

$$v_{th} = \sqrt{\frac{3kT}{m_n}} \quad (3.5)$$

The time constants can be finally written on the following form:

$$\tau_{ei} = \frac{1}{e_{ni}} = \frac{\exp\left(\frac{E_C - E_{Ti}}{kT}\right)}{\sigma_{ni} v_{th} N_C} \quad (3.6)$$

By adjusting equations 3.3, 3.4, 3.5 and 3.6, the following form can be found:

$$\tau_{ei} T^2 = \frac{\exp\left(\frac{E_C - E_{Ti}}{kT}\right)}{\sigma_{ni} \gamma_n} \quad (3.7)$$

γ_n takes the following form [Sch 06], for the GaN that has an effective mass of $m_n = 0.2m_0$, γ_n can be evaluated as $6.5 \times 10^{20} \text{ cm}^{-2} \text{ s}^{-1} \text{ K}^{-2}$. This value is used in all measurements made in this chapter.

$$\gamma_n = 3.25 \times 10^{21} \left(\frac{m_n}{m_0}\right) \quad (3.8)$$

Finally, Eq.3.7 can be written in the following form:

$$\ln(\tau_{ei} T^2) = \frac{E_C - E_{Ti}}{kT} - \ln(\sigma_{ni} \gamma_n) \quad (3.9)$$

So by drawing $\ln(\tau_{ei} T^2)$ as a function of $\frac{q}{kT}$, we fall with a slope that gives directly the activation energy and the intersection with the x-axis which gives a value equal to $\ln(\sigma_{ni} \gamma_n)$. In the next subsections, we present the experimental results.

3.3.4 Drain lag of the GaN Systems commercial devices

In our measurements, we present essentially two cases (high and low) sampling rate; this presentation is essential to detect relatively low and high time constants.

3.3.4.1 High sampling rate (200 μs)

The stress parameters are presented in the following table; we chose the stress parameters according to some criteria as follows. For the gate voltage in the OFF state, the choice is based on the most negative voltage of the component to be blocked entirely. For the gate voltage in the ON state, the choice is based on a very low voltage value for maintaining a low conduction current. It should be noted that the threshold voltage of these components was in the range of 1.3 – 1.7 V. For the OFF drain voltage, we found that 200V – 400V is large enough to activate traps and at the same time is not approaching to the operating limits to avoid problems like the breakdown at high temperatures. The ON drain voltage was fixed at a low level to maintain a low current and avoid self-heating. The OFF state time was fixed after several campaigns; it was found as a compromise to activate traps in the measurement time range.

Parameter	Corresponding value
$V_{GS_{OFF}}$	-6V
$V_{GS_{ON}}$	2V
$V_{DS_{OFF}}$	200V
$V_{DS_{ON}}$	1V
$I_{DS_{ON}} \text{ limit}$	1A
Sampling interval	200 μs
OFF Stress time	1s

Table 3.5: Drain lag with high sampling rate test parameters.

3.3. TRANSIENT CURRENT MEASUREMENTS & EXTRACTION OF TRAPS PARAMETERS

Transient current and observations

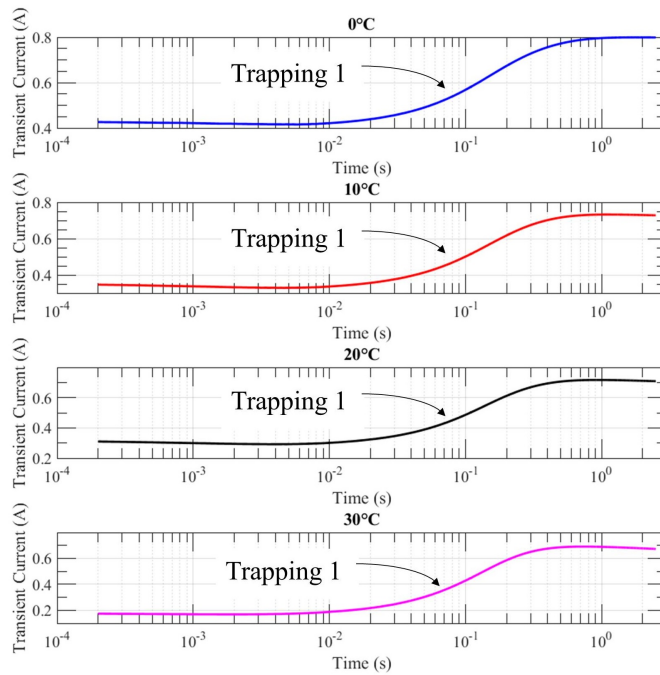


Figure 3.15: Transient measurements (200 μs sampling rate) for a temperature range from 0 °C to 30 °C.

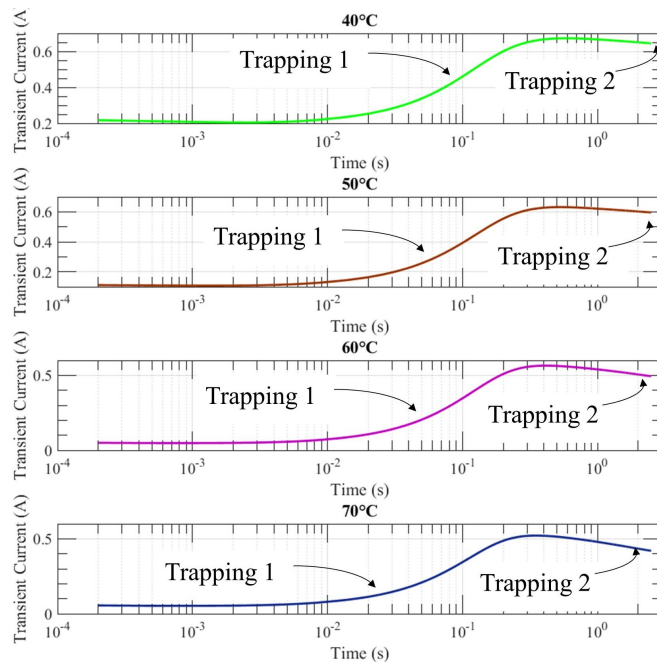


Figure 3.16: Transient measurements (200 μs sampling rate) for a temperature range from 40 °C to 70 °C.

It is shown in *Figure 3.15*, *Figure 3.16* and *Figure 3.17* the transient measurements performed for

3.3. TRANSIENT CURRENT MEASUREMENTS & EXTRACTION OF TRAPS PARAMETERS

a temperature range from 0°C to 100°C. We can observe a faster behavior of the transient current with the temperature increase which reflects the traps behavior. By increasing the temperature, as shown, we found a second trapping behavior that starts to appear at 40 °C. The word "trapping" is used for both capture and emission in the following figure.

At 90°C, there is a third curvature which begins to appear that reflects the existence of a third trap mechanism with a higher time constant. One of the issues of these transient measurements is the difficulty to follow all the trapping behaviors. As we have seen, there have been three trapping behaviors some of which can be hidden at low temperatures. This problem makes extracting the traps physical parameters a complicated task since we had to get a sufficient number of time constants function of the temperature.

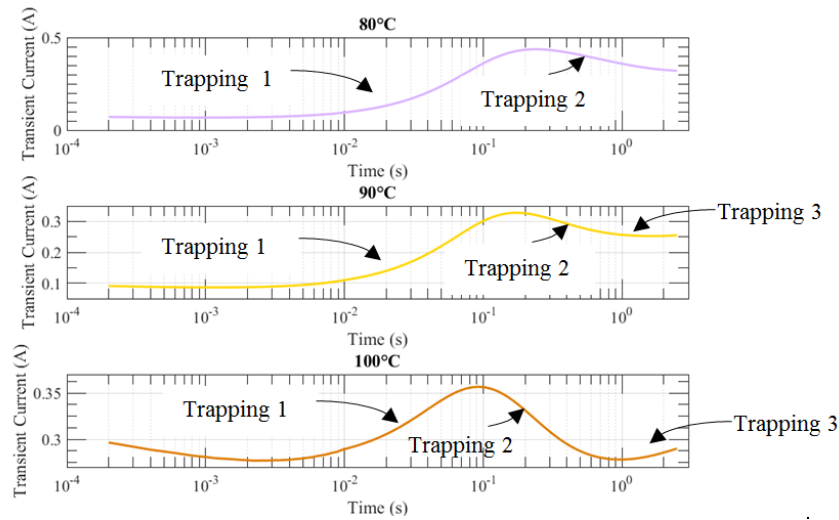


Figure 3.17: Transient measurements (200 μ s sampling rate) for a temperature range from 80 °C to 100 °C.

Regarding the emission and capture mechanisms, it is difficult to identify which mechanism occurs at each rise or fall of the transient current. We can have a detrapping mechanism in the AlGaIn layer which enhances the 2DEG density; charges emission will increase the ionized traps density which will, therefore, induces an increase in the electric field at the heterointerface. We can also have a detrapping mechanism in the GaN layer which will weaken the electric field at the heterointerface and therefore the 2DEG density. So, in most cases, it is a little complicated to justify the trapping or detrapping mechanism.

Extraction of time constants with Prony's method:

The original signal fitted by the Prony procedure is presented in the following figures (linear scale) for two temperatures (40°C and 100°C). We have seen that at a high temperature 100°C, a higher order of the Prony model is needed. The methodology requires using Prony method with a high order to fit correctly with the experimental measurements. Then, we use the higher amplitudes of this fitting, and we follow the evolution of the correspondence time constants with temperature.

3.3. TRANSIENT CURRENT MEASUREMENTS & EXTRACTION OF TRAPS PARAMETERS

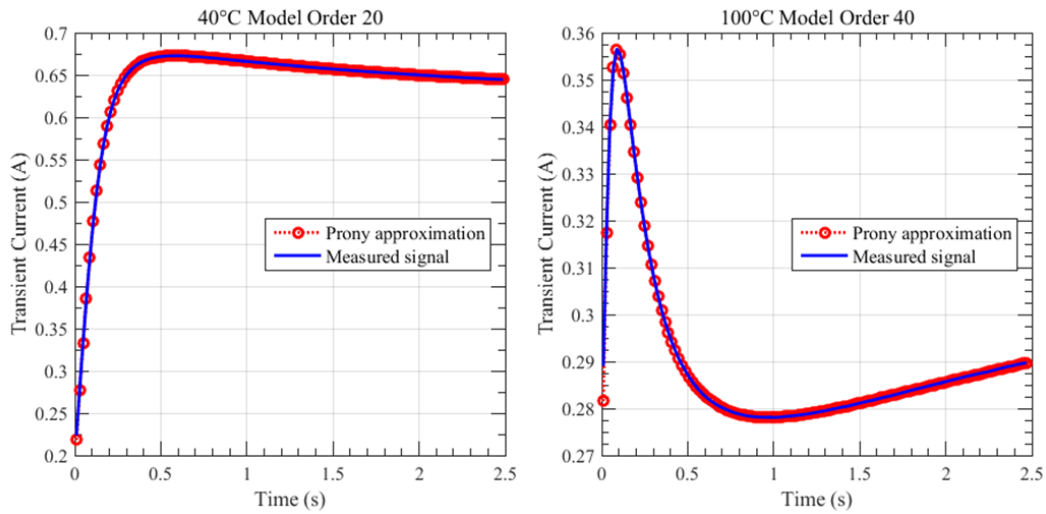


Figure 3.18: Prony fitting with measured signals (200 μ s for sampling rate) for two temperatures (40 $^{\circ}$ C and 100 $^{\circ}$ C) – linear scale.

Using these measurements, one activation energy ($E_a = 0.07\text{eV}$) associated with a cross section ($\sigma_n = 1.13 \times 10^{-18}\text{cm}^2$) have been successfully extracted as shown in the following figure. We did not succeed to get a perfect linear Arrhenius plot with the extracted time constants using the presented method. It was necessary to fit the experimental results using a linear regression.

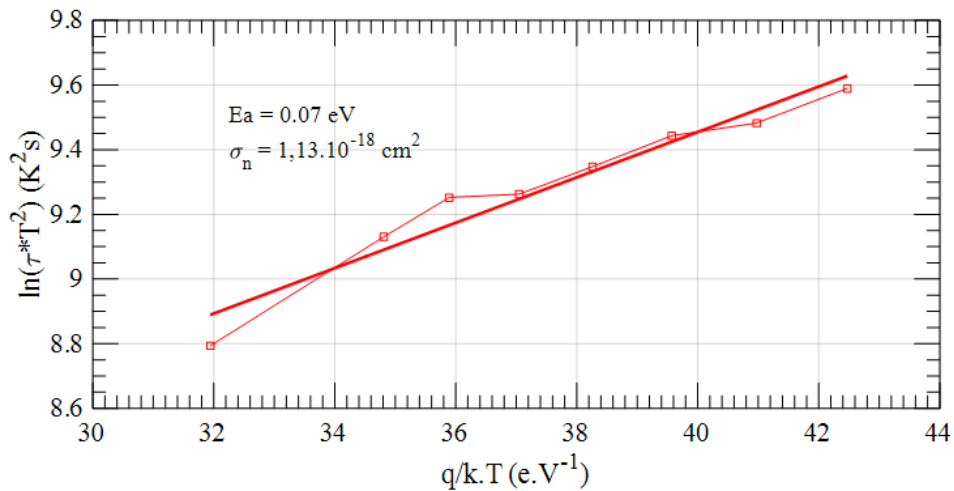


Figure 3.19: Arrhenius plot for activation energy for Drain Lag measurements for high sampling rate.

Performing a single current transient measurement is not enough as there are long time constants (trapping 2 and 3) that have not been successfully detected at this timescale with full information. So, we had to perform measurements with longer timescales.

3.3.4.2 Low sampling rate (10 ms)

The sampling rate was increased to identify the long-term traps, as shown in the following figures, we were able to detect longer trap behavior. The sampling rate has been multiplied by 50.

3.3. TRANSIENT CURRENT MEASUREMENTS & EXTRACTION OF TRAPS PARAMETERS

Parameter	Corresponding value
$V_{GS_{OFF}}$	-6V
$V_{GS_{ON}}$	2V
$V_{DS_{OFF}}$	200V
$V_{DS_{ON}}$	1V
$I_{DS_{ON} \text{ limit}}$	1A
Sampling interval	10ms
OFF Stress time	1s

Table 3.6: Drain lag with high sampling rate test parameters.

Transient current:

We note that trapping 1 observed with the sampling rate $200 \mu\text{s}$ has lost information, especially in high temperature. On the other hand, we have found more information on trapping 2 and 3. In these transient currents, we presented only transients for temperatures between 80°C and 100°C to show the evolution of information especially for trapping 3.

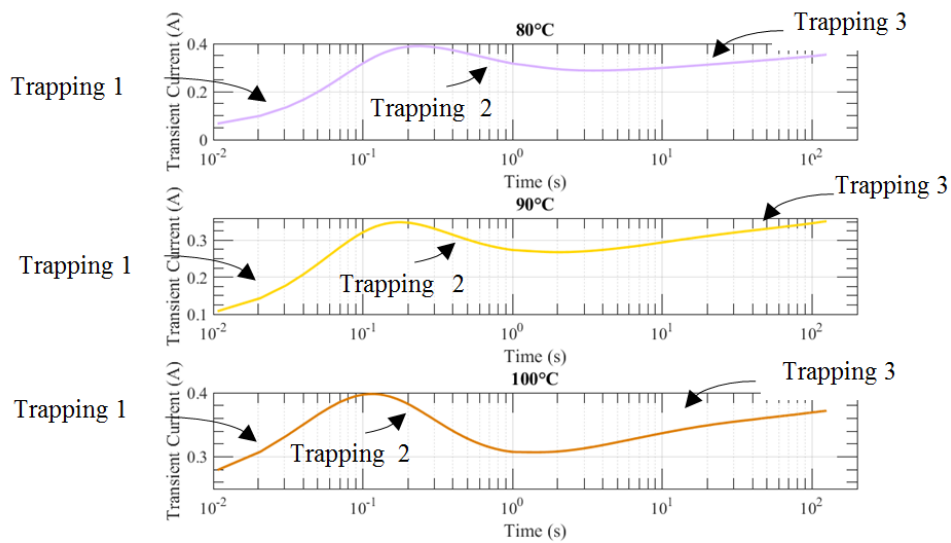


Figure 3.20: Transient measurements (10ms sampling rate) for a temperature range from 80°C to 100°C .

Extraction of time constants with Prony's method:

After the decimation and signal processing phase, we find a few points describing trapping 1 used for parameter extraction.

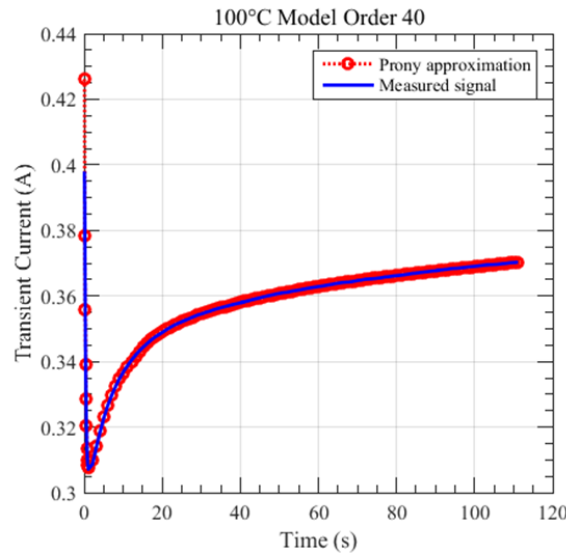


Figure 3.21: Prony fitting with measured signals (10 ms of sampling rate) for 100°C – linear scale.

3.3.4.3 Traps physical parameters extraction from Arrhenius law - Drain lag:

By combining the measurements made for low and high sampling rate, we extracted four activation energies; one activation energies were extracted with the high sampling rate and three activation energies were extracted with low sampling rate. We have extracted two signatures for trapping 1; we consider that trapping 1 identified by high sampling rate is more accurate.

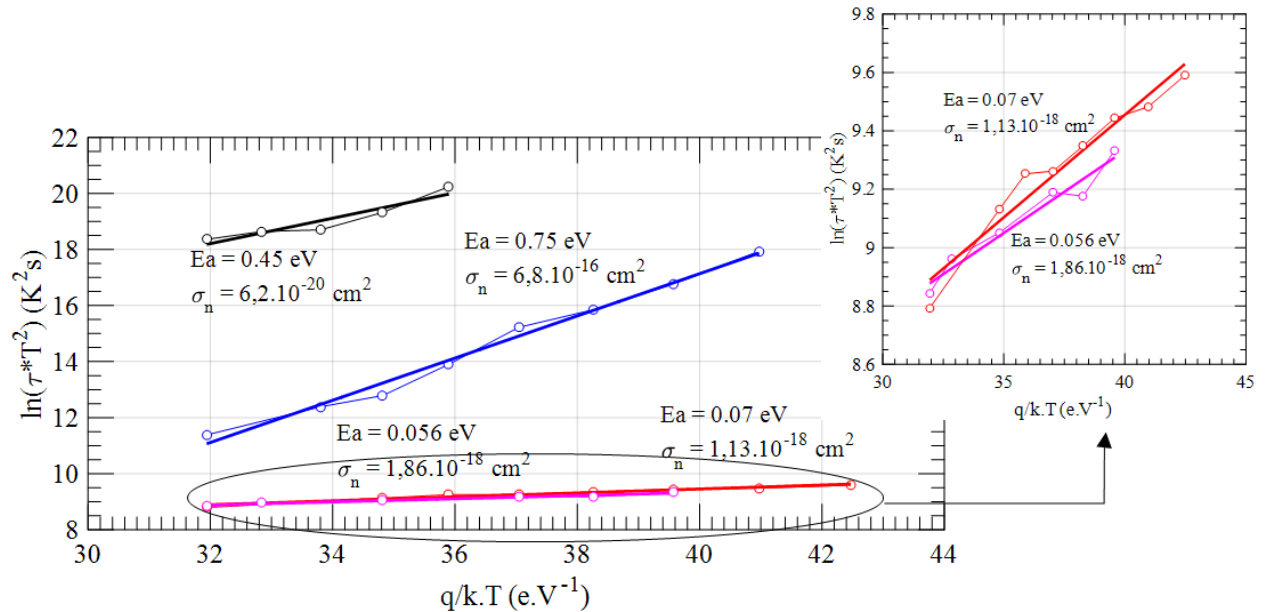


Figure 3.22: Arrhenius plot for activation energy for Drain Lag measurements for high and low sampling rate.

The activation energies and cross sections for traps, sampling rate and the identification of their sources are grouped in the following table. The identification was assigned based on the results found in the literature.

3.3. TRANSIENT CURRENT MEASUREMENTS & EXTRACTION OF TRAPS PARAMETERS

Traps physical parameters	Sampling rate	Identification
$E_a = 0.056eV$ $\sigma_n = 1.86 \times 10^{-18}cm^2$	Low sampling rate	Corresponding to trapping 1 It may also be correlated with N vacancy (V_N) [Gas 08]
$E_a = 0.07eV$ $\sigma_n = 1.13 \times 10^{-18}cm^2$	High sampling rate	Corresponding to trapping 1 Traps reported only for the electron irradiated MOCVD and HVPE GaN [Gas 08]
$E_a = 0.45eV$ $\sigma_n = 6.2 \times 10^{-20}cm^2$	Low sampling rate	Corresponding to trapping 2 Carbon, Oxygen or Hydrogen in Nitrogen substitutional position [Bis 13]
$E_a = 0.75eV$ $\sigma_n = 6.8 \times 10^{-16}cm^2$	Low sampling rate	Corresponding to trapping 3 Nitrogen interstitials [Bis 13]

Table 3.7: Traps physical parameters extraction from Arrhenius.

3.3.4.4 A sensitivity study for transient current measurements OFF Stress level:

We present a comparison between the different transient currents by varying the OFF stress level. We swept three values of the OFF stress level (200V, 300V, and 400V) for two different temperatures (0°C and 60°C). We noticed that there is no change in the quality of the curves by changing the OFF-state stress level.

Parameter	Corresponding value
$V_{GS_{OFF}}$	-6V
$V_{GS_{ON}}$	2V
$V_{DS_{OFF}}$	200V, 300V and 400V
$V_{DS_{ON}}$	1V
$I_{DS_{ON} \text{ limit}}$	1A
Sampling interval	10ms
OFF Stress time	1s

Table 3.8: Sensitivity study test parameters.

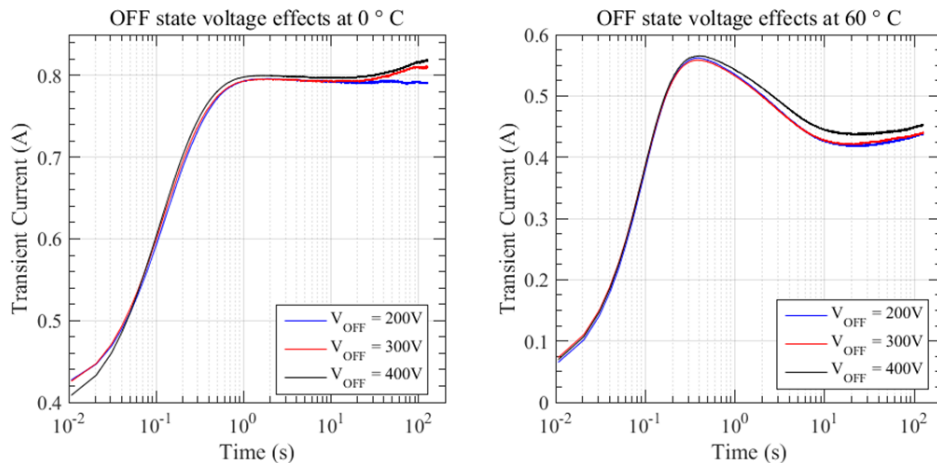


Figure 3.23: (Drain Lag) Transient current with OFF-Stress Time = 1s (Left 0 °C), (right 60 °C).

We have limited the sweep of the OFF state stress level as an irreversible degradation can occur when approaching the limits of the component at high voltage (600 V). We have also limited the OFF stress time for these measurements to 1s because by increasing this time, we have observed that there are longer traps that begin to manifest. We fall finally with a collapse of the current for a long time that exceeds the measurement limit of the used equipment.

Finally, it should be noted that these transient drain lag measurements are not totally related to the change in the polarization state of the drain. In fact, there is also an effect of the gate lag, since there is a change also in the polarization on the gate.

3.3.5 Gate lag of the GaN—Systems commercial devices:

We followed the same measurements flow for the gate lag measurements. We will not present all the steps, but we will present a sensitivity study on the OFF-stress time that affects the transient measurements and the extraction of the traps physical parameters. For all measurements we have fixed a gate voltage at -6 V, the drain voltage has been applied in the OFF and the ON state at 1 V to avoid the drain lag effect. The sampling interval is fixed at 10 ms. It should be noted that we went directly to estimate the time constants for transient measurements with a low sampling rate. So an error can deal with extracting parameters for fast trapping process. We applied the stress for a longer temperature since the stress is not critical and no degradation was experienced with these test conditions at high temperature.

In the following figures, we present the transient measurements for a temperature range from 10 °C to 130 °C for OFF stress time of 1s, 50s, and 100s.

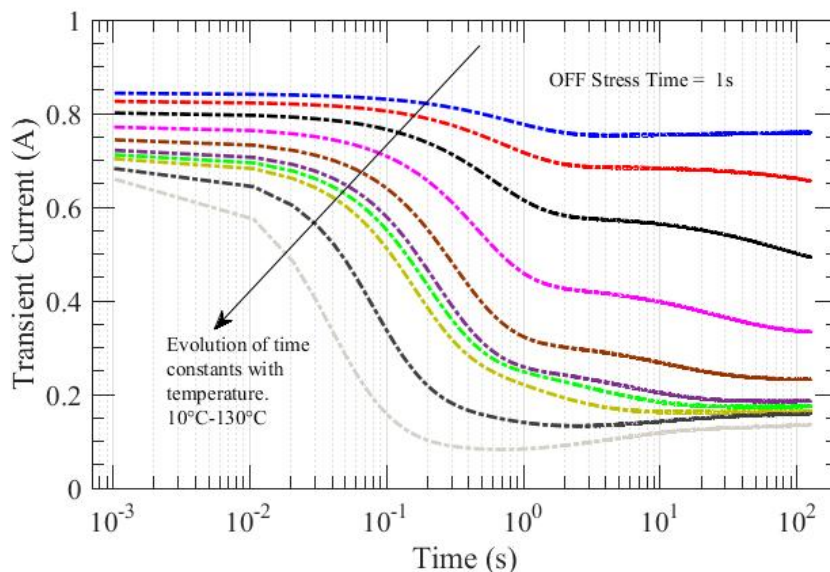


Figure 3.24: (Gate Lag) Transient current with OFF-Stress Time = 1s.

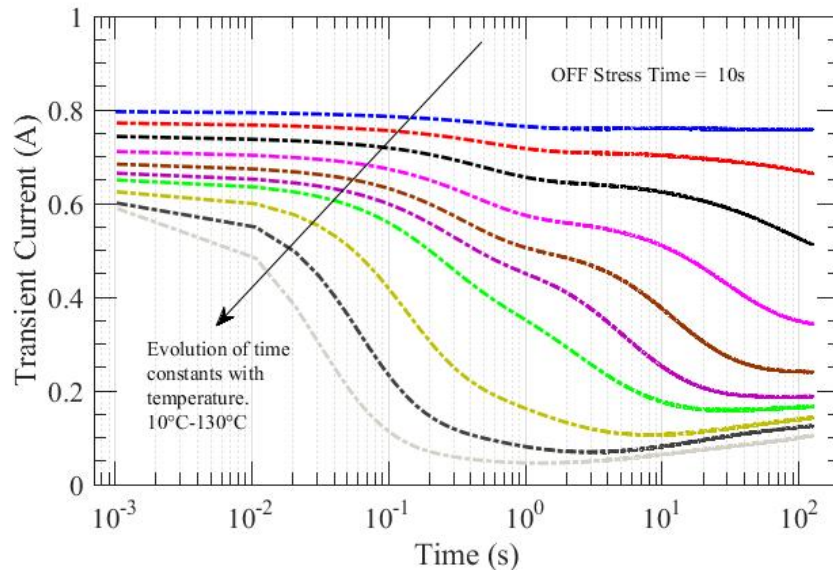


Figure 3.25: (Gate Lag) Transient current with OFF–Stress Time = 50s.

As expected, the higher the temperature and the more the current is affected. These time constants are rather related to the capture process of donors in either AlGa_N or GaN layer. Therefore, it may have a contradictive effect on the 2DEG charge density depending on whether they occur in GaN or AlGa_N layers or their balance in these two materials. This is why we can observe transient current rise or fall with time for a single curve. This may reflect the donors' existence in the two AlGa_N and GaN layers in which capture electrons can occur with different time constants. There are some time constants that have a larger amplitude only when increasing the stress time in the OFF state. So some traps needed more time to be emitted. So, when the OFF stress duration is not sufficient, traps haven't sufficient time to be emitted and aren't detected.

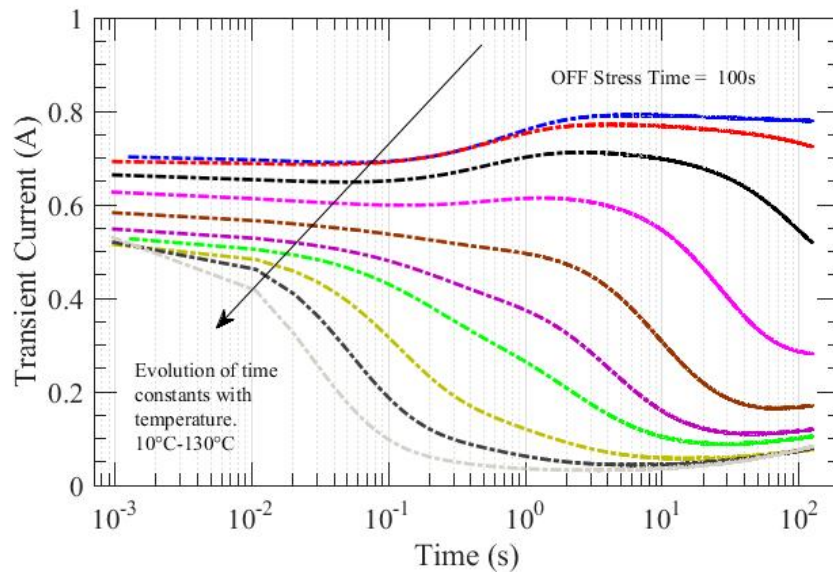


Figure 3.26: (Gate Lag) Transient current with OFF–Stress Time = 100s.

3.3. TRANSIENT CURRENT MEASUREMENTS & EXTRACTION OF TRAPS PARAMETERS

Since a single transient current will not be sufficient, we performed the Arrhenius plot for the current transient measurements with the different OFF-Stress time.

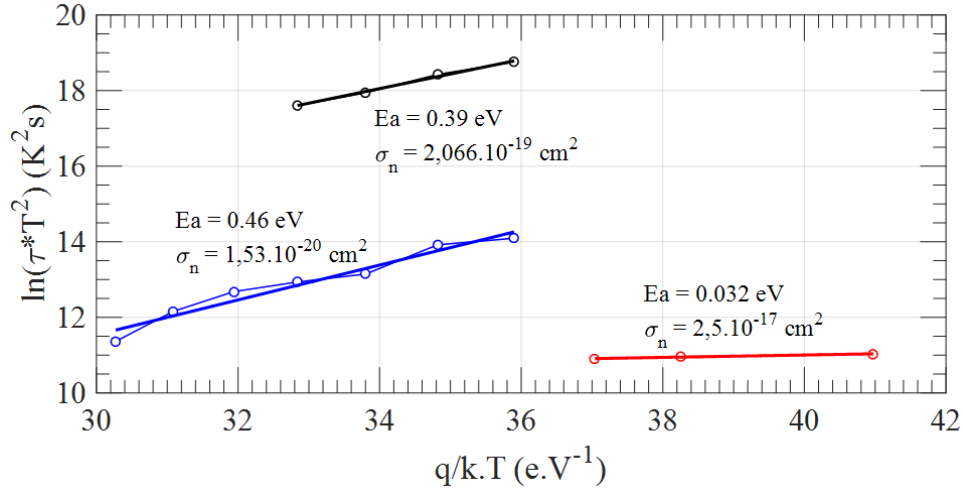


Figure 3.27: Arrhenius plot for activation energy for Gate Lag measurements for different OFF-Stress time.

The activation energies and cross sections for traps, OFF stress time and the identification of their sources are grouped in the following table:

Traps physical parameters	OFF Stress Time	Identification
$E_a = 0.032 \text{ eV}$ $\sigma_n = 2.5 \times 10^{-17} \text{ cm}^2$	1s	Corresponding to trapping 1 It may be correlated with N vacancy (V_N) [Gas 08]
$E_a = 0.39 \text{ eV}$ $\sigma_n = 2.066 \times 10^{-19} \text{ cm}^2$	50s	Corresponding to trapping 1 Very close value to AlGaN surface states that can exist under the gate [Bis 13]
$E_a = 0.46 \text{ eV}$ $\sigma_n = 1.53 \times 10^{-20} \text{ cm}^2$	100s	(As found with drain lag) Carbon, Oxygen or Hydrogen in Nitrogen substitutional position [Bis 13]

Table 3.9: Traps physical parameters extraction from Arrhenius.

3.4 Conclusion:

In this chapter, we presented the current transient measurements made for the GaN—systems commercial devices. We studied the drain and gate lag measurements. We have presented the equipment used, and the flow of the measurements. The parameters of these measurements greatly affect transient currents. They can also affect the accuracy of extraction of trap parameters such as the comparison shown for the transient measurements between high (200 μs) and low (10 ms) sampling rates of drain and gate lag. We also studied the effect of OFF stress time on the transient measurements of gate lag. we presented the results for a temperature range from 10 °C to 130 °C for 3 OST values 1s, 50s, and 100s. For all these measurements, we have fixed a gate voltage at -6 V.

For these measurements, the trap parameters extraction gave the possibility of detecting and identifying traps. The detected signatures may be correlated with N vacancy (V_N), they may also be close to AlGaN surface states that may exist under the gate, they may also be assigned to Carbon, Oxygen or Hydrogen in Nitrogen substitutional position.

For the drain lag measurements, three levels of stress in the OFF state were tested 200V, 300V and 400V. The attribution of traps to these measurements may be correlated with the presence of N vacancy, carbon, oxygen or hydrogen in nitrogen substitution position or nitrogen interstitial. Furthermore there is a traps signature that was reported only for the electron irradiated MOCVD.

Finally, we tried to identify the origin of the traps based on the results of the literature. In consequence, the GaN—systems commercial components always have instabilities, and its R_{ON} dynamics vary significantly. This instability was due to the traps identified in this chapter.

Chapter 4

Power cycling reliability testing of Al₂O₃/AlGaN/GaN on Si devices

4.1 Introduction

In this chapter, we present the results of the experimental tests carried out to study the effect of accelerated reliability test on the electrical behavior of the GaN power devices. We will rather focus on the test effect on the evolution of the traps state in the structure. These tests are in general used to age the power devices by applying electrical or thermal stresses. It exerts two fundamental types of these tests: active power cycling and passive thermal cycling. The principle of the first type (active power cycling) is based on the injection of electric power into the device that will induce a self-heating of the component. The injection is repeated over several cycles and may lead to ageing through thermal fatigue. The second type is based on submitting the device to the variation of environment temperature.

The ageing may lead to irreversible degradation of the device electrical characteristics. These power components are usually integrated into power modules. Thus, the degradation modes can occur either at the semiconductor level or the assembly level. For power modules based on silicon transistors, degradation at the assembly level may probably arise, and it is infrequent to have deterioration at the semiconductor level. This is due to the maturity of the silicon-based component technology. However, regarding the degradations that can occur at the assembly level, we can have a delamination of one of the materials layers of the assembly, degradation at the solder level is also widespread and deterioration at the bonding wires level. These degradations are mainly due to the accumulated effect induced by self-heating at each cycle. These accumulated effects are reflected in the evolution of the mechanical state of the materials. Some materials can enter the plastic zone under the impact of mechanical stress (like Copper). For fragile materials such as ceramics (Si_3N_4), they can break directly after exceeding the yield limit. Concerning the induced degradation at the device level, the semiconductor may be degraded either by a direct mechanical stress generated from the assembly on the device or by an indirect mechanical stress caused by the power injected induced self-heating into the device. In both cases, a modification at the micro-structural level may alter the device electrical characteristics, for example, a density of additional defects may be generated inside the crystal. However, these accelerated tests are well known for studying the reliability of power components and to estimate the device lifetime.

For GaN devices, it is different, the mechanisms of ageing at the device level is not yet fully revealed. For the reliability tests which were carried out in the literature (presented in chapter 1), degradation at the device level is more recognized. This deterioration is reflected in part by a change in the state of the traps which degrades the electrical characteristics of the components. In this chapter, we will try to answer this question using the active power cycling tests. We will investigate the traps state evolution with this reliability test.

In this chapter, we will present a study carried out on the Normally-ON components fabricated by the CEA and reported on a direct copper bonding (DCB) substrate. A single ageing campaign on two components will be presented. We will first introduce the concept of power cycling tests then we will present the test bench used. The experimental results of these power cycling tests and the ageing behavior on the evolution of traps states will be detailed by performing electrical characterizations before and after the test. It should be finally noted that we carried out several ageing campaigns on commercial components GaN Systems, but a significant instabilities source, non-understandable behaviors and also the non-maturity of the component after ageing make these campaigns results unworkable. For example, we carried out campaigns where the devices were directly broken during the first measurements after ageing; this point presented much blocking to be able to carry out analyzes. Furthermore, the complex industrial packaging system and the secrets of the internal structure have made the problem more complicated to understand.

4.2 Device presentation and its characteristics

We first start by presenting the characteristics of the device mounted on the DCB substrate.

4.2.1 Electrical and thermal characteristics

Table 4.1 presents the primary typical electrical and thermal characteristics of these devices. These characteristics are essential to define the conditions and limits of the power cycling tests. It should be noted that these values are typical and a dispersion of these characteristics have been found between several devices.

Electrical specifications	Maximum drain – source voltage $V_{DS(max)}$	600V
	Maximum drain – source current at 25 °C (per pad) $I_{DS(max)}$	10A
	Maximum gate voltage $V_{GS(max)}$	3V
	Minimum gate voltage $V_{GS(min)}$	-7V
	Drain – source leakage current I_{DSS} (Typical value)	3 μ A
	Threshold voltage $V_{GS(th)}$	-3.5V
Thermal specifications	On-state resistance R_{DSon}	100m Ω
	Maximum temperature supported by the chip	300°C
	Maximum junction temperature $T_{j(max)}$	200 °C
	Minimum junction temperature $T_{j(min)}$	-40 °C

Table 4.1: Electrical and thermal characteristics of the DUT at 25°C.

4.2.2 DUT external structure mounted on DCB

As shown in Figure 4.1 (left), concerning the external structure of the component, the device is composed of 6 blocks (3 blocks drain and three source blocks and a gate block). Each drain-source pair can pass a maximum of 10A. Each pad is designed by thousands of unit cells presented in chapter 2 and connected in parallel.

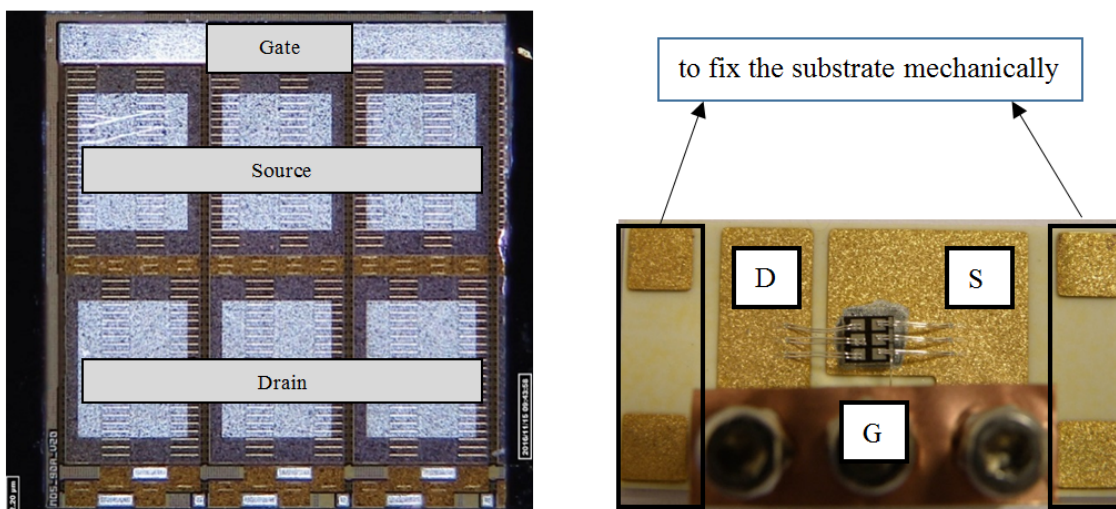


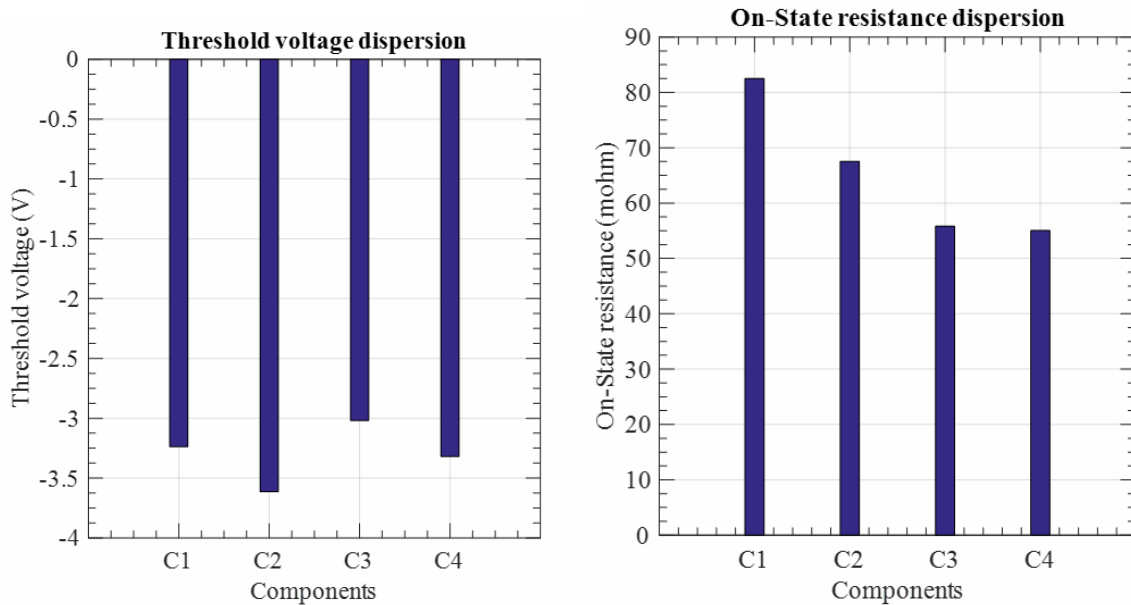
Figure 4.1: The external component structure composed of three pairs of drain/source (Left), the component mounted on a DCB (right).

4.2. DEVICE PRESENTATION AND ITS CHARACTERISTICS

To use this component in power tests, we need to mount them on a DCB. A DCB was designed as shown in *Figure 4.1 (right)* that meets these needs. This DCB was made of Cu/Al₂O₃/Cu with flash Au, with four blocks electrically disconnected from the device which is used to fix the substrate mechanically. This design was then realized and implemented by the 3D Power Hybrid Integration platform (3DPHI) of Toulouse III University - Paul Sabatier.

4.2.3 Diversity of devices electrical characteristics

A significant dispersion in the devices electrical characteristics was found with these devices. This dispersion presents a real issue to establish the power cycling tests on several components simultaneously. We present a dispersion study carried out on four different devices. The threshold voltage and the on-state resistance dispersion are shown in *Figure 4.2*. A maximum dispersion of 0.6 V was observed for the threshold voltage and a difference of 27 mΩ for the on-state resistance. However, this dispersion is probably related to technological process, a change in the traps density in the initial state, which can differ from one component to another, can be one of the reasons of this dispersion. The measurement conditions of the threshold voltage (*Table 4.2*) and the on-state resistance (*Table 4.3*) are presented as following:



(a) Threshold voltage dispersion of 4 different components, (b) On-state resistance dispersion of 4 different components. C stands for component.

Figure 4.2: Dispersion of electrical characteristics for 4 different components, C stands for component.

Threshold voltage dispersion:

Test settings	Corresponding values
V_{DS} constant	100 mV
Criteria	$V_{th} = V_{GS}@ (I_{DS} = 10mA)$
V_{GS} sweep	(-6 to -2) V
Temperature	30 °C

Table 4.2: Test settings of the threshold voltage.

4.2. DEVICE PRESENTATION AND ITS CHARACTERISTICS

On-state resistance dispersion:

Test settings	Corresponding values
I_{DS} constant (Linear region)	5A
V_{GS} (completely open)	0V
Temperature	30 °C

Table 4.3: Test settings of the on-state resistance.

The dispersion of these two parameters will consequently affect the $I_{DS} - V_{DS}$ and $I_{DS} - V_{GS}$ characteristics as shown in *Figure 4.3*. This diversity can cause some limitations in the ability to set similar stress conditions of power cycling tests. The settings tests of these measurements are presented in *Table 4.4* and *Table 4.5*. These measurements were carried out at a temperature of 30 °C.

Test settings ($I_{DS} - V_{DS}$)	Corresponding values
V_{DS} pulse duration	50 μ s
V_{GS}	-3V
V_{GS} pulse duration	500 μ s
Delay between pulses	50 μ s
Polarization gate point in the OFF state	-6V
Polarization drain point in the OFF state	0V
Pulse period	1s
Measurement time	Average on 50 μ s at the end of the pulse

Table 4.4: Test settings of the ($I_{DS} - V_{DS}$.)

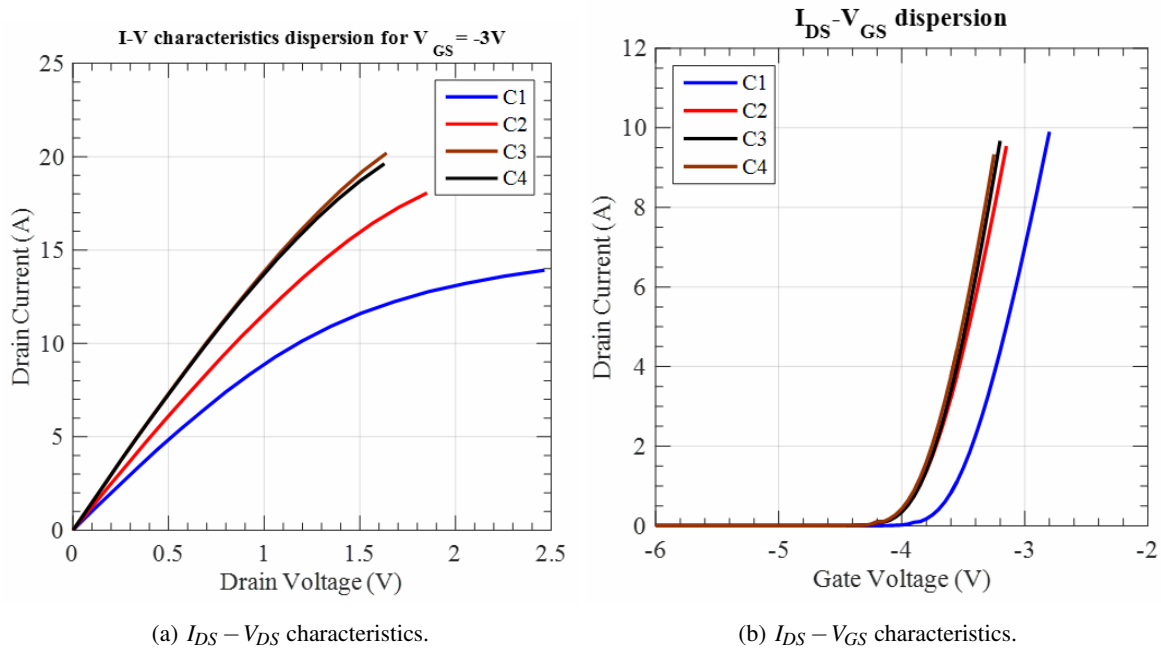


Figure 4.3: Electrical characteristics of the 4 components.

Test settings ($I_{DS} - V_{GS}$)	Corresponding values
V_{GS} pulse duration	500 μ s

4.3. GENERAL METHODOLOGY OF POWER CYCLING

V_{DS} constant	800mV
V_{GS} sweep	(-6 to -2)V
Polarization gate point in the OFF state	-6V
Pulse period	2s
Measurement time	Average on 20 μ s at the end of the pulse

Table 4.5: Test settings of the ($I_{DS} - V_{GS}$.)

The test conditions must be then carefully chosen to be applied to components with different electrical characteristics in order to overtake this diversity problem.

4.3 General methodology of power cycling

Figure 4.4 presents a schematic presented by [Ibr 16] explains the principle behind DC power cycling for three devices consecutively. The concept is based on the injection of a DC current for a specific duration (t_{on}), this duration and the current power level are adjusted to heat the component to a targeted maximum junction temperature (T_{jmax}). T_{jmin} or T_{ref} is the reference temperature where the component is cooled down at each cycle. t_{off} is the cooling time necessary for the component to reach the T_{ref} temperature. The difference $T_{jmax} - T_{jmin}$ is the temperature difference adjusted and repeated each cycle in order to age the device. The sense current I_{sense} is used for junction temperature measurement; it is the same as the calibration current for the thermosensitive parameter (TSEP). The substrate temperature (T_{Case}) is also measured.

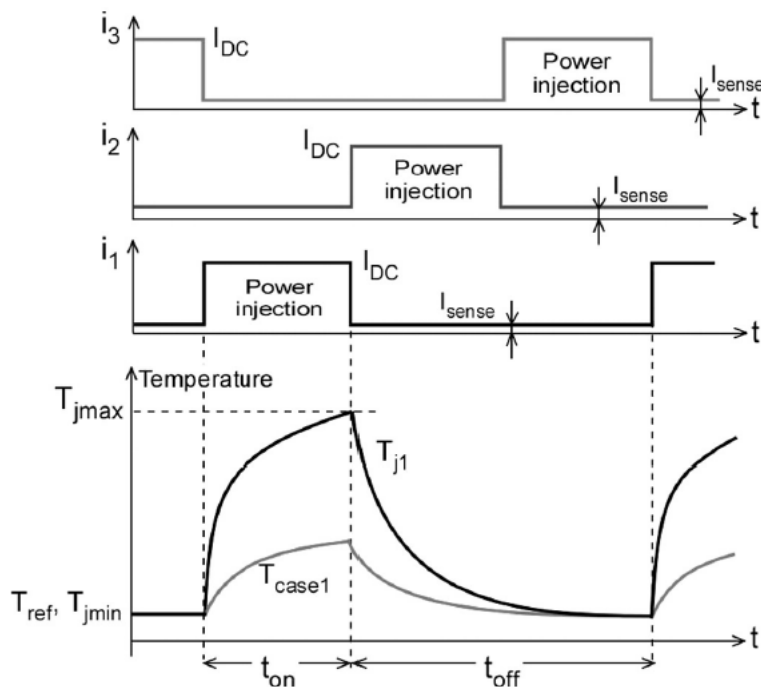


Figure 4.4: Conventional test bench and concept of power cycling [Ibr 16].

The steps of the tests can briefly be summarized as follows:

4.3. GENERAL METHODOLOGY OF POWER CYCLING

1. Pre-tests: To conduct these ageing tests, before launching them, some steps are needed to define the test conditions and preliminary calibrations.
 - Junction temperature measurements: The junction temperature measurement during the tests is essential in order to check the stress conditions and to follow the ageing. The measurement method must be first defined before launching the tests. There are two methods:
 - (a) The direct and localized measurement carried out by an optical fiber or by an infrared camera.
 - (b) The indirect measurement carried out using a thermo-sensitive electrical parameter (TSEP). This method requires finding an electrical parameter which is sensitive to the temperature (this method is the one used in the works presented in this chapter).
 - Thermo-sensitive calibration (in the case of indirect temperature measurements): This step is done by defining the thermosensitive parameter and by establishing its behavior with the temperature. The relationship between this parameter and the temperature is established as follows: the component is placed on a metal plate, this metal plate is linked to a thermal conditioner to regulate its temperature. The thermosensitive parameter is measured the function of the temperature. A thermocouple is connected to the component substrate to verify that the junction temperature will be the same as the conditioner temperature. A certain time (typically 15 minutes) is required for each temperature step to ascertain the stability of the junction temperature. Finally, a law is established between the temperature and the thermosensitive parameter which will be used later during ageing. For example, the drain-source voltage at low current (for GaN devices < 500 mA) provide a linear relation with the temperature without self-heating effects. The calibration curve used for the tests realized in this chapter is presented in *Figure 4.23*.
 - Initial characterizations of ageing indicators: some detailed electrical characterizations (I_{DS} - V_{DS} characteristics, transconductance, threshold voltage and traps measurements) must be carried out to compare the effect of this test on the device electrical characteristics between before and after ageing.
2. Power cycling and "online measurements":
 - Power cycling tests: Using the relationship between the temperature and thermosensitive parameter, a ΔT based on the injected current level and the injection duration is defined. The reference temperature T_{ref} is also set and the OFF state time is controlled in order to reach this T_{ref} . These repeated ΔT cycles will lead to thermo-mechanical fatigue and electrical failure.
 - Online measurements: As explained by [Hel 97 and Sme 11], online measurements or measurements without interrupting the power cycling test can provide information on the ageing monitoring. These online measurements can be performed on electrical or thermal parameters during the test to monitor the evolution of the device. These online measurements are necessary to follow the ageing process. The stopping criteria are fixed on the maximum percentage of the evolution of an electrical or thermal parameter. For silicon, a percentage of 5% of the measured V_{DS} or 20% of the thermal resistance R_{TH} is considered as the limits to say that the components have aged. The criteria of ageing are also relative and can be changed from one component to another depending on the semiconductor device and its maturity.
3. Post-tests
 - Complete final characterizations: After the component is being aged, to better understand the degradation mechanisms, electrical measurements, spectroscopy and micro-structural analyzes are necessary to explain the degradation mechanisms.

4.4 Equipment

As shown in *Figure 4.6*, the test bench consists mainly of:

1. Power supply: used for the injection of the power current into the device.
2. Electrical switch: it is used to switch the injected current between devices in order to cycle several devices in a row. In our bench test, there is the possibility of cycling three components in a row.
3. Thermal regulator: used for fixing a reference for device case temperature.
4. Heat sink plate: it plays the role of mechanical support where the devices will be fixed, this plate is linked to the thermal conditioner. Solder thermal interface is used to ensure the thermal contact between the devices and the metal plate.
5. Thermocouple: It is used to measure the temperature of the device substrate. It is always necessary for this thermocouple to touch exactly the point of the substrate where the component is reported. As shown in *Figure 4.5*, the system with the thermocouple connected to the substrate.

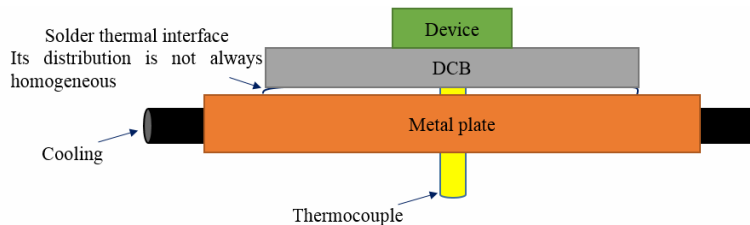


Figure 4.5: Method of fixing the component on a metal plate.

6. Microcontroller: It is used to control and supervise the ageing test protocol. It is also used to switch between different devices of the system.

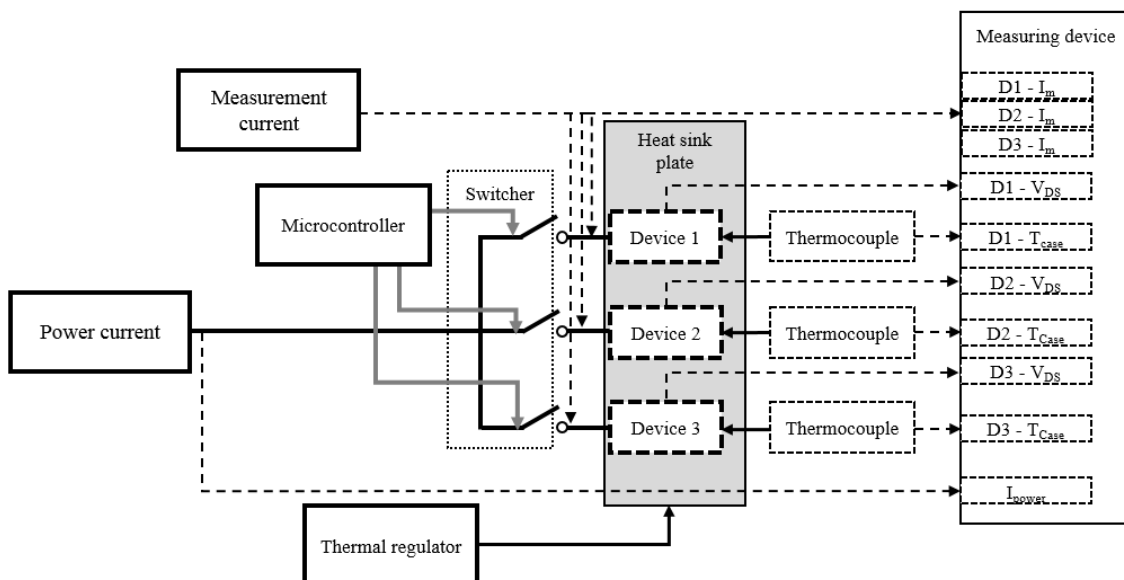


Figure 4.6: Test bench schematic.

7. Measuring device: Use for online measurements during power cycling. The measured parameters are the drain-source voltage, the substrate temperature, the calibration current and the injected power current. In the case of direct temperature measurements, fiber optic measurements are performed online.

Now we will discuss the performed campaign on the Normally-ON Al₂O₃/AlGaIn/GaN on Si provided by our partner CEA.

4.5 Characterizations before ageing

In this section, we present the electrical characterizations carried out before the power cycling tests. These initial characterizations will enable to study the evolution of the device characteristics after ageing.

4.5.1 Characterization methodology

As explained in chapter 1, unlike the silicon-based components, these GaN components are highly unstable. This instability does not only manifest in the characterizations themselves, after any performed characterization, the component also does not return to its initial state quickly and takes a certain time to return to its initial state. This time is highly dependent on the test type and the test parameters like the temperature and the applied polarization conditions. For example, if the component is subjected to high voltage for a relatively long duration (like 100s), we have to wait a certain amount of time which may even reach 30 minutes before any further measurements. For other characterizations like I_{DS}-V_{DS} or V_{th}, the component returns to its initial state more quickly. This point is very critical since one will not be able to carry out consecutive measurements easily. A complete characterization flow can take much time. So in order to be effective, we have established a characterization flow methodology. We start with measurements where the component returns to its initial state quickly; we then perform other measurements until reach the last measurement where it takes the longest duration to return to its initial state. This methodology has been found to be good for performing measurements as a function of temperature. The time to return to the initial state is used to change the temperature step which also takes a certain time (15 minutes) for thermal stabilization. In addition, we found that the measurements should be done in a single day, leaving the component for a day causes more instability in the measurements sequences. Even for these measurements, we have chosen configurations that give information without spending much time to return to the initial state. For example, traps measurements with a high emission time that may take hours have been eliminated therefore all our traps measurements have been performed to detect traps with relatively long time constants (>10ms).

As shown in *Figure 4.7*, we always started with pulsed I-V measurements, V_{th} and R_{DS, on}. For these measurements, 2 minutes were found to be sufficient. We go through the current collapse measurements, where we always start with the gate lag then the drain lag. For the gate lag tests, it has been found that 3 minutes are sufficient whatever the configuration. On the other hand, for drain lag tests, they are considered as severe tests, 5 minutes was found to be sufficient. This methodology is repeated for each temperature level. It should be noted that this methodology may vary from one component to another and also according to the manufacturer. During this thesis, we made measurements on the commercial component GaN Systems where the return time to the initial state was longer compared to those manufactured by the CEA.

4.5. CHARACTERIZATIONS BEFORE AGEING

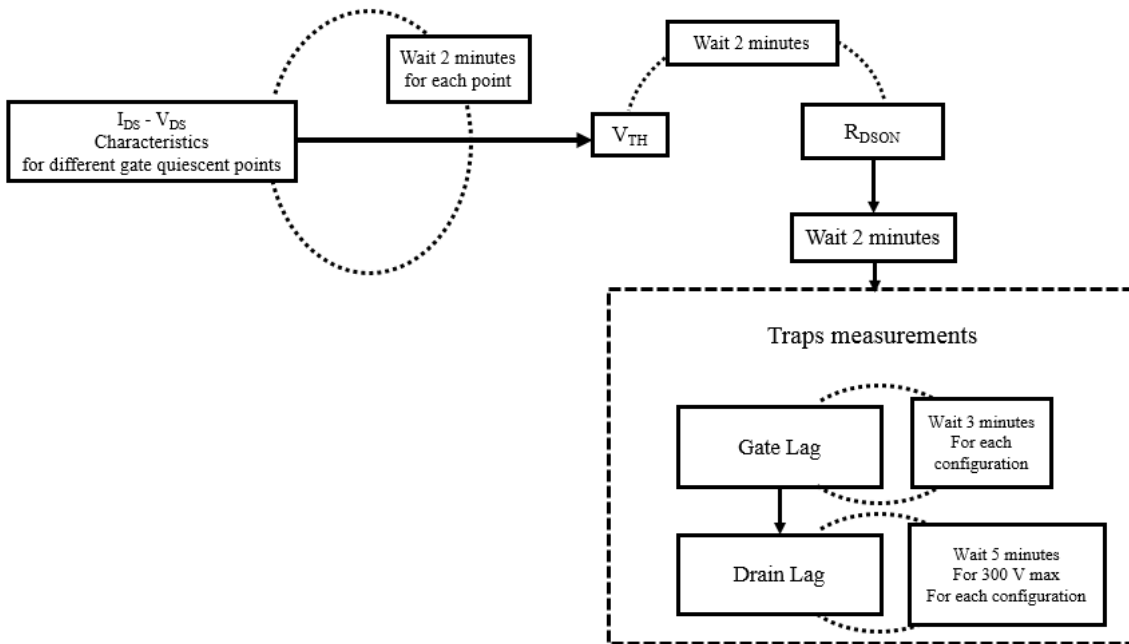


Figure 4.7: Methodology used for characterization before/after ageing.

Now we will move to characterization results before ageing. Concerning the configuration that will be presented for the characterizations, these configurations were chosen to have the best stability in the characteristics and the fast return to the initial state. It should also be noted that the presented campaign was carried out on only two components. This is due to the lack of components, and some breaks that were happened while using these components on the test bench.

4.5.1.1 General characterizations before ageing

- I_{DS} - V_{DS} characteristics:

We start with the electrical characteristics I_{DS} - V_{DS} for the two devices. As shown in *Figure 4.8*, we can observe a difference between the current-voltage characteristics of the two devices. This change can be due mainly to the difference in the threshold voltage and the on-state resistance between these devices. *Table 4.6* presents the test settings for these electrical measurements. These components are normally-ON, and therefore the applied gate voltage is negative (-3.5V up to -2V). In order to minimize the self-heating effect, the V_{DS} applied pulse was chosen to be very short (50 μ s). A delay between the drain and gate pulses was fixed to (50 μ s). This delay was found to give more stability to the measurements. The drain bias is set to be zero in the OFF state in order to minimize the effect of the drain lag on the measurements. The threshold voltage is estimated to be around (-4V), so we fixed (-6V) as a bias to block the device in the OFF state. Finally, a pulse period of 1s was found to give more stability to the measurements. The component is able to return to its initial state after each pulse.

Test settings (I_{DS} - V_{DS})	Corresponding values
V_{DS} pulse duration	50 μ s
V_{GS}	(-3.5 to -2)V with linear step of 0.5 V
V_{GS} pulse duration	500 μ s
Delay between pulses	50 μ s

4.5. CHARACTERIZATIONS BEFORE AGEING

Polarization gate point in the OFF state	-6V
Polarization drain point in the OFF state	0V
Pulse period	1s
Measurement time	Average on 50 μ s at the end of the pulse
Temperature	30 $^{\circ}$ C

Table 4.6: Test settings of the ($I_{DS} - V_{DS}$.)

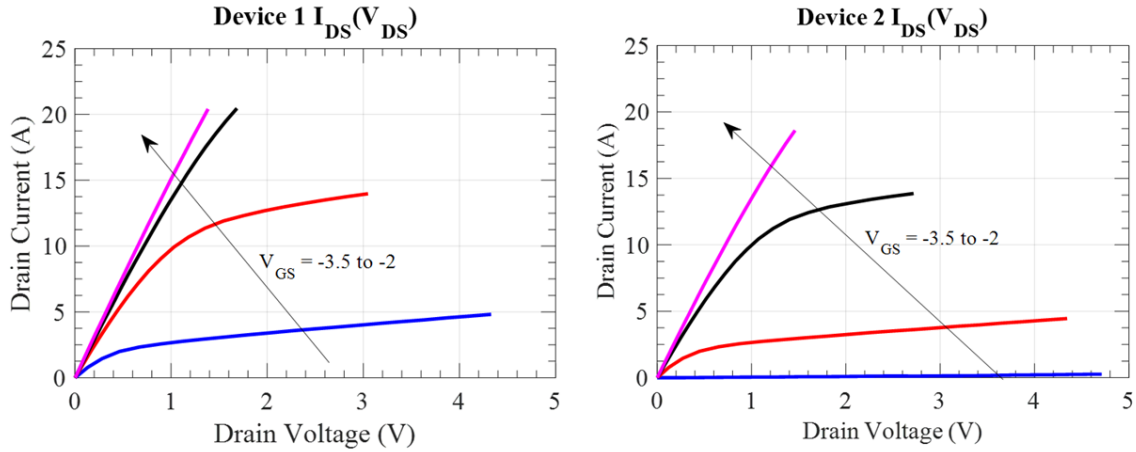


Figure 4.8: $I_{DS} - V_{DS}$ for the two devices.

- I_{DS} - V_{GS} and transconductance characteristics:

Now we will go through the I_{DS} - V_{GS} and transconductance characteristics of the devices. The measurements were performed by setting a drain voltage of 100 mV and sweeping the gate voltage. We notice that both components switch to the ON state at different values of the gate voltage. This is due to the difference in the threshold voltage. The value of the threshold voltage was estimated at 10 mA drain current. The first component has a threshold voltage value of -3.978 V and the second component has a threshold voltage of -3.124 V.

Test settings ($I_{DS} - V_{GS}$)	Corresponding values
V_{GS} pulse duration	500 μ s
V_{DS} constant	100mV
V_{GS} sweep	(-6 to -2)V
Polarization gate point in the OFF state	-6V
Pulse period	2s
Measurement time	Average on 20 μ s at the end of the pulse
Temperature	30 $^{\circ}$ C

Table 4.7: Test settings of the ($I_{DS} - V_{GS}$.)

4.5. CHARACTERIZATIONS BEFORE AGEING

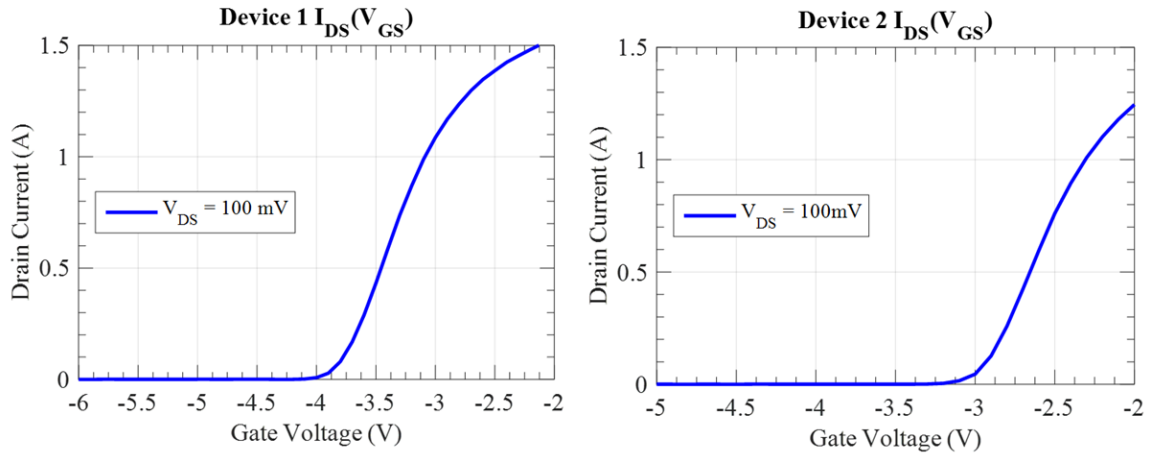


Figure 4.9: $I_{DS} - V_{GS}$ for the two devices.

As shown in *Figure 4.10*, the transconductance was deduced directly from the $I_{DS} - V_{GS}$ measurements as the slope of its curve.

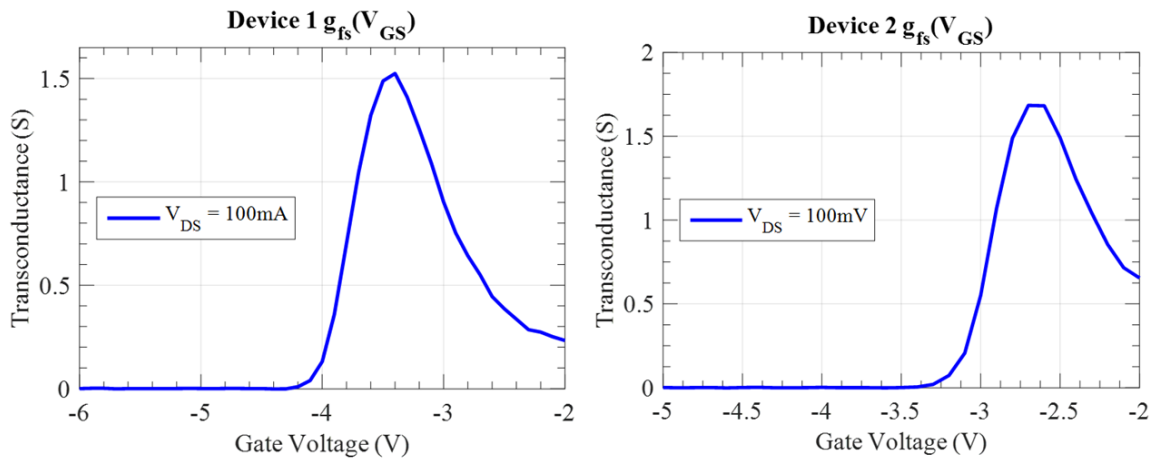


Figure 4.10: Deduced trans-conductance for the 2 devices.

- $I_{DS} - V_{DS}$ characteristics (With temperature):

The $I_{DS} - V_{DS}$ characteristics measurements were performed over a range of 30°C up to 90°C for a gate voltage $V_{GS} = -3V$. They are presented in *Figure 4.11* for both devices. The test settings are presented in *Table 4.8*.

Test settings ($I_{DS} - V_{DS}$)	Corresponding values
Temperature range	30°C to 90 ° with a linear step of 20 °C
V_{DS} pulse duration	50 μ s
V_{GS}	-3V
V_{GS} pulse duration	500 μ s
Delay between pulses	50 μ s
Polarization gate point in the OFF state	-6V
Polarization drain point in the OFF state	0V
Pulse period	1s

4.5. CHARACTERIZATIONS BEFORE AGEING

Measurement time	Average on 50 μs at the end of the pulse
------------------	---

Table 4.8: Test settings of the ($I_{DS} - V_{DS}$ -function of the temperature.)

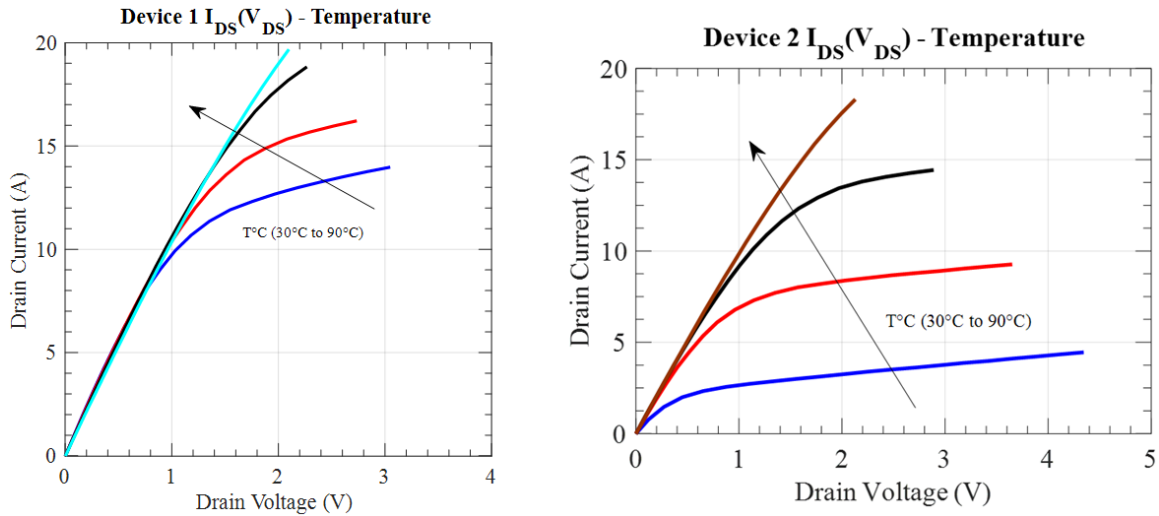


Figure 4.11: $I_{DS} - V_{DS}$ Characteristics of the 2 devices with temperature for $V_{GS} = -3\text{V}$ with a linear step of the temperature of 20°C .

- $I_{DS} - V_{GS}$ and threshold voltage characteristics (With temperature):

We noticed that the threshold voltage decreases with the temperature for both devices. $\Delta_{th1} = |V_{th(90\text{degC})} - V_{th(30\text{degC})} = 0.445\text{V}$ and $\Delta_{th2} = |V_{th(90\text{degC})} - V_{th(30\text{degC})} = 1.041\text{V}$.

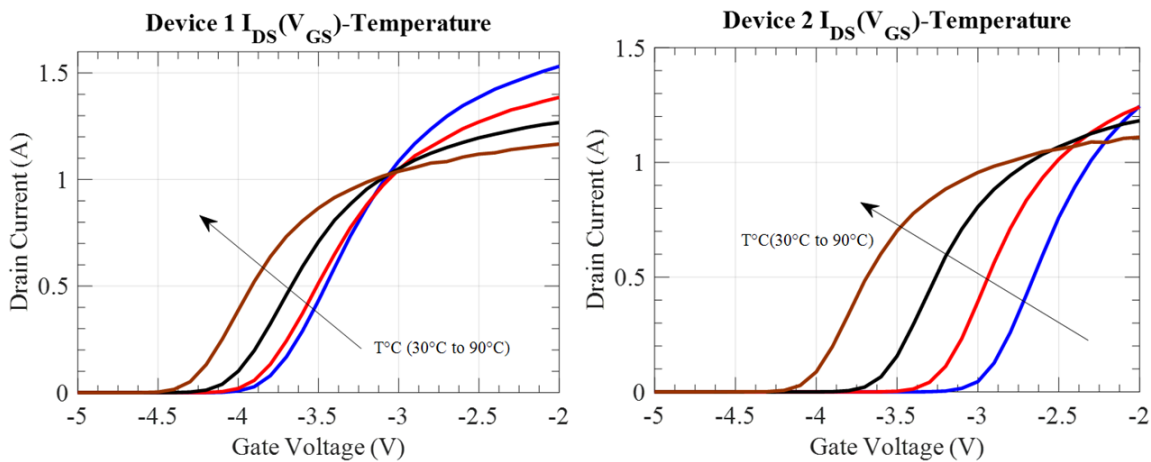


Figure 4.12: $I_{DS} - V_{GS}$ characteristics of the 2 devices with temperature for $V_{DS} = 100\text{mV}$ with a linear step of 20°C .

We observe that $\Delta_{V_{th}}$ changes from one component to another, this observation could be due to the weight of the physical parameters constituting the threshold voltage as a function of the temperature. The threshold voltage measurements were performed exactly as presented for the room temperature, the V_{DS} voltage is set to 100 mV, and the threshold voltage is equal to the gate voltage

4.5. CHARACTERIZATIONS BEFORE AGEING

for a 10 mA drain current. I_{DS} - V_{GS} measurements and threshold voltage measurements of both devices are presented in *Figure 4.12* and *Figure 4.13* respectively.

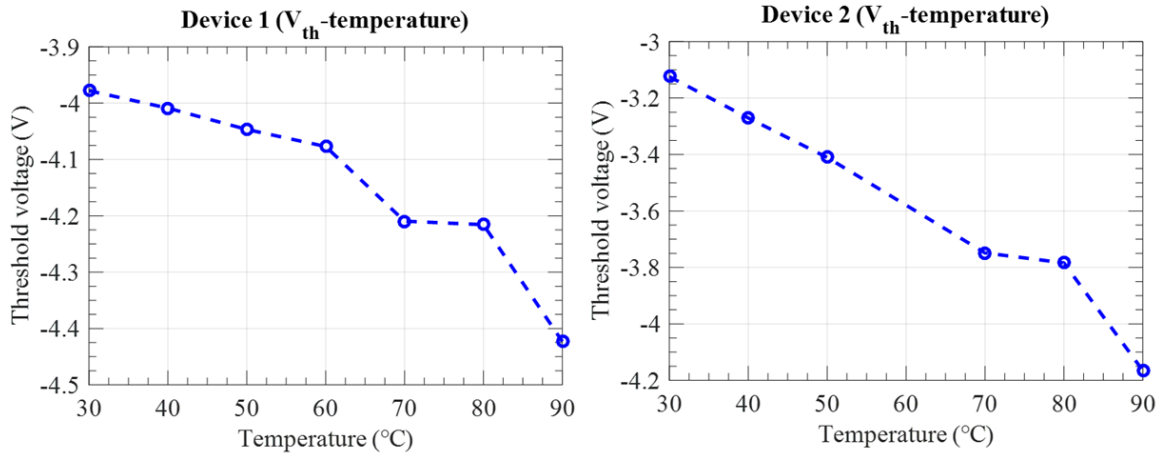


Figure 4.13: Threshold voltage for the two devices with temperature.

The behavior for the second device was almost linear comparing to the first device.

4.5.2 Traps measurements before ageing

Traps measurements before ageing will be presented in this section. For the details of the theoretical, measurement method and installation, one can consult chapter 3. The activation energies extraction will not always be performed because of the difficulty of following the time constants for some transient current measurements as will be presented for drain lag measurements. Then, a comparison of current transients before and after ageing will be presented. The percentage of change of the dynamic transient current $\Delta I_{DS}(t)$ between two maxima will also be another parameter that will be followed by ageing.

4.5.2.1 Drain lag measurements before ageing and difficulty for parameters extraction

The test settings of this current transient test (drain lag) are shown in *Table 4.9*. It should be noted that we were limited to 100 V for stress in the OFF state because several campaigns (especially with the commercial components 30A-650 V GaN Systems) were directly broken after ageing by applying a high drain voltage. Therefore, the device was roughly estimated to resist this bias after ageing.

It should also be noted that we have observed that performing traps measurements in a single day is necessary for better stability to follow the transient behavior as a function of the temperature. In order to reduce the measurements time, the number of the transient measurements was reduced. This reduction was based on performing the transient measurements for an intermediate sampling rate (2 ms) between low sampling rate (10 ms) and high sampling rate (200 μ s). We found that the measurements give a sufficient information of the quality of the current transients.

Test settings (Drain lag)	Corresponding values
Gate OFF stress	-7V
Gate ON stress	-3V
Drain OFF stress	100V
Drain ON stress	700mV

4.5. CHARACTERIZATIONS BEFORE AGEING

OFF stress Time	1s
Sampling interval	2ms

Table 4.9: Test settings for drain lag measurements.

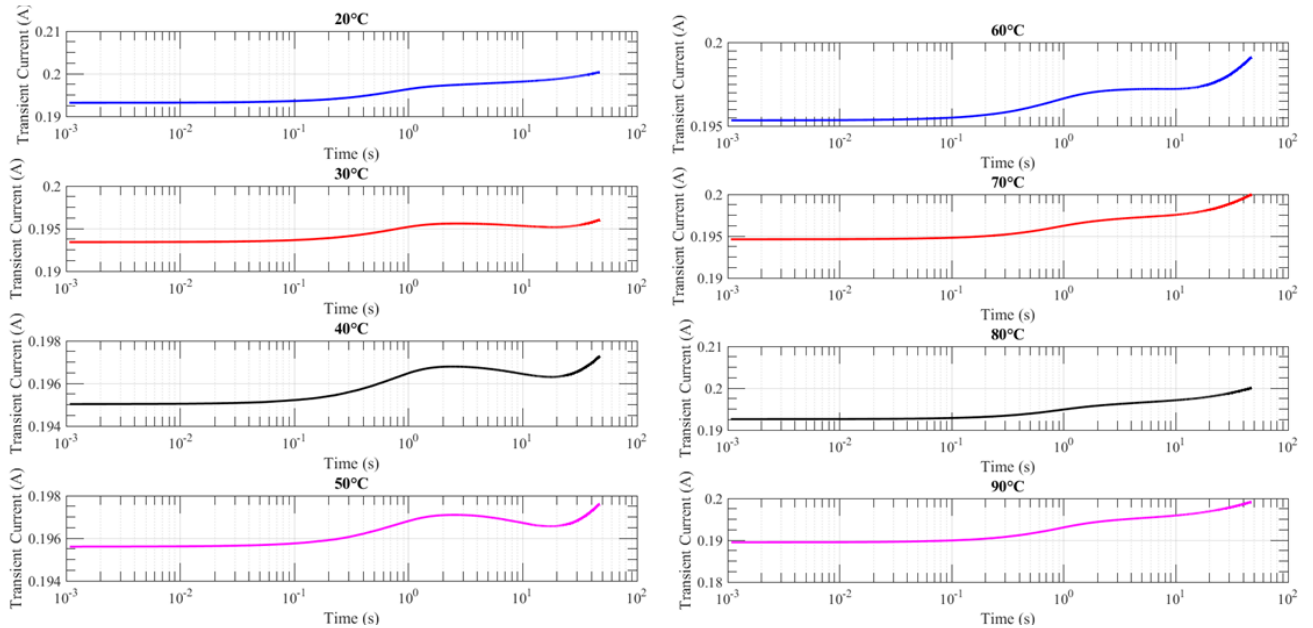


Figure 4.14: Drain lag transient measurements (with temperature).

The drain lag measurements are presented in *Figure 4.14* for the first device. A traps behavior that can be followed was not easily revealed with these measurements. There is an overlap between several traps time constants. This overlap was found for measurements performed for both devices. For low temperature (20°C and 30°C) and for high temperature (70°C-90°C), time constants are almost no detectable. It is for this reason that we have decided to compare only the transient current before and after ageing without trapping parameters extraction for these measurements. One explanation for this observed transient current is rather that drain and gate lag phenomena may occur simultaneously.

4.5.3 Gate lag measurements before ageing

A traps behavior that can be followed has been successfully revealed with these measurements for both devices. As shown in *Figure 4.15*, selected transient current measurements with temperature (40°C, 50°C, 70°C and 90°C) are presented for both devices.

4.5. CHARACTERIZATIONS BEFORE AGEING

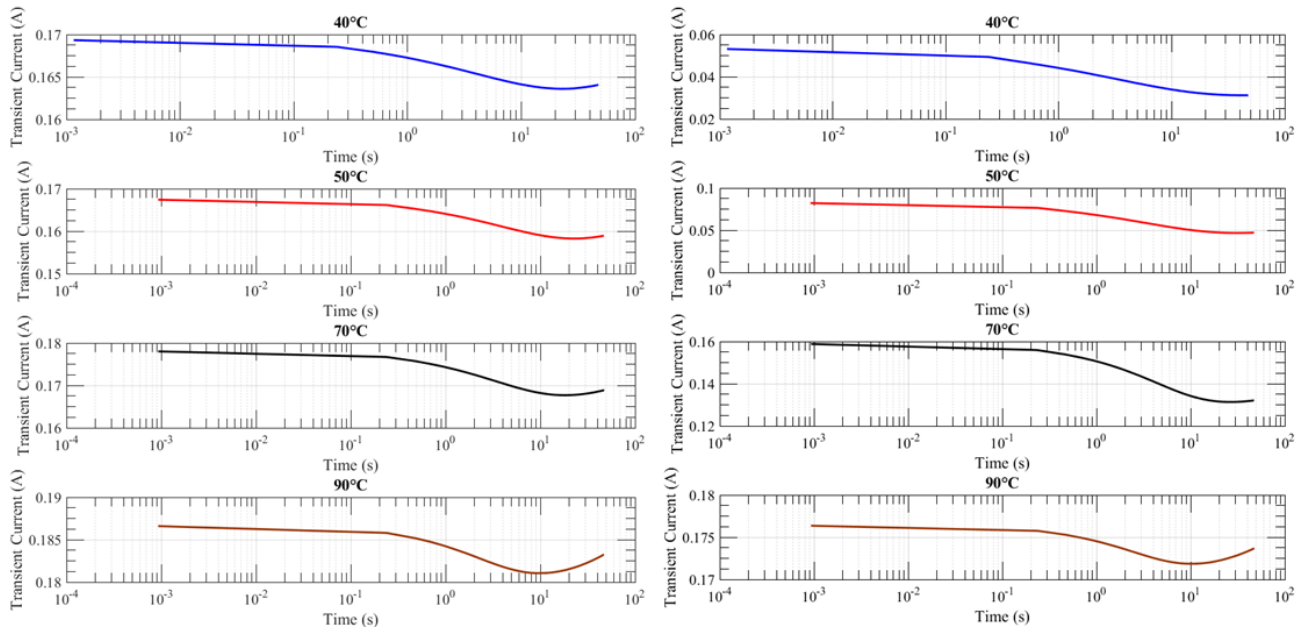


Figure 4.15: Transient gate lag measurements for some chosen temperatures (40°C, 50°C, 70°C and 90°C) for both devices (First device-left) and (Second device-right)

Test settings (Gate lag)	Corresponding values
Gate OFF stress	-7V
Gate ON stress	-3V
Drain OFF stress	1V
Drain ON stress	700mV
OFF stress Time	1s
Sampling interval	2ms

Table 4.10: Test settings for gate lag measurements.

Activation energies for both device:

General note: Regarding the extraction of trap parameters, for these components, the detected transient current could not give (using the prony method) perfectly linear relations between $\frac{q}{kT}$ and $\ln(\tau T^2)$. This problem makes the attribution of activation energies is very approximate. Furthermore, the number of points or the measurements were made was not sufficient to have more certainty. The difficulty of carrying out the characterization methodology with a large number of measurement points should be taken into account. It was important to take into account the very long traps time constants which sometimes forced to carry out the characterization campaign in a single day. This methodology can actually be improved to better detect and analyze and especially extract the traps parameters.

However, for the first device, three activation energies have been successfully revealed. The extraction parameters method is presented in chapter 3.

4.5. CHARACTERIZATIONS BEFORE AGEING

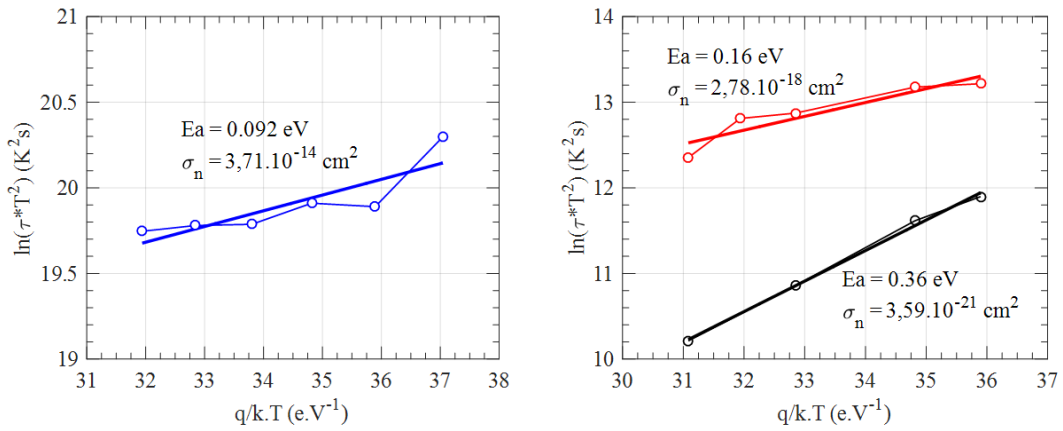


Figure 4.16: Arrhenius before ageing (First device).

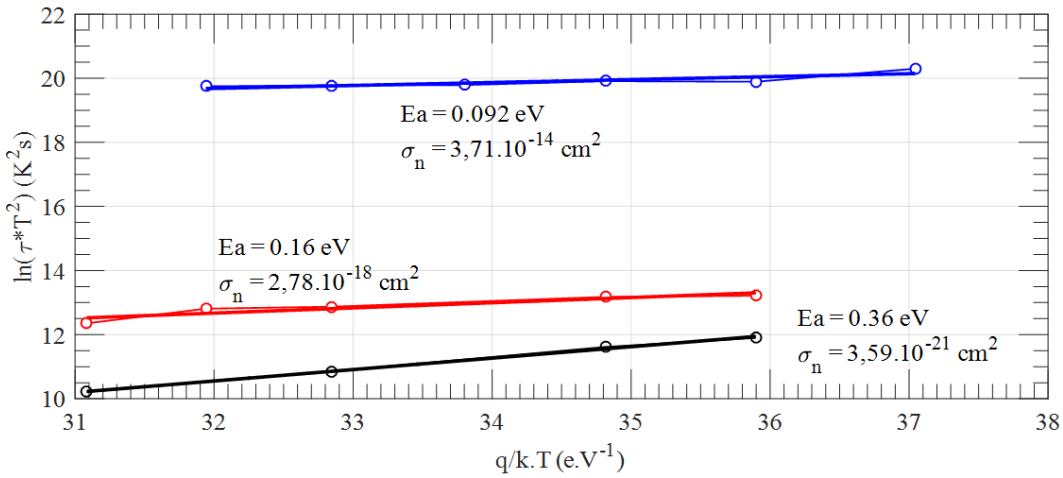


Figure 4.17: Arrhenius before ageing (First device) – different scale.

A linear regression has been used to identify the activation energies, this method is very approximated and an error in these values can occur.

The identification of these activation energies is presented in the following table. We have also found, like the GaN Systems devices, signatures that correspond to N- vacancy and impurities that can be attributed to hydrogen or carbon. Signature that corresponds to N- vacancy near surface traps or traps generated into the GaN material has also been revealed.

Traps physical parameters	Identification
$E_a = 0.092\text{eV}$ $\sigma_n = 3.71 \times 10^{-14}\text{cm}^2$	It may be correlated with N vacancy (V_N) [Gas 08]
$E_a = 0.16\text{eV}$ $\sigma_n = 2.78 \times 10^{-18}\text{cm}^2$	It can be correlated with hydrogen or carbon impurities [Bis 13]
$E_a = 0.36\text{eV}$ $\sigma_n = 3.59 \times 10^{-21}\text{cm}^2$	N-Vacancy near surface traps [Has 03] or Traps located in the GaN layer [Mar 03]

Table 4.11: Traps physical parameters extraction from Arrhenius.

4.5. CHARACTERIZATIONS BEFORE AGEING

On the other hand, for the second device, only two activation energies have been successfully revealed.

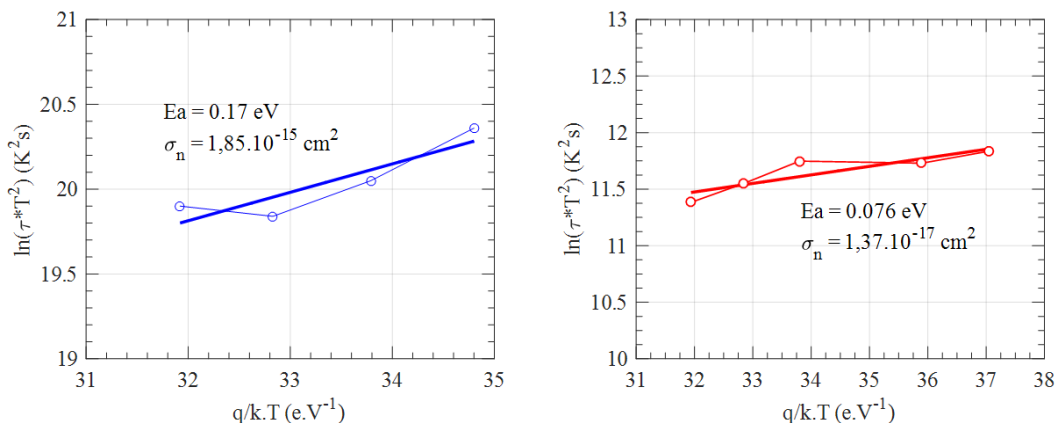


Figure 4.18: Arrhenius before ageing (Second device).

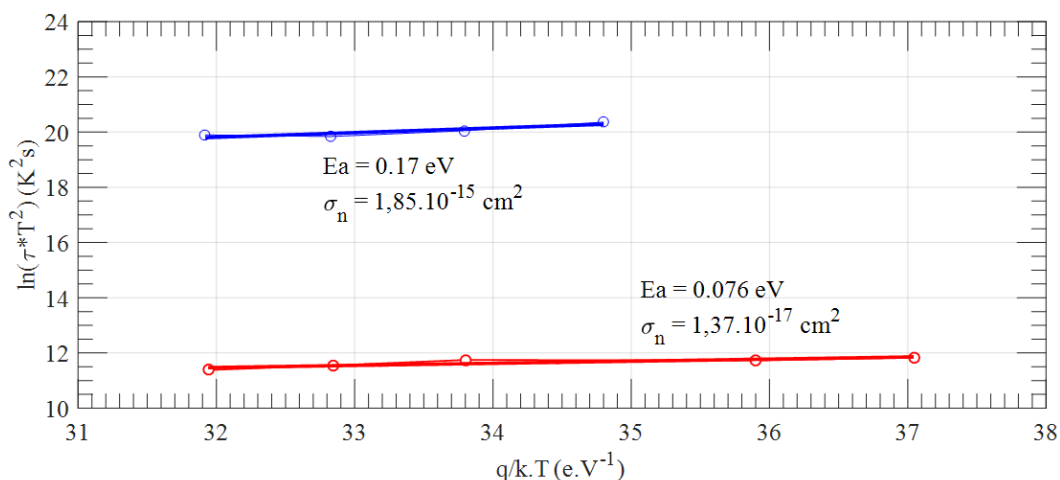


Figure 4.19: Arrhenius before ageing (Second device)— different scale.

We should also note that during the extraction of trap parameters, there is sometimes a single point of temperature that does not follow the expected trapping behavior, which may reflect a measurement error. In this case, this temperature point is neglected.

The identification of these activation energies is presented in the following table. We have also found signatures close to N vacancy and impurities that close to be attributed to hydrogen or carbon.

Traps physical parameters	Identification
$E_a = 0.076 \text{ eV}$ $\sigma_n = 1.85 \times 10^{-15} \text{ cm}^2$	(It is not an exactly known signature) It is close to N vacancy (V_N) [Gas 08]
$E_a = 0.17 \text{ eV}$ $\sigma_n = 1.37 \times 10^{-17} \text{ cm}^2$	(It is not an exactly known signature) It may be correlated with hydrogen or carbon impurities [Bis 13]

Table 4.12: Traps physical parameters extraction from Arrhenius.

4.6 Power cycling test results

4.6.1 Test-bench:

The used test bench presented in *Figure 4.20* was carried out to be able to cycle 12 components simultaneously; for this reason, it can be remarkable that there are several thermocouple and wires not usable. The connections of these parts of the bench test are presented in *Figure 4.6*.

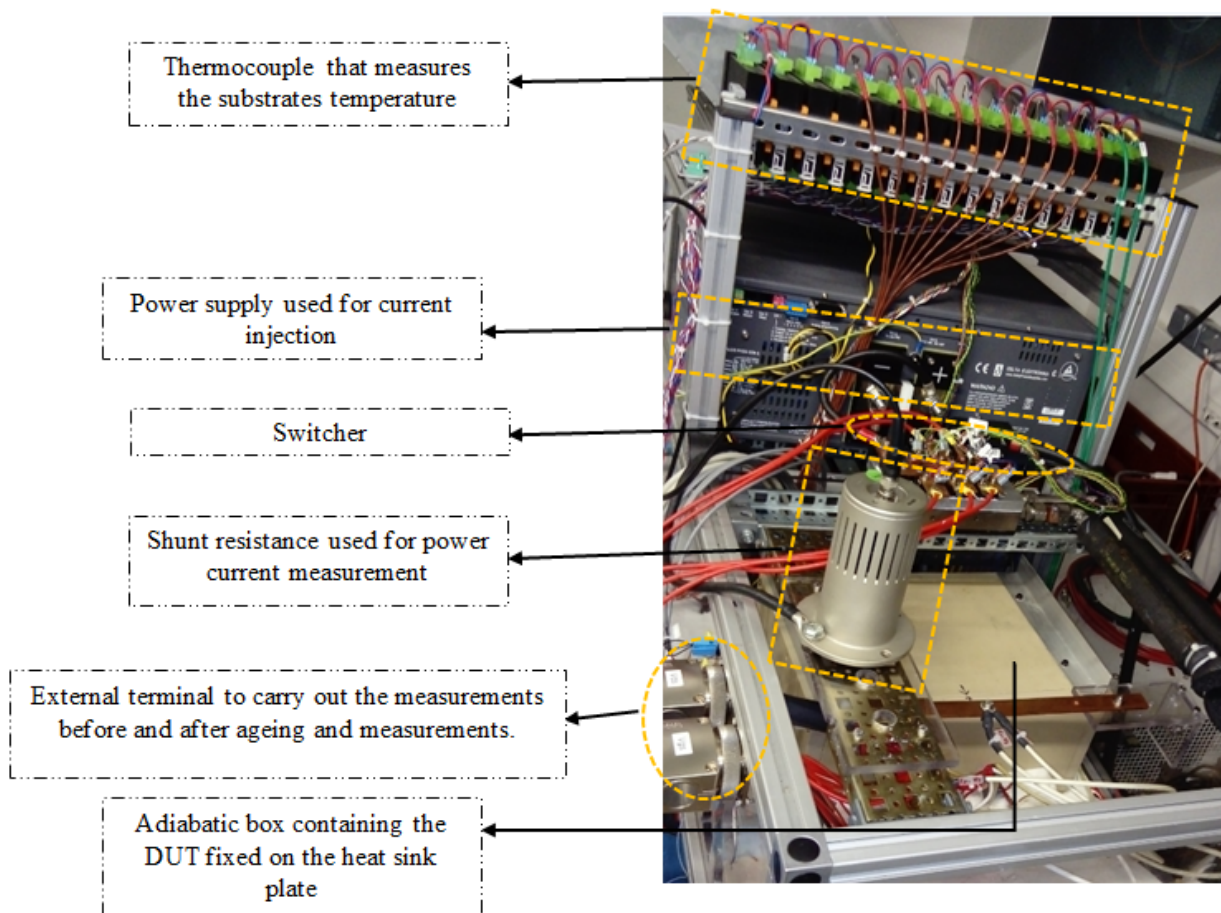


Figure 4.20: Test bench.

As shown in *Figure 4.21*, the two devices reported on the DCB have been reported on the heat-sink plate, by inserting a thin layer of thermal grease at the interface as explained in the general methodology section. These cables maintain the high temperature ($>200^{\circ}\text{C}$). There are power and measurement cables. For each device, we have six connections: two for the drain (power and measurement), one for the applied gate voltage and three for the source (power and measurement).

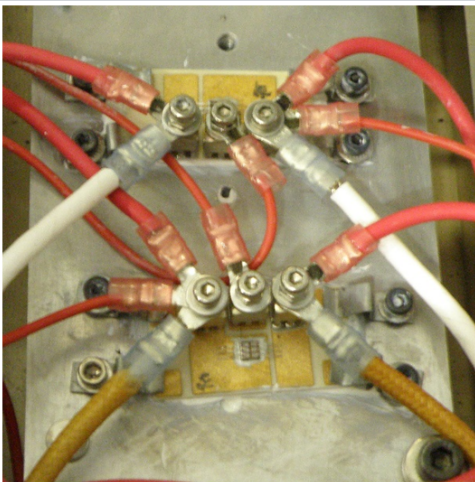


Figure 4.21: Devices reported on DCB mounted on the metal plate.

4.6.2 Thermosensitive parameter

The thermo-sensitive electrical parameter was chosen to be the drain-source voltage. We found a temperature-dependence of this parameter. Furthermore, this dependence has been found to be linear. In order to establish the relation between the measured drain-source voltage and the junction temperature, we follow the next flow. After the DCB being fixed on the heat-sink plate, we adjust the device temperature and we measure the substrate temperature. A time of 30 minutes was found to be required for the temperature stabilization. After this time, we consider that the junction temperature (T_j) has almost the same value for the substrate temperature (T_s). A DC current level of 500 mA (I_{sense}) is then applied, the self-heating is estimated to be negligible at this current level. The drain-to source voltage is measured at these conditions. We repeat these steps at each temperature level. Finally, we establish a mathematical relationship that will be used to estimate the junction temperature by measuring the drain-source voltage during the power cycling test.

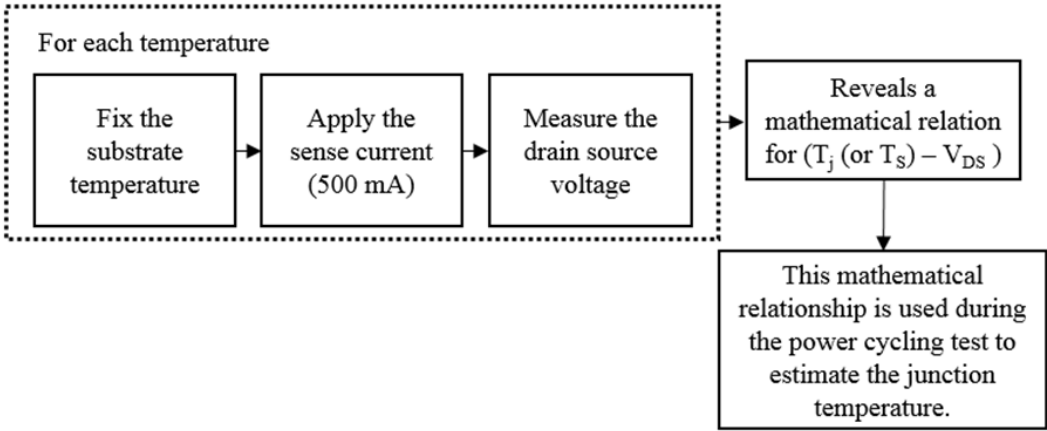


Figure 4.22: Measurements flow to establish and use the thermosensitive parameter (T_j is assumed to be T_s).

The mathematical relations deduced by a linear regression from experimental measurements for both devices under test can be written as follows:

4.6. POWER CYCLING TEST RESULTS

$$V_{DS1} = 2.1873 \times 10^{-4} \times T_{s1} + 0.0208 \quad (4.1)$$

$$V_{DS2} = 2.2457 \times 10^{-4} \times T_{s2} + 0.0216 \quad (4.2)$$

V_{DS1} , V_{DS2} are the drain-source voltages of the first and the second device respectively, T_{s1} , T_{s2} are the substrate temperatures (estimated to be equal to the junction temperature) for the first and the second device respectively. Experimental measurements and linear regression are presented in *Figure 4.23*.

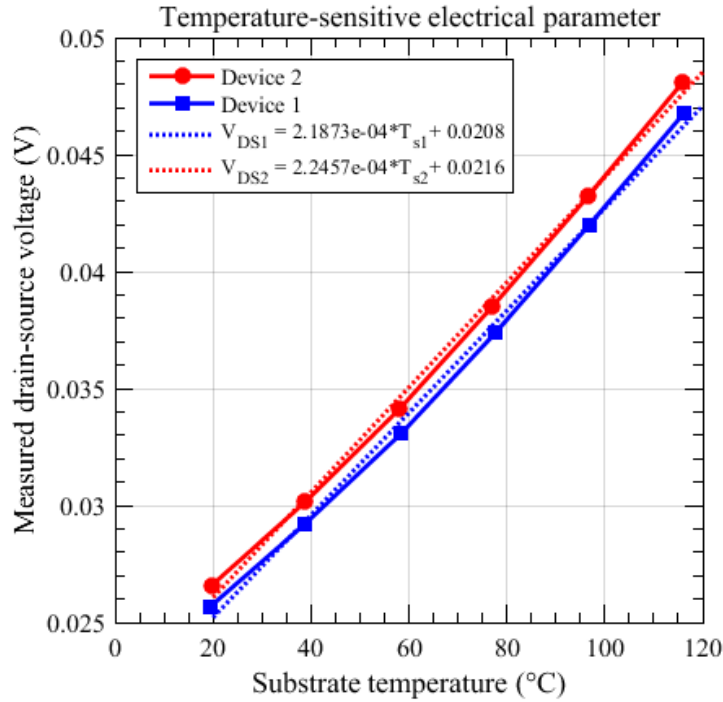


Figure 4.23: Relationship between the junction temperature and the voltage measurement ($I_{sense}=500mA$).

Although the TSEP method has been used, it can not be estimate correctly the junction temperature. After the shift of the electrical characteristics during ageing, the calibration curves will not be very accurate for an estimation of the junction temperature. So even though the TSEP method was used, we also checked the component's non-overstress during power cycling. This verification was based on the ageing behavior of the component which is towards negative values of threshold voltage. This shift induces a higher power current and the linear function of the measurement with temperature will be lower. we estimate that for this type of components, the junction temperature decreases with ageing. One solution for this problem is to have a direct measurement of the fiber optic junction temperature. During our ageing campaign, we added a component with an optical fiber, but the component was broken during ageing.

4.6.3 Experimental results

4.6.3.1 Power cycles

The test conditions are the following. A constant current of 20 A is passed throughout the device for a duration of 2s. This current induces a self-heating in the device by $\Delta T \approx 100^\circ C$. Then, the device

4.6. POWER CYCLING TEST RESULTS

is cooling down during 6s. A typical cycle for the two devices is presented in *Figure 4.24*. The top figures present the constant injected power current measured by shunt resistance, and the measured the drain-source voltage. For the figure below, the substrate temperature measured by the thermocouple is presented. The temperature of the thermal conditioner was fixed at ($T_{ref} = 20\text{ }^{\circ}\text{C}$). Due to losses linked to a thermal contact, the temperature at the substrate was not found to be exactly equal to the temperature at the thermal conditioner, a difference between 1°C and 2°C was found.

From this cycle, we observe the following:

1. The evolution of the drain-source voltage increases during the power current injection. This evolution reflects the evolution of the junction temperature. This evolution was linear with the junction temperature as presented in the relation of the thermo-sensitive parameter.
2. This measured drain-source voltage reaches a maximum value before the cut of the injected power current. The temperature at this point presents the maximum junction temperature T_{Jmax} . This temperature is measured just after the power current switch-off. The measured drain source voltage continues to decrease reflecting the cooling process until reaching the reference temperature imposed by the thermal conditioner (T_{Jmin}).
3. After the injection of the power current, the substrate begins to warm up but with a delayed response. This delay reflects the time taken for the heat transfer before reaching the substrate. A temperature swing (ΔT_s) at the substrate level up to 3.8°C was measured.

As the injected current is measured by Shunt resistance, so it is visualized in both figures as a total measure. The micro-controller acts as a switch between the two components. The test conditions are the same for both devices (2s) of current power injection and (6s) of cooling.

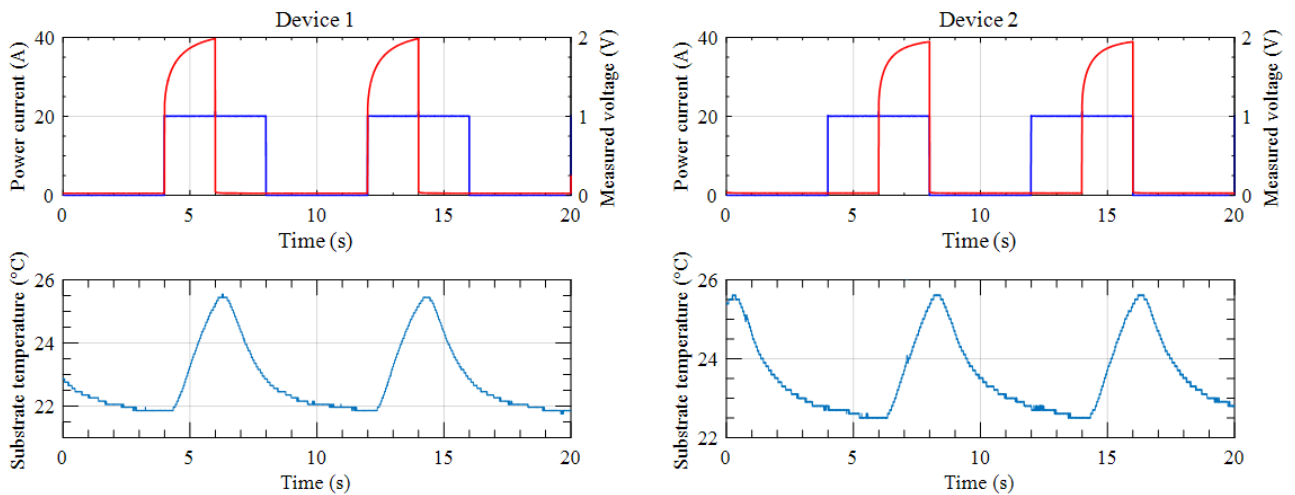


Figure 4.24: Power cycling test for both devices-two cycles in a row; the color red presents the measured drain-source voltage while the color blue presents the power current.

4.6.3.2 Ageing monitoring

The follow-up of ageing was performed by online measurements consisted mainly of measurements of the power and sense current, the drain-source voltage and the substrate temperature. As shown in *Figure 4.25*, the estimated maximum junction temperature T_{jmax} is about 122°C and the temperature swing $\Delta T_j = T_{jmax} - T_{jmin}$ is approximately 98°C .

4.6. POWER CYCLING TEST RESULTS

As an example of the ageing monitoring, we present the evolution of the junction temperature difference and the measured drain-source voltage at the power current cut for the first device for the first 500 cycles.

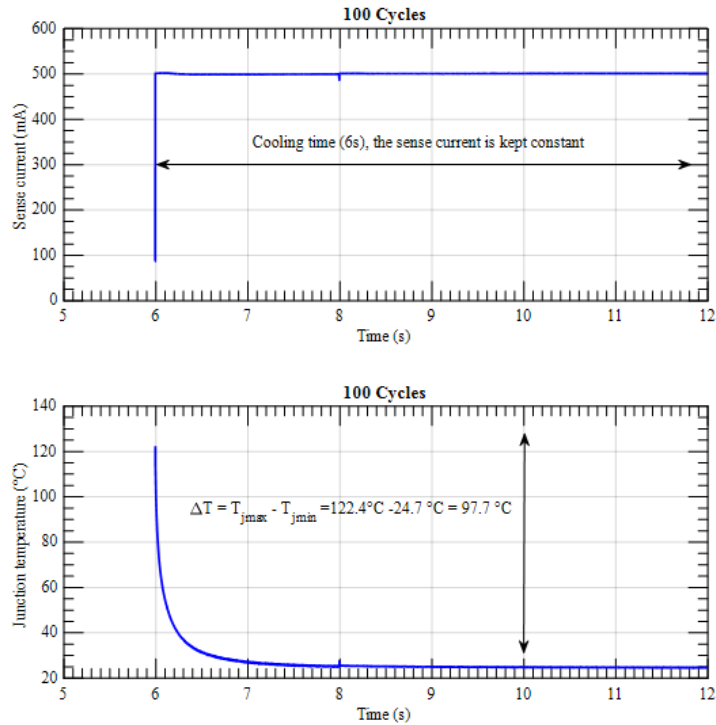


Figure 4.25: Sense current and deduced junction temperature during cooling.

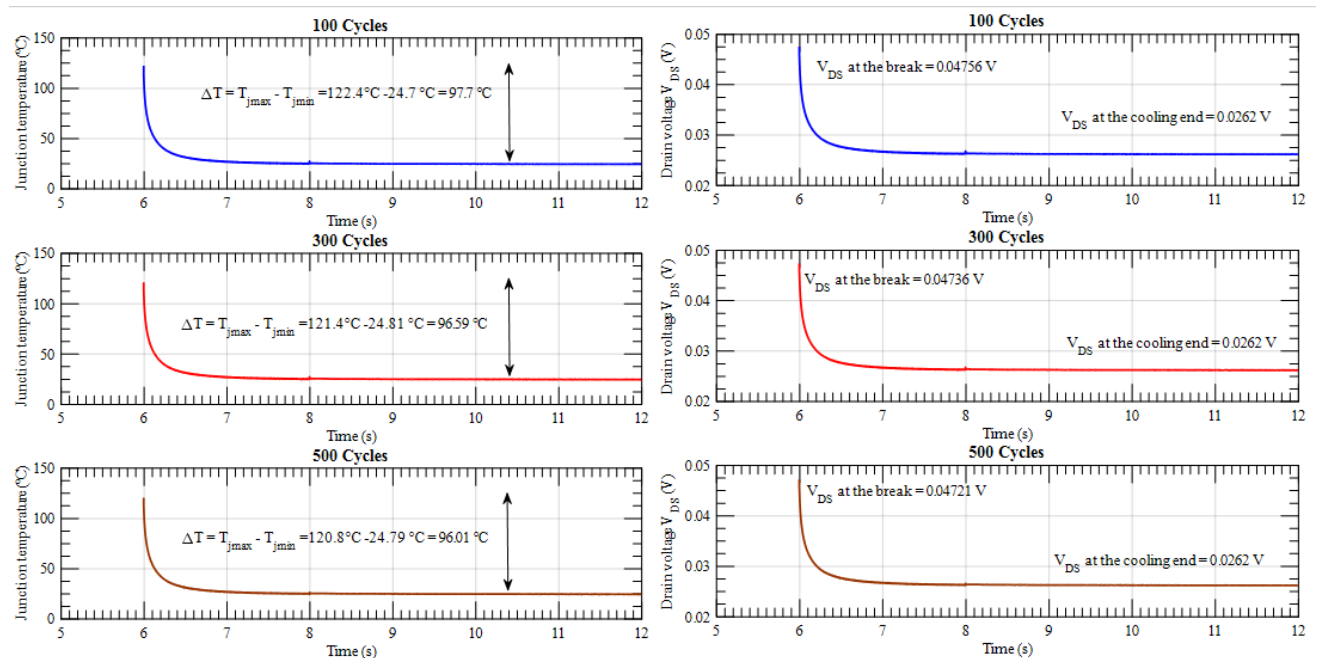


Figure 4.26: Deduced junction temperature during cooling and measured drain-source voltage for the cut for the first device for the first 500 cycles.

We noticed that the maximum junction temperature decreased slightly with the number of cycles. Although a temperature of 122°C was measured at 100 cycles, a temperature of 121°C was raised at 500 cycles. Similarly, the drain-source measured voltage value of 0.04756 V was measured at 100 cycles, this value decreased to 0.04721 V for 500 cycles. These two components were cycled until 2140 cycles where we noticed a continuation of this degradation. So we stopped the experimental tests, and we started the analyses to try to understand the evolution of the device characteristics. It should be noted that we are interested in this thesis to study the effect of ageing on the traps evolution and not an estimation of the lifetime or a detailed follow-up of degradations. It is for this reason that we have not gone too deep into the details and the follow-up of the power cycling test itself.

4.7 Characterizations and analysis after ageing

Now, we will go to analyses after ageing; We have chosen some characteristics to make a comparison. Beginning with the I-V characteristics, we observed that the electrical characteristics improved with the power cycling test for this structure. This result may be surprising, but we found it for both components.

Test settings ($I_{DS} - V_{DS}$)	Corresponding values
V_{DS} pulse duration	50 μ s
V_{GS} range	(-3.5 to -3) V with linear step of (0.5 V)
V_{GS} pulse duration	500 μ s
Delay between pulses	50 μ s
Polarization gate point in the OFF state	-6V
Polarization drain point in the OFF state	0V
Pulse period	1s
Measurement time	Average on 50 μ s at the end of the pulse
Temperature	30°C

Table 4.13: Test settings of the ($I_{DS} - V_{DS}$.)

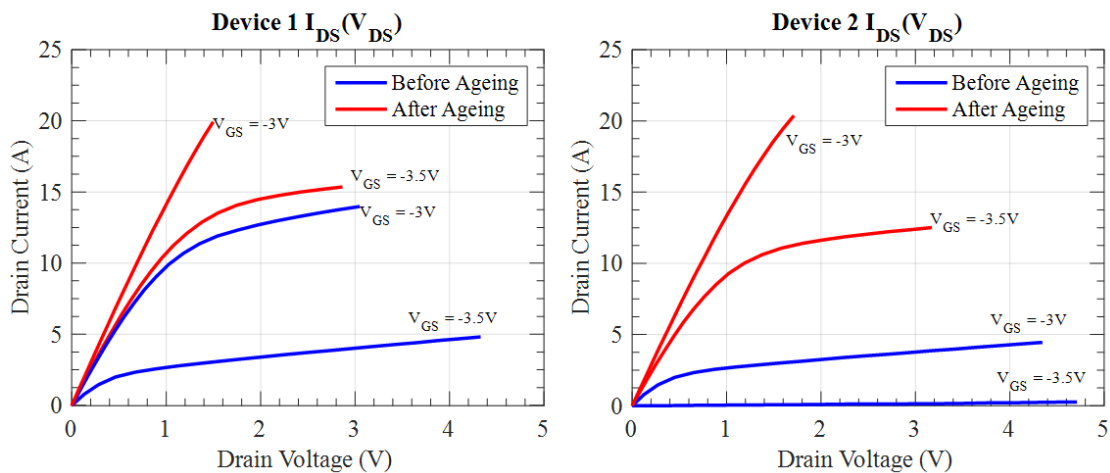


Figure 4.27: $I_{DS} - V_{DS}$ characteristics before and after ageing for the two devices.

As shown in Figure 4.28 and Figure 4.29, $I_{DS} - V_{GS}$ and transconductance measurements showed a reason for this characteristics shift. We noticed that in both components, there is a shift towards a more

4.7. CHARACTERIZATIONS AND ANALYSIS AFTER AGEING

negative value of the threshold voltage comparing before and after ageing. We observed that there was a larger shift for the second component. We also noticed that the values in the final state are much closer to the two components.

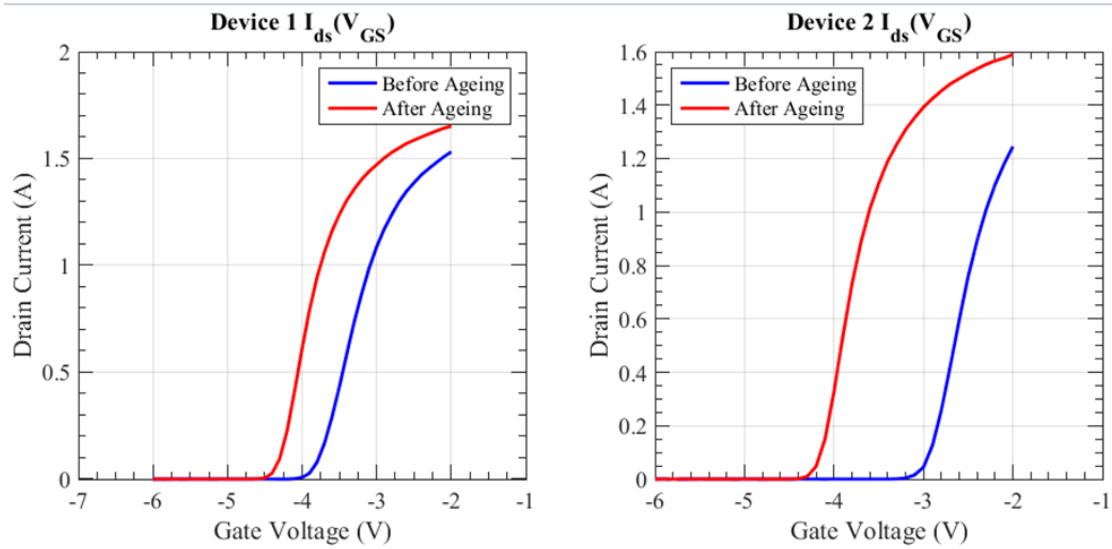


Figure 4.28: $I_{DS} - V_{GS}$ characteristics before and after ageing for the two devices.

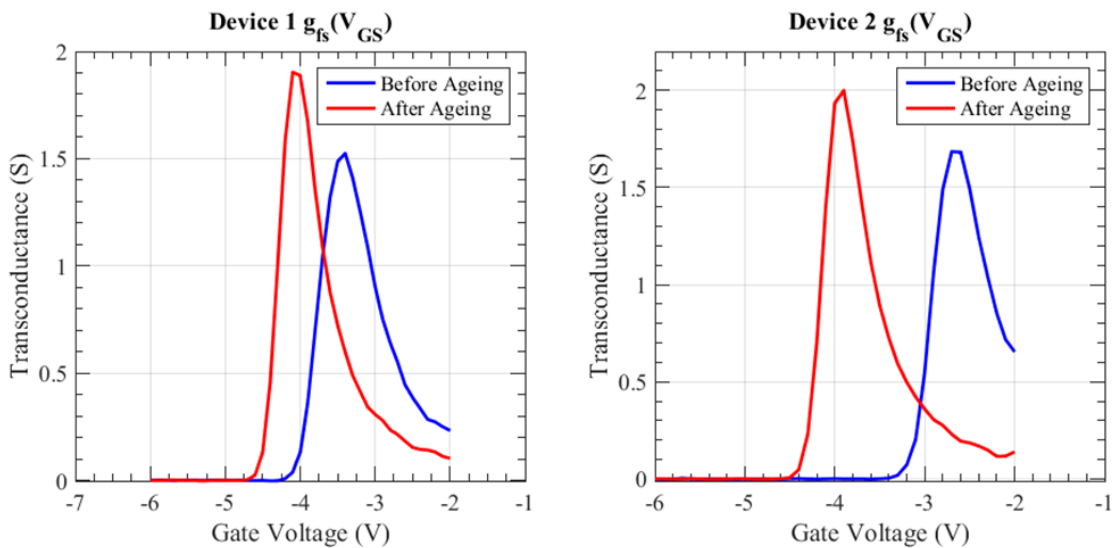


Figure 4.29: Trans-conductance characteristics before and after ageing for the two devices.

Test settings ($I_{DS} - V_{GS}$)	Corresponding values
V_{GS} pulse duration	500 μ s
V_{DS} constant	100mV
V_{GS} sweep	(-6 to -2)V
Polarization gate point in the OFF state	-6V
Pulse period	2s

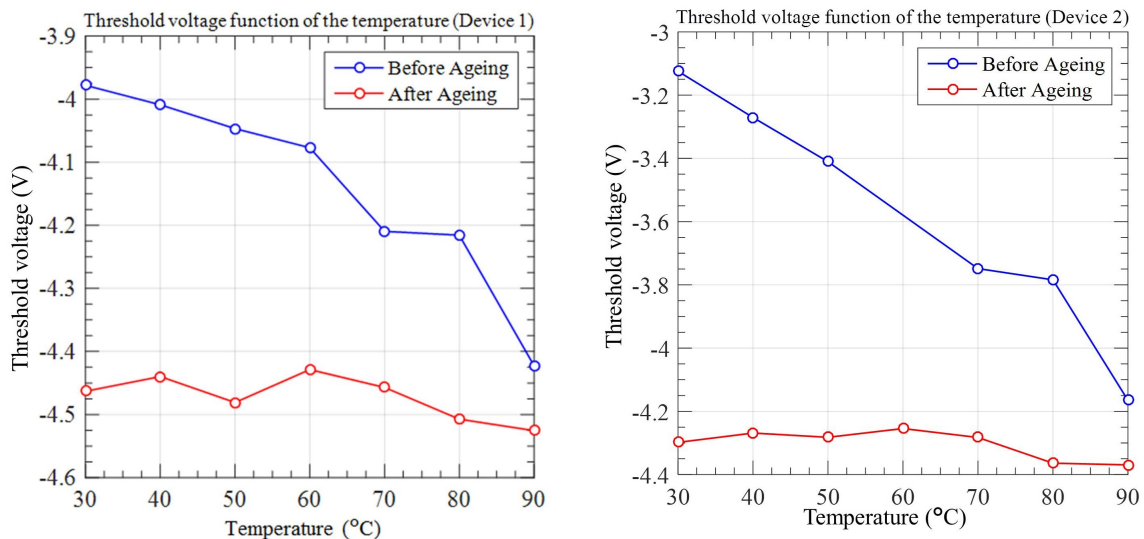
4.7. CHARACTERIZATIONS AND ANALYSIS AFTER AGEING

Measurement time	Average on 20 μs at the end of the pulse
Temperature	30 $^{\circ}\text{C}$

Table 4.14: Test settings of the ($I_{DS} - V_{GS}$.)

For the first component, the threshold voltage is estimated to be -3.978 V before ageing and -4.463 V after ageing. For the second device, before ageing, it was -3.124 V and after it turned to -4.298 V. So a threshold voltage shift is estimated to be -0.485 V for the first component and 1.174 V for the second device. These values are sufficient to create a huge shift in the device characteristics. Furthermore, we have also noted that the threshold voltage final value of the two devices is much related, which possibly means that there exist more traps that were generated.

Threshold voltage characteristics (with temperature): We present in the following the dependence of the threshold voltage with the temperature. We observed on both components a smaller variation ($|V_{th(90\text{degC})} - V_{th(30\text{degC})} = 0.063\text{V}$) on the first component and ($|V_{th(90\text{degC})} - V_{th(30\text{degC})} = 0.071\text{V}$) on the second component after ageing. So a quasi-stable behavior of the threshold voltage with the temperature was observed. There is no clear reason for this variation, but there is a possibility that the traps state dependence under the gate after ageing is not strongly dependent on temperature.



(a) Threshold voltage characteristics (with temperature) comparison before and after ageing (Device 1). (b) Threshold voltage characteristics (with temperature) comparison before and after ageing (Device 2).

Figure 4.30: Threshold voltage characteristics (with temperature) comparison before and after ageing.

In order to better understand the change in electrical characteristics after ageing, traps analysis is performed after ageing.

Drain lag transient measurements before and after ageing: The transient measurements of the drain lag before and after ageing for both devices are shown in *Figure 4.31*. We present only measurements for three different temperatures (70 $^{\circ}\text{C}$, 80 $^{\circ}\text{C}$ and 90 $^{\circ}\text{C}$). We recall that the transient measurements carried out before the ageing did not make it possible to extract activation energies.

4.7. CHARACTERIZATIONS AND ANALYSIS AFTER AGEING

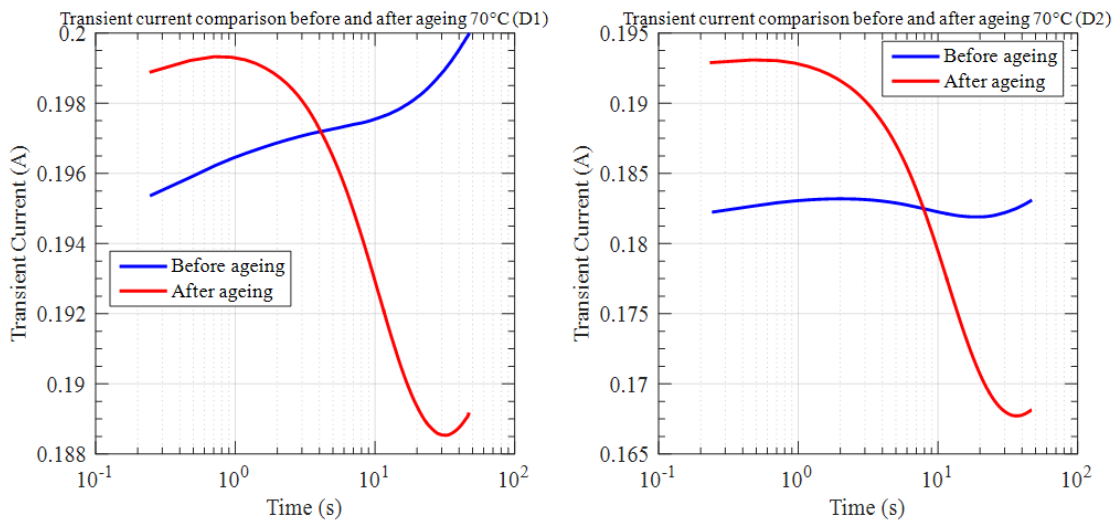


Figure 4.31: Transient measurements of the drain lag before and after ageing for both devices for (70 °C).

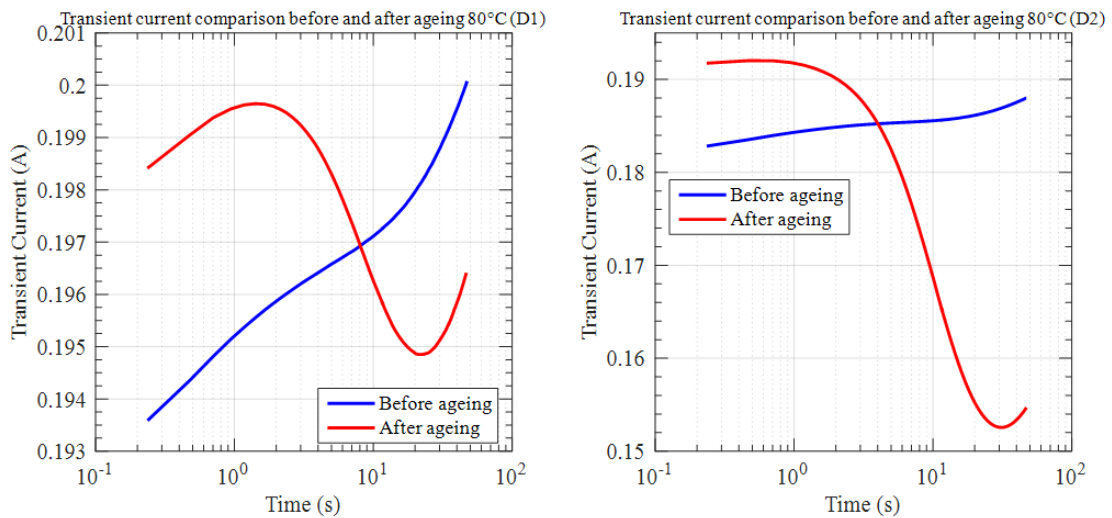


Figure 4.32: Transient measurements of the drain lag before and after ageing for both devices for (80 °C).

By these measurements, we observe that the quality of curves has changed in a very remarkable way for both components. This probably means that there has been a density of additional traps that has just been introduced into the structure and that affect the behavior of the transient current after ageing.

4.7. CHARACTERIZATIONS AND ANALYSIS AFTER AGEING

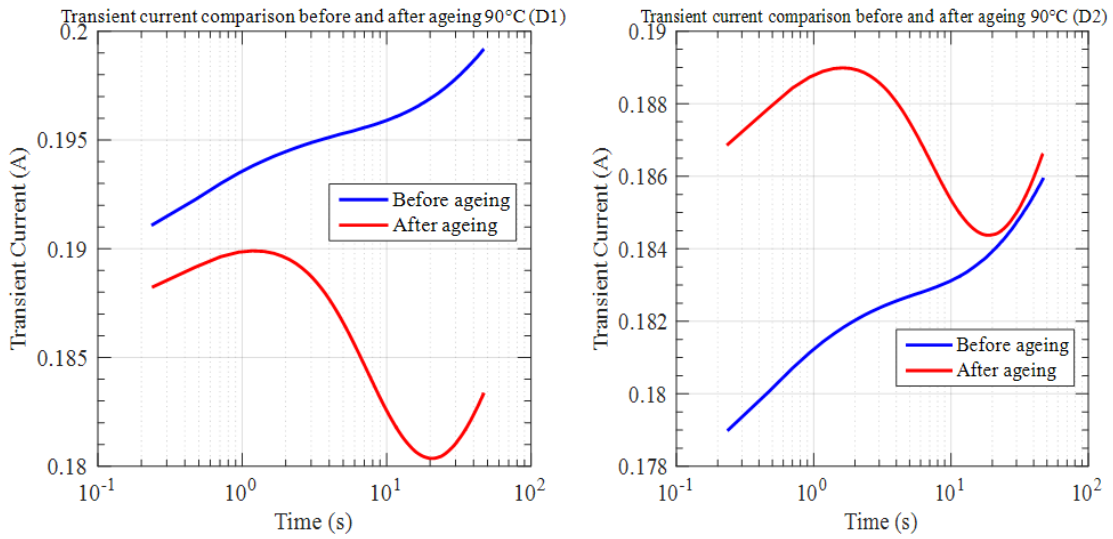


Figure 4.33: Transient measurements of the drain lag before and after ageing for both devices for (90 °C).

Gate lag transient measurements before and after ageing: For the gate lag, we have already noticed that we find almost the same quality of curves before and after ageing (*Figure 4.34*).

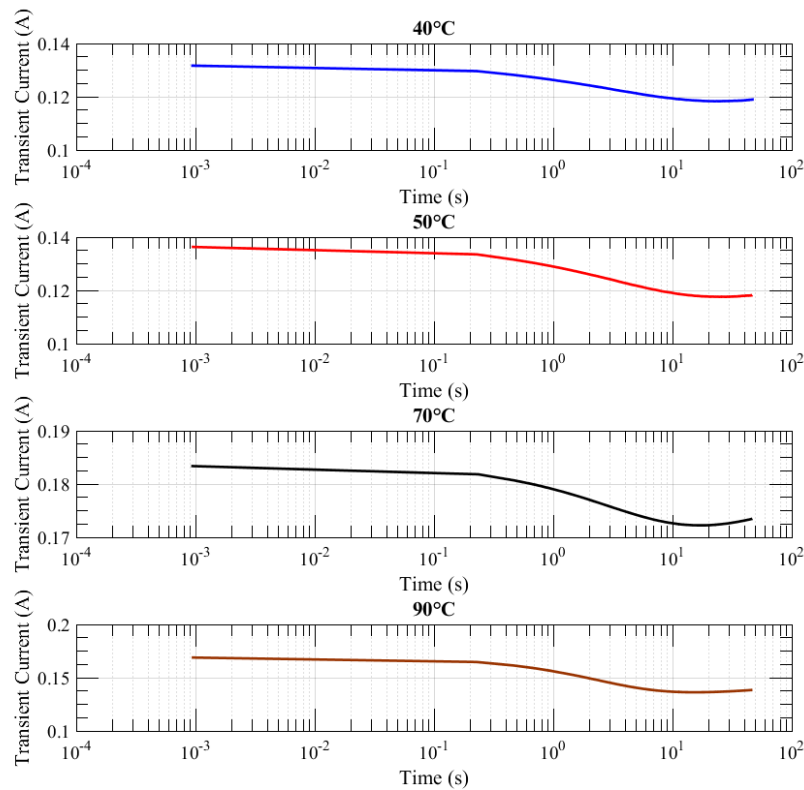


Figure 4.34: Transient current of the gate lag after ageing- First device.

4.7. CHARACTERIZATIONS AND ANALYSIS AFTER AGEING

However, a quantitative change has been detected. For this purpose, as shown in *Figure 4.35*, we have calculated the percentage change of the current transient that can reach 17% and that could perhaps be explained by an increase in the density of defects under the gate after the ageing test.

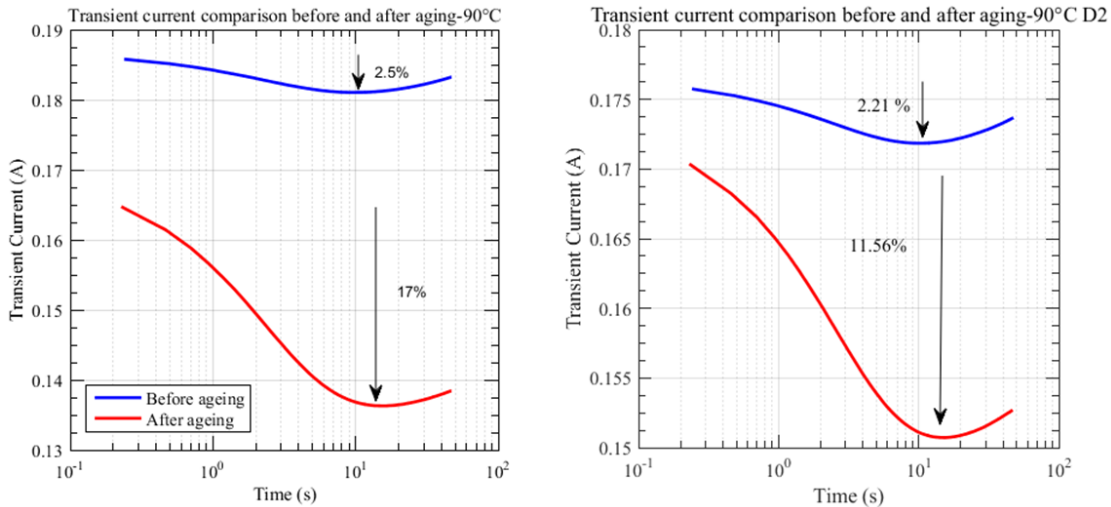


Figure 4.35: Comparison of transient current of gate lag before and after ageing.

Finally, we present the results of the Arrhenius law and the identification of traps signatures for both devices based on the gate lag transient measurements.

First device before and after ageing (Arrhenius):

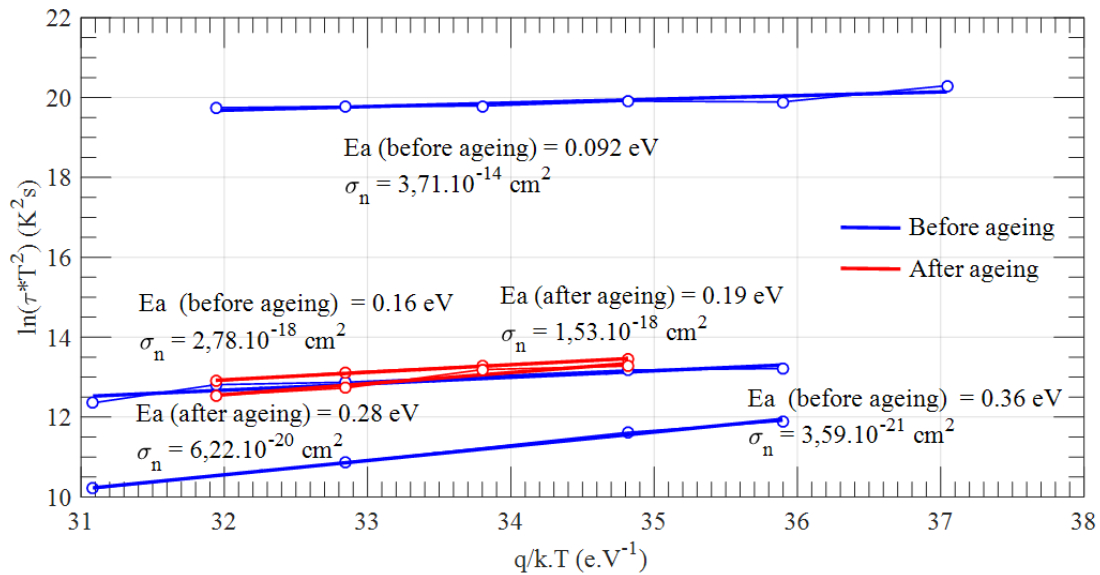
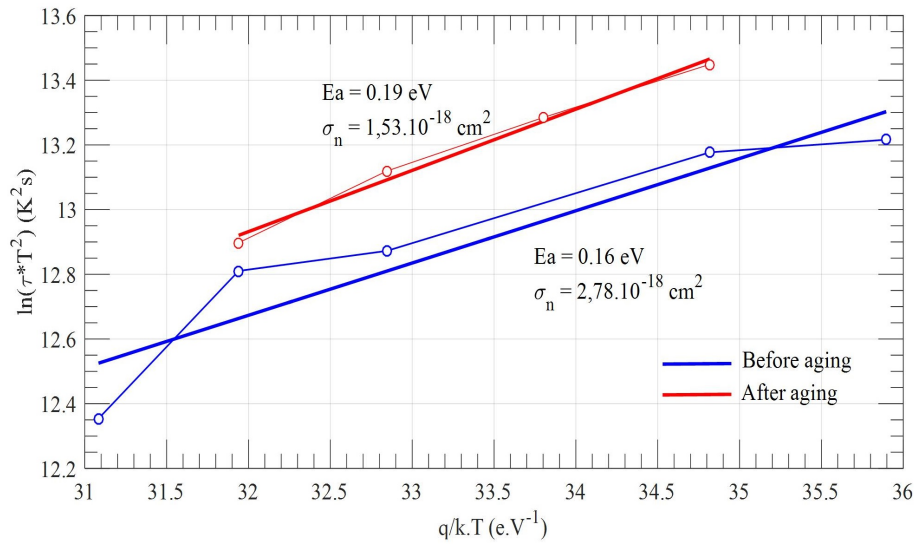
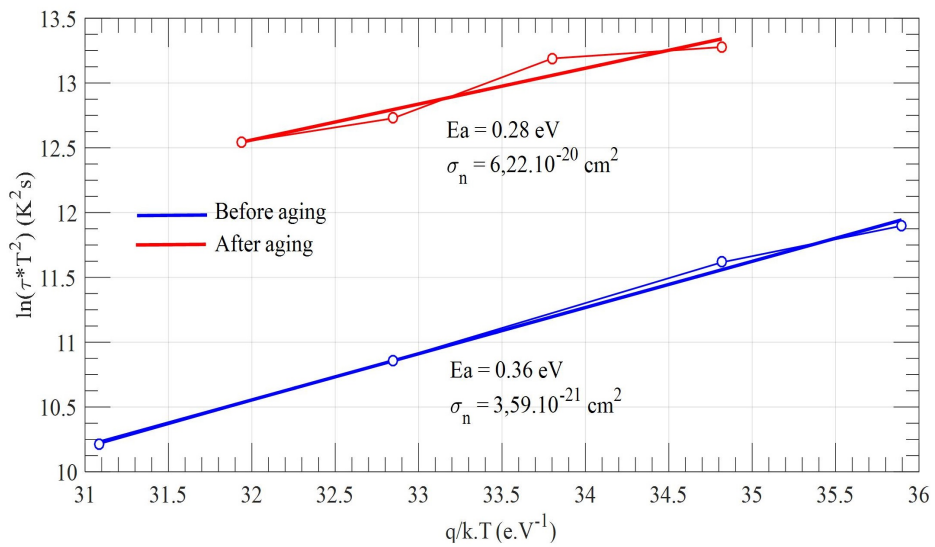


Figure 4.36: Arrhenius before and after ageing (First device).

4.7. CHARACTERIZATIONS AND ANALYSIS AFTER AGEING



(a) Different scale of 2 activation energies.



(b) Different scale of 2 activation energies.

Figure 4.37: Arrhenius before and after ageing (First device)-Different scales.

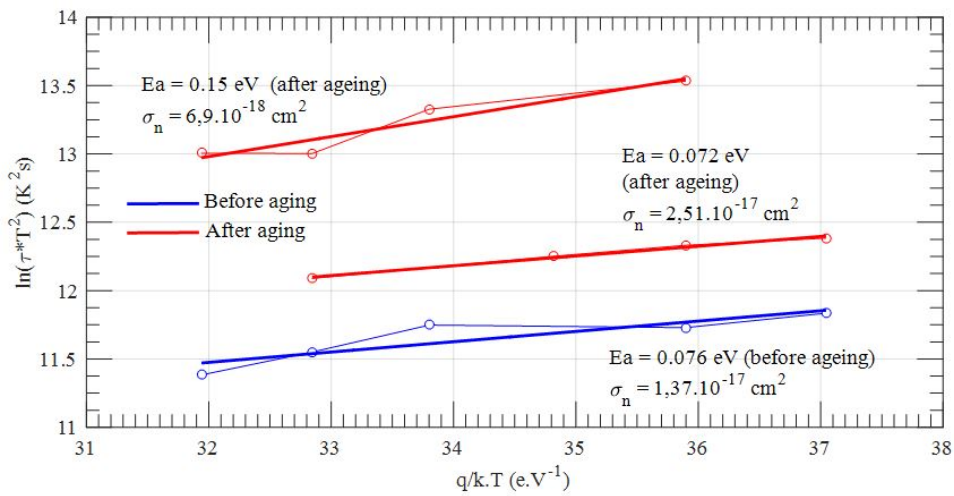
Traps physical parameters	Identification
$E_a = 0.092eV$ $\sigma_n = 3.71 \times 10^{-14} \text{ cm}^2$ (Before ageing)	It may be correlated with N vacancy (V_N) [Gas 08]
$E_a = 0.16eV$ $\sigma_n = 2.78 \times 10^{-18} \text{ cm}^2$ (Before ageing)	It can be correlated with hydrogen or carbon impurities [Bis 13]
$E_a = 0.36eV$ $\sigma_n = 3.59 \times 10^{-21} \text{ cm}^2$ (Before ageing)	N-Vacancy near surface traps [Has 03] or Traps located in the GaN layer [Mar 03]

4.7. CHARACTERIZATIONS AND ANALYSIS AFTER AGEING

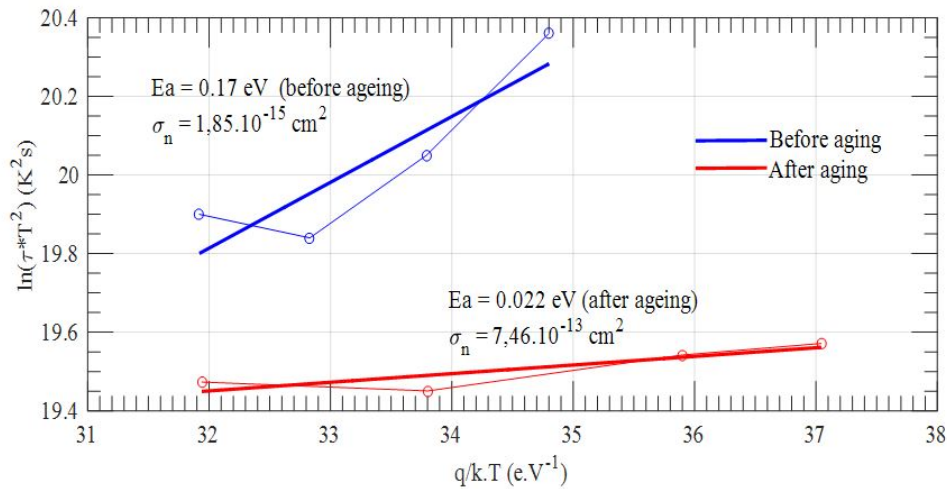
$E_a = 0.28\text{eV}$ $\sigma_n = 6.22 \times 10^{-20}\text{cm}^2$ (After ageing)	Very close to AlGaIn surface states (0.3 eV) [Bis 13]
$E_a = 0.19\text{eV}$ $\sigma_n = 1.53 \times 10^{-18}\text{cm}^2$ (After ageing)	Traps located between the 2DEG and the substrate [Gas 06]

Table 4.15: Identification of traps signatures before and after ageing- First device.

Second device before and after ageing (Arrhenius):



(a) Different scale of 3 activation energies.



(b) Different scale of 2 activation energies.

Figure 4.38: Arrhenius before and after ageing (Second device)-Different scales.

4.7. CHARACTERIZATIONS AND ANALYSIS AFTER AGEING

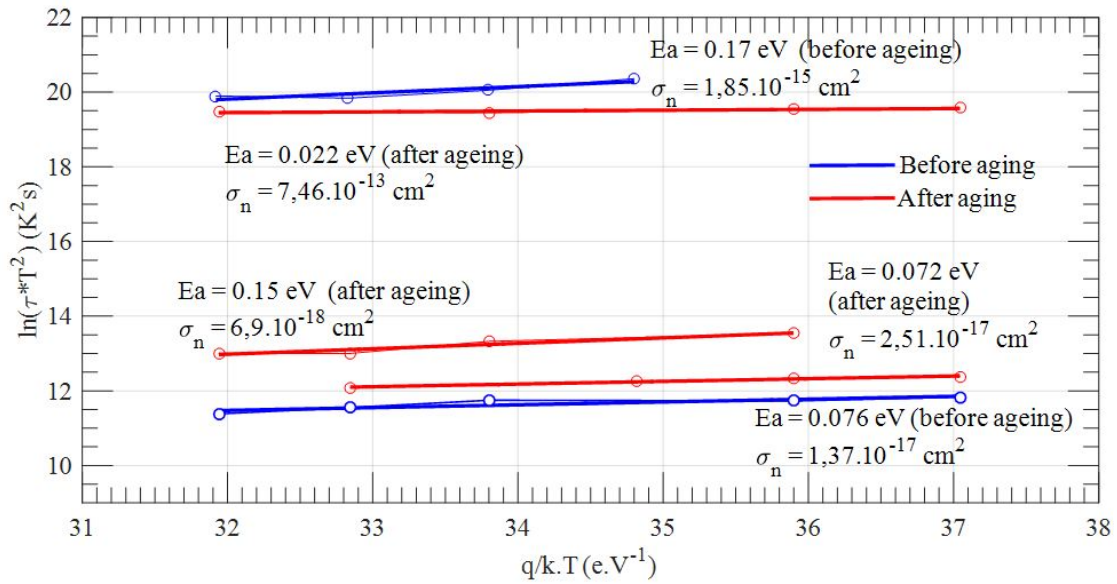


Figure 4.39: Arrhenius before and after ageing (Second device).

Traps physical parameters	Identification
$E_a = 0.076eV$ $\sigma_n = 1.85 \times 10^{-15}cm^2$ (Before ageing)	(It is not an exactly known signature) It is close to N vacancy (V_N) [Gas 08]
$E_a = 0.17eV$ $\sigma_n = 1.37 \times 10^{-17}cm^2$ (Before ageing)	(It is not an exactly known signature) It may be correlated with hydrogen or carbon impurities [Bis 13]
$E_a = 0.22eV$ $\sigma_n = 7.46 \times 10^{-13}cm^2$ (After ageing)	It may also correspond to N-Vacancy (V_N) [Gas 08]
$E_a = 0.15eV$ $\sigma_n = 6.9 \times 10^{-18}cm^2$ (After ageing)	(It is not an exactly known signature) It may be correlated with hydrogen or carbon impurities [Bis 13]
$E_a = 0.072eV$ $\sigma_n = 2.51 \times 10^{-17}cm^2$ (After ageing)	(It is not an exactly known signature) It may also correspond to N-Vacancy (V_N) [Gas 08]

Table 4.16: Identification of traps signatures before and after ageing- Second device.

4.8 Conclusion

Ageing tests based on power cycling were performed on $\text{Al}_2\text{O}_3/\text{AlGaIn}/\text{GaIn}$ MOS–HEMTs manufactured by CEA–LETI to understand its effect on the traps evolution for the first time. Power stress of 20A for 2s which induces a self-heating of $\Delta T \approx 100^\circ\text{C}$ was applied to both components for 2140 cycles. A degradation at the drain-source voltage was detected. The ageing campaign was stopped at this point. Analyzes after ageing showed indeed a shift in the threshold voltage which is mainly due to an evolution of the traps. For the first component, the threshold voltage is estimated to be -3.978 V before ageing and -4.463 V after ageing. For the second device, before ageing, it was 3.124 V and after ageing it turned to -4.298 V. So a threshold voltage shift is estimated to be -0.485 V for the first component and 1.174 V for the second device. In fact, these values are sufficient to create an important shift in the device electrical characteristics. These analyzes were supported by the gate and drain lag measurements. The method flow of chapter 3 was used to extract the traps parameters before and after ageing. Regarding the transient measurements of drain lag, we have observed a qualitative and quantitative change in the transient measurements that changes with the temperature. Due to the difficulty of extracting traps parameters from these measurements, the transient current measurements were only presented. Concerning the gate lag measurements, we have observed a rather quantitative change, we have calculated the percentage change of the current transient. Effectively, a percentage that can reach 17% has been detected compared to 2.5% for the first device, while a percentage of 11.56% has been detected compared to 2.21% for the second device. Regarding traps parameters extraction, activation energies of $E_a = 0.092, 0.16$ and 0.36 was revealed before ageing compared to $E_a = 0.28$ and 0.19 after ageing for the first device. For the second device, the activation energies of $E_a = 0.076, 0.16$ and 0.36 compared to $E_a = 0.28$ and 0.19 after ageing was revealed.

General conclusion and perspectives

In this thesis, we presented some elements of GaN HEMTs reliability studies. We presented some points of contributions at the theoretical and experimental levels. The research work on GaN devices is still expanding as these components are still shown interest to the scientific community. The thesis work was focalized on the traps phenomenon as it affects these device electrical characteristics greatly.

First of all, we started by presenting a bibliographical study relative to the work of the thesis. They represented 4 axes: 1-The physical understanding of the traps phenomenon that we used to understand the behavior of traps. 2-The electrical characterization of these traps, we have detailed a single method which is the transient drain current measurements; this method was used in the thesis to characterize and analyze the traps in these devices. 3-Physical modeling of HEMTs to develop it in order to take the traps into consideration. 4-Reliability tests that induce reversible degradation or irreversible.

This bibliographical study served as a basis for the presentation of the work of the thesis. This study has shown us that there is not yet an analytical or semi-analytical model that describes the behavior of traps introduced in the barrier. Although transient current measurements have been well presented, there is no work that describes these measurements on the GaN Systems commercial components. Finally, the reliability tests were not all performed and there is a lack of power cycling tests on the $\text{Al}_2\text{O}_3/\text{AlGaIn}/\text{GaN}$ HEMTs.

Then, a new semi-analytical model has been presented to investigate the effects of the trap in HEMTs devices; the study was focused on studying the behavior of the barrier Oxygen traps unintentional introduced into the AlGaIn barrier. The model was applied to an $\text{Al}_2\text{O}_3/\text{AlGaIn}/\text{GaN}$ on Si structure; the structure parameters were given by the project partner CEA-LETI. The model was used to especially study the weight between surface and heterostructure charges (including barrier traps) on the 2DEG density. The Oxygen traps parameters were used from experimental measurements performed on $\text{Al}_2\text{O}_3/\text{AlGaIn}/\text{GaN}$ structure; the interface traps were taken from the literature for a similar device with and without N_2O radical surface treatment. The results of the model showed that there is no absolute dominance of interface traps or barrier traps, but, depending on the polarization conditions, the weight of these traps change. It has been shown that, in the case of a surface treatment, the barrier traps manifest clearly on the total charges behavior. We have also shown a non-linear relation between the gate voltage and the 2DEG density that depends on the different trap densities and the gate polarization condition either for the interface or the barrier. This model may be more developed to model the 2D traps to estimate their effects on the On-state resistance.

A current transient measurements made for the GaN Systems commercial devices were presented for the first time. Drain and gate lag measurements have been presented. The equipment used and the flow of the measurements have been detailed. The parameters of these measurements have been found to affect the transient currents greatly. They can also affect the extraction of trap parameters such as the comparison shown for the transient measurements between high and low sampling rates of the drain. We also studied the effect of OFF stress time on the transient measurements of gate lag. Finally, we tried to identify the origin of the traps based on the results of the literature. From drain lag measurements, traps corresponding to N-Vacancy, foreign atoms like hydrogen, oxygen or carbon

that come in nitrogen substitutional position and Nitrogen interstitials have been identified. From gate lag measurements, traps corresponding to N-Vacancy, foreign atoms like hydrogen, oxygen or carbon that come in nitrogen substitutional position and traps correlated to AlGaN surface states have been identified. In consequence, the GaN-systems commercial components always have instabilities and its dynamics R_{ON} varies significantly. This method was used in chapter 4 to study the effect of ageing by power cycling on the traps state of the $Al_2O_3/AlGaN/GaN$ structure.

Power cycling tests have been done on $Al_2O_3/AlGaN/GaN$ structure for 2140 cycles; a degradation at the measured drain-source voltage was detected. The ageing campaign was stopped at this point. Analyzes after ageing showed indeed a shift in the threshold voltage which mainly due to an evolution of the traps. Concerning transient measurements performed, due to the difficulty of extracting traps parameters from drain lag measurements, the transient current measurements were only presented. Concerning the gate lag measurements, we have observed a rather quantitative change, we have calculated the percentage change of the current transient. Effectively, a percentage that can reach 17% has been detected compared to 2.5% for the first device, while a percentage of 11.56% has been detected compared to 2.21% for the second device. Regarding traps parameters extraction, activation energies of $E_a = 0.092, 0.16$ and 0.36 was revealed before ageing compared to $E_a = 0.28$ and 0.19 after ageing for the first device. For the second device, the activation energies of $E_a = 0.076, 0.16$ and 0.36 compared to $E_a = 0.28$ and 0.19 after ageing was revealed.

In conclusion, the theoretical study has shown that it is not always the interface traps that are responsible for the current collapse in $Al_2O_3/AlGaN/GaN$ devices. There is a weight between these traps and bulk traps which change according to the polarization conditions. Experimental measurements of the GaN systems traps revealed a very unstable behavior that varies according to the polarization conditions. Finally, the power cycling test showed an important effect on the evolution of the traps state in $Al_2O_3/AlGaN/GaN$ devices. However, GaN-based power devices are not yet mature; there is still a lot of work to improve the technology. More detailed theoretical studies should be done to better understand the effect of traps on the other electrical parameters such as the on-state resistance. A verification of the traps signatures, revealed by the electric method presented in this manuscript, is necessary by means of characterization at the microstructural level. Microstructural analyzes are also needed to understand the degradation that occurred after the ageing by power cycling and the source of change in the traps states.

Perspectives

This work can be complete in many directions:

- The modeling of the 2DEG taking into account the traps can be generalized to take other types of traps in the AlGaN layer. It can also be used to model the p-GaN structures, by replacing the oxide layer with the thin p-GaN layer. This modeling can also predict the degradation effect of the oxide layer on the 2DEG density. Furthermore, it can be more developed to take into account the traps in the GaN layer. The semi-analytical formulation can also be improved to simulate the traps effect on the electrical of the component such as I-V characteristics. The simulation results between the 2DEG density and the applied gate voltage can itself be derived in order to estimate the total capacitance under the gate.
- Current transient measurements can also be improved by performing further measurements with more parameter variations. Understanding the variation of the R_{ON} with a high number of points of the off-stress polarization and the duration in the OFF-state will enlighten the traps behavior for GaN devices. The parameters extraction methodology can also be improved by comparing with other methods such as the extraction method using the Marquardt-Levenberg algorithm.
- Other campaigns of ageing must be done to confirm these first results. A direct measurement of the junction temperature can be also performed in order to ensure the estimated non-stress during the presented aging campaigns. Finally, lifetime models can be developed for these GaN devices.

Publications

- [Zak 18a] Fadi Zaki, Zoubir Khatir, René Escoffier, and Ali Ibrahim, "Theoretical investigation of the charges weight between interface and the oxygen traps in barrier layer on the 2DEG density of $\text{Al}_2\text{O}_3/\text{AlGaIn}/\text{GaN}$ HEMTs," *Journal of Computational Electronics*, 2018.
- [Zak 18b] Fadi Zaki, Malika Elharizi, Ali Ibrahim, Zoubir Khatir, Jean-Pierre Ousten, "Effect of power cycling tests on traps under the gate of $\text{Al}_2\text{O}_3/\text{AlGaIn}/\text{GaN}$ normally-ON devices", *Micro-electronics reliability. Under review*
- [Zak 18c] Fadi Zaki, Malika Elharizi, Ali Ibrahim, Zoubir Khatir, Jean-Pierre Ousten, "Effect of power cycling tests on traps under the gate of $\text{Al}_2\text{O}_3/\text{AlGaIn}/\text{GaN}$ normally-ON devices", 29th European Symposium on Reliability of Electron Devices, Failure Physics and Analysis conference, 2018. *Accepted*
- [Lan 17] Matthieu Landel, Stéphane Lefebvre, Denis Labrousse, Cyrille Gautier, Fadi Zaki, Zoubir Khatir, "Dispersion of electrical characteristics and short-circuit robustness of 600V E-mode GaN transistors", *Power Conversion and Intelligent Motion Europe Conference*, 2017.
- [Tho 16] Benoit Thollin, Fadi Zaki, Zoubir Khatir, Regis Meuret, Donatien Martineau, Clement Fita, Pierre-Olivier Jeannin, Johan Delaine, Pierre Lefranc, Laurent Mendizabal, René Escoffier, Farid Hamrani, Laurent Quellec, Eric Lorin, "Design of a GaN HEMT based Inverter Leg Power Module for Aeronautic Applications", 6th Electronic System-Integration Technology Conference, 2016.

References

- [Abo 93] A. Abou-Elnour and K. Schuenemann, "A comparison between different numerical methods used to solve Poisson's and Schroedinger's equations in semiconductor heterostructures," *Journal of Applied Physics*, vol. 74, no. 5, pp. 3273-3276, 1993.
- [Acu 17] E. Acurio, F. Crupi, P. Magnone, L. Trojman, G. Meneghesso, and F. Iucolano, "On recoverable behavior of PBTI in AlGaIn/GaN MOS-HEMT," *Solid-State Electronics*, vol. 132, pp. 49-56, 2017.
- [Ala 09] J. D. Alamo and J. Joh, "GaN HEMT reliability," *Microelectronics Reliability*, vol. 49, no. 9-11, pp. 1200-1206, 2009.
- [Amb 00] O. Ambacher, B. Foutz, J. Smart, J. R. Shealy, N. G. Weimann, K. Chu, M. Murphy, A. J. Sierakowski, W. J. Schaff, L. F. Eastman, R. Dimitrov, A. Mitchell, and M. Stutzmann, "Two dimensional electron gases induced by spontaneous and piezoelectric polarization in undoped and doped AlGaIn/GaN heterostructures," *Journal of Applied Physics*, vol. 87, no. 1, pp. 334-344, 2000.
- [Amb 99] O. Ambacher, J. Smart, J. R. Shealy, N. G. Weimann, K. Chu, M. Murphy, W. J. Schaff, L. F. Eastman, R. Dimitrov, L. Wittmer, M. Stutzmann, W. Rieger, and J. Hilsenbeck, "Two-dimensional electron gases induced by spontaneous and piezoelectric polarization charges in N- and Ga-face AlGaIn/GaN heterostructures," *Journal of Applied Physics*, vol. 85, no. 6, pp. 3222-3233, 1999.
- [And 03] Y. Ando, Y. Okamoto, K. Hataya, T. Nakayama, H. Miyamoto, T. Inoue, and M. Kuzuhara, "12 W/mm recessed-gate AlGaIn/GaN heterojunction field-plate FET," *IEEE International Electron Devices Meeting 2003*.
- [Are 08] A. R. Arehart, A. Corrión, C. Poblenz, J. S. Speck, U. K. Mishra, and S. A. Ringel, "Deep level optical and thermal spectroscopy of traps in n-GaN grown by ammonia molecular beam epitaxy," *Applied Physics Letters*, vol. 93, no. 11, p. 112101, 2008.
- [Arm 06] A. Armstrong, A. Chakraborty, J. S. Speck, S. P. Denbaars, U. K. Mishra, and S. A. Ringel, "Quantitative observation and discrimination of AlGaIn- and GaN-related deep levels in AlGaIn/GaN heterostructures using capacitance deep level optical spectroscopy," *Applied Physics Letters*, vol. 89, no. 26, p. 262116, 2006.
- [Aru 04] S. Arulkumaran, T. Egawa, H. Ishikawa, T. Jimbo, and Y. Sano, "Surface passivation effects on AlGaIn/GaN high-electron-mobility transistors with SiO₂, Si₃N₄, and silicon oxynitride," *Applied Physics Letters*, vol. 84, no. 4, pp. 613-615, 2004.
- [Aur 04] F. D. Auret, W. E. Meyer, L. Wu, M. Hayes, M. J. Legodi, B. Beaumont, and P. Gibart, "Electrical Characterization of hole traps in n-type GaN," *physica status solidi (a)*, vol. 201, no. 10, pp. 2271-2276, 2004.

-
- [Aur 98] F. D. Auret, S. A. Goodman, F. K. Koschnick, J.-M. Spaeth, B. Beaumont, and P. Gibart, "Electrical Characterization of two deep electron traps introduced in epitaxially grown n-GaN during He-ion irradiation," *Applied Physics Letters*, vol. 73, no. 25, pp. 3745-3747, 1998.
- [Aur 99] F. D. Auret, S. A. Goodman, F. K. Koschnick, J.-M. Spaeth, B. Beaumont, and P. Gibart, "Proton bombardment-induced electron traps in epitaxially grown n-GaN," *Applied Physics Letters*, vol. 74, no. 3, pp. 407-409, 1999.
- [Bal 93] Baliga, BJ: Silicon carbide power MOSFET with floating field ring and floating field plate. In: US Patent 5,233,215 (1993).
- [Bas 89] E. M. Bastida, G. P. Donzelli and L. Scopelliti, "GaAs Monolithic Microwave Integrated Circuits using Broadband Tunable Active Inductors," 1989 19th European Microwave Conference, London, UK, 1989, pp. 1282-1287.
- [Ber 09] F. Bertoluzza, N. Delmonte, and R. Menozzi, "Three-dimensional finite-element thermal simulation of GaN-based HEMTs," *Microelectronics Reliability*, vol. 49, no. 5, pp. 468-473, 2009.
- [Ber 97] F. Bernardini, V. Fiorentini, and D. Vanderbilt, "Spontaneous polarization and piezoelectric constants of III-V nitrides," *Physical Review B*, vol. 56, no. 16, 1997.
- [Ber 98] H. Berg and E. Wolfgang, "Advanced IGBT modules for railway traction applications: Reliability testing," *Microelectronics Reliability*, vol. 38, no. 6-8, pp. 1319-1323, 1998.
- [Bin 01] S. Binari, K. Ikossi, J. Roussos, W. Kruppa, D. Park, H. Dietrich, D. Koleske, A. Wickenden, and R. Henry, "Trapping effects and microwave power performance in AlGaIn/GaN HEMTs," *IEEE Transactions on Electron Devices*, vol. 48, no. 3, pp. 465-471, 2001.
- [Bin 02] S. Binari, P. Klein, and T. Kazior, "Trapping effects in GaN and SiC microwave FETs," *Proceedings of the IEEE*, vol. 90, no. 6, pp. 1048-1058, 2002.
- [Bis 13] D. Bisi, M. Meneghini, C. D. Santi, A. Chini, M. Dammann, P. Bruckner, M. Mikulla, G. Meneghesso, and E. Zanoni, "Deep-Level Characterization in GaN HEMTs-Part I: Advantages and Limitations of Drain Current Transient Measurements," *IEEE Transactions on Electron Devices*, vol. 60, no. 10, pp. 3166-3175, 2013.
- [Bla 04] F. Blaabjerg, Z. Chen, and S. Kjaer, "Power Electronics as Efficient Interface in Dispersed Power Generation Systems," *IEEE Transactions on Power Electronics*, vol. 19, no. 5, pp. 1184-1194, 2004.
- [Bla 95] F. Blaabjerg, U. Jaeger, and S. Munk-Nielsen, "Power losses in PWM-VSI inverter using NPT or PT IGBT devices," *IEEE Transactions on Power Electronics*, vol. 10, no. 3, pp. 358-367, 1995.
- [Bot 89] D. Botez, L. Zinkiewicz, T. Roth, L. Mawst, and G. Peterson, "Low-threshold-current-density vertical-cavity surface-emitting AlGaAs/GaAs diode lasers," *IEEE Photonics Technology Letters*, vol. 1, no. 8, pp. 205-208, 1989.
- [Bou 09] K. Boutros, S. Burnham, D. Wong, K. Shinohara, B. Hughes, D. Zehnder, and C. Mcguire, "Normally-off 5A/1100V GaN-on-silicon device for high voltage applications," 2009 IEEE International Electron Devices Meeting (IEDM), 2009.

-
- [Bul 91] Bulucea, C. and Rossen, R. (1991). Trench DMOS power transistor with field-shaping body profile and three-dimensional geometry, US5072266 A.
- [Byk 96] A. D. Bykhovski, V. V. Kaminski, M. S. Shur, Q. C. Chen, and M. A. Khan, "Pyroelectricity in gallium nitride thin films," *Applied Physics Letters*, vol. 69, no. 21, pp. 3254-3256, 1996.
- [Cab 04] P. Cabral, J. Pedro, and N. Carvalho, "Nonlinear Device Model of Microwave Power GaN HEMTs for High Power-Amplifier Design," *IEEE Transactions on Microwave Theory and Techniques*, vol. 52, no. 11, pp. 2585-2592, 2004.
- [Cao 09] X. A. Cao, A. A. Syed, and H. Piao, "Investigation of the electronic properties of nitrogen vacancies in AlGa_N," *Journal of Applied Physics*, vol. 105, no. 6, p. 063707, 2009.
- [Cha 05] Y. Chang, K. Y. Tong, and C. Surya, "Numerical simulation of current-voltage characteristics of AlGa_N/Ga_N HEMTs at high temperatures," *Semiconductor Science and Technology*, vol. 20, no. 2, pp. 188-192, Jun. 2005.
- [Cha 15] T.-F. Chang, T.-C. Hsiao, C.-F. Huang, W.-H. Kuo, S.-F. Lin, G. S. Samudra, and Y. C. Liang, "Phenomenon of Drain Current Instability on p-GaN Gate AlGa_N/Ga_N HEMTs," *IEEE Transactions on Electron Devices*, vol. 62, no. 2, pp. 339-345, 2015.
- [Cha 81] D. Chattopadhyay and H. J. Queisser, "Electron scattering by ionized impurities in semiconductors," *Reviews of Modern Physics*, vol. 53, no. 4, pp. 745-768, Jan. 1981.
- [Che 09a] X. Cheng, M. Li, and Y. Wang, "Physics-Based Compact Model for AlGa_N/Ga_N MODFETs with close-Formed *I-V* and *C-V* Characteristics," *IEEE Transactions on Electron Devices*, vol. 56, no. 12, pp. 2881-2887, 2009.
- [Che 09b] W. Chen, K.-Y. Wong, and K. Chen, "Single-Chip Boost Converter Using Monolithically Integrated AlGa_N/Ga_N Lateral Field-Effect Rectifier and Normally Off HEMT," *IEEE Electron Device Letters*, vol. 30, no. 5, pp. 430-432, 2009.
- [Che 10] X. Cheng, M. Li, and Y. Wang, "An analytical model for current-voltage characteristics of AlGa_N/Ga_N HEMTs in presence of self-heating effect," *Solid-State Electronics*, vol. 54, no. 1, pp. 42-47, 2010.
- [Che 12] D. Cheney, E. Douglas, L. Liu, C.-F. Lo, B. Gila, F. Ren, and S. Pearton, "Degradation Mechanisms for Ga_N and GaAs High Speed Transistors," *Materials*, vol. 5, no. 12, pp. 2498-2520, 2012.
- [Che 88] H. Z. Chen, J. Pasklaski, A. Yariv, and H. Morkoř, "High-frequency modulation of Al-GaAs/GaAs lasers grown on Si substrate by molecular beam epitaxy," *Applied Physics Letters*, vol. 52, no. 8, pp. 605-606, 1988.
- [Che 95] E. I. Chen, N. Holonyak, and S. A. Maranowski, "Al_xGa_{1-x}As-GaAs metal-oxide semiconductor field effect transistors formed by lateral water vapor oxidation of AlAs," *Applied Physics Letters*, vol. 66, no. 20, pp. 2688-2690, 1995.
- [Cho 01] H. Cho, K. Kim, C.-H. Hong, and H. Lee, "Electron traps and growth rate of buffer layers in unintentionally doped Ga_N," *Journal of Crystal Growth*, vol. 223, no. 1-2, pp. 38-42, 2001.

-
- [Chu 08] R. Chu, Z. Chen, S. Denbaars, and U. Mishra, "V-Gate GaN HEMTs With Engineered Buffer for Normally Off Operation," *IEEE Electron Device Letters*, vol. 29, no. 11, pp. 1184-1186, 2008.
- [Con 50] E. Conwell and V. F. Weisskopf, "Theory of Impurity Scattering in Semiconductors," *Physical Review*, vol. 77, no. 3, pp. 388-390, Jan. 1950.
- [Dan 99] X. Z. Dang, P. M. Asbeck, E. T. Yu, G. J. Sullivan, M. Y. Chen, B. T. Mcdermott, K. S. Boutros, and J. M. Redwing, "Measurement of drift mobility in AlGa_xN/GaN heterostructure field-effect transistor," *Applied Physics Letters*, vol. 74, no. 25, pp. 3890-3892, 1999.
- [Das 93] L. Dasaro, L. Chirovsky, E. Laskowski, S. Pei, T. Woodward, A. Lentine, R. Leibenguth, M. Focht, J. Freund, G. Guth, and L. Smith, "Batch fabrication and operation of GaAs-Al/sub x /Ga/sub $1-x$ /As field-effect transistor-self-electrooptic effect device (FET-SEED) smart pixel arrays," *IEEE Journal of Quantum Electronics*, vol. 29, no. 2, pp. 670-677, 1993.
- [Del 82] D. Delagebeaudeuf and N. Linh, "Metal-(n) AlGaAs-GaAs two-dimensional electron gas FET," *IEEE Transactions on Electron Devices*, vol. 29, no. 6, pp. 955-960, 1982.
- [Don 06] Y. Dong, R. M. Feenstra, and J. E. Northrup, "Oxidized GaN(0001) surfaces studied by scanning tunneling microscopy and spectroscopy and by first-principles theory," *Journal of Vacuum Science & Technology B: Microelectronics and Nanometer Structures*, vol. 24, no. 4, p. 2080, 2006.
- [Ela 02] A. Elasser and T. Chow, "Silicon carbide benefits and advantages for power electronics circuits and systems," *Proceedings of the IEEE*, vol. 90, no. 6, pp. 969-986, 2002.
- [Fag 10] M. Fagerlind, F. Allerstam, E. O. Sveinbjornsson, N. Rorsman, A. Kakanakova-Georgieva, A. Lundskog, U. Forsberg, and E. Janzen, "Investigation of the interface between silicon nitride passivations and AlGa_xN/AlN/GaN heterostructures by C(V) Characterization of metal-insulator-semiconductor-heterostructure capacitors," *Journal of Applied Physics*, vol. 108, no. 1, p. 014508, 2010.
- [Fan 05] Z.-Q. Fang, D. C. Look, D. H. Kim, and I. Adesida, "Traps in AlGa_xN/GaN/SiC heterostructures studied by deep level transient spectroscopy," *Applied Physics Letters*, vol. 87, no. 18, p. 182115, 2005.
- [Fan 10] Z.-Q. Fang, B. Claffin, D. C. Look, D. S. Green, and R. Vetury, "Deep traps in AlGa_xN/GaN heterostructures studied by deep level transient spectroscopy: Effect of carbon concentration in GaN buffer layers," *Journal of Applied Physics*, vol. 108, no. 6, p. 063706, 2010.
- [Fan 98] Z.-Q. Fang, D. C. Look, W. Kim, Z. Fan, A. Botchkarev, and H. Morkoř, "Deep centers in n-GaN grown by reactive molecular beam epitaxy," *Applied Physics Letters*, vol. 72, no. 18, pp. 2277-2279, Apr. 1998.
- [Faq 07] M. Faqir, G. Verzellesi, F. Fantini, F. Danesin, F. Rampazzo, G. Meneghesso, E. Zanoni, A. Cavallini, A. Castaldini, N. Labat, A. Touboul, and C. Dua, "Characterization and analysis of trap-related effects in AlGa_xN-GaN HEMTs," *Microelectronics Reliability*, vol. 47, no. 9-11, pp. 1639-1642, 2007.
- [Gaj 16] D. A. Gajewski, B. Hull, D. J. Lichtenwalner, S.-H. Ryu, E. Bonelli, H. Mustain, G. Wang, S. T. Allen, and J. W. Palmour, "SiC power device reliability," 2016 IEEE International Integrated Reliability Workshop (IIRW), 2016.
- [Gal 17] "Gallium Nitride Transistors," GaN Systems. [Online]. Available: <http://www.gansystems.com> [Accessed: 10-Jul-2017].

-
- [Gas 06] M. Gassoumi, J. Bluet, F. Chekir, I. Dermoul, H. Maaref, G. Guillot, A. Minko, V. Hoel, and C. Gaquiere, "Investigation of traps in AlGaIn/GaN HEMTs by current transient spectroscopy," *Materials Science and Engineering: C*, vol. 26, no. 2-3, pp. 383-386, 2006.
- [Gas 08] M. Gassoumi, J. Bluet, G. Guillot, C. Gaquiere, and H. Maaref, "Characterization of deep levels in high electron mobility transistor by conductance deep level transient spectroscopy," *Materials Science and Engineering: C*, vol. 28, no. 5-6, pp. 787-790, 2008.
- [Gas 12] M. Gassoumi, B. Grimbert, C. Gaquiere, and H. Maaref, "Evidence of surface states for AlGaIn/GaN/SiC HEMTs passivated Si₃N₄ by CDLTS," *Semiconductors*, vol. 46, no. 3, pp. 382-385, 2012.
- [Gla 11] J. S. Glaser, J. J. Nasadoski, P. A. Losee, A. S. Kashyap, K. S. Matocha, J. L. Garrett, and L. D. Stevanovic, "Direct comparison of silicon and silicon carbide power transistors in high-frequency hard-switched applications," 2011 Twenty-Sixth Annual IEEE Applied Power Electronics Conference and Exposition (APEC), 2011.
- [Gre 00] B. Green, K. Chu, E. Chumbes, J. Smart, J. Shealy, and L. Eastman, "The effect of surface passivation on the microwave characteristics of undoped AlGaIn/GaN HEMTs," *IEEE Electron Device Letters*, vol. 21, no. 6, pp. 268-270, 2000.
- [Gre 07] D. Gregusova, R. Stoklas, K. Cico, T. Lalinsky, and P. Kordos, "AlGaIn/GaN metal-oxide-semiconductor heterostructure field-effect transistors with 4 nm thick Al₂O₃ gate oxide," *Semiconductor Science and Technology*, vol. 22, no. 8, pp. 947-951, 2007.
- [Gre 08] D. S. Green, B. Vembu, D. Hepper, S. R. Gibb, D. Jin, R. Vetry, J. B. Shealy, L. T. Beechem, and S. Graham, "GaN HEMT thermal behavior and implications for reliability testing and analysis," *physica status solidi (c)*, vol. 5, no. 6, pp. 2026-2029, 2008.
- [Has 03] T. Hashizume, S. Ootomo, and H. Hasegawa, "Suppression of current collapse in insulated gate AlGaIn/GaN heterostructure field-effect transistors using ultrathin Al₂O₃ dielectric," *Applied Physics Letters*, vol. 83, no. 14, pp. 2952-2954, Jun. 2003.
- [Has 03] T. Hashizume, S. Ootomo, T. Inagaki, and H. Hasegawa, "Surface passivation of GaN and GaN/AlGaIn heterostructures by dielectric films and its application to insulated-gate heterostructure transistors," *Journal of Vacuum Science & Technology B: Microelectronics and Nanometer Structures*, vol. 21, no. 4, p. 1828, 2003.
- [Has 04a] T. Hashizume, S. Anantathanasarn, N. Negoro, E. Sano, H. Hasegawa, K. Kumakura, and T. Makimoto, "Al₂O₃ Insulated-Gate Structure for AlGaIn/GaN Heterostructure Field Effect Transistors Having Thin AlGaIn Barrier Layers," *Japanese Journal of Applied Physics*, vol. 43, no. No. 6B, 2004.
- [Has 96] Y. Hasegawa, T. Egawa, T. Jimbo, and M. Umeno, "AlGaAs/GaAs light-emitting diode on a Si substrate with a self-formed GaAs islands active region grown by droplet epitaxy," *Applied Physics Letters*, vol. 68, no. 4, pp. 523-525, 1996.
- [Hel 97] M. Held, P. Jacob, G. Nicoletti, P. Scacco, and M.-H. Poech, "Fast power cycling test of IGBT modules in traction application," *Proceedings of Second International Conference on Power Electronics and Drive Systems*, 1997.
- [Hil 10] O. Hilt, A. Knauer, F. Brunner, E. Bahat-Treidel and J. WÄijrfl, "Normally-off AlGaIn/GaN HFET with p-type Ga Gate and AlGaIn buffer," 2010 22nd International Symposium on Power Semiconductor Devices & IC's (ISPSD), Hiroshima, 2010, pp. 347-350.

-
- [Hir 14] T. Hirose, M. Imai, K. Joshin, K. Watanabe, T. Ogino, Y. Miyazaki, K. Shono, T. Hosoda, and Y. Asai, "Dynamic performances of GaN-HEMT on Si in cascode configuration," 2014 IEEE Applied Power Electronics Conference and Exposition - APEC 2014, 2014.
- [Hor 13] Y. Hori, Z. Yatabe, and T. Hashizume, "Characterization of interface states in $\text{Al}_2\text{O}_3/\text{AlGaIn}/\text{GaN}$ structures for improved performance of high-electron-mobility transistors," *Journal of Applied Physics*, vol. 114, no. 24, p. 244503, 2013.
- [Hu 09] W. D. Hu, X. S. Chen, F. Yin, J. B. Zhang, and W. Lu, "Two-dimensional transient simulations of drain lag and current collapse in GaN-based high-electron-mobility transistors," *Journal of Applied Physics*, vol. 105, no. 8, p. 084502, 2009.
- [Hu 97] J. Hu, R. G. Beck, T. Deng, R. M. Westervelt, K. D. Maranowski, A. C. Gossard, and G. M. Whitesides, "Using soft lithography to fabricate GaAs/AlGaAs heterostructure field effect transistors," *Applied Physics Letters*, vol. 71, no. 14, pp. 2020-2022, Jun. 1997.
- [Hua 11] S. Huang, S. Yang, J. Roberts, and K. J. Chen, "Threshold Voltage Instability in $\text{Al}_2\text{O}_3/\text{GaN}/\text{AlGaIn}/\text{GaN}$ Metal-Insulator-Semiconductor High-Electron Mobility Transistors," *Japanese Journal of Applied Physics*, vol. 50, no. 11R, p. 110202, Jan. 2011.
- [Hua 14] X. Huang, Z. Liu, Q. Li, and F. C. Lee, "Evaluation and Application of 600 V GaN HEMT in Cascode Structure," *IEEE Transactions on Power Electronics*, vol. 29, no. 5, pp. 2453-2461, 2014.
- [Ibb 00] J. P. Ibbetson, P. T. Fini, K. D. Ness, S. P. Denbaars, J. S. Speck, and U. K. Mishra, "Polarization effects, surface states, and the source of electrons in AlGaIn/GaN heterostructure field effect transistors," *Applied Physics Letters*, vol. 77, no. 2, pp. 250-252, Oct. 2000.
- [IEEE Madison Section] Ieee-msn.truenym.net. (2017). IEEE Madison Section - 2007 Meeting Archive. [Online] Available at: <http://ieeee-msn.truenym.net/meet2007.html> [Accessed 8 Sep. 2017].
- [Ike 10] N. Ikeda, Y. Niiyama, H. Kambayashi, Y. Sato, T. Nomura, S. Kato, and S. Yoshida, "GaN Power Transistors on Si Substrates for Switching Applications," *Proceedings of the IEEE*, vol. 98, no. 7, pp. 1151-1161, 2010.
- [Jan 04] H. W. Jang, J. M. Baik, M.-K. Lee, H.-J. Shin, and J.-L. Lee, "Incorporation of Oxygen Donors in AlGaIn," *Journal of The Electrochemical Society*, vol. 151, no. 8, 2004.
- [Jar 07] O. Jardel, F. D. Groote, T. Reveyrand, J.-C. Jacquet, C. Charbonniaud, J.-P. Teyssier, D. Floriot, and R. Quere, "An Electrothermal Model for AlGaIn/GaN Power HEMTs Including Trapping Effects to Improve Large-Signal Simulation Results on High VSWR," *IEEE Transactions on Microwave Theory and Techniques*, vol. 55, no. 12, pp. 2660-2669, 2007.
- [Jen 00] D. Jena, A. C. Gossard, and U. K. Mishra, "Dipole scattering in polarization induced III-V nitride two-dimensional electron gases," *Journal of Applied Physics*, vol. 88, no. 8, p. 4734, 2000.
- [Jen 08] Jena, Debdeep: Polarization Effects on Low-Field Transport & Mobility in III-V Nitride HEMTs. In: *Polarization Effects in Semiconductors*. Boston, MA : Springer US, 2008, S. 161-216.
- [Joz 10] K. Jozwikowski, M. Kopytko, and A. Rogalski, "Enhanced numerical analysis of current-voltage characteristics of long wavelength infrared p-on-n HgCdTe photodiodes," *Bulletin of the Polish Academy of Sciences: Technical Sciences*, vol. 58, no. 4, Jan. 2010.

-
- [Kan 10] M. Kanamura et al., "Enhancement-Mode GaN MIS-HEMTs With n-GaN/i-AlN/n-GaN Triple Cap Layer and High- k Gate Dielectrics," in *IEEE Electron Device Letters*, vol. 31, no. 3, pp. 189-191, March 2010.
- [Kat 84] Y. Katayama, M. Morioka, Y. Sawada, K. Ueyanagi, T. Mishima, Y. Ono, T. Usagawa, and Y. Shiraki, "A New Two-Dimensional Electron Gas Field-Effect Transistor Fabricated on Undoped AlGaAs-GaAs Heterostructure," *Japanese Journal of Applied Physics*, vol. 23, no. Part 2, No. 3, 1984.
- [Key 15] Keysight Technologies N1267A HVSMU/HCSMU Fast Switch Manuel, 2015.
- [Kha 11] S. Khandelwal, N. Goyal, and T. A. Fjeldly, "A Physics-Based Analytical Model for 2DEG Charge Density in AlGaN/GaN HEMT Devices," *IEEE Transactions on Electron Devices*, vol. 58, no. 10, pp. 3622-3625, 2011.
- [Kha 12] S. Khandelwal and T. Fjeldly, "A physics-based compact model of I-V and C-V characteristics in AlGaN/GaN HEMT devices," *Solid-State Electronics*, vol. 76, pp. 60-66, 2012.
- [Kim 03a] H. Kim, R. Thompson, V. Tilak, T. Prunty, J. Shealy, and L. Eastman, "Effects of SiN passivation and high-electric field on AlGaN-GaN HFET degradation," *IEEE Electron Device Letters*, vol. 24, no. 7, pp. 421-423, 2003.
- [Kim 03b] H. Kim, A. Vertiatchikh, R. M. Thompson, V. Tilak, T. R. Prunty, J. R. Shealy, and L. F. Eastman, "Hot electron induced degradation of undoped AlGaN/GaN HFETs," *Microelectronics Reliability*, vol. 43, no. 6, pp. 823-827, 2003.
- [Koc 90] A. Kock, E. Gornik, M. Hauser, and W. Beinstingl, "Strongly directional emission from AlGaAs/GaAs light-emitting diodes," *Applied Physics Letters*, vol. 57, no. 22, pp. 2327-2329, 1990.
- [Kol 88] S. Kola, J. Golio, and G. Maracas, "An analytical expression for Fermi level versus sheet carrier concentration for HEMT modeling," *IEEE Electron Device Letters*, vol. 9, no. 3, pp. 136-138, 1988.
- [Kor 10] P. Kordos, R. Stoklas, D. Gregusova, S. Gazi, and J. Novak, "Trapping effects in Al₂O₃/AlGaN/GaN metal-oxide-semiconductor heterostructure field-effect transistor investigated by temperature dependent conductance measurements," *Applied Physics Letters*, vol. 96, no. 1, p. 013505, Apr. 2010.
- [Kos 13] E. D. Kosten, J. H. Atwater, J. Parsons, A. Polman, and H. A. Atwater, "Highly efficient GaAs solar cells by limiting light emission angle," *Light: Science & Applications*, vol. 2, no. 1, 2013.
- [Lad 86] P. H. Ladbrooke, "GaAs MESFETs and High Mobility Transistors (HEMT)," in H. Thomas, D. V. Morgan, B. Thomas, J. E. Aubrey, and G. B. Morgan, Eds., *Gallium Arsenide for Devices and Integrated Circuits*, Peregrinus, London, 1986.
- [Lag 12] P. Lagger, C. Ostermaier, G. Pobegen, and D. Pogany, "Towards understanding the origin of threshold voltage instability of AlGaN/GaN MIS-HEMTs," 2012 International Electron Devices Meeting, 2012.

-
- [Lar 91] L. E. Larson, R. H. Hackett, M. A. Melendes and R. F. Lohr, "Micromachined microwave actuator (MIMAC) technology-a new tuning approach for microwave integrated circuits," IEEE 1991 Microwave and Millimeter-Wave Monolithic Circuits Symposium. Digest of Papers, Boston, MA, USA, 1991, pp. 27-30.
- [Lee 02] K.-W. Lee, D.-W. Chou, H.-R. Wu, J.-J. Huang, Y.-H. Wang, M.-P. Houg, S.-J. Chang, and Y.-K. Su, "GaN MOSFET with liquid phase deposited oxide gate," Electronics Letters, vol. 38, no. 15, p. 829, 2002.
- [Lee 04] J.-W. Lee and K. Webb, "A Temperature-Dependent Nonlinear Analytic Model for AlGaIn-GaN HEMTs on SiC," IEEE Transactions on Microwave Theory and Techniques, vol. 52, no. 1, pp. 2-9, 2004.
- [Lee 12] Lee, YC; Wang, CY; Kao, TT: Threshold voltage control of recessed-gate III-N HFETs using an electrode-less wet etching technique. In: CS MANTECH (2012)
- [Len 11] T. R. Lenka and A. K. Panda, "Characteristics study of 2DEG transport properties of Al-GaN/GaN and AlGaAs/GaAs-based HEMT," Semiconductors, vol. 45, no. 5, pp. 650-656, 2011.
- [Li 08] M. Li and Y. Wang, "2-D Analytical Model for Current-Voltage Characteristics and Transconductance of AlGaIn/GaN MODFETs," IEEE Transactions on Electron Devices, vol. 55, no. 1, pp. 261-267, 2008.
- [Li 16] X. Li, G. Xie, C. Tang, and K. Sheng, "Charge trapping related channel modulation instability in P-GaN gate HEMTs," Microelectronics Reliability, vol. 65, pp. 35-40, 2016.
- [Lia 16] Y. Liang, L. Jia, Z. He, Z. Fan, Y. Zhang, and F. Yang, "The study of the contribution of the surface and bulk traps to the dynamic Rdson in AlGaIn/GaN HEMT by light illumination," Applied Physics Letters, vol. 109, no. 18, p. 182103, 2016.
- [Lin 05] H. C. Lin, P. D. Ye, and G. D. Wilk, "Leakage current and breakdown electric-field studies on ultrathin atomic-layer-deposited Al₂O₃ on GaAs," Applied Physics Letters, vol. 87, no. 18, p. 182904, 2005.
- [Liu 99] W. Liu, Fundamentals of III-V devices: HBTs, MESFETs, and HFETs/HEMTs. New York: John Wiley & Sons, 1999.
- [Liu 11] Z. H. Liu, G. I. Ng, H. Zhou, S. Arulkumaran, and Y. K. T. Maung, "Reduced surface leakage current and trapping effects in AlGaIn/GaN high electron mobility transistors on silicon with SiN/Al₂O₃ passivation," Applied Physics Letters, vol. 98, no. 11, p. 113506, 2011.
- [Loo 05] D. Look, Z.-Q. Fang, and B. Claffin, "Identification of donors, acceptors, and traps in bulk-like HVPE GaN," Journal of Crystal Growth, vol. 281, no. 1, pp. 143-150, 2005.
- [Lu 12] B. Lu, E. Matioli, and T. Palacios, "Tri-Gate Normally-Off GaN Power MISFET," IEEE Electron Device Letters, vol. 33, no. 3, pp. 360-362, 2012.
- [Lu 13] Y. Lu, S. Yang, Q. Jiang, Z. Tang, B. Li, and K. J. Chen, "Characterization of VT-instability in enhancement-mode Al₂O₃-AlGaIn/GaN MIS-HEMTs," physica status solidi (c), vol. 10, no. 11, pp. 1397-1400, 2013.

-
- [Ma 13] X.-H. Ma, J.-J. Zhu, X.-Y. Liao, T. Yue, W.-W. Chen, and Y. Hao, "Quantitative Characterization of interface traps in Al₂O₃/AlGa_N/Ga_N metal-oxide-semiconductor high-electron-mobility transistors by dynamic capacitance dispersion technique," *Applied Physics Letters*, vol. 103, no. 3, p. 033510, 2013.
- [Mak 82] S. Makram-Ebeid and M. Lannoo, "Quantum model for phonon-assisted tunnel ionization of deep levels in a semiconductor," *Physical Review B*, vol. 25, no. 10, pp. 6406-6424, 1982.
- [Mar 03] M. Marso, M. Wolter, P. Javorka, P. Kordos, and H. Luth, "Investigation of buffer traps in an AlGa_N/Ga_N/Si high electron mobility transistor by backgating current deep level transient spectroscopy," *Applied Physics Letters*, vol. 82, no. 4, pp. 633-635, 2003.
- [Men 04] G. Meneghesso, G. Verzellesi, R. Pierobon, F. Rampazzo, A. Chini, U. Mishra, C. Canali, and E. Zanoni, "Surface-Related Drain Current Dispersion Effects in AlGa_N-Ga_N HEMTs," *IEEE Transactions on Electron Devices*, vol. 51, no. 10, pp. 1554-1561, 2004.
- [Men 08] G. Meneghesso, G. Verzellesi, F. Danesin, F. Rampazzo, F. Zanon, A. Tazzoli, M. Meneghini, and E. Zanoni, "Reliability of Ga_N High-Electron-Mobility Transistors: State of the Art and Perspectives," *IEEE Transactions on Device and Materials Reliability*, vol. 8, no. 2, pp. 332-343, 2008.
- [Men 09] G. Meneghesso, F. Zanon, M. Uren, and E. Zanoni, "Anomalous Kink Effect in Ga_N High Electron Mobility Transistors," *IEEE Electron Device Letters*, vol. 30, no. 2, pp. 100-102, 2009.
- [Men 11] M. Meneghini, N. Ronchi, A. Stocco, G. Meneghesso, U. K. Mishra, Y. Pei, and E. Zanoni, "Investigation of Trapping and Hot-Electron Effects in Ga_N HEMTs by Means of a Combined Electrooptical Method," *IEEE Transactions on Electron Devices*, vol. 58, no. 9, pp. 2996-3003, 2011.
- [Men 13] G. Meneghesso, M. Meneghini, D. Bisi, I. Rossetto, A. Cester, U. K. Mishra, and E. Zanoni, "Trapping phenomena in AlGa_N/Ga_N HEMTs: a study based on pulsed and transient measurements," *Semiconductor Science and Technology*, vol. 28, no. 7, p. 074021, 2013.
- [Men 14] M. Meneghini, I. Rossetto, D. Bisi, A. Stocco, A. Chini, A. Pantellini, C. Lanzieri, A. Nanni, G. Meneghesso, and E. Zanoni, "Buffer Traps in Fe-Doped AlGa_N/Ga_N HEMTs: Investigation of the Physical Properties Based on Pulsed and Transient Measurements," *IEEE Transactions on Electron Devices*, vol. 61, no. 12, pp. 4070-4077, 2014.
- [Men 16a] G. Meneghesso, M. Meneghini, I. Rossetto, D. Bisi, S. Stoffels, M. V. Hove, S. Decoutere, and E. Zanoni, "Reliability and parasitic issues in Ga_N-based power HEMTs: a review," *Semiconductor Science and Technology*, vol. 31, no. 9, p. 093004, 2016.
- [Men 16b] M. Meneghini, I. Rossetto, D. Bisi, M. Ruzzarin, M. V. Hove, S. Stoffels, T.-L. Wu, D. Marcon, S. Decoutere, G. Meneghesso, and E. Zanoni, "Negative Bias-Induced Threshold Voltage Instability in Ga_N-on-Si Power HEMTs," *IEEE Electron Device Letters*, vol. 37, no. 4, pp. 474-477, 2016.
- [Men 17a] M. Meneghini, O. Hilt, J. Wuerfl, and G. Meneghesso, "Technology and Reliability of Normally-Off Ga_N HEMTs with p-Type Gate," *Energies*, vol. 10, no. 2, p. 153, 2017.
- [Men 17b] Meneghini, M.; Meneghesso, G.; Zanoni, E. (Hrsg.): *Power Ga_N Devices, Power Electronics and Power Systems*. Cham : Springer International Publishing, 2017 - ISBN 978-3-319-43197-0

-
- [Men 17c] M. Meneghini, I. Rossetto, C. D. Santi, F. Rampazzo, A. Tajalli, A. Barbato, M. Ruzzarin, M. Borga, E. Canato, E. Zanoni, and G. Meneghesso, "Reliability and failure analysis in power GaN-HEMTs: An overview," 2017 IEEE International Reliability Physics Symposium (IRPS), 2017.
- [Mia 07] L. Miao and W. Yan, "A Physics-Based Compact Direct-Current and Alternating-Current Model for AlGaN/GaN High Electron Mobility Transistors," *Chinese Physics Letters*, vol. 24, no. 10, pp. 2998-3001, 2007.
- [Mic 08] M. Miczek, C. Mizue, T. Hashizume, and B. Adamowicz, "Effects of interface states and temperature on the C-V behavior of metal/insulator/AlGaN/GaN heterostructure capacitors," *Journal of Applied Physics*, vol. 103, no. 10, p. 104510, 2008.
- [Mim 80] T. Mimura, S. Hiyamizu, T. Fujii, and K. Nanbu, "A New Field-Effect Transistor with Selectively Doped GaAs/n-Al_xGa_{1-x}As Heterojunctions," *Japanese Journal of Applied Physics*, vol. 19, no. 5, 1980.
- [Mit 03] O. Mitrofanov, "Mechanisms of gate lag in GaN/AlGaN/GaN high electron mobility transistors," *Superlattices and Microstructures*, vol. 34, no. 1-2, pp. 33-53, 2003.
- [Mit 04] O. Mitrofanov and M. Manfra, "Poole-Frenkel electron emission from the traps in AlGaN/GaN transistors," *Journal of Applied Physics*, vol. 95, no. 11, pp. 6414-6419, 2004.
- [Miz 03] T. Mizutani, Y. Ohno, M. Akita, S. Kishimoto, and K. Maezawa, "A study on current collapse in AlGaN/GaN HEMTs induced by bias stress," *IEEE Transactions on Electron Devices*, vol. 50, no. 10, pp. 2015-2020, 2003.
- [Miz 07] T. Mizutani, M. Ito, S. Kishimoto, and F. Nakamura, "AlGaN/GaN HEMTs With Thin InGaN Cap Layer for Normally Off Operation," *IEEE Electron Device Letters*, vol. 28, no. 7, pp. 549-551, 2007.
- [Miz 11] C. Mizue, Y. Hori, M. Miczek, and T. Hashizume, "Capacitance-Voltage Characteristics of Al₂O₃/AlGaN/GaN Structures and State Density Distribution at Al₂O₃/AlGaN Interface," *Japanese Journal of Applied Physics*, vol. 50, no. 2R, p. 021001, Jan. 2011.
- [Nak 08] A. Nakajima, K. Takao, M. Shimizu, H. Okumura, and H. Ohashi, "Equivalent circuit model for GaN-HEMTs in a switching simulation," *INTELEC 2008 - 2008 IEEE 30th International Telecommunications Energy Conference*, 2008.
- [Neg 07] R. Negra, T. Chu, M. Helaoui, S. Boumaiza, G. Hegazi, and F. Ghannouchi, "Switch-based GaN HEMT model suitable for highly-efficient RF power amplifier design," *2007 IEEE/MTT-S International Microwave Symposium*, 2007.
- [Nel 78] N. J. Nelson, K. K. Johnson, R. L. Moon, H. A. V. Plas, and L. W. James, "Organometallic-sourced VPE AlGaAs/GaAs concentrator solar cells having conversion efficiencies of 19%," *Applied Physics Letters*, vol. 33, no. 1, pp. 26-27, 1978.
- [Oka 04] Y. Okamoto, Y. Ando, K. Hataya, T. Nakayama, H. Miyamoto, T. Inoue, M. Senda, K. Hirata, M. Kosaki, N. Shibata, and M. Kuzuhara, "A 149W recessed-gate AlGaN/GaN FP-FET," *2004 IEEE MTT-S International Microwave Symposium Digest (IEEE Cat. No.04CH37535)*.
- [Oka 08] T. Oka and T. Nozawa, "AlGaN/GaN Recessed MIS-Gate HFET With High-Threshold-Voltage Normally-Off Operation for Power Electronics Applications," *IEEE Electron Device Letters*, vol. 29, no. 7, pp. 668-670, 2008.

-
- [Oki 03] T. Okino, M. Ochiai, Y. Ohno, S. Kishimoto, K. Maezawa, and T. Mizutani, "Drain Current DLTS of AlGa_N/Ga_N MIS-HEMTs," Extended Abstracts of the 2003 International Conference on Solid State Devices and Materials, 2003.
- [Oki 04] T. Okino, M. Ochiai, Y. Ohno, S. Kishimoto, K. Maezawa, and T. Mizutani, "Drain Current DLTS of AlGa_N-Ga_N MIS-HEMTs," IEEE Electron Device Letters, vol. 25, no. 8, pp. 523-525, 2004.
- [Ong 07] A. Ong, J. Carr, J. Balda, and A. Mantooth, "A Comparison of Silicon and Silicon Carbide MOSFET Switching Characteristics," 2007 IEEE Region 5 Technical Conference, 2007.
- [Ota 09] K. Ota, K. Endo, Y. Okamoto, Y. Ando, H. Miyamoto, and H. Shimawaki, "A normally-off Ga_N FET with high threshold voltage uniformity using a novel piezo neutralization technique," 2009 IEEE International Electron Devices Meeting (IEDM), 2009.
- [Par 09] S. Park, C. Floresca, U. Chowdhury, J. L. Jimenez, C. Lee, E. Beam, P. Saunier, T. Balistreri, and M. J. Kim, "Physical degradation of Ga_N HEMT devices under high drain bias reliability testing," Microelectronics Reliability, vol. 49, no. 5, pp. 478-483, 2009.
- [Par 10] Y. S. Park, M. Lee, K. Jeon, I. T. Yoon, Y. Shon, H. Im, C. J. Park, H. Y. Cho, and M.-S. Han, "Deep level transient spectroscopy in plasma-assisted molecular beam epitaxy grown Al_{0.2}Ga_{0.8}N/Ga_N interface and the rapid thermal annealing effect," Applied Physics Letters, vol. 97, no. 11, p. 112110, 2010.
- [Pol 02] A. Y. Polyakov, N. B. Smirnov, A. V. Govorkov, Z.-Q. Fang, D. C. Look, R. J. Molnar, and A. V. Osinsky, "Deep hole traps in n-Ga_N films grown by hydride vapor phase epitaxy," Journal of Applied Physics, vol. 91, no. 10, p. 6580, 2002.
- [Pol 03] A. Y. Polyakov, N. B. Smirnov, A. V. Govorkov, V. N. Danilin, T. A. Zhukova, B. Luo, F. Ren, B. P. Gila, A. H. Onstine, C. R. Abernathy, and S. J. Pearton, "Deep traps in unpassivated and Sc₂O₃-passivated AlGa_N/Ga_N high electron mobility transistors," Applied Physics Letters, vol. 83, no. 13, pp. 2608-2610, 2003.
- [Pol 07] A. Y. Polyakov, N. B. Smirnov, A. V. Govorkov, A. V. Markov, A. M. Dabiran, A. M. Wowchak, A. V. Osinsky, B. Cui, P. P. Chow, and S. J. Pearton, "Deep traps responsible for hysteresis in capacitance-voltage characteristics of AlGa_N/Ga_N heterostructure transistors," Applied Physics Letters, vol. 91, no. 23, p. 232116, Mar. 2007.
- [Rab 12] J. Rabkowski, D. Pefitsis, and H. Nee, "Silicon Carbide Power Transistors: A New Era in Power Electronics Is Initiated," IEEE Industrial Electronics Magazine, vol. 6, no. 2, pp. 17-26, 2012.
- [Rac 14] J. Racko, P. Benko, I. Hotovy, L. Harmatha, M. Mikolasek, R. Granzner, M. Kittler, F. Schwierz, and J. Breza, "A model of trap-assisted tunneling in Ga_N/AlGa_N/Ga_N heterostructure based on exchange times," Applied Surface Science, vol. 312, pp. 68-73, 2014.
- [Ras 02] Rashmi, A. Kranti, S. Haldar, and R. Gupta, "An accurate charge control model for spontaneous and piezoelectric polarization dependent two-dimensional electron gas sheet charge density of lattice-mismatched AlGa_N/Ga_N HEMTs," Solid-State Electronics, vol. 46, no. 5, pp. 621-630, 2002.
- [Ras 10] M. A. Rashid, Power electronics handbook: devices, circuits, and applications. Burlington: Elsevier/Academic Press, 2010.

-
- [Ren 96] F. Ren, M. Hong, W. Hobson, J. Kuo, J. Lothian, J. Mannaerts, J. Kwo, Y. Chen, and A. Cho, "Enhancement-mode p-channel GaAs MOSFETs on semi-insulating substrates," International Electron Devices Meeting. Technical Digest, 1996.
- [Rib 01] P. F. Ribeiro, B. K. Johnson, M. L. Crow, A. Arsoy and Y. Liu, "Energy storage systems for advanced power applications," in Proceedings of the IEEE, vol. 89, no. 12, pp. 1744-1756, Dec 2001.
- [Ris 77] C. Risch and C. Voumard, "Self-pulsation in the output intensity and spectrum of GaAs-AlGaAs cw diode lasers coupled to a frequency-selective external optical cavity," Journal of Applied Physics, vol. 48, no. 5, pp. 2083-2085, 1977.
- [Ros 17] I. Rossetto, M. Meneghini, A. Tajalli, S. Dalcanale, C. D. Santi, P. Moens, A. Banerjee, E. Zanoni, and G. Meneghesso, "Evidence of Hot-Electron Effects During Hard Switching of AlGaIn/GaN HEMTs," IEEE Transactions on Electron Devices, vol. 64, no. 9, pp. 3734-3739, 2017.
- [Ruz 16] M. Ruzzarin, M. Meneghini, I. Rossetto, M. V. Hove, S. Stoffels, T.-L. Wu, S. Decoutere, G. Meneghesso, and E. Zanoni, "Evidence of Hot-Electron Degradation in GaN-Based MIS-HEMTs Submitted to High Temperature Constant Source Current Stress," IEEE Electron Device Letters, vol. 37, no. 11, pp. 1415-1417, 2016.
- [Sai 03] W. Saito, Y. Takada, M. Kuraguchi, K. Tsuda, I. Omura, T. Ogura, and H. Ohashi, "High breakdown voltage AlGaIn-GaN power-HEMT design and high current density switching behavior," IEEE Transactions on Electron Devices, vol. 50, no. 12, pp. 2528-2531, 2003.
- [Sai 05] W. Saito, M. Kuraguchi, Y. Takada, K. Tsuda, I. Omura, and T. Ogura, "Influence of Surface Defect Charge at AlGaIn-GaN-HEMT Upon Schottky Gate Leakage Current and Breakdown Voltage," IEEE Transactions on Electron Devices, vol. 52, no. 2, pp. 159-164, 2005.
- [Sai 06] W. Saito, Y. Takada, M. Kuraguchi, K. Tsuda, and I. Omura, "Recessed-gate structure approach toward normally off high-voltage AlGaIn/GaN HEMT for power electronics applications," IEEE Transactions on Electron Devices, vol. 53, no. 2, pp. 356-362, 2006.
- [Sak 91] T. Saku, Y. Hirayama, and Y. Horikoshi, "High Electron Mobility in AlGaAs/GaAs Modulation-Doped Structures," Japanese Journal of Applied Physics, vol. 30, no. Part 1, No. 5, pp. 902-905, 1991.
- [Sak 96] T. Saku, Y. Horikoshi, and Y. Tokura, "Limit of Electron Mobility in AlGaAs/GaAs Modulation-doped Heterostructures," Japanese Journal of Applied Physics, vol. 35, no. Part 1, No. 1A, pp. 34-38, 1996.
- [Sal 09] Sallan, J., Villa, J., Llombart, A. and Sanz, J. (2009). Optimal Design of ICPT Systems Applied to Electric Vehicle Battery Charge. IEEE Transactions on Industrial Electronics, 56(6), pp.2140-2149.
- [San 87] C. J. Sandroff, R. N. Nottenburg, J. C. Bischoff, and R. Bhat, "Dramatic enhancement in the gain of a GaAs/AlGaAs heterostructure bipolar transistor by surface chemical passivation," Applied Physics Letters, vol. 51, no. 1, pp. 33-35, Jun. 1987.
- [Sas 12] A. Sasikumar, A. Arehart, S. A. Ringel, S. Kaun, M. H. Wong, U. K. Mishra, and J. S. Speck, "Direct correlation between specific trap formation and electric stress-induced degradation in MBE-grown AlGaIn/GaN HEMTs," 2012 IEEE International Reliability Physics Symposium (IRPS), 2012.

-
- [Sas 13] A. Sasikumar, A. R. Arehart, S. Martin-Horcajo, M. F. Romero, Y. Pei, D. Brown, F. Recht, M. A. D. Forte-Poisson, F. Calle, M. J. Tadjer, S. Keller, S. P. Denbaars, U. K. Mishra, and S. A. Ringel, "Direct comparison of traps in InAlN/GaN and AlGaIn/GaN high electron mobility transistors using constant drain current deep level transient spectroscopy," *Applied Physics Letters*, vol. 103, no. 3, p. 033509, 2013.
- [Sas 14] A. Sasikumar, D. W. Cardwell, A. R. Arehart, J. Lu, S. W. Kaun, S. Keller, U. K. Mishra, J. S. Speck, J. P. Pelz, and S. A. Ringel, "Toward a physical understanding of the reliability-limiting EC-0.57 eV trap in GaN HEMTs," 2014 IEEE International Reliability Physics Symposium, 2014.
- [Sch 93] I. Schnitzer, E. Yablonovitch, C. Caneau, T. J. Gmitter, and A. Scherer, "30% external quantum efficiency from surface textured, thin-film light-emitting diodes," *Applied Physics Letters*, vol. 63, no. 16, pp. 2174-2176, 1993.
- [Sch 06] D. K. Schroder, *Semiconductor material and device Characterization*. Piscataway, NJ: IEEE Press, 2006.
- [Shi 16] Y. Shi, Q. Zhou, Y. Jin, B. Chen, W. Chen, W. Huang, and B. Zhang, "Impact of interface traps on switching behavior of normally-OFF AlGaIn/GaN MOS-HEMTs," *physica status solidi (c)*, vol. 13, no. 5-6, pp. 328-331, Mar. 2016.
- [Shu 98] M. S. Shur, A. D. Bykhovski, and R. Gaska, "Pyroelectric and Piezoelectric Properties of GaN-Based Materials," *MRS Proceedings*, vol. 537, 1998.
- [Sin 06] R. Singh, "Reliability and performance limitations in SiC power devices," *Microelectronics Reliability*, vol. 46, no. 5-6, pp. 713-730, 2006.
- [Sme 11] V. Smet, F. Forest, J.-J. Huselstein, F. Richardeau, Z. Khatir, S. Lefebvre, and M. Berkani, "Ageing and Failure Modes of IGBT Modules in High-Temperature Power Cycling," *IEEE Transactions on Industrial Electronics*, vol. 58, no. 10, pp. 4931-4941, 2011.
- [Sol 84] P. Solomon and H. Morkoc, "Modulation-doped GaAs/AlGaAs heterojunction field-effect transistors (MODFETs), ultrahigh-speed device for supercomputers," *IEEE Transactions on Electron Devices*, vol. 31, no. 8, pp. 1015-1027, 1984.
- [Sug 88] H. Sugiura, C. Amano, A. Yamamoto, and M. Yamaguchi, "Double Heterostructure GaAs Tunnel Junction for a AlGaAs/GaAs Tandem Solar Cell," *Japanese Journal of Applied Physics*, vol. 27, no. Part 1, No. 2, pp. 269-272, 1988.
- [Sun 13] X. Sun, O. I. Saadat, K. S. Chang-Liao, T. Palacios, S. Cui, and T. P. Ma, "Study of gate oxide traps in HfO₂/AlGaIn/GaN metal-oxide-semiconductor high-electron-mobility transistors by use of ac transconductance method," *Applied Physics Letters*, vol. 102, no. 10, p. 103504, Nov. 2013.
- [Sze 07] S. M. Sze and K. K. Ng, *Physics of semiconductor devices*. Hoboken, NJ: Wiley-Interscience, 2007.
- [Tan 13] Z. Tang, Q. Jiang, Y. Lu, S. Huang, S. Yang, X. Tang, and K. J. Chen, "600-V Normally Off SiN_x/AlGaIn/GaN MIS-HEMT With Large Gate Swing and Low Current Collapse," *IEEE Electron Device Letters*, vol. 34, no. 11, pp. 1373-1375, 2013.

-
- [Tap 10] M. Tapajna, R. J. T. Simms, Y. Pei, U. K. Mishra, and M. Kuball, "Integrated Optical and Electrical Analysis: Identifying Location and Properties of Traps in AlGa_N/Ga_N HEMTs During Electrical Stress," *IEEE Electron Device Letters*, vol. 31, no. 7, pp. 662-664, 2010.
- [Tap 12] M. Tapajna and J. Kuzmik, "A comprehensive analytical model for threshold voltage calculation in Ga_N based metal-oxide-semiconductor high-electron-mobility transistors," *Applied Physics Letters*, vol. 100, no. 11, p. 113509, Dec. 2012.
- [Tir 07] J. M. Tirado, J. L. Sanchez-Rojas and J. I. Izpura, "Trapping Effects in the Transient Response of AlGa_N/Ga_N HEMT Devices," in *IEEE Transactions on Electron Devices*, vol. 54, no. 3, pp. 410-417, March 2007.
- [Tom 10] K. Tomioka, J. Motohisa, S. Hara, K. Hiruma, and T. Fukui, "GaAs/AlGaAs Core Multishell Nanowire-Based Light-Emitting Diodes on Si," *Nano Letters*, vol. 10, no. 5, pp. 1639-1644, Dec. 2010.
- [Tra 99] S. Trassaert, B. Boudart, Gaquiere C., Theron D., Y. Crosnier, F. Huet, and M. Poisson, "Trap effects studies in Ga_N MESFETs by pulsed measurements," *Electronics Letters*, vol. 35, no. 16, p. 1386, 1999.
- [Tre 10] M. Treu, R. Rupp, and G. Solkner, "Reliability of SiC power devices and its influence on their commercialization - review, status, and remaining issues," 2010 IEEE International Reliability Physics Symposium, 2010.
- [Tur 13] S. Turuvekere, N. Karumuri, A. A. Rahman, A. Bhattacharya, A. Dasgupta, and N. Dasgupta, "Gate Leakage Mechanisms in AlGa_N/Ga_N and AlInN/Ga_N HEMTs: Comparison and Modeling," *IEEE Transactions on Electron Devices*, vol. 60, no. 10, pp. 3157-3165, 2013.
- [Uem 07] Y. Uemoto, M. Hikita, H. Ueno, H. Matsuo, H. Ishida, M. Yanagihara, T. Ueda, T. Tanaka, and D. Ueda, "Gate Injection Transistor (GIT)-A Normally-Off AlGa_N/Ga_N Power Transistor Using Conductivity Modulation," *IEEE Transactions on Electron Devices*, vol. 54, no. 12, pp. 3393-3399, 2007.
- [Ver 02] A. Vertiatchikh, L. Eastman, W. Schaff, and T. Prunty, "Effect of surface passivation of AlGa_N/Ga_N heterostructure field-effect transistor," *Electronics Letters*, vol. 38, no. 8, p. 388, 2002.
- [Vet 01] R. Vetury, N. Zhang, S. Keller, and U. Mishra, "The impact of surface states on the DC and RF characteristics of AlGa_N/Ga_N HFETs," *IEEE Transactions on Electron Devices*, vol. 48, no. 3, pp. 560-566, 2001.
- [Vit 12] S. Vitanov, V. Palankovski, S. Maroldt, R. Quay, S. Murad, T. Rodle, and S. Selberherr, "Physics-Based Modeling of Ga_N HEMTs," *IEEE Transactions on Electron Devices*, vol. 59, no. 3, pp. 685-693, 2012.
- [Wal 98] C. G. V. D. Walle, C. Stampfl, and J. Neugebauer, "Theory of doping and defects in III-V nitrides," *Journal of Crystal Growth*, vol. 189-190, pp. 505-510, 1998.
- [Wan 05] Wang, C., Stielau, O. and Covic, G. (2005). Design Considerations for a Contactless Electric Vehicle Battery Charger. *IEEE Transactions on Industrial Electronics*, 52(5), pp.1308-1314.
- [Wan 13] Y.-H. Wang, Y. C. Liang, G. S. Samudra, T.-F. Chang, C.-F. Huang, L. Yuan, and G.-Q. Lo, "Analytical modeling of high temperature characteristics on the DC responses for Schottky-gate AlGa_N/Ga_N HEMT devices," 2013 IEEE ECCE Asia Downunder, 2013.

-
- [Wei 88] K. J. Weingarten, M. J. W. Rodwel and D. M. Bloom, "Picosecond optical sampling of GaAs integrated circuits," in *IEEE Journal of Quantum Electronics*, vol. 24, no. 2, pp. 198-220, Feb. 1988.
- [Win 84] T. H. Windhorn, G. M. Metze, B. Y. Tsaur, and J. C. C. Fan, "AlGaAs double-heterostructure diode lasers fabricated on a monolithic GaAs/Si substrate," *Applied Physics Letters*, vol. 45, no. 4, pp. 309-311, 1984.
- [Win 85] T. H. Windhorn and G. M. Metze, "Room-temperature operation of GaAs/AlGaAs diode lasers fabricated on a monolithic GaAs/Si substrate," *Applied Physics Letters*, vol. 47, no. 10, pp. 1031-1033, 1985.
- [Wol 70] C. M. Wolfe, G. E. Stillman, W. T. Lindley, "Electron Mobility in High-Purity GaAs," in *Journal of Applied Physics* vol. 41, no. 7, pp. 3088-3091, 1970.
- [Woo 08] C. E. C. Wood and D. Jena, *Polarization effects in semiconductors: from ab initio theory to device applications*. New York: Springer, 2008.
- [Wu 15a] T.-L. Wu, D. Marcon, N. Ronchi, B. Bakeroot, S. You, S. Stoffels, M. V. Hove, D. Bisi, M. Meneghini, G. Groeseneken, and S. Decoutere, "Analysis of slow de-trapping phenomena after a positive gate bias on AlGaN/GaN MIS-HEMTs with in-situ Si₃N₄/Al₂O₃ bilayer gate dielectrics," *Solid-State Electronics*, vol. 103, pp. 127-130, 2015.
- [Wu 15b] T.-L. Wu, D. Marcon, B. D. Jaeger, M. V. Hove, B. Bakeroot, S. Stoffels, G. Groeseneken, S. Decoutere, and R. Roelofs, "Time dependent dielectric breakdown (TDDB) evaluation of PE-ALD SiN gate dielectrics on AlGaN/GaN recessed gate D-mode MIS-HEMTs and E-mode MIS-FETs," 2015 IEEE International Reliability Physics Symposium, 2015.
- [Yab 89] E. Yablonovitch, E. Kapon, T. Gmitter, C. Yun, and R. Bhat, "Double heterostructure GaAs/AlGaAs thin film diode lasers on glass substrates," *IEEE Photonics Technology Letters*, vol. 1, no. 2, pp. 41-42, 1989.
- [Yam 85] M. Yamaguchi and C. Amano, "Efficiency calculations of thin-film GaAs solar cells on Si substrates," *Journal of Applied Physics*, vol. 58, no. 9, pp. 3601-3606, 1985.
- [Yan 13] S. Yang, Z. Tang, K.-Y. Wong, Y.-S. Lin, C. Liu, Y. Lu, S. Huang, and K. J. Chen, "High-Quality Interface in MIS Structures With In Situ Pre-Gate Plasma Nitridation," *IEEE Electron Device Letters*, vol. 34, no. 12, pp. 1497-1499, 2013.
- [Yan 14] S. Yang, C. Zhou, Q. Jiang, J. Lu, B. Huang, and K. J. Chen, "Investigation of buffer traps in AlGaN/GaN-on-Si devices by thermally stimulated current spectroscopy and back-gating measurement," *Applied Physics Letters*, vol. 104, no. 1, p. 013504, Jun. 2014.
- [Ye 05] P. D. Ye, B. Yang, K. K. Ng, J. Bude, G. D. Wilk, S. Halder, and J. C. M. Hwang, "GaN metal-oxide-semiconductor high-electron-mobility-transistor with atomic layer deposited Al₂O₃ as gate dielectric," *Applied Physics Letters*, vol. 86, no. 6, p. 063501, Jul. 2005.
- [Yim 06] Yimin Gao and Ehsani, M. (2006). Parametric design of the traction motor and energy storage for series hybrid off-road and military vehicles. *IEEE Transactions on Power Electronics*, 21(3), pp.749-755.
- [Yos 97] I. Yoshida, "2-GHz Si power MOSFET technology," *International Electron Devices Meeting. IEDM Technical Digest*, Washington, DC, USA, 1997, pp. 51-54.

-
- [Yu 99] E. T. Yu, X. Z. Dang, P. M. Asbeck, S. S. Lau, and G. J. Sullivan, "Spontaneous and piezoelectric polarization effects in III-V nitride heterostructures," *Journal of Vacuum Science & Technology B: Microelectronics and Nanometer Structures*, vol. 17, no. 4, p. 1742, 1999.
- [Yua 07] Y. Yuan-Zheng, H. Yue, F. Qian, Z. Jin-Cheng, M. Xiao-Hua, and N. Jin-Yu, "GaN MOS-HEMT Using Ultra-Thin Al₂O₃ Dielectric Grown by Atomic Layer Deposition," *Chinese Physics Letters*, vol. 24, no. 8, pp. 2419-2422, 2007.
- [Zha 04] W. Zhao and D. Jena, "Dipole scattering in highly polar semiconductor alloys," *Journal of Applied Physics*, vol. 96, no. 4, pp. 2095-2101, 2004.
- [Zha 13] Y. Zhang, M. Sun, S. J. Joglekar, T. Fujishima, and T. Palacios, "Threshold voltage control by gate oxide thickness in fluorinated GaN metal-oxide-semiconductor high-electron-mobility transistors," *Applied Physics Letters*, vol. 103, no. 3, p. 033524, 2013.
- [Zin 89] L. M. Zinkiewicz, T. J. Roth, L. J. Mawst, D. Tran, and D. Botez, "High-power vertical-cavity surface-emitting AlGaAs/GaAs diode lasers," *Applied Physics Letters* (1989)
-

Appendix A

General implementation method of the semi-analytical model using the object-oriented programming

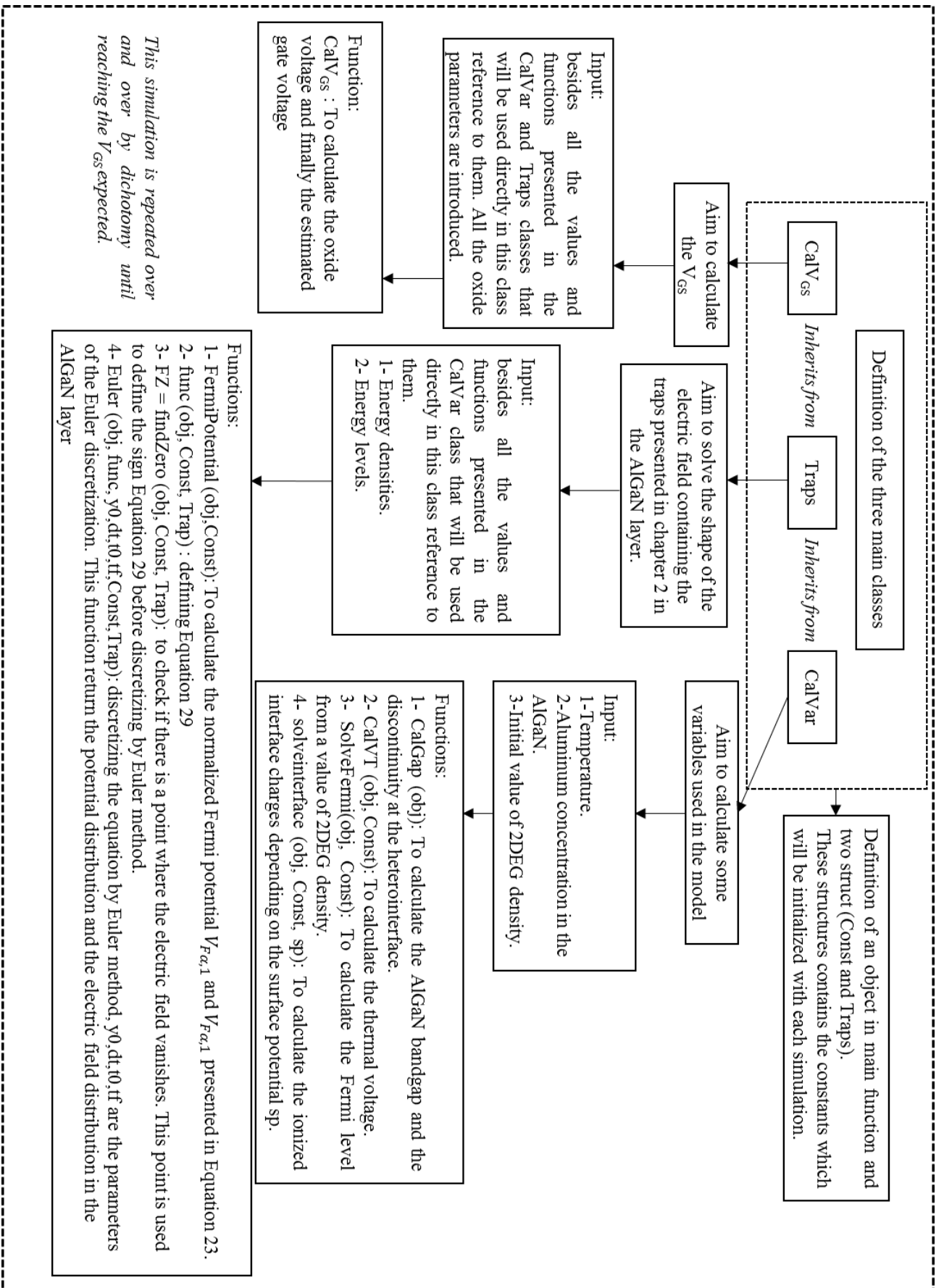


Figure A.1: Implementation method of the semi-analytical using the OOP.

Appendix B

Alternative analytical model

B.1 Physical problem:

In this appendix, we present an essay of an analytical formulation developed during the thesis in order to integrate the traps located in the AlGaN barrier.

The behavior of the potential in this barrier is the basis of our analytical integration. Knowing that the potential maximum is located in this layer, we can then conclude that the electric field vanishes at this point. A second useful information is that traps are deep levels in the bandgap compared to donors, which are intentionally doped in the structure. Traps level cannot be considered as ionized in a homogeneous way. Based on these hypotheses, we can divide the AlGaN layer into three main regions as shown in *Figure B.1*, and *Figure B.2* presents the corresponding possible cases for the electric field distribution.

Figure B.2a presents a typical case where the Fermi level crosses the energy level of the traps in the AlGaN layer. Then, we find three different regions, two regions at the extremities where there is an ionization of traps and a region in the middle where the traps are not ionized. Donor impurities (ND) (not shown in the energy band diagram) are considered ionized in the whole layer (over the three zones). For *Figure B.2b* and *Figure B.2c*, they are also typical cases where a relatively high positive voltage is applied (b) which there is only an ionization in the hetero-interface side, or a relatively high negative voltage is applied (c).

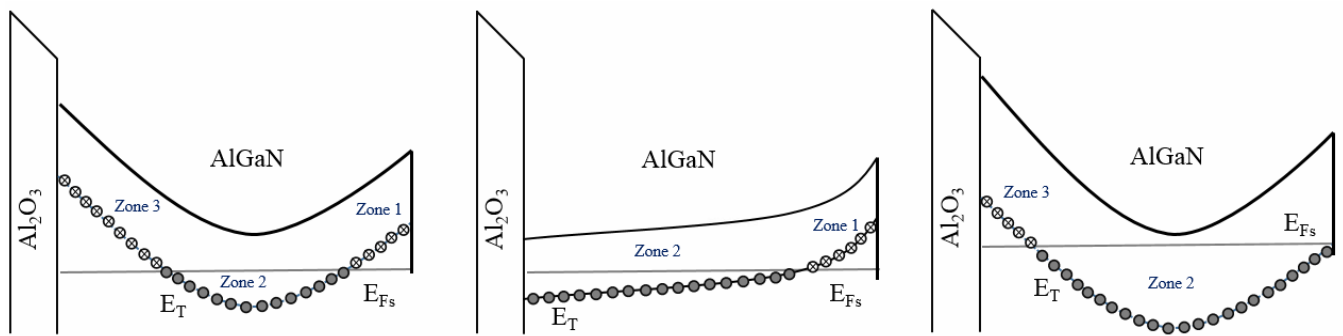


Figure B.1: Possible potential distribution.

B.2. MATHEMATICAL DESCRIPTION:

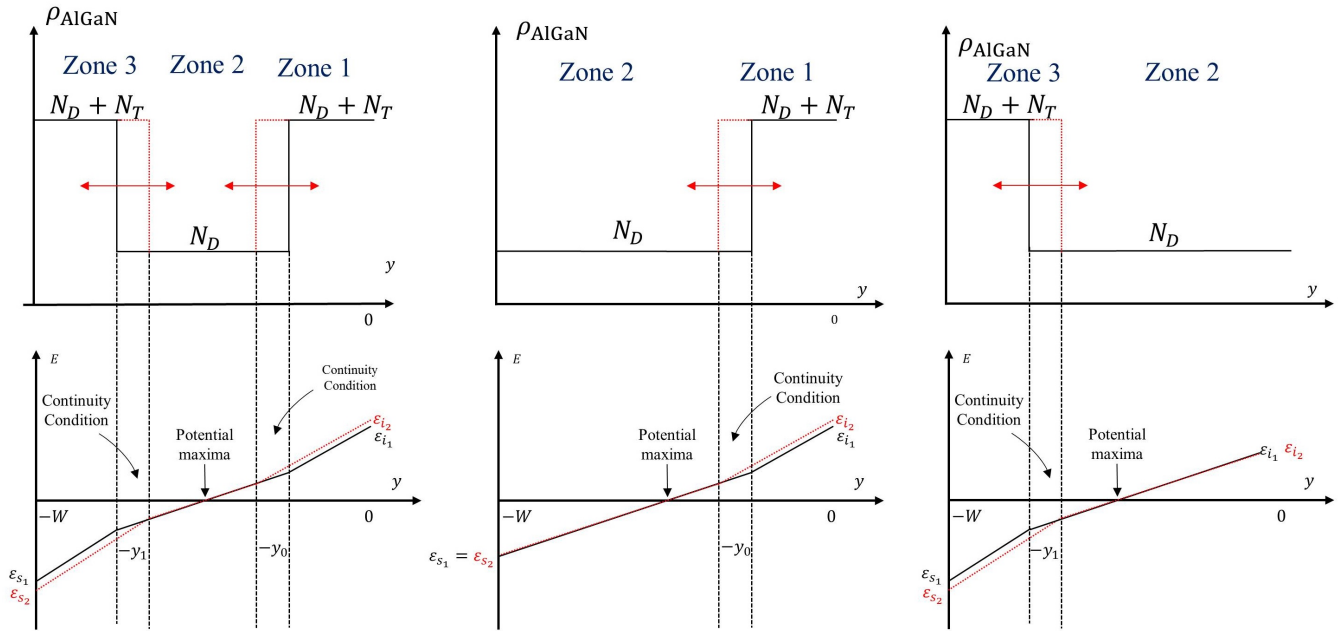


Figure B.2: Possible electric field distribution, a) General case , b) Case when high positive voltage is applied , c) Case when a high negative voltage is applied.

Now we can introduce the details of the mathematical description.

B.2 Mathematical description:

It is necessary to define some notations, which are grouped in the following table:

$y_0(nm)$	First point of intersection between Fermi level and trap energy level
$y_1(nm)$	Second point of intersection between Fermi level and trap energy level
$N_T(cm^{-1})$	Homogeneous trap density
$N_D(cm^{-1})$	Homogeneous donor density
$W(nm)$	AlGaN layer width

Table B.1: Notations used for this mathematical integration.

The main idea of the mathematical formulations presented is to focus on solving the 1D Poisson equation on three zones by respecting the continuity conditions. For each zone, we describe the expressions of the potential and electric field distribution, and we show the continuity conditions.

B.2.1 Electric field distribution:

B.2.1.1 Zone1:

Electric field distribution:

$$E(y) = \frac{q(N_D + N_T)}{\epsilon}y + \frac{qn_s}{\epsilon} \quad (\text{B.1})$$

Boundary condition:

B.2. MATHEMATICAL DESCRIPTION:

$$E(-y_0) = \frac{q(N_D + N_T)}{\epsilon}y_0 + \frac{qn_s}{\epsilon} \quad (\text{B.2})$$

Zone 1 → Zone 2 continuity condition for electric field:

$$E^-(y_0) = E^+(y_0) \quad (\text{B.3})$$

$$\frac{-q(N_D + N_T)}{\epsilon}y_0 + \frac{qn_s}{\epsilon} = \frac{-qN_D}{\epsilon}y_0 + C_1 \quad (\text{B.4})$$

$$C_1 = \frac{q}{\epsilon}(n_s - N_T y_0) \quad (\text{B.5})$$

B.2.1.2 Zone2:

Electric field distribution:

$$E(y) = \frac{qN_D}{\epsilon}y + C_1 \quad (\text{B.6})$$

Boundary condition:

$$E(-y_0) = \frac{-qN_D}{\epsilon}y_0 + C_1 \quad (\text{B.7})$$

$$E(-y_1) = \frac{-qN_D}{\epsilon}y_1 + C_1 \quad (\text{B.8})$$

Zone 2 → Zone 3 continuity condition for electric field:

$$E^-(y_1) = E^+(y_1) \quad (\text{B.9})$$

$$\frac{-qN_D}{\epsilon}y_1 + \frac{q}{\epsilon}(n_s - N_T y_0) = \frac{-q(N_D + N_T)}{\epsilon}y_1 + C_2 \quad (\text{B.10})$$

$$C_2 = \frac{q}{\epsilon}(n_s + N_T(y_1 - y_0)) \quad (\text{B.11})$$

B.2.1.3 Zone3:

Electric field distribution:

$$E(y) = \frac{q(N_D + N_T)}{\epsilon}y + C_2 \quad (\text{B.12})$$

Boundary condition:

$$E(-y_1) = \frac{-q(N_D + N_T)}{\epsilon}y_1 + C_2 \quad (\text{B.13})$$

B.2.2 Potential distribution:

B.2.2.1 Zone1:

$$V(y) = -\frac{q(N_D + N_T)}{\epsilon}y^2 - \frac{qn_s}{\epsilon}y + C'_1 \quad (\text{B.14})$$

B.2. MATHEMATICAL DESCRIPTION:

Boundary condition:

$$V(0) = 0 \rightarrow C'_1 = 0 \quad (\text{B.15})$$

$$V(-y_0) = -\frac{q(N_D + N_T)}{2\epsilon} y_0^2 + \frac{qn_s}{\epsilon} y_0 \quad (\text{B.16})$$

Zone 1 \rightarrow Zone 2 continuity condition for the potential distribution:

$$V^-(-y_0) = V^+(-y_0) \quad (\text{B.17})$$

$$-\frac{q(N_D + N_T)}{2\epsilon} y_0^2 + \frac{qn_s}{\epsilon} y_0 = -\frac{qN_D}{2\epsilon} y_0^2 + \frac{q}{\epsilon} (n_s - N_T y_0) y_0 + C'_2 \quad (\text{B.18})$$

$$C'_2 = \frac{q}{2\epsilon} (N_T y_0^2) \quad (\text{B.19})$$

B.2.2.2 Zone2:

Potential distribution:

$$V(y) = -\frac{qN_D}{2\epsilon} y^2 - \frac{q}{\epsilon} (n_s - N_T y_0) y + C'_2 \quad (\text{B.20})$$

Boundary condition:

$$V(-y_0) = -\frac{qN_D}{2\epsilon} y_0^2 + \frac{q}{\epsilon} (n_s - N_T y_0) y_0 + C'_2 \quad (\text{B.21})$$

$$V(-y_1) = -\frac{qN_D}{2\epsilon} y_1^2 + \frac{q}{\epsilon} (n_s - N_T y_0) y_1 + C'_2 \quad (\text{B.22})$$

Zone 2 \rightarrow Zone 3 continuity condition for the potential distribution:

$$V^-(-y_1) = V^+(-y_1) \quad (\text{B.23})$$

$$-\frac{qN_D}{2\epsilon} y_1^2 + \frac{q}{\epsilon} (n_s - N_T y_0) y_1 + \frac{q}{2\epsilon} (N_T y_0^2) = -\frac{q(N_D + N_T)}{2\epsilon} y_1^2 + \frac{q}{\epsilon} (n_s + N_T (y_1 - y_0)) y_1 + C'_3 \quad (\text{B.24})$$

$$C'_3 = \frac{qN_T}{2\epsilon} (y_0^2 - y_1^2) \quad (\text{B.25})$$

B.2.2.3 Zone3:

Potential distribution:

$$V(y) = -\frac{q(N_D + N_T)}{2\epsilon} y^2 - \frac{q}{\epsilon} (n_s + N_T (y_1 - y_0)) y + C'_3 \quad (\text{B.26})$$

Boundary condition:

B.2. MATHEMATICAL DESCRIPTION:

$$V(-y_1) = -\frac{q(N_D + N_T)}{2\epsilon}y_1^2 + \frac{q}{\epsilon}(n_s + N_T(y_1 - y_0))y_1 + C'_3 \quad (\text{B.27})$$

However, this model was replaced by the semi-analytical model because this model presented some limitations, they work well only in cases where the level of the trap cross the Fermi level twice.

Appendix C

Basic features of the B1505A Power Device Analyzer/Curve Tracer

This part is referenced from the device analyzer manual. The Keysight Technologies, Inc. B1505A Power Device Analyzer/Curve Tracer is a single-box solution with next-generation curve tracer functionality that can accurately evaluate and characterize power devices at up to 10 kV and 1500 A. The B1505A is capable of handling all types of power device evaluation, with features that include a wide voltage and current range, fast pulsing capability (10 μ s), $\mu\Omega$ level on-resistance measurement resolution and sub-pA level current measurement capability. In addition, an oscilloscope view permits visual verification of both current and voltage pulsed waveforms.

Two independent analog-to-digital (A/D) converters on each channel support a 2 μ s sampling rate for accurate monitoring of the critical timings that can affect device behavior.

Precision measurement across a wide range of operating conditions:

- All-in-one solution for power device characterization up to 1500 A/10 kV.
- Medium current measurement with high voltage bias (e.g. 500 mA at 1200 V).
- $\mu\Omega$ resistance measurement capability.
- Accurate sub-picoamp level current measurement at high voltage bias.
- Fully automated thermal test from -50 to +250 °C.

Extensive device evaluation capabilities:

- Fully automated Capacitance (C_{iss} , C_{oss} , C_{rss} , etc.) measurement at up to 3000 V of DC bias.
- High power pulsed measurements down to 10 μ s.
- Gate charge measurement covering Nch MOSFETs and IGBTs both in package and on wafer.
- High voltage/high current fast switch option to characterize GaN current collapse effect.
- Up to 5 high voltage (3 kV) source/measure unit channels for reliability applications.
- Perform both hot and cold temperature dependency testing in an interlock equipped test fixture.

Improved measurement efficiency:

- Switch between high-voltage and high-current measurements without the need to recable.
- Automated reconfiguration of test circuitry for transistor capacitance measurement (C_{iss} , C_{oss} , C_{rss} , C_{gs} , C_{gd} , C_{ds} , etc.) for both packaged and on-wafer devices.
- Standard test fixtures with interlock for safe packaged power device testing.
- Supported and secure on-wafer high-power testing over 200 A and up to 10 kV.
- Oscilloscope view allows verification of applied voltage and current waveforms.
- MS Windows-based EasyEXPERT group+ software facilitates data management and simplifies data analysis.

Appendix D

Role of the diode used in the N1267A HVSMU/HCSMU fast switcher

This part is also referenced from the Fast switcher device manual.

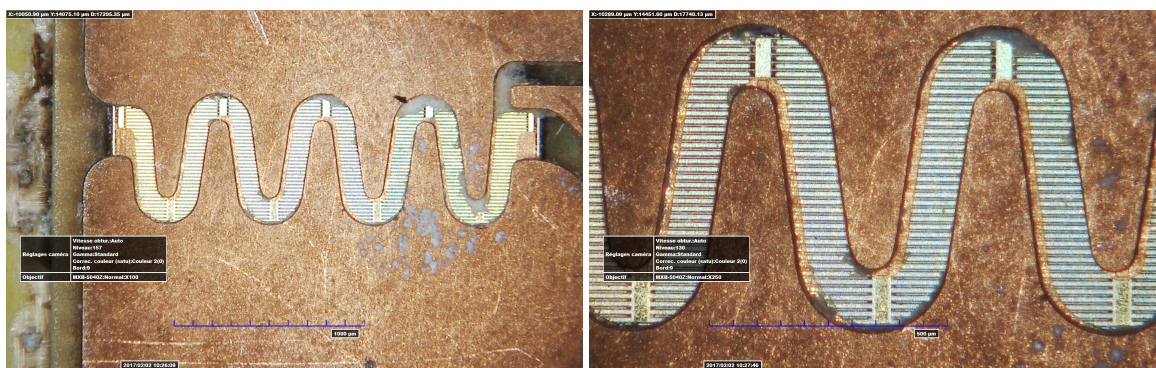
The N1267A HVSMU/HCSMU fast switch is used to switch HVSMU and HCSMU synchronized with the switching of the device under test (DUT) itself. But, direct switching between the HVSMU and HCSMU will cause some glitch or spike because it is switched while each module is outputting voltage or current (wet switching). To avoid this kind of unexpected spike or glitch, N1267A employs a diode to switch between them.

During the off-state of the device, if I_d (off) is smaller than the maximum output current, the output voltage of the HVSMU is fully applied onto the DUT. During this, the output voltage of the HCSMU is set around on-state voltage of the device, and the diode switch is reverse-biased and the HCSMU is disconnected from the DUT. When the DUT is turned on, a drain current starts flowing into the DUT as I_d (on). If the I_d (on) is larger than the maximum current capability, the output voltage is driven down by the DUT. And it moves into its constant current mode with its current compliance. Once the drain voltage is driven down, the diode switch becomes forward-biased and the drain current starts flowing from the HCSMU. Of course, to push the current through the diode, the output voltage has to be larger than the forward voltage (V_f) of the diode switch. Even if the diode switch is turned on, the HVSMU keeps outputting its maximum current too. So the drain current becomes a sum of the output current of the HCSMU (I_{HC}) and the HVSMU (I_{HV}). Also, the drain voltage is slightly different from the output voltage due to the forward voltage of the diode switch. Based on the operation of the diode switch explained above, if the on-current is smaller than the maximum current of the HVSMU, the diode switch is not turned on even if the DUT is turned on. The maximum setting current of the HVSMU is 8 mA in its 1500 V range and 8 mA in the 3000 V range, but it can output around 12 mA during its transient condition between the voltage output mode and the compliance mode (constant current mode). Also, to make switching speed faster, the compliance current of the HVSMU is normally set as its maximum current value. So, if the on-current is about 12 mA or less, the diode switch does not work well. To switch the HVSMU and HCSMU in such a situation, the N1267A has a FET switch in parallel to the diode switch of it.

Appendix E

Optical microscope images of decapsulated GaN Systems component

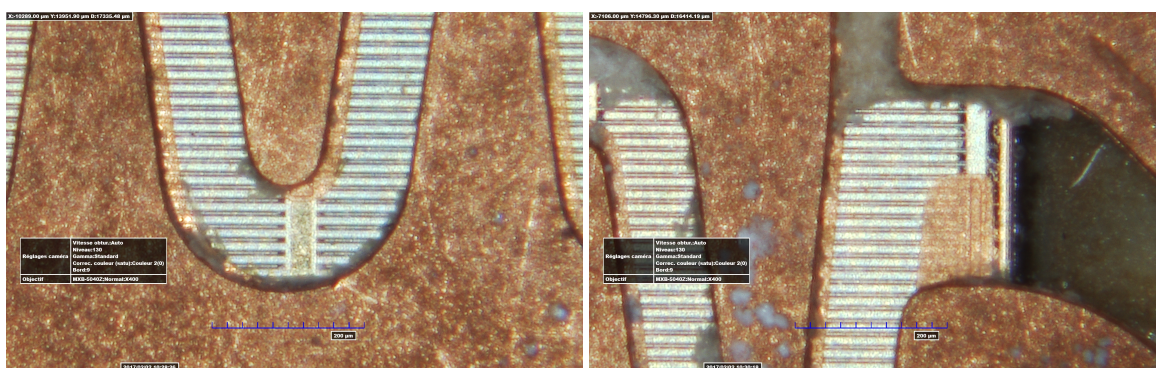
The decapsulation of the commercial components GaN Systems was carried out by placing the components on a heating plate. Then, sulphuric acid H_2SO_4 was used in order to remove the protected layer and finally, the acetone is used to clean the decapsulated device. Electrical characterizations were performed before and after decapsulation. However, a slight error (5 to 10%) represented by a shift in the electrical characteristics has been observed. This decapsulation was carried out in collaboration with Andres Echeverri from the GPM laboratory. The device was decapsulated in order to measure a local temperature by optical fiber



(a) Scale 1:1000 μm .

(b) Scale 1:500 μm .

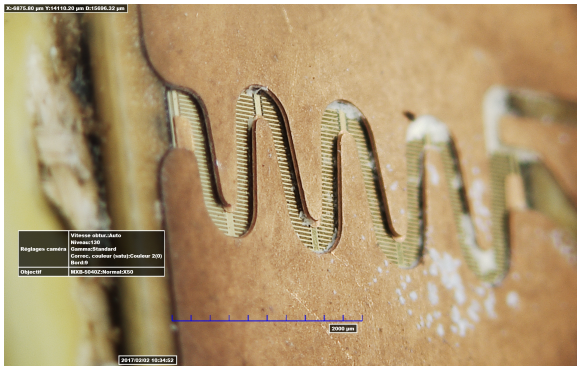
Figure E.1: Different top view of the decapsulated component.



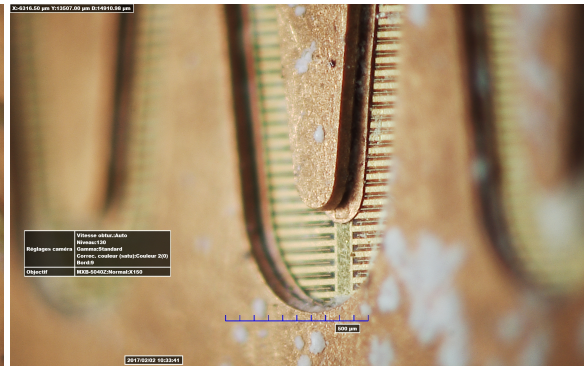
(a) Scale 1:200 μm .

(b) Scale 1:200 μm .

Figure E.2: Different top view of the decapsulated component.

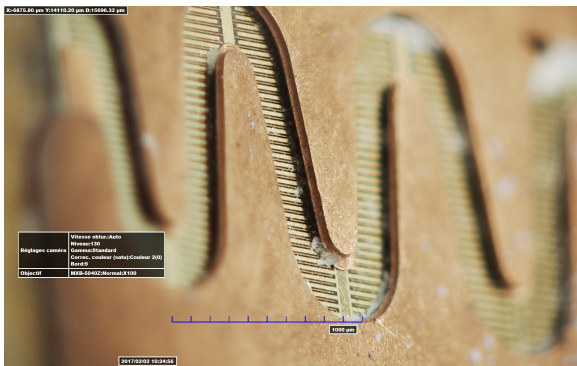


(a) Scale 1:2000 μm .



(b) Scale 1:500 μm .

Figure E.3: Different oblique view of the decapsulated component.



(a) Scale 1:1000 μm



(b) Scale 1:1000 μm .

Figure E.4: Different oblique view of the decapsulated component.

Titre : Caractérisation, Modélisation et Comportement au vieillissement de transistors GaN de puissance.

Mots clés : Modélisation physique, nitrure de gallium, modélisation semi-analytique, caractérisations des pièges, test de cyclage de puissance.

Résumé: L'objectif principal de cette thèse est d'étudier certains éléments de la fiabilité des transistors GaN à haute mobilité d'électrons (HEMT) pour les applications de puissance. Dans la première partie, nous présentons une étude théorique du poids de charges entre les pièges d'oxygène dans la couche barrière AlGaN et les pièges d'interface $\text{Al}_2\text{O}_3/\text{AlGaN}$ sur la densité 2DEG pour des différentes conditions de polarisation de la grille. Pour ce faire, un modèle de charge 1D semi-analytique sera également présenté en utilisant le couplage des équations Poisson-Schrödinger non linéaires. Ce modèle est basé sur une nouvelle expression analytique de la distribution du

champ électrique sous la grille incluant le profil d'oxygène ionisé dans la barrière AlGaN. Dans la deuxième partie, nous présentons un flux de caractérisation des paramètres des pièges tels que des énergies d'activation et des *cross-sections* des composants commerciaux GaN-systems. Le flux de caractérisation sera présenté et la méthode d'extraction des paramètres sera détaillée. Finalement, dans la troisième partie de ce manuscrit, des essais de vieillissement basés sur des tests de cyclage de puissance seront présentés sur des structures $\text{Al}_2\text{O}_3/\text{AlGaN}/\text{GaN}$ MOS-HEMT afin d'étudier et comprendre son effet sur l'évolution de l'état des pièges.

Title: Characterization, modeling and aging behavior of GaN transistors.

Keywords: Physical modeling, gallium nitride, semi-analytical modeling, trap characterization, power cycling test.

Abstract: The primary objective of this thesis is to study some elements of the reliability of high electron mobility (HEMT) GaN transistors for power applications. In the first part, we present a theoretical study of the charges weight between the oxygen traps in the AlGaN barrier layer and the $\text{Al}_2\text{O}_3/\text{AlGaN}$ interface traps on the 2DEG density for different gate polarization conditions. In order to carry out this study, a semi-analytical 1D charge model will be presented based on the nonlinear Poisson-Schrödinger coupled equations. This model is based on a new analytical expression of the electric field distribution under the gate

including the ionized Oxygen profile in the AlGaN barrier. In the second part of this thesis, we present long-term traps parameters characterization such as activation energies and cross-sections of GaN-Systems commercial devices. The characterization flow will be presented, and the method of extracting the physical parameters will be detailed. Finally, in the third part of this thesis, aging tests based on power cycling experimental tests were performed on $\text{Al}_2\text{O}_3/\text{AlGaN}/\text{GaN}$ MOS-HEMT in order to study and understand its effect on the evolution of the traps state.
